Cell. Mol. Life Sci.
DOI 10.1007/s00018-012-1203-2

Cellular and Molecular Life Sciences

RESEARCH ARTICLE

TULA-2, a novel histidine phosphatase, regulates bone remodeling by modulating osteoclast function

Steven H. Back · Naga Suresh Adapala · Mary F. Barbe · Nick C. Carpino · Alexander Y. Tsygankov · Archana Sanjay

Received: 18 September 2012 / Revised: 16 October 2012 / Accepted: 18 October 2012

Abstract Bone is a dynamic tissue that depends on the intricate relationship between protein tyrosine kinases (PTK) and protein tyrosine phosphatases (PTP) for maintaining homeostasis. PTKs and PTPs act like molecular on and off switches and help modulate differentiation and the attachment of osteoclasts to bone matrix regulating bone resorption. The protein T cell ubiquitin ligand-2 (TULA-2), which is abundantly expressed in osteoclasts, is a novel histidine phosphatase. Our results show that of the two family members, only TULA-2 is expressed in osteoclasts and that its expression is sustained throughout the course of osteoclast differentiation, suggesting that TULA-2 may play a role during early as well late stages of osteoclast differentiation. Skeletal analysis of mice that do not express TULA or TULA-2 proteins (DKO mice) revealed that there was a decrease in bone volume due to increased osteoclast numbers and function. Furthermore, in vitro experiments indicated that bone marrow precursor cells from DKO mice have an increased potential to form osteoclasts. At the molecular level, the absence of TULA-2 in osteoclasts results in increased Syk phosphorylation at the Y352 and Y525/526 residues and activation of phospholipase C gamma 2 (PLCγ2) upon engagement of immune-receptor-tyrosine-based-activation-motif (ITAM)—mediated signaling. Furthermore, expression of a phosphatase-dead TULA-2 leads to increased osteoclast function. Taken together, these results suggest that TULA-2 negatively regulates osteoclast differentiation and function.

Keywords Syk · ITAM · Fc receptor · PLCγ · Tyrosine kinase

Electronic supplementary material The online version of this article (doi:10.1007/s00018-012-1203-2) contains supplementary material, which is available to authorized users.

S. H. Back · M. F. Barbe · A. Sanjay
Department of Anatomy and Cell Biology, Temple University School of Medicine, Philadelphia, PA, USA

A. Y. Tsygankov
Department of Microbiology and Immunology, Temple University School of Medicine, Philadelphia, PA, USA

N. C. Carpino
Department of Molecular Genetics and Microbiology, Stony Brook University, Stony Brook, NY, USA

N. S. Adapala · A. Sanjay (✉)
Department of Orthopaedic Surgery, New England Musculoskeletal Institute, University of Connecticut Health Center, Farmington, CT, USA
e-mail: asanjay@uchc.edu

Introduction

Osteoclasts are large multinucleated cells whose major function in the body is to resorb bone under physiological and pathological conditions. These cells are of monocyte-macrophage lineage, and require macrophage colony stimulating factor (M-CSF) and receptor activator of NFκB ligand (RANKL), factors produced by bone marrow stromal cells for their differentiation and maturation [1]. Reversible phosphorylation of tyrosine residues is a central regulator of cellular functions and is controlled by the opposing actions of tyrosine kinases and tyrosine phosphatases [2]. Many signaling pathways in osteoclasts depend crucially on tyrosine phosphorylation. Defective signaling by specific tyrosine kinases is implicated in several osteopetrotic mice, e.g., c-Src$^{-/-}$, Pyk2$^{-/-}$ mice [3, 4]. The normal function of these signaling mechanisms

Published online: 13 November 2012

requires regulated tyrosine phosphorylation of effector proteins, both in terms of time and amplitude, by dephosphorylation catalyzed by protein tyrosine phosphatases (PTPs). Consequently, dysregulation of PTPs produces skeletal abnormalities, as discussed briefly below.

Osteoclasts express several different types of tyrosine phosphatases [5]. It has been shown that mice carrying the *moth-eaten* mutation that inactivates the Src homology 2 (SH2) domain-containing tyrosine phosphatase 1 (SHP-1) have reduced bone mass due to the increased number and hyperactivity of osteoclasts [6]. This suggests that this PTP is a negative regulator of osteoclastogenesis and possibly osteoclast bone resorbing activity. PTP-PEST is a non-receptor phosphatase that is also expressed by osteoclasts, and inhibition of PTP-PEST with RNAi reduces pit formation indicating it has a positive role in osteoclast function [7]. Mice lacking PTPe exhibit a mild bone phenotype suggesting compensatory activity by other family members that have been reported in osteoclasts [8]. In general, however, the role of phosphatases in bone biology is not well known [5].

The TULA/UBASH3/STS family members, TULA/UBASH3A/STS-2 and TULA-2/UBASH3B/p70/STS-1 encoded on different chromosomes, were discovered a few years ago by several groups, including ours [9–12]. Notably, TULA-family proteins belong to the superfamily of histidine phosphatases, sharing a conserved catalytic core centered on a reactive histidine residue [13]. T cell ubiquitin ligand proteins clearly differ from classical cysteine PTPs, such as SHP-1, which is involved in the regulation of osteoclasts. TULA-family proteins exhibit a unique architecture, featuring the ubiquitin-associated (UBA), Src-homology 3 (SH3), and phosphatase domains. In spite of a substantial homology ($\sim$60 % of identity + similarity), TULA-1 and TULA-2 are quite different [14–16]. First, TULA-2 is ubiquitously expressed in mammalian cells [9, 10], whereas TULA-1 is expressed mostly in lymphocytes [10, 11] and possibly, in mast cells [17]. Second, TULA-2 is an active PTP, while the phosphatase activity of TULA-1 is drastically lower [18–20].

It has previously been shown that the lack of TULA-family proteins renders T lymphocytes hyper-reactive [10]. This finding indicates an immunomodulatory effect of TULA-family proteins. Protein tyrosine phosphatases activity of TULA-2 is essential for this effect [20]. Although the mechanism by which TULA modulates T cell reactivity is less clear, it may act as a PTP or through other mechanisms [11, 21, 22]. Protein tyrosine phosphatases activity is also essential for the regulatory role TULA-2 plays in platelets, in which the lack of TULA-2 facilitates activation in response to signaling induced through the GPVI receptor for collagen [23].

In this report, we set out to determine the role of TULA-2, a novel phosphatase in osteoclast differentiation and function. Our results show that the absence of TULA proteins in mice results in decreased bone volume due increased osteoclast numbers and function. We also demonstrate that TULA-2 regulates Syk dephosphorylation in osteoclasts and that the absence of TULA-2 in osteoclasts results in increased osteoclast bone resorption possibly through increased Syk phosphorylation and Syk-mediated signaling events.

Materials and methods

Mice

Generation of mice deficient in both TULA and TULA-2 (DKO) are previously described [10]. Mice were obtained from Dr. Nick Carpino, SUNY NY. Both DKO and the counterpart wild-type mice were maintained on a mixed C57BL/6JX129SvJ background. All mice-related experiments were performed in compliance with the Institutional Animal Care and Use Committee at University of Connecticut Health Center.

Materials

M-CSF and RANKL were purchased from R&D systems (Minneapolis, MN). Bacterial collagenase and dispase were purchased from Calbiochem (San Diego, CA). Anti-TULA-2 antibodies were raised in rabbits against synthetic peptide corresponding to either a N- or C-terminal sequence of human TULA-2: REELYSKVTPRRNRQQR PGT or GPTGGFNWRETLLQE, respectively. (The N-terminal peptide starts at the residue four of TULA-2.) It has been confirmed that both mouse and human TULA-2 react with both antibodies; this is consistent with the identity (C-terminal) or near identity (90 %) of the corresponding sequences for mouse and human TULA-2 are identical. Each antibody was affinity purified on the corresponding antigenic peptide. Both antibodies were used for Western-blot analysis. Antibody against phospho-tyrosine 4G10 was purchased from Millipore. Antibodies to phosphoTyr525/526Syk, phosphoTyr352Syk, phosphoTyr1217PLCγ2, PLCγ2 and GAPDH were purchased from Cell Signaling Technology (Danvers, MA). Antibodies against Syk and 1,25-dihydroxyvitamin D3 and prostaglandin E2 and the leukocyte acid phosphatase kit for tartrate-resistant acid phosphatase (TRAP), reagents required for differentiation and characterization of osteoclasts were obtained from Sigma. Collagen gel was obtained from Nitta Gelatin Co., Osaka, Japan. Osteo

Assay tissue culture plates for pit forming assay were purchased from Corning Life Sciences.

Skeletal analysis

High-resolution microcomputed tomography (microCT) was performed as described previously [24]. Briefly, images of long bones from 8-week-old male mice were acquired using a Skyscan 1172, 12 MPix model (Microphotonics, Allentown, PA). Proximal tibiae and distal femora were scanned with a source voltage of 59 kV, a source current of 167, an image pixel size of approximately 5.75 μm, and a 0.5-mm aluminum filter. Imaging started at the distal end of the femur or the proximal end of the tibiae and included approximately 7 mm (1,335 slices) of the total bone length. Using the CTAn software, trabecular bone was separated from cortical bone with a region of interest tool. Trabecular morphometric traits were computed from binarized images using direct 3D techniques that do not rely on prior assumptions from the underlying structures. The volume of interest for trabecular microarchitectural variables was bounded to the endocortical margin, starting 1.5 mm from the proximal tibial condyles in the direction of the metaphysis, and then extending from this position for 250 slices (1.5 mm). Upper and lower thresholds of 255 and 80 were used to delineate each pixel as ''bone'' or ''non-bone,'' and trabecular bone volume per total volume (BV/TV), mean trabecular thickness (Tb.Th.), mean trabecular number (Tb.N.), and mean trabecular separation (Tb.Sp.) indices were computed.

For histological and histomorphometric analysis, 12-week-old mice were used. To measure dynamic bone formation parameters, mice were injected with calcein (30 mg/kg body weight) 10 and 3 days before sacrifice. Tibiae and femora were dissected and fixed in 3.7 % formaldehyde in phosphate-buffered saline, preserved in 70 % ethanol, and embedded in methyl methacrylate resin. Sections (5 μm) were deplasticized and stained with von Kossa or were left unstained for the measurement of calcein labeling. Some sections were processed for TRAP staining as per manufacturer's instructions (Sigma). For histomorphometric analysis, to assess changes in bone structure and remodeling, tibial sections were measured in the proximal metaphysis beginning 340 μm below the chondro-osseous junction of the secondary spongiosa using image analysis software (BIOQUANT Osteo II, Bioquant Image Analysis Corp., Nashville, TN) as described by Parfitt et al. [25]. Osteoblast numbers per bone surface (Ob.N./B.S.) on trabecular surfaces was determined in toluidine blue-stained sections. Osteoclast numbers per bone surface (Oc.N./B.S.; $TRAP^+$ cells) and osteoclast surfaces on bone surfaces (Oc.S./B.S.) were determined on trabecular surfaces in the secondary spongiosa of TRAP-stained sections. Bone formation rate was calculated from calcein labeled sections.

Determination of serum collagen telopeptide

Serum was prepared from blood collected by cardiac puncture. Concentrations of C-telopeptide (CTX), a degradation product of type I collagen, in serum of 12-week-old mice were determined using the Rat Laps ELISA (Osteometer BioTech A/S, Herlev, Denmark).

Adenoviral constructs

Adenovirus vectors carrying the reporter gene encoding green fluorescent protein (GFP; AxGFP) and the FLAG-tagged TULA-2 phosphatase-dead mutant (AxTULA-2H391A) mutant were generated, as previously described [26, 27].

Analysis of osteoclast precursors by fluorescence activated cell-sorter

Antibodies used for flow cytometric analysis were as the following: anti-mouse CD3 APCe780, anti-mouse B220 APCe780, anti-mouse CD11b FITC. Anti-mouse CD115-biotin was used in combination with streptavidin–phycoerythrin (PE). All antibodies were purchased from eBiosciences (San Diego, CA). To obtain cells, tibiae and femora of 8-week-old mice were flushed with staining medium (1× Hanks balanced salt solution (HBSS), 10 mM HEPES, 2 % newborn calf serum) using 25-gauge needle. After washing cells, red blood cells were lysed with ammonium chloride and cells were filtered through a 40-μm cell strainer to remove cellular debris. Cells were incubated with primary antibodies for 45 min on ice. After washing, cells were incubated with secondary antibodies, when necessary, for 45 min time on ice. Cells were washed and resuspended in staining medium containing propidium iodide (1 μg/ml) and populations of interest were analyzed by using LSRII flow cytometer (BD Biosciences) excluding the dead cells. For some experiments cells were first gated on CD45R, CD3, and NK1.1 negative (Triple Negative) population and then separated as CD11b−/low CD115+ population. To measure LSK ($Sca1^+$, c-Kit^+ Lin^+) population, cells were labeled with biotinylated mouse lineage panel antibodies (BD Bioscience) followed by PerCP-conjugated streptavidin and stem cell markers Sca-1 (FITC-conjugated) and c-Kit (APCe780-conjugated). A lineage negative (Lin-) population was gated for further analysis of stem cell phenotypes ($Sca1^+$, c-Kit^+ Lin^-).

Colony-forming unit assay

Colony-forming assays were performed, as previously described [28]. Briefly, bone marrow cells (1×10^5 cells) were cultured in α-MEM containing 3 % methylcellulose, 20 % FBS, 1 % bovine serum albumin (BSA) and recombinant murine GM-CSF (1 ng/ml). Cells were plated in volume of 1 ml in 35-mm culture dishes and incubated at 37 °C in a humidified atmosphere of 5 % CO_2-air for 7 days. Colonies composed of 50 or more cells were counted after 7 days using an inverted microscope.

Cell culture

For generation of osteoclast-like cells (OCLs), bone marrow was isolated from tibia and femur of 4 to 6-week-old mice. Following overnight incubation, the non-adherent cells were plated at $2.5 \times 10^5/cm^2$ in α-MEM medium containing 10 % FBS and 20 ng/ml M-CSF. Subsequently, cells were treated with M-CSF (20 ng/ml) and RANKL (50 ng/ml) for additional 5–6 days. For some experiments, OCLs were also generated by the co-culture method as previously described [29, 30]. Briefly, mouse primary osteoblastic cells were obtained from 1-day-old mouse calvaria by enzymatic digestion. Bone marrow cells (10^5 cells/cm^2) were co-cultured with calvarial cells (2×10^4 cells/cm^2) on tissue culture plates or collagen gel-coated plates in the presence of 10 nM 1,25-dihydroxy vitamin D3 and 1 μM prostaglandin E2 (Sigma). For some experiments, osteoclasts were infected with adenoviruses bearing TULA-2 mutants as described previously [29, 30].

For the generation of the bone marrow macrophages (BMMs), cells isolated from long bones were plated onto polystyrene culture plates and cultured α-MEM containing 10 % FBS, and 50 ng/ml M-CSF for 72 h. Cells were then trypsinized, counted and plated onto six-well culture plate (10^6 cells/well).

RAW 264.7 cells were cultured in Dulbecco's modified essential medium supplemented with 10 % FBS. Cell lysates were prepared as described below.

RT-PCR analysis

The expression levels of osteoclast differentiation and fusion markers were analyzed by quantitative real-time PCR. Sequences for the primers and details of the procedure are described previously [31].

Pit formation assay

Functionally active OCLs were formed in co-cultures, as described above. An aliquot of the crude OCL preparation was transferred onto hydroxyapatite-coated dishes and cultured for an additional 48 h. The resorbed area was measured using an image analysis system linked to a light microscope (Bioquant Osteo II). A similar aliquot was cultured onto a 24-well dish and cells were TRAP stained after 6 h.

Survival assay

Following differentiation with MCSF and RANKL on day 5, one set of 96-well plate was fixed with 10 % formaldehyde in PBS. Other sets were either kept in α-MEM or were treated with RANKL (50 ng/ml) for 24 h. Cells were fixed and TRAP stained using a commercial kit (Sigma, St. Louis). Total number of TRAP + multinucleated cells were counted and expressed as percentage of the number of cells at the start of the experiment on day 5.

Preparation of cell lysates and immunoprecipitation

For M-CSF and RANKL stimulation, cells were serum starved for 1 h and stimulated with either M-CSF (50 ng/ml) or RANKL (50 ng/ml) for the indicated time period. For Fc receptor stimulation, cells were washed once with serum-free medium and incubated with 10 μg/ml mouse IgG primary antibody (Jackson ImmunoResearch, West Grove, PA) for 30 min at 4 °C. Cells were washed once with serum-free medium and incubated for additional 15 min at 37 °C. Cells were then stimulated by cross-linking with goat anti-mouse secondary antibody (Jackson ImmunoResearch) for the indicated time period at 37 °C. Stimulation of cells was terminated by washing the cells once with ice-cold PBS and flash freezing with liquid N_2. Flash-frozen samples were thawed on ice and lysed in lysis buffer containing 20 mM HEPES (pH 7.4), 150 mM NaCl, 0.05 % Nonidet P-40, 10 % glycerol, 10 mM EDTA, 1 mM Na_3VO_4, 10 μg/ml leupeptin, 10 μg/ml aprotinin, and 1 mM phenylmethylsulfonyl fluoride. After 30 min on ice, lysates were cleared by centrifugation at $12{,}000 \times g$ for 20 min. Lysates were then used for analysis of proteins by Western blotting as previously described. For immunoprecipitation, lysate (750 μg) was incubated with primary antibody (1 μg) for 30 min on ice. Washed Sepharose beads were resuspended in PBS and at a ratio of 1:5 and 40 μl of the suspended beads were added to the lysate/antibody mixture and incubated at 4 °C for 1 h on end-on-end rocking shaker. Beads were then washed three times in the above lysis buffer. Proteins bound to beads were eluted by incubating beads with equal volume of 10 mM glycine (pH 3.0) at room temperature for 30 min. Eluted proteins were mixed with equal volume of SDS loading buffer and boiled for 5 min and loaded on to SDS-PAGE gel.

Statistics

Each experiment was repeated at least three times, unless indicated otherwise. The results obtained from a typical experiment were expressed as the mean ± standard deviation. Statistical analysis was performed using GraphPad Prism 4. Significant differences were determined using students t test; $p < 0.05$ was considered significant.

Results

TULA-2 is the only family member expressed in osteoclasts precursors and mature osteoclasts

Previous reports indicated that in contrast to TULA, which exhibits expression restricted to certain cell types, TULA-2 is ubiquitously expressed [14–16]. We examined the expression pattern of TULA-2 mRNA during osteoclast differentiation and compared it to that of PU.1, RANK and Calcitonin receptor (CalcR), proteins differentially expressed in the process of osteoclast maturation. As shown in Fig. 1a, TULA-2 is expressed already in osteoclast precursors, and, based on an increase in the intensity of the amplified bands, its expression appears to increase after addition of M-CSF or M-CSF + RANKL. In contrast, expression of TULA was undetectable during osteoclastogenesis corroborating previous reports that TULA expression is restricted [10]. These results were confirmed using Western-blot analysis, which clearly revealed the presence of TULA-2 in the precursors and its increase in the course of differentiation (Fig. 1b) and the lack of detectable TULA (data not shown). Together, these results indicate that of the TULA-family of proteins, only TULA-2 is expressed in osteoclast precursors and mature osteoclasts.

Next, in order to determine the intrinsic effects of the loss of TULA-2 during osteoclast differentiation, bone marrow cells from mice deficient in TULA and TULA-2 (DKO) were used. Bone marrow precursors were differentiated into mature osteoclasts in the presence of M-CSF and RANKL. Following TRAP staining, the total number of TRAP positive cells and the number of osteoclasts with more than 20 nuclei were counted. As indicated in Fig. 2a and b, both total numbers of cells and cells with 20+ nuclei were significantly increased in DKO cultures. To test if the observed increase in osteoclasts in the DKO cultures is due to enhanced differentiation or fusion of osteoclast precursor cells, expression of osteoclast differentiation markers was examined by real-time PCR analysis. No significant differences were found between the expression levels of PU.1, RANK, Calcitonin Receptor and TRAP, which are used as differentiation markers (Fig. 2d–g). Similarly,

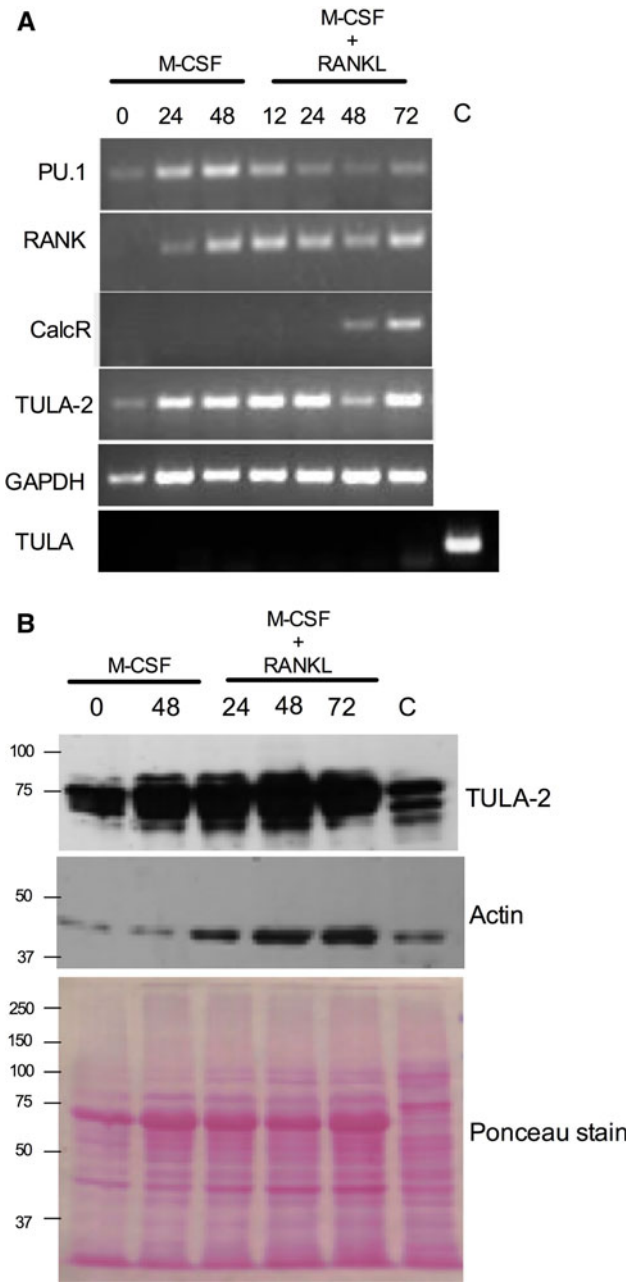

Fig. 1 Expression profile of TULA-2 during osteoclast differentiation. **a** Bone marrow precursors were cultured in the presence of macrophage colony stimulating factor (M-CSF)alone or with M-CSF and receptor activator of NFκB ligand (RANKL), for the indicated number of hours. Expression levels of PU.1, RANK, Calcitonin receptor, TULA-2, TULA and GAPDH were determined by using specific primers. Five microliters of sample was loaded onto an agarose gel to visualize bands. cDNA derived from primary T cells was used as a positive control (*C*). **b** Expression of TULA-2 protein was determined in precursor and mature osteoclast lysates (OCLs). Cells were treated with cytokines for indicated hours. Total cell lysates were electrophoresed and Western blotted with anti-TULA-2 antibodies (*top panel*). Cell lysate derived from macrophage cell line RAW297.4 was used as a positive control (*C*). Blot was re-probed with anti-actin antibodies (*middle panel*) to determine protein loading. Prior to addition of antibodies blot was also stained with Ponceau stain (*lower panel*) to detect protein transfer onto the nitrocellulose paper

expression of DC-STAMP and OC-STAMP, fusion markers, was comparable between the WT and DKO cells (Fig. 2h, i).

An increase in osteoclast numbers could be due to enhanced ability of cells to survive. Therefore, we next examined the ability of mature osteoclasts to survive in cultures in response to MCSF or RANKL. Two sets of osteoclast cultures were derived from bone marrow, as described above. Upon the appearance of large multinucleated cells, one set was fixed and the second set was incubated in serum-free media supplemented MCSF or RANKL for an additional 24 h. Cells were then TRAP-stained and the percent survival was calculated by normalizing the number of TRAP-stained osteoclasts counted after the additional 24-h incubation period to the number of osteoclasts fixed immediately after the appearance of osteoclasts. Comparable survival was observed between WT and DKO cultures under all conditions (Supplementary Figure 1).

Numbers of osteoclast precursors in the bone marrow are increased in the absence of TULA proteins

Osteoclasts are of hematopoietic origin and share the same lineage as macrophages. It has been reported that bone marrow (BM) cells that negative for markers of

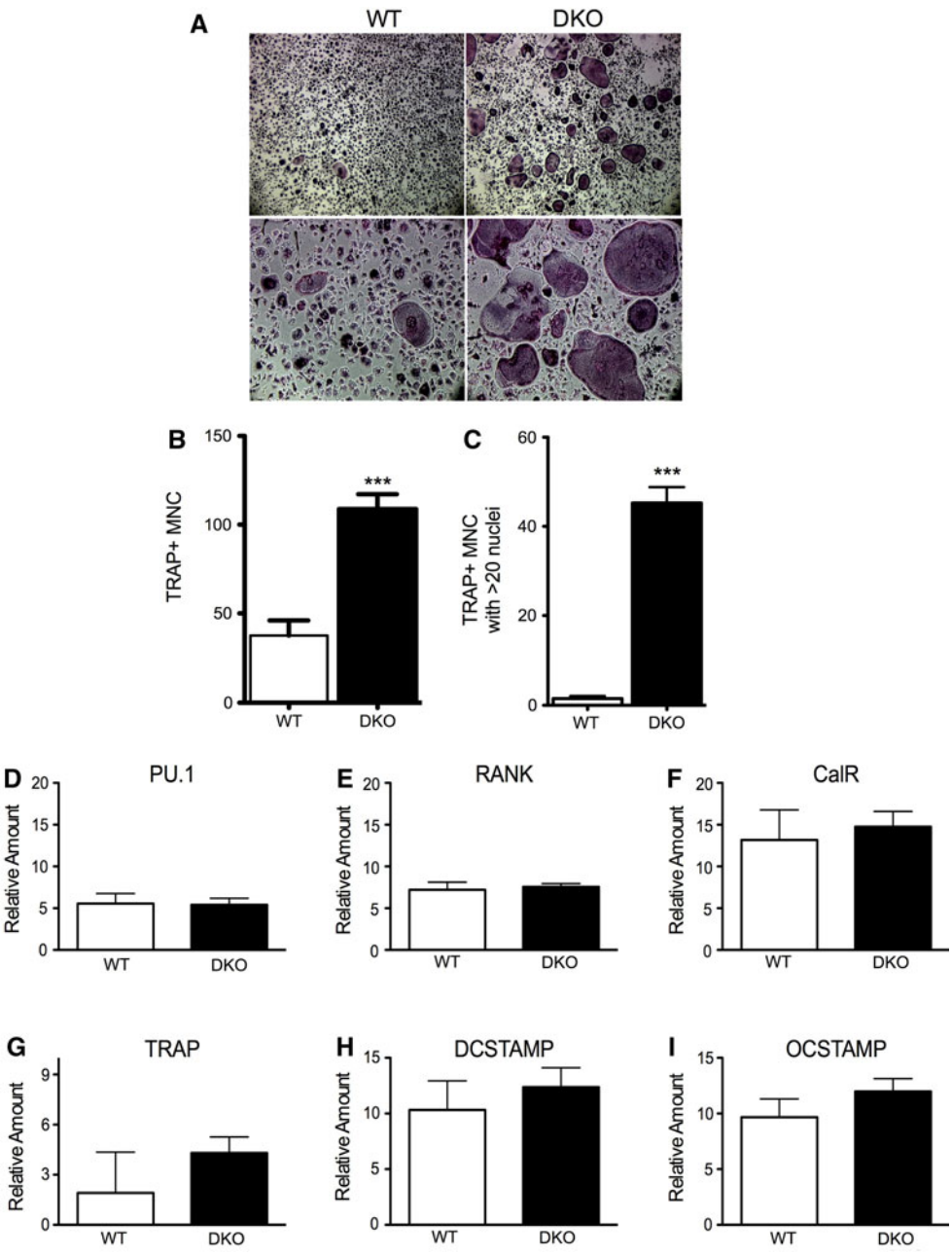

Fig. 2 Absence of TULA proteins results in increased osteoclast numbers in ex vivo cultures. **a** Non-adherent bone marrow precursors were cultured in the presence of M-CSF for 2 days and for additional 3 days in the presence of M-CSF and RANKL. TRAP staining showed increased in numbers of TRAP+ cells in DKO cultures on day 5. Photomicrographs show TRAP-stained OCLs at 4× (*upper panels*) and 20× (*lower panels*) magnification. **b** The numbers of TRAP+ multinucleated osteoclasts (MNCs) in the DKO cultures (*black bars*) were significantly greater than in WT cultures (*white bars*) at day 5. **c** Cells with more than 20–50 nuclei were increased in numbers DKO cultures. **d–i**. Bone marrow cells were cultured in the presence of MCSF (20 μg/ml) and RANKL (50 μg/ml) for 5 days and expression of the following osteoclast differentiation markers **d** PU.1; **e** RANK; **f** CalcR; and **g** TRAP; and fusion markers **h** DC-STAMP and **i** OC-STAMP was determined by real-time PCRs

B-lymphocytes (CD45R, also known as B220), and macrophages (CD11b), but positive for M-CSF receptor c-Fms (CD115), are osteoclast precursors [32, 33]. These populations are distinct from hematopoietic stem cells because of their lack of reactivity to Sca-1 antibody. This population represents less than 2 % of the fresh BM preparations and has the highest levels of in vitro osteoclastogenic activity [33]. Our FACS analysis results comparing the WT and DKO BM cells demonstrated that the numbers of $CD11b^{+}$ cells were comparable, while the number of $CD45^{-}CD3^{-}CD11b^{-/low}$ $CD115^{+}$ cells were doubled in the DKO mice, as compared to the WT mice (Fig. 3a–d). The granulocyte macrophage progenitor (CFU-GM) is the earliest identifiable osteoclast precursor and can become

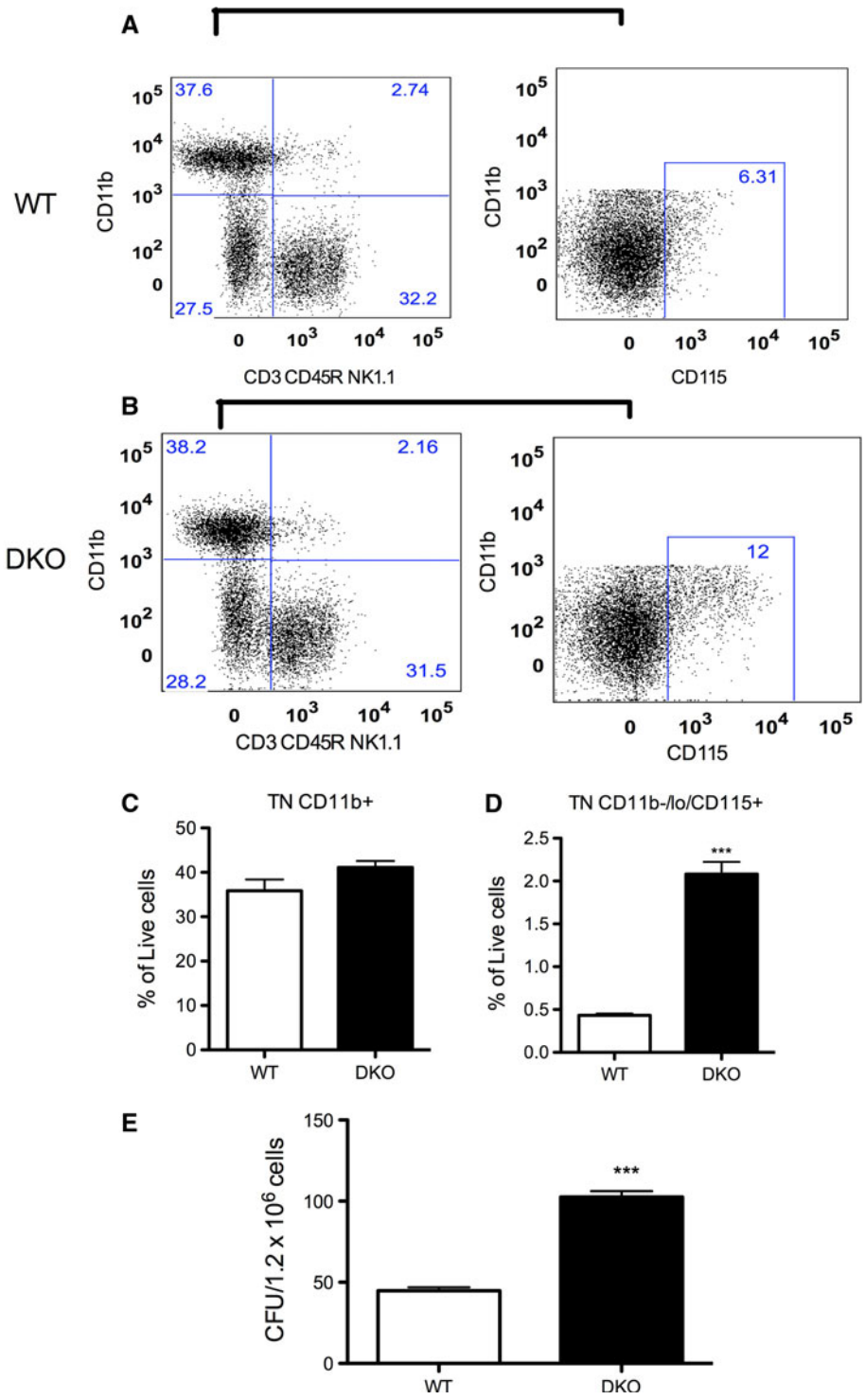

Fig. 3 Numbers of osteoclast precursors are increased in DKO mice. Bone marrow cells obtained from long bones were analyzed for the expression of CD11b and CD115 by FACS analysis. *Dot plots* demonstrating gating parameters and frequencies of different subpopulations for a representative WT (**a**) and DKO (**b**) mouse is shown. *Numbers* represent percentages of parent population. **c** *Bar graphs* represents percentage of total live cells in bone marrow for $CD45R^{-}$, $CD3^{-}$, $NK1.1^{-}$ (TN), $CD11b^{+}$ cells. **d** *Bar graphs* represents percentage of total live cells in bone marrow $CD45R^{-}$, $CD3^{-}$, $NK1.1^{-}$ (TN), CD11b−/low CD115+. $n = 3$ mice/group, mean ± SD; $^{**}p < 0.0001$ compared to WT. **e** BM cells (1×10^5 cells/culture) were prepared for colony-forming assays as described in methods. The cultures were incubated in humidified chamber for 7 days. Clusters of 50 or more cells were scored as a colony. *Bar graph* shows the number of colonies formed. $n = 7$ samples, mean ± SD shown; $^{**}p < 0.0001$ compared to WT. The experiment was repeated twice

osteoclasts in addition to macrophages or granulocytes [28]. Colony-forming unit assays showed that in the presence of GM-CSF DKO BM cells formed twice as many colonies than WT cells (Fig. 3e), suggesting that DKO mice have more osteoclast precursors.

DKO mice have decreased bone volume due to increased numbers and functions of osteoclasts

Gross radiological analysis of long bones from 12-week-old DKO mice showed decreased bone density in the femur and tibia as compared to the age-matched control WT mice (Supplementary Figure 2). MicroCT analysis of long bones of the hind limb indicate that bone volume was significantly decreased in the DKO mice (Fig. 4). In the DKO long bones, although trabecular separation was not affected, a significant decrease in trabecular thickness and number was observed, compared to WT samples (Fig. 4b, d). Histological examination of von Kossa-stained sagittal sections of the proximal tibia from age-matched WT and DKO mice indicated a significant decrease in mineralized trabecular bone in DKO mice as compared to WT (Fig. 5a). This result was confirmed with histomorphometry of von Kossa-stained bone sections (data not shown). Also, no differences were observed in cortical thickness (data not shown). A decrease in bone volume can result from either a decrease in bone formation by osteoblasts or an increase in bone resorption by osteoclasts. Therefore, in order to determine which cell type contributed to the decreased bone volume in DKO mice, we compared the number and activity of both osteoblasts and osteoclasts in DKO and WT mice. Toluidine blue staining of the long bones indicated that the numbers of osteoblasts were comparable in WT and DKO samples (Fig. 5c). Similarly, bone formation rate as measured by calcein double labeling was also comparable between the WT and DKO mice (Fig. 5d). On the other hand, quantification of TRAP-stained cells in the cancellous bone indicated that there was a twofold increase in osteoclast numbers and osteoclast surface/bone surface, in DKO mice as compared to WT (Fig. 5b, e, f).

We next examined the effect of absence of TULA-2 on osteoclast function. Serum levels of the C-terminal collagen telopeptide (CTX), a serum biomarker of osteoclast activity, were increased in DKO mice as compared to WT mice (Fig. 6a). To confirm this defect of DKO osteoclast function, we then examined bone resorption using in vitro pit formation assay. DKO and WT OCLs were generated by co-culture with osteoblasts on collagen gel, as described previously [29]. After 5 days in culture, a portion of the crude OCL preparation was placed on hydroxyapatite-coated tissue culture plates for an additional 48 h. The resorbed area was quantified using image analysis and normalized to the number of OCLs. DKO OCLs resorbed more surface area/cell than the WT OCLs (Fig. 6b, c), confirming the cell autonomous nature of the observed defect in osteoclast function. Thus, the decreased bone volume in the adult DKO mice and increased bone resorption in vivo and in vitro is, at least in part, due to impaired osteoclast function. Taken together, these results suggest that bone resorption under basal conditions is affected in DKO mice.

Syk phosphorylation and Syk-mediated signaling is augmented in DKO cells

The increased bone resorption by osteoclasts in the absence of TULA-2 (Fig. 6) suggested that osteoclast function is modified by DKO, because signaling events are perturbed by the absence of TULA-2. Therefore, we next determined the effects of the loss of TULA-2 on response of BMMs and osteoclasts to M-CSF and RANKL, key physiological stimuli of this cell lineage (Fig. 7a, data not shown). Upon stimulation with RANKL, no significant increase in total tyrosine phosphorylation was evident in either WT or DKO osteoclasts. However, an increase in protein phosphorylation was observed both in WT and DKO cells upon treatment with M-CSF. Notably, both the M-CSF-caused increase and the basal tyrosine phosphorylation were elevated, albeit modestly, in DKO cells as compared to WT cells (Fig. 7a).

Syk is a known substrate of TULA-2 [19] and a key factor in transmitting the ITAM-mediated signaling downstream of FcγR in several cell types, including BMMs [34]. Downstream of ITAM-mediated signaling Syk is also required for osteoclast development and function [35–37]. Therefore, we next examined the phosphorylation events upon engagement of FcγR in BMMs. After Fc receptor crosslinking, there was a robust increase in total tyrosine phosphorylation, which was higher in DKO BMM than in WT BMM (Fig. 7b). Tyrosine phosphorylation of proteins migrating at approximately 75 kD and above was enhanced in DKO cells as compared to WT cells. To reduce background caused by cross-reactivity, we enriched tyrosine-phosphorylated proteins by immunoprecipitating them using anti-pTyr antibody and then immunoblotted the obtained immunoprecipitates for total tyrosine phosphorylation and Syk. An increase in tyrosine phosphorylation was observed in the DKO as compared to WT lysates. Multiple tyrosine-phosphorylated proteins were detected in BMM starting at 72 kDa and above it with approximately 10 kDa increments; the number of discernable bands is much higher in DKO cells than in WT cells (Fig. 7c). Total anti-pTyr reactivity normalized to the amount of Syk is increased by ~1.8-fold in DKO vs. WT cells (Fig. 7c).

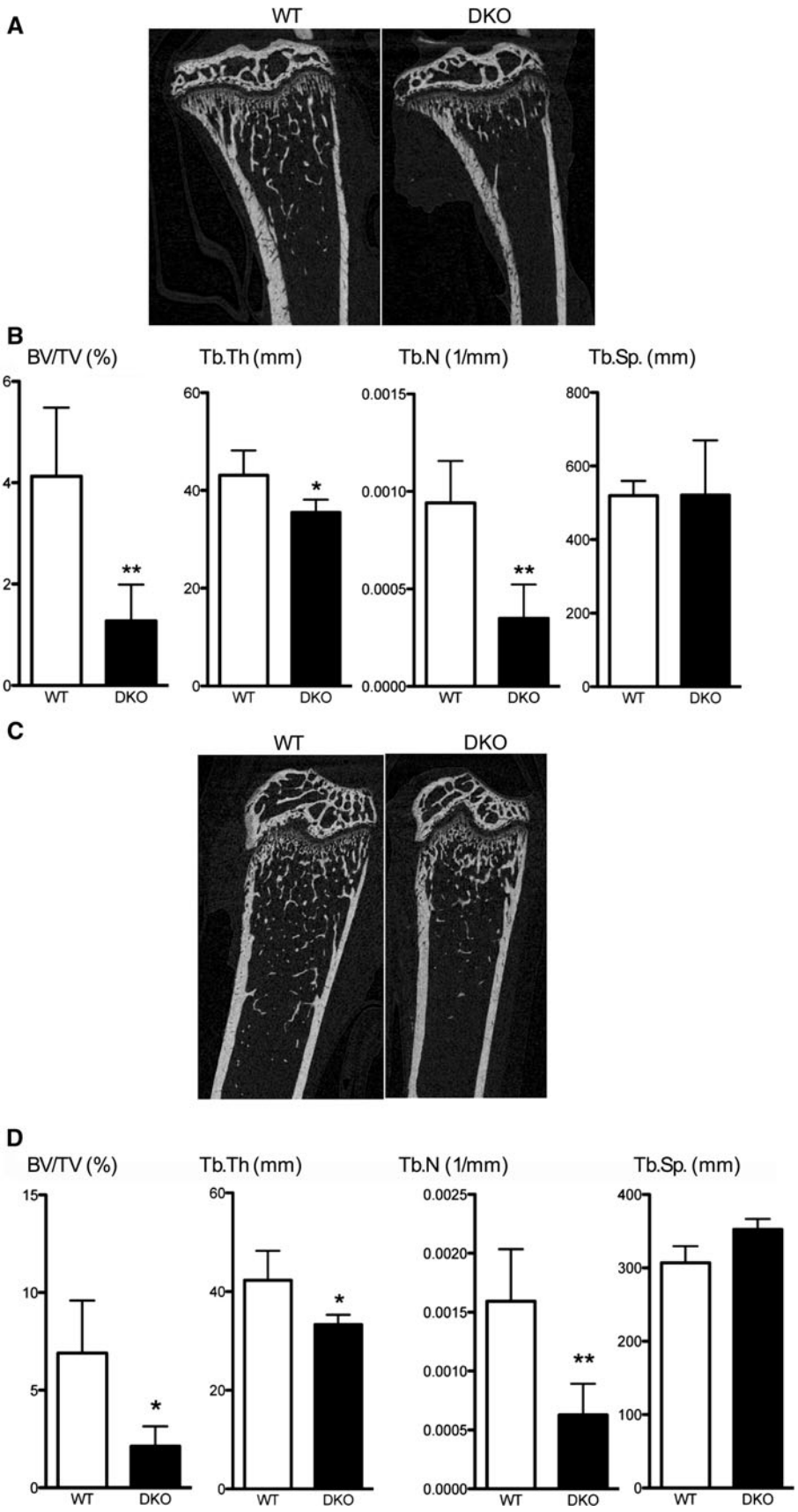

Fig. 4 Absence of TULA proteins results in decreased bone volume. Micro-CT analysis of tibia (**a**) and femur (**c**) from WT and DKO mice. **a** and **c** shows representative sagittal sections of tibia and femur, respectively. Histograms show the trabecular parameters of tibia (**b**) and femur (**d**). $n = 4$ per genotype, 8-week-old male mice, mean ± SD shown; $^{*}p < 0.05$, $^{**}p < 0.01$ compared to WT

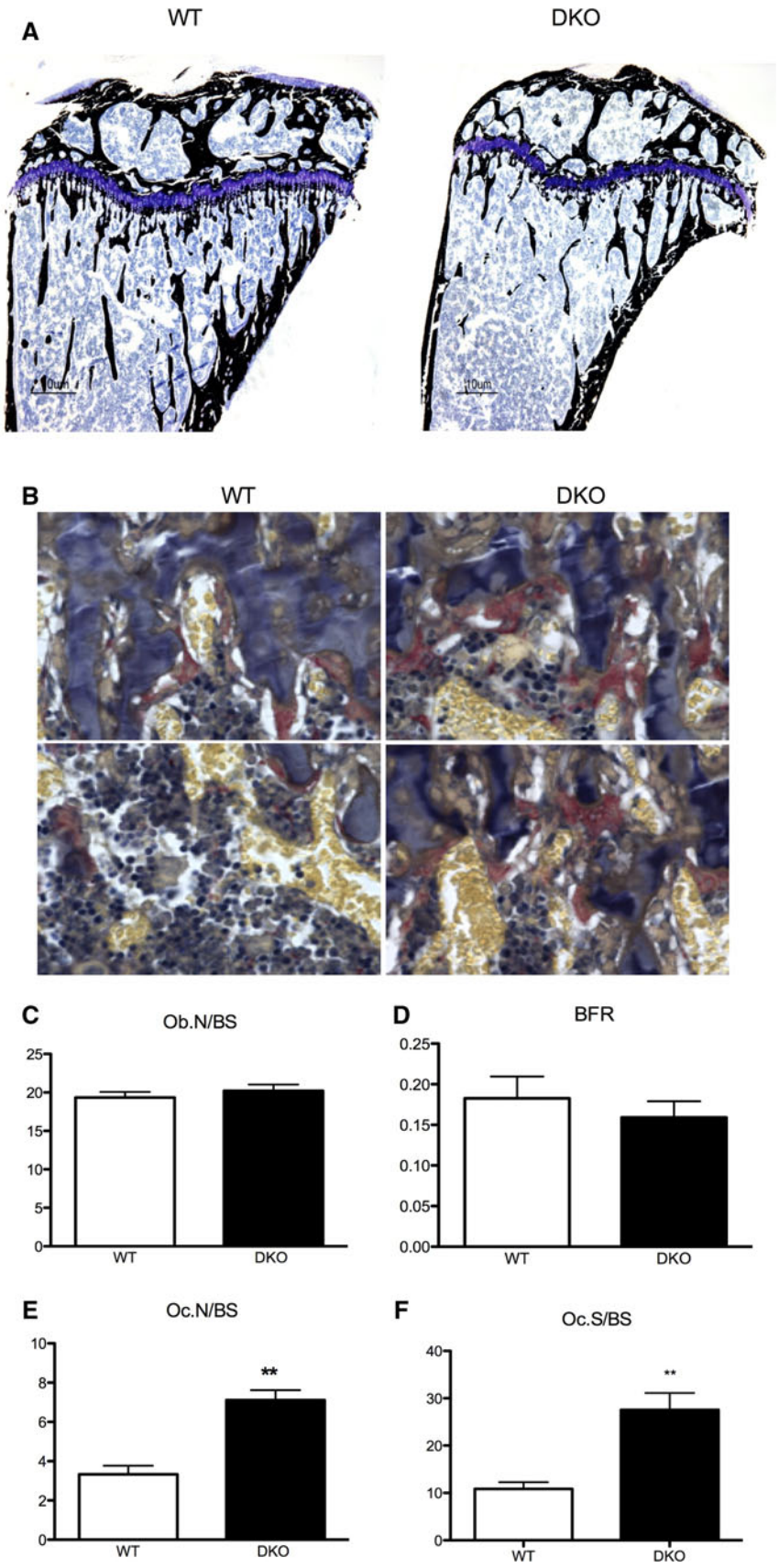

Fig. 5 Absence of TULA proteins results in decreased bone volume due to increased osteoclast numbers. **a** Representative histological sections of proximal tibiae of 12-week-old WT and DKO mice stained with Von Kossa and counterstained with Toluidine blue shows decreased mineralized bone in the metaphyseal trabecular region of DKO samples. Images were taken using a 10× objective. **b** Tibial sections from 12-week-old WT and YF were stained for TRAP (400× magnification). Two different sections for each genotype are shown. **c** Quantification of number of osteoblasts/bone surface (Ob.N./BS), and **d** dynamic parameters of bone formation were assessed using tibias harvested from 8-week-old WT and YF mice that were injected with calcein. as described in the methods. Bone formation rate/bone surface (BFR/BS, $\mu m^2/\mu m/day$) is shown. **e** Osteoclast numbers/bone surface (Oc.N./BS %), and **f** osteoclast surface/bone surface (Oc.S./BS). $n = 4$ mice per genotype; mean ± SD shown; $^{**}p < 0.01$, compared to WT

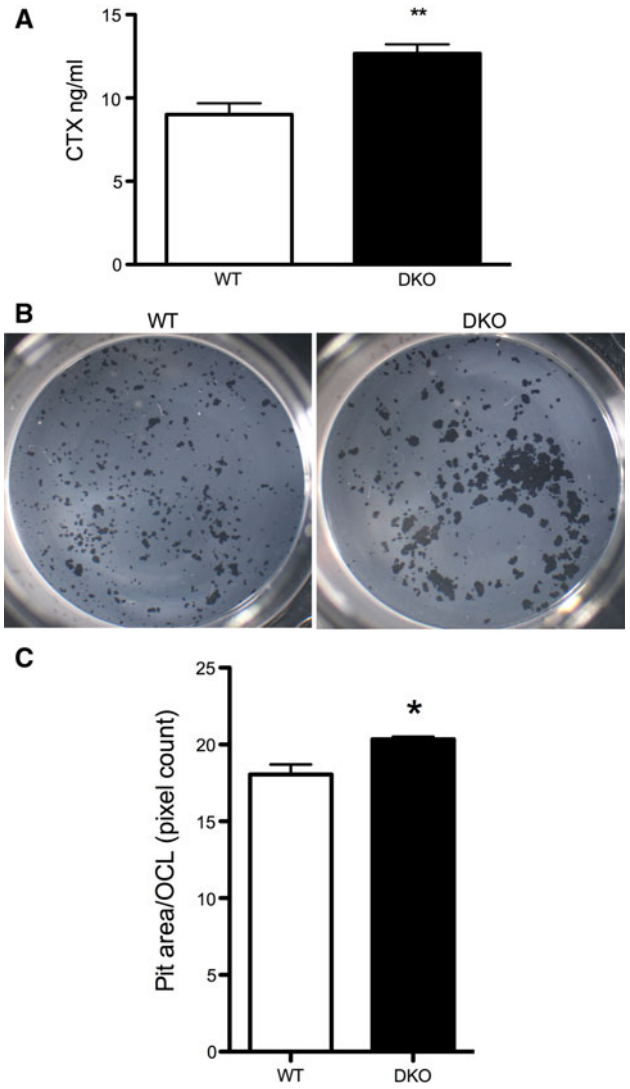

Fig. 6 Absence of TULA-2 in osteoclasts results in increased activity both in vivo and in vitro. **a** Measurement of serum collagen telopeptide (CTX) demonstrated increased osteoclast activity in the DKO mice ($n = 4$ male mice per genotype; mean ± SD shown; $^{**}p < 0.01$, compared to WT). **b** Photomicrographs of the resorbed area. **c** *Bar graph* demonstrating pit formation activity of DKO osteoclasts. Osteoclasts were generated by co-culture method, as described in the methods. After removing adherent cells, resorbed area was quantified and normalized for the number of osteoclasts. Data are presented as mean SE ($n = 9$). $^{**}p < 0.001$ compared to the WT samples

Given that Syk has several tyrosine residues that can be differentially phosphorylated in DKO and WT cells and may exhibit differential reactivity to a total anti-pTyr antibody, we next analyzed the phosphorylation status of individual tyrosine residues of Syk using specific anti-phosphotyrosine site antibodies. For this analysis we selected Y352 and Y525/Y526; the former is the site known to preferentially dephosphorylated by TULA-2 [19], while the latter is a site of known importance for Syk function [38, 39]. As expected, Western-blot analysis showed an increase in tyrosine phosphorylation for both Y525/526 and Y352 sites in both WT and DKO cells. However, tyrosine phosphorylation in DKO cells was elevated as compared to that in WT cells by ~1.5- to 2-fold (Fig. 7d). We next examined tyrosine phosphorylation of PLCγ2, a key signaling protein involved in Syk-mediated signaling, in WT and DKO cells. Although, in the absence of stimulation, basal phosphorylation of PLCγ2 tyrosine 1,217 was higher in DKO than in WT, it was substantially increased in response to Fc receptor crosslinking (Fig. 7e).

To further elucidate the involvement of Syk in these events, we treated cells in our experiments with piceatannol, a Syk specific inhibitor [37]. Phosphorylation of the Syk sites examined did not change profoundly, while the observed increase in PLCγ2 tyrosine 1,217 phosphorylation was dramatically decreased (Fig. 7e). This suggests that phosphorylation of Syk Y352 and Syk Y525/526 in this cellular context is largely independent of Syk enzymatic activity (it can be carried out by Src-family kinases, for example), while phosphorylation of PLCγ2 is clearly Syk-dependent. Thus, differential phosphorylation of Syk caused by differential activity of TULA-2 is expected to exert a strong effect on PLCγ2 phosphorylation, which is a key event of signaling via FcRγ and other osteoclast/macrophage receptors and other cells of immune system [36, 40, 41].

TULA-2 phosphatase activity is needed for osteoclast-mediated bone resorption

TULA-2 is highly expressed in osteoclasts (Fig. 1); its absence in osteoclasts resulted in increased phosphorylation of Syk (Fig. 7d). To investigate the role of TULA-2 phosphatase activity in osteoclast function, we constructed adenoviruses containing FLAG-tagged phosphatase-dead TULA-2 (AxTULA-2H391A). We used a replication-deficient adenovirus vector that contains a reporter gene encoding GFP (AxGFP) as a control vector. Expression of TULA-2 in OCLs isolated from co-cultures infected with the recombinant viruses was verified after 3 days of infection using Western blotting with anti-FLAG and anti-TULA-2 antibodies (data not shown). To investigate the functional consequences of overexpressing phosphatase-deadTULA-2, the bone-resorbing activity of OCLs was quantified by measuring the areas of pits formed on hydroxyl apatite-coated resorption surface. The activity of OCLs phosphatase-dead TULA-2 was significantly augmented when compared to control and GFP-expressing osteoclasts (Fig. 8a, b). This indicates that TULA-2 phosphatase activity is required for bone resorption.

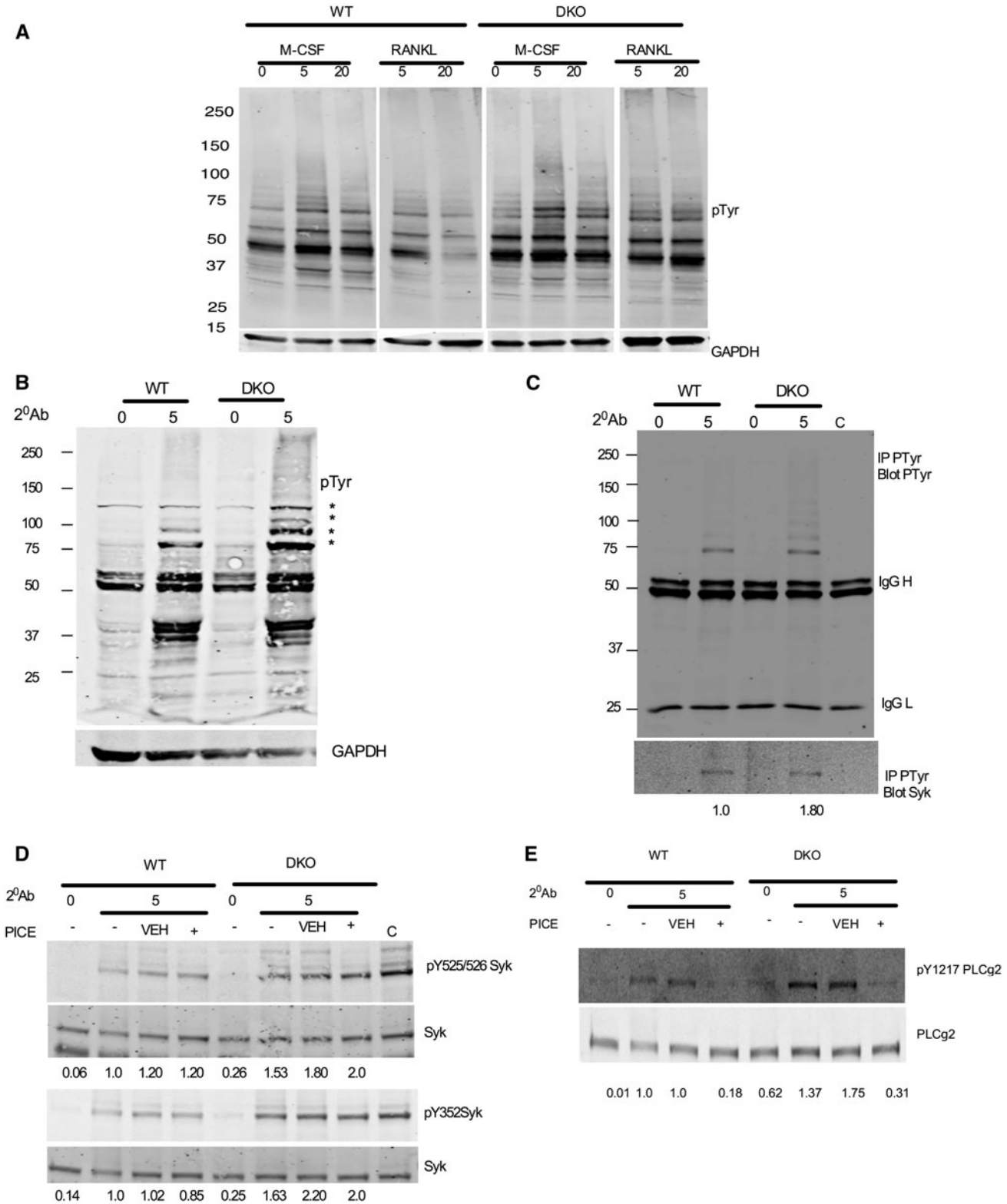

Discussion

We have shown in the present study that the absence of TULA-2, a novel PTP that belongs to the histidine phosphatase superfamily, leads to the decreased bone volume in TULA-2-deficient/null mice (Figs. 4, 5). This is apparently due to both the marked increase in the ability of the hematopoietic precursor cells to differentiate into

◀ **Fig. 7** Loss of TULA-2 leads to enhanced signaling down stream of ITAM-mediated co-stimulatory pathway. Bone marrow macrophages (BMMs) were generated from the bone marrow of WT and DKO mice. **a** BMMs were stimulated by with M-CSF (50 ng/ml) or RANKL (50 ng/ml) at indicated time points, shown in minutes. Blots were probed with anti-phosphotyrosine antibodies (*upper panels*) to visualize phosphorylated proteins. Blots were then reprobed with anti-GAPDH antibodies to determine protein loading. **b** BMMs were stimulated by cross-linking Fc receptor to activate the signaling pathway downstream of ITAM receptors. Blot was probed with anti-phosphotyrosine antibodies (*upper panel*). *Asterisk* indicates location of proteins that are hyper-phosphorylated upon stimulation in DKO samples. Blots were reprobed with anti-GAPDH antibodies to determine protein loading. **c** BMMs were stimulated by cross-linking Fc receptor and immunoprecipitation with anti-PTyr was performed as described in the methods. Blot was probed with anti-PTyr antibodies (*upper panel*) and reprobed with anti-Syk antibodies (*lower panel*). The amounts of total proteins in individual bands were quantified by using Odyssey Infrared Imaging Systems software 2.1 (LICOR Biosciences). The ratio of tyrosine phosphorylation to amount of total protein is shown at the *bottom of the panel*. **d**, **e** BMMs were pretreated with either 50 μg/ml of the Syk inhibitor piceatannol (PICE) or DMSO (VEH) and were then stimulated to engage the ITAM receptors as described above. **d** Blot was probed with anti pY525/526 Syk or pY352Syk as indicated. Blots were then probed with anti-Syk antibodies to determine loading. **e** To determine PLCγ2 phosphorylation blots were probed with anti-pY1217PLCγ2 antibodies and then reprobed with anti-PLCγ2 antibodies to determine protein loading. The amounts of total proteins in individual bands were quantified by using Odyssey Infrared Imaging Systems software 2.1 (LICOR Biosciences). The ratio of tyrosine phosphorylation to amount of total protein is shown at the *bottom of the panel*

osteoclasts (Fig. 2a, b) and the enhanced ability of osteoclasts to resorb bone both in vivo and in vitro (Fig. 6). At the molecular level, our studies show that in osteoclast precursors, TULA-2 mediates dephosphorylation of Syk, which is known to regulate osteoclast differentiation and function via ITAM signaling [36, 42].

Both members of the TULA family have been proposed to be negative regulators of signaling. Deletion of both TULA and TULA-2 is required for causing dramatic hyperactivation of T cells [10]. Re-expression of WT, but not inactivated TULA-2 in cells that lack both TULA-family members results in substantial reversal of the phenotype, indicating that TULA-2 PTP activity is responsible, at least in part, for the hyper-responsiveness of T cells [20]. In the present study, we show that only TULA-2 is expressed in developing and mature osteoclasts to a measurable extent (Fig. 1). This finding is in line with the observation that TULA has limited expression [14, 15]. Therefore, any effect seen in osteoclasts in the DKO mice can be attributable to TULA-2 deficiency.

The overall effect of the lack of TULA-2 on the bone/bone phenotype is due to increased osteoclast numbers in vivo (Fig. 5e) and in vitro (Fig. 2a–c) and increased osteoclast function (Fig. 6). We cannot, however, rule out the possibility that the absence of TULA proteins also affects the osteoblast lineage and this effect of TULA/

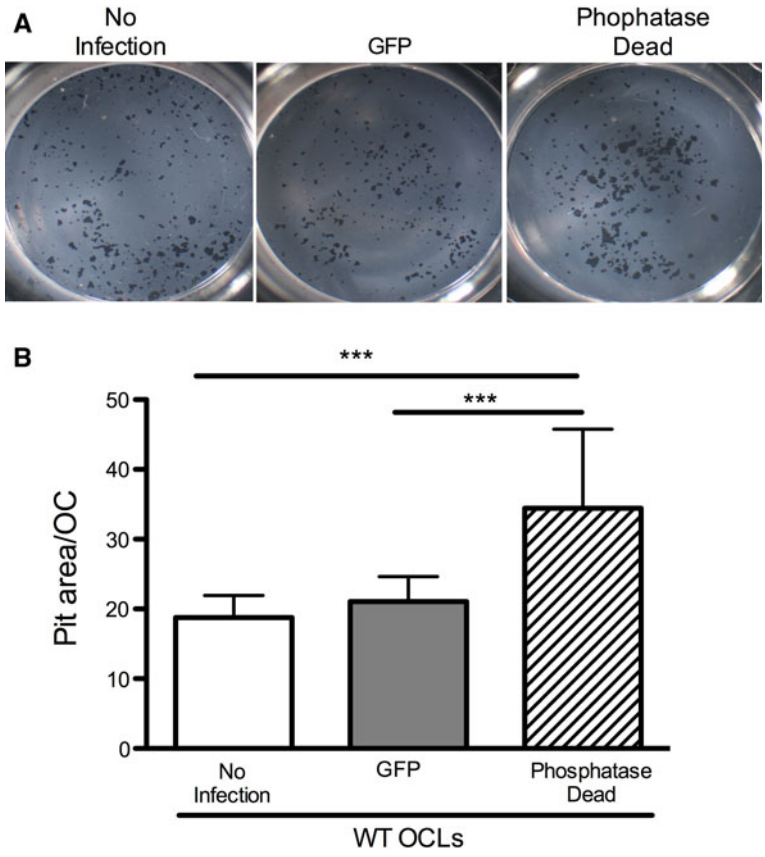

Fig. 8 TULA-2 phosphatase activity is required for proper osteoclast function. Osteoclasts were either left un-infected, or were infected at 500 MOI with an adenoviral GFP (AxGFP) or adenoviral construct expressing phosphatase-dead form of TULA 2 (AxTULA-2H380A) for 48 h. Infected cells were replated onto the resorbable tissue culture surface and incubated for 48 h as described in the methods section. **a** *Photomicrographs* show of resorbed surface for each condition. **b** After removing adherent cells, resorbed area was quantified and normalized for the numbers of OCLs. Data are presented as mean SE ($n = 9$). $^{**}p < 0.001$ compared to the uninfected control samples. The results are representative of two experiments

TULA-2 deficiency on osteoblasts contributes to the osteopenic phenotype. This possibility is supported by a decrease in trabecular thickness and trabecular numbers in DKO mice, when compared to the WT mice (Fig. 4). Although further studies would be needed to elucidate how loss of TULA proteins might affect the function of osteoblasts, it is likely that this effect would be indirect, being mediated, for example, by changes in cytokine production. The finding that an increase in osteoclastogenesis in DKO mice is intrinsic to the hematopoietic lineage excludes the possibility that the observed increase is due to an increase in osteoprotegerin ligand (OPGL) or a decrease in osteoprotegerin production by cells of the stromal lineage or osteoblasts [43, 44].

Given the distinct sequential and essential effects by M-CSF on osteoclast precursor monocyte proliferation and survival, and by RANKL on osteoclast differentiation [1], we attempted to dissect the roles of these cytokines in the enhanced osteoclastogenesis that accompanies TULA-2 deficiency. A modest increase in phosphorylation was seen in the DKO osteoclast precursors or mature osteoclasts as compared to their WT counterparts stimulated with M-CSF (Fig. 7a). Furthermore, a significant increase in phosphorylation of several proteins, including Syk, was observed in DKO cells as compared to WT cells when ITAM-mediated signaling was engaged (Fig. 7b, c, e). Although the exact molecular mechanisms responsible for TULA-2-modulated regulation of osteoclastogenesis remain unresolved, we postulate that decreased TULA-2 activity elevates tyrosine phosphorylation of Syk and, hence, of its substrates, thus leading to increased osteoclastogenesis in TULA-2-deficient mice, analogous to the osteopenia observed in SHP-1-deficient *mev/mev* mice [6]. Under normal remodeling conditions, bone resorption is thought to stimulate an equivalent level of bone formation. Osteoclast and osteoblast "coupling", is fine-tuned through variations in local cytokine expression or release, from cell to cell, or from cell to matrix induced signals [45]. However, our studies in DKO mice show that increased osteoclastogenesis occurs independently of osteoblastogenesis, consistent with other studies where osteoclast resorptive activity appears dispensable for coupling [46]. Thus, the increase in osteoclast levels and activity that we observed histologically, functionally, and independently of bone formation contribute to the significant loss of trabecular bone volume in DKO mice. Therefore, overall bone-remodeling rates appear to be reduced arguing further for uncoupling of osteoclast and osteoblast functions in the DKO mice.

Although the total numbers of bone marrow cells and hematopoietic progenitors ($Lin^{-}Sca\text{-}1^{+}c\text{-}kit^{+}$ cells) remained unchanged in the DKO mice, the numbers of osteoclast precursors ($CD11^{b-/low}$, $CD115^{+}$, $CD117^{+}$) were significantly increased (Fig. 3 and data not shown). This finding is consistent with increased osteoclastogenesis wherein DKO osteoclast precursor cells differentiate into osteoclasts (Fig. 2) and have increased resorption (Fig. 6). In addition to bone formation, bone remodeling is also tightly linked to hematopoiesis. Indeed, osteoclasts appear to have a unique, direct role in hematopoietic progenitor mobilization [47]. Thus, our findings also suggest the possibility that enhanced osteoclastogenesis could have a positive feedback effect on hematopoietic progenitors and drive their differentiation toward different lineages, due in part to release of soluble factors from the osteoid matrix degraded by the increased osteoclast activity in the DKO mice. Overall, the absence of TULA proteins and, in particular TULA-2, since only TULA-2 is expressed in osteoclasts, leads to bone loss.

Taken together, these results indicate that, under normal physiological conditions TULA-2 could down-regulate signaling in response to factor(s) that activate differentiation of osteoclasts and possibly osteoclast function. Although the exact mechanisms mediating the role of TULA-2 remain to be elucidated further, the obtained results allow us to propose a molecular explanation for the positive effect of the loss of TULA-2 activity on osteoclastogenesis and bone resorption in DKO mice. Considering that the protein tyrosine kinase Syk as a key element of the signaling mechanism in macrophages and osteoclasts [36, 40, 41] and that Syk has been identified as a bona fide substrate of TULA-2 [18, 19], it is likely that the lack of TULA-2 facilitates phosphorylation of Syk. Indeed, our results indicate that phosphorylation of Syk and, in particular, phosphorylation of Tyr 525/526 and Tyr 352 sites is increased in TULA-2-deficient cells. It has been shown previously that the elevated phosphorylation of these sites is indicative of elevated enzymatic activity of Syk [34]. The hyper phosphorylation of Syk demonstrated in this report is similar to that reported for TULA-2-deficient platelets [23].

Likewise, we have shown that tyrosine phosphorylation of PLCγ2 is also elevated in the osteoclast precursors derived from DKO mice as compared to WT precursors. An increase in PLCγ2 phosphorylation in DKO cells is likely due to the increase in Syk activity caused by the lack of TULA-2, since we (Fig. 7e) and others have shown that PLCγ2 phosphorylation is Syk-dependent [23]. Direct dephosphorylation of PLCγ2 pTyr 1,217 by TULA-2 is less likely, since this site lacks some critical specificity determinants defining it as a substrate of TULA-2 [19].

In addition to Syk, Src-family kinases (SFKs) may also be targets of TULA-2 phosphatase activity. Several SFKs also regulate bone remodeling by directly affecting osteoclast differentiation and function. While absence of c-Src does not affect osteoclast differentiation, it severely affects osteoclast function, thus causing osteopetrosis in mice [4]. In contrast, while the lack of Lyn does not impact the

activity of mature osteoclasts under basal condition, Lyn-null mice undergo accelerated osteoclastogenesis and bone loss in response to RANKL [48]. Similarly, while Fyn-deficient mice show no overt changes in the skeletal phenotype, the absence of Fyn results in decreased osteoclast differentiation in culture [49]. Thus, if TULA-2 regulates kinase activities of SFKs, its absence in osteoclast may result in dysregulation of SFKs and could lead to the increased numbers of osteoclasts and an increase in osteoclastic activity.

In conclusion, the absence of TULA-2 leads to osteopenia accompanied by increased bone resorption. Both osteoclast differentiation and osteoclast activity appear to be increased in the absence TULA-2, suggesting that this tyrosine phosphatase is a negative regulator of osteoclastogenesis and, possibly, of osteoclast resorbing activity.

Acknowledgments This work was supported by a grant from the Pennsylvania Department of Health to S. B and by the National Institute of Health Grant (AR055601) to A. S. The authors also thank Dr. Hector Aguila (Department of Immunology, University of Connecticut Health Center) for antibodies and help with FACS analysis. We also acknowledge the support of the MicroCT Core Facility at Temple University.

References

1. Teitelbaum SL, Ross FP (2003) Genetic regulation of osteoclast development and function. Nat Rev Genet 4:638–649
2. Hunter T (1995) Protein kinases and phosphatases: the yin and yang of protein phosphorylation and signaling. Cell 80:225–236
3. Gil-Henn H, Destaing O, Sims NA, Aoki K, Alles N, Neff L, Sanjay A, Bruzzaniti A, De Camilli P, Baron R, Schlessinger J (2007) Defective microtubule-dependent podosome organization in osteoclasts leads to increased bone density in Pyk2(−/−) mice. J Cell Biol 178:1053–1064
4. Soriano P, Montgomery C, Geske R, Bradley A (1991) Targeted disruption of the c-src proto-oncogene leads to osteopetrosis in mice. Cell 64:693–702
5. Granot-Attas S, Elson A (2008) Protein tyrosine phosphatases in osteoclast differentiation, adhesion, and bone resorption. Eur J Cell Biol 87:479–490
6. Aoki K, DiDomenico E, Sims NA, Mukhopadhyay K, Neff L, Houghton A, Amling M, Levy JB, Horne WC, Baron R (1999) The tyrosine phosphatase SHP-1 is a negative regulator of osteoclastogenesis and osteoclast resorbing activity: increased resorption and osteopenia in *me*^{v}/*me*^{v} mutant mice. Bone 25:261–267
7. Chellaiah MA, Kuppuswamy D, Lasky L, Linder S (2007) Phosphorylation of a Wiskott–Aldrich syndrome protein-associated signal complex is critical in osteoclast bone resorption. J Biol Chem 282:10104–10116
8. Chiusaroli R, Knobler H, Luxenburg C, Sanjay A, Granot-Attas S, Tiran Z, Miyazaki T, Harmelin A, Baron R, Elson A (2004) Tyrosine phosphatase epsilon is a positive regulator of osteoclast function in vitro and in vivo. Mol Biol Cell 15:234–244
9. Carpino N, Kobayashi R, Zang H, Takahashi Y, Jou ST, Feng J, Nakajima H, Ihle JN (2002) Identification, cDNA cloning, and targeted deletion of p70, a novel, ubiquitously expressed SH3 domain-containing protein. Mol Cell Biol 22:7491–7500
10. Carpino N, Turner S, Mekala D, Takahashi Y, Zang H, Geiger TL, Doherty P, Ihle JN (2004) Regulation of ZAP-70 activation and TCR signaling by two related proteins, Sts-1 and Sts-2. Immunity 20:37–46
11. Feshchenko EA, Smirnova EV, Swaminathan G, Teckchandani AM, Agrawal R, Band H, Zhang X, Annan RS, Carr SA, Tsygankov AY (2004) TULA: an SH3- and UBA-containing protein that binds to c-Cbl and ubiquitin. Oncogene 23:4690–4706
12. Wattenhofer M, Shibuya K, Kudoh J, Lyle R, Michaud J, Rossier C, Kawasaki K, Asakawa S, Minoshima S, Berry A, Bonne-Tamir B, Shimizu N, Antonarakis SE, Scott HS (2001) Isolation and characterization of the UBASH3A gene on 21q22.3 encoding a potential nuclear protein with a novel combination of domains. Hum Genet 108:140–147
13. Rigden DJ (2008) The histidine phosphatase superfamily: structure and function. Biochem J 409:333–348
14. Tsygankov AY (2008) Multidomain STS/TULA proteins are novel cellular regulators. IUBMB Life 60:224–231
15. Tsygankov AY (2009) TULA-family proteins: an odd couple. Cell Mol Life Sci 66:2949–2952
16. Tsygankov AY (2012) TULA-family proteins: a new class of cellular regulators. J Cell Physiol 228(1):43–49
17. de Castro RO, Zhang J, Groves JR, Barbu EA, Siraganian RP (2012) Once phosphorylated, tyrosines in carboxyl terminus of protein-tyrosine kinase Syk interact with signaling proteins, including TULA-2, a negative regulator of mast cell degranulation. J Biol Chem 287:8194–8204
18. Agrawal R, Carpino N, Tsygankov A (2008) TULA proteins regulate activity of the protein tyrosine kinase Syk. J Cell Biochem 104(3):953–964
19. Chen X, Ren L, Kim S, Carpino N, Daniel JL, Kunapuli SP, Tsygankov AY, Pei D (2010) Determination of the substrate specificity of protein-tyrosine phosphatase TULA-2 and identification of Syk as a TULA-2 substrate. J Biol Chem 285:31268–31276
20. Mikhailik A, Ford B, Keller J, Chen Y, Nassar N, Carpino N (2007) A phosphatase activity of Sts-1 contributes to the suppression of TCR signaling. Mol Cell 27:486–497
21. Smirnova EV, Collingwood TS, Bisbal C, Tsygankova OM, Bogush M, Meinkoth JL, Henderson EE, Annan RS, Tsygankov AY (2008) TULA proteins bind to ABCE-1, a host factor of HIV-1 assembly, and inhibit HIV-1 biogenesis in a UBA-dependent fashion. Virology 372:10–23
22. Collingwood TS, Smirnova EV, Bogush M, Carpino N, Annan RS, Tsygankov AY (2007) T-cell ubiquitin ligand affects cell death through a functional interaction with apoptosis-inducing factor, a key factor of caspase-independent apoptosis. J Biol Chem 282:30920–30928
23. Thomas DH, Getz TM, Newman TN, Dangelmaier CA, Carpino N, Kunapuli SP, Tsygankov AY, Daniel JL (2010) A novel histidine tyrosine phosphatase, TULA-2, associates with Syk and negatively regulates GPVI signaling in platelets. Blood 116:2570–2578
24. Brennan T, Adapala NS, Barbe MF, Yingling V, Sanjay A (2011) Abrogation of Cbl-PI3K interaction increases bone formation and osteoblast proliferation. Calcif Tissue Int 89:396–410
25. Parfitt AM, Drezner MK, Glorieux FH, Kanis JA, Malluche H, Meunier PJ, Ott SM, Recker RR (1987) Bone histomorphometry: standardization of nomenclature, symbols, and units. Report of the ASBMR Histomorphometry Nomenclature Committee. J Bone Miner Res 2:595–610
26. Miyazaki T, Takayanagi H, Isshiki M, Takahashi T, Okada M, Fukui Y, Oda H, Nakamura K, Hirai H, Kurokawa T, Tanaka S (2000) In vitro and in vivo suppression of osteoclast function by adenovirus vector-induced *csk* gene. J Bone Miner Res 15:41–51
27. Miyazaki T, Katagiri H, Kanegae Y, Takayanagi H, Sawada Y, Yamamoto A, Pando MP, Asano T, Verma IM, Oda H, Nakamura

K, Tanaka S (2000) Reciprocal role of ERK and NF-κB pathways in survival and activation of osteoclasts. J Cell Biol 148:333–342
28. Menaa C, Kurihara N, Roodman GD (2000) CFU-GM-derived cells form osteoclasts at a very high efficiency. Biochem Biophys Res Commun 267:943–946
29. Miyazaki T, Sanjay A, Neff L, Tanaka S, Horne WC, Baron R (2004) Src kinase activity is essential for osteoclast function. J Biol Chem 279:17660–17666
30. Sanjay A, Miyazaki T, Itzstein C, Purev E, Horne WC, Baron R (2006) Identification and functional characterization of an Src homology domain 3 domain-binding site on Cbl. FEBS J 273:5442–5456
31. Adapala NS, Barbe MF, Langdon WY, Nakamura MC, Tsygankov AY, Sanjay A (2010) The loss of Cbl-phosphatidylinositol 3-kinase interaction perturbs RANKL-mediated signaling, inhibiting bone resorption and promoting osteoclast survival. J Biol Chem 285:36745–36758
32. Arai F, Miyamoto T, Ohneda O, Inada T, Sudo T, Brasel K, Miyata T, Anderson DM, Suda T (1999) Commitment and differentiation of osteoclast precursor cells by the sequential expression of c-Fms and receptor activator of nuclear factor kappaB (RANK) receptors. J Exp Med 190:1741–1754
33. Jacquin C, Gran DE, Lee SK, Lorenzo JA, Aguila HL (2006) Identification of multiple osteoclast precursor populations in murine bone marrow. J Bone Miner Res (the official J Am Soc Bone Miner Res) 21:67–77
34. Mocsai A, Ruland J, Tybulewicz VL (2010) The SYK tyrosine kinase: a crucial player in diverse biological functions. Nat Rev Immunol 10:387–402
35. Faccio R, Zou W, Colaianni G, Teitelbaum SL, Ross FP (2003) High dose M-CSF partially rescues the Dap12−/− osteoclast phenotype. J Cell Biochem 90:871–883
36. Mocsai A, Humphrey MB, Van Ziffle JA, Hu Y, Burghardt A, Spusta SC, Majumdar S, Lanier LL, Lowell CA, Nakamura MC (2004) The immunomodulatory adapter proteins DAP12 and Fc receptor gamma-chain (FcRgamma) regulate development of functional osteoclasts through the Syk tyrosine kinase. Proc Natl Acad Sci USA 101:6158–6163
37. Zou W, Kitaura H, Reeve J, Long F, Tybulewicz VL, Shattil SJ, Ginsberg MH, Ross FP, Teitelbaum SL (2007) Syk, c-Src, the alphavbeta3 integrin, and ITAM immunoreceptors, in concert, regulate osteoclastic bone resorption. J Cell Biol 176:877–888
38. Lupher ML, Rao N, Lill NL, Andoniou CE, Miyake S, Clark EA, Druker B, Band H (1998) Cbl-mediated negative regulation of the Syk tyrosine kinase. A critical role for Cbl phosphotyrosine-binding domain binding to Syk phosphotyrosine 323. J Biol Chem 273:35273–35281
39. Rao N, Ghosh AK, Ota S, Zhou P, Reddi AL, Hakezi K, Druker BK, Wu J, Band H (2001) The non-receptor tyrosine kinase Syk is a target of Cbl-mediated ubiquitylation upon B-cell receptor stimulation. EMBO J 20:7085–7095
40. Epple H, Cremasco V, Zhang K, Mao D, Longmore GD, Faccio R (2008) Phospholipase C gamma 2 modulates integrin signaling in the osteoclast by affecting the localization and activation of Src kinase. Mol Cell Biol 28:3610–3622
41. Mocsai A, Zhou M, Meng F, Tybulewicz VL, Lowell CA (2002) Syk is required for integrin signaling in neutrophils. Immunity 16:547–558
42. Koga T, Inui M, Inoue K, Kim S, Suematsu A, Kobayashi E, Iwata T, Ohnishi H, Matozaki T, Kodama T, Taniguchi T, Takayanagi H, Takai T (2004) Costimulatory signals mediated by the ITAM motif cooperate with RANKL for bone homeostasis. Nature 428:758–763
43. Lacey DL, Timms E, Tan H-L, Kelley MJ, Dunstan CR, Burgess T, Elliott R, Colombero A, Elliott G, Scully S, Hsu H, Sullivan J, Hawkins N, Davy E, Capparelli C, Eli A, Qian Y-X, Kaufman S, Sarosi I, Shalhoub V, Senaldi G, Guo J, Delaney J, Boyle WJ (1998) Osteoprotegerin ligand is a cytokine that regulates osteoclast differentiation and activation. Cell 93:165–176
44. Simonet WS, Lacey DL, Dunstan CR, Kelley M, Chang M-S, Luthy R, Nguyen HQ, Wooden S, Bennett L, Boone T, Shimamoto G, DeRose M, Elliott R, Colombero A, Tan H-L, Trail G, Sullivan J, Davy E, Bucay N, Renshaw-Gegg L, Hughes TM, Hill D, Pattison W, Campbell P, Sander S, Van G, Tarpley J, Derby P, Lee R, Boyle WJ (1997) Osteoprotegerin: a novel secreted protein involved in the regulation of bone density. Cell 89:309–319
45. Teitelbaum SL (2000) Bone resorption by osteoclasts. Science 289:1504–1508
46. Karsdal MA, Martin TJ, Bollerslev J, Christiansen C, Henriksen K (2007) Are nonresorbing osteoclasts sources of bone anabolic activity? J Bone Miner Res 22:487–494
47. Kollet O, Dar A, Shivtiel S, Kalinkovich A, Lapid K, Sztainberg Y, Tesio M, Samstein RM, Goichberg P, Spiegel A, Elson A, Lapidot T (2006) Osteoclasts degrade endosteal components and promote mobilization of hematopoietic progenitor cells. Nat Med 12:657–664
48. Kim HJ, Zhang K, Zhang L, Ross FP, Teitelbaum SL, Faccio R (2009) The Src family kinase, Lyn, suppresses osteoclastogenesis in vitro and in vivo. Proc Natl Acad Sci USA 106:2325–2330
49. Kim HJ, Warren JT, Kim SY, Chappel JC, DeSelm CJ, Ross FP, Zou W, Teitelbaum SL (2010) Fyn promotes proliferation, differentiation, survival and function of osteoclast lineage cells. J Cell Biochem 111:1107–1113

Bone 110 (2018) 267–283

Contents lists available at ScienceDirect

Bone

journal homepage: www.elsevier.com/locate/bone

Prolonged high force high repetition pulling induces osteocyte apoptosis and trabecular bone loss in distal radius, while low force high repetition pulling induces bone anabolism

Mary F. Barbe [a,*], Vicky S. Massicotte [a], Soroush Assari [b], M. Alexandra Monroy [c], Nagat Frara [a], Michele Y. Harris [a], Mamta Amin [a], Tamara King [d], Geneva E. Cruz [a], Steve N. Popoff [a]

[a] Lewis Katz School of Medicine at Temple University, Department of Anatomy and Cell Biology, Philadelphia, PA 19140, United States
[b] Temple University College of Engineering, Department of Mechanical Engineering, Philadelphia, PA 19122, United States
[c] Perelman School of Medicine, University of Pennsylvania, Department of Radiation Oncology, Philadelphia, PA 19104, United States
[d] College of Osteopathic Medicine, Department of Biomedical Sciences, Biddeford, ME 04005, United States

ARTICLE INFO

Article history:
Received 19 September 2017
Revised 23 January 2018
Accepted 16 February 2018
Available online 22 February 2018

Keywords:
Overuse injury
Mechanical loading
Osteoprotegerin
Osteoactivin
Sclerostin
RANKL
RANK

ABSTRACT

We have an operant rat model of upper extremity reaching and grasping in which we examined the impact of performing a high force high repetition (High-ForceHR) versus a low force low repetition (Low-ForceHR) task for 18 weeks on the radius and ulna, compared to age-matched controls. High-ForceHR rats performed at 4 reaches/min and 50% of their maximum voluntary pulling force for 2 h/day, 3 days/week. Low-ForceHR rats performed at 6% maximum voluntary pulling force. High-ForceHR rats showed decreased trabecular bone volume in the distal metaphyseal radius, decreased anabolic indices in this same bone region (e.g., decreased osteoblasts and bone formation rate), and increased catabolic indices (e.g., microcracks, increased osteocyte apoptosis, secreted sclerostin, RANKL, and osteoclast numbers), compared to controls. Distal metaphyseal trabeculae in the ulna of High-ForceHR rats showed a non-significant decrease in bone volume, some catabolic indices (e.g., decreased trabecular numbers) yet also some anabolic indices (e.g., increased osteoblasts and trabecular thickness). In contrast, the mid-diaphyseal region of High-ForceHR rats' radial and ulnar bones showed few to no microarchitecture differences and no changes in apoptosis, sclerostin or RANKL levels, compared to controls. In further contrast, Low-ForceHR rats showed increased trabecular bone volume in the radius in the distal metaphysis and increased cortical bone area its mid-diaphysis. These changes were accompanied by increased anabolic indices, no microcracks or osteocyte apoptosis, and decreased RANKL in each region, compared to controls. Ulnar bones of Low-ForceHR rats also showed increased anabolic indices, although fewer than in the adjacent radius. Thus, prolonged performance of an upper extremity reaching and grasping task is loading-, region-, and bone-dependent, with high force loads at high repetition rates inducing region-specific increases in bone degradative changes that were most prominent in distal radial trabeculae, while low force task loads at high repetition rates induced adaptive bone responses.

1. Introduction

Most types of physical activity are considered beneficial, whether sports, planned exercise, household work or occupational tasks [1,2]. Yet, work activities are not considered exercise; the former typically lacking any cardiovascular benefits [3]. Involvement in heavy manual occupations is linked to higher incidence of musculoskeletal injuries than nonmanual and light manual occupations [4,5]. The negative effects of repetitive and high compressive forces on lumbar spine structures when performing occupational jobs are well established [6–8]. A small number of studies showing increased incidence of hand/wrist osteoarthritis and reduced bone mass in the hand and wrist in individuals with heavy or one-sided hand workloads [9–12]. This is a concern because incidence of distal radial bone fractures is increasing in the U.S. and worldwide [13,14]. There is also a need for etiologic research examining mechanisms underlying tissue degradative changes occurring with high demand upper extremity occupational tasks [15].

Although not yet investigated with overuse injuries occurring as a consequence of occupational tasks, RANKL (Receptor activator of nuclear factor kappa-B ligand) is expressed by osteoblasts and osteocytes [16], and stimulates differentiation and activation of osteoclasts by

* Corresponding author at: Department of Anatomy and Cell Biology, Temple University School of Medicine, 3500 North Broad St., Philadelphia, PA 19140, United States.
E-mail address: mary.barbe@temple.edu (M.F. Barbe).

https://doi.org/10.1016/j.bone.2018.02.014
8756-3282/

binding to its receptor, RANK [17,18]. Osteocytes show metabolic responsiveness to bone loading or unloading [19,20], and RANKL is one protein released by apoptotic osteocytes following loading-induced microdamage [17,21]. Such microdamage has a catabolic effect on bones by promoting osteoclast activity in a RANKL-dependent manner [22]. Osteoprotegerin (OPG) is a RANK decoy receptor that binds RANKL, segregating the ligand and preventing activation of the RANKL/RANK pathway [23]. While osteocyte apoptosis and their subsequent release of RANKL is essential for bone remodeling, a prolonged shift in the RANKL and OPG ratio towards more RANKL enhances osteoclastogenesis and net bone resorption [17].

Sclerostin is another protein expressed by osteocytes [24] that has yet to be examined with overuse occupational injuries. It is the product of the *SOST* gene and a negative regulator of osteoblast differentiation and function, making it a potent inhibitor of bone formation [25,26]. Although the exact mechanisms by which sclerostin inhibits bone formation are still unclear, it is known that sclerostin selectively inhibits Wnt proteins from binding to low-density lipoprotein receptor-related protein 5/6 (LPR5/6) receptors, a change that antagonizes Wnt signaling [27]. The Wnt pathway is essential for loading-induced osteogenesis [28], and its inhibition suppresses osteoblast activity and reduces osteoblast and osteocyte viability [27]. Applied mechanical loads typically suppress sclerostin production, a change that releases the break on Wnt signaling and allows for bone formation [19]. However, loading-induced matrix microdamage in which osteocyte apoptosis occurs is associated with an enhanced release of both sclerostin and RANKL [26], changes that promote bone catabolism.

We have developed an operant and clinically relevant rat model of upper extremity WMSDs in which rats learn a reaching and lever bar pulling task for a food reward [29]. Rats reach forward using their whole forearm to pull on a lever bar located outside of the chamber (which is attached to a force transducer) at learned and defined reach rates and target forces for a food reward. Young adult rats performing the task at low force loads and high repetition rates (Low-ForceHR) for 12 weeks show adaptive bone changes, including increased trabecular bone volume in the distal metaphysis of the radius [29,30]. This is consistent with studies reporting bone anabolism in response to loading [31]. In contrast, rats performing a high force high repetition (High-ForceHR) task for 12 weeks show significant trabecular bone loss in the distal metaphysis [29,32]. Initially, an underlying inflammatory mechanism contributed to this overuse-induced trabecular bone loss, a mechanism confirmed with findings that anti-inflammatory treatments reduced this loss when provided in task weeks 4 through 12 since the inflammatory changes peaked in task week 6 [32,33]. These inflammatory responses were resolved in serum and muscles in 18 week High-ForceHR task rats [34]. However, we hypothesized that trabecular bone catabolism would persist in distal radial metaphysis of 18 week High-ForceHR rats in association with increased microdamage, osteocyte apoptosis, sclerostin and RANKL. These findings would be consistent with a Damage-Repair Theory for bone in which persistent high loading causes an accumulation of damage in bone if the loading is so high that self-repair mechanisms cannot keep pace with the level of damage or overload-induced resorption [35–38]. That said, as stated in a recent review: "the contributions of varied, but unique, stimuli generated by muscle to bone remains to be established" [39].

To explore this hypothesis, we compared radial and ulnar bone microarchitecture changes in rats performing a High-ForceHR reaching and lever pulling task for 18 weeks to those occurring in rats performing a Low-ForceHR task for 18 weeks (extending our past 12 week studies), versus resting control (C) rats. We examined for indices of bone microdamage and changes in proteins known to modulate loading-induced bone resorption versus formation (e.g., RANKL, RANK, OPG and sclerostin), proteins not yet examined in our operant repetitive loading model or in other models of chronic muscle-contraction loading of bone.

2. Materials and methods

2.1. Animals and overview

The Temple University Institutional Animal Care and Use Committee approved all experiments in compliance with NIH guidelines for the care and use of laboratory animals. A total of 70 young (2.5 months of age at onset) female Sprague-Dawley rats were used (one rat was excluded after onset of experiments reducing the total number of rats used to 69; Fig. 1A). All rats were housed in a central animal facility in separate cages with a 12 hour light:dark cycle, with free access to water and environment enrichment toys. All rats were initially food-restricted for 7 days to no >10–15% less than their naive weight to encourage interest in 45 mg food reward pellets (a 1:1 mix of purified grain and banana flavored pellets; Bioserve, NJ, USA). Then, the food-restricted rats were given extra rat chow and allowed to gain weight thereafter, to no >5% less than age-matched normal control rats (used for weight comparison only). Randomly chosen rats first learned to pull the lever bar at high force during a 6-wk shaping period of 10–15 min/day for 5 days/wk, before performing a high force high repetition (High-ForceHR) task that involved reaching and grasping of a lever bar for 2 h/day, 3 days/wk for 18 wk ($n = 20$) (Fig. 1A). As indicated above, one High-ForceHR rat was removed from the study when a tumor was detected, reducing the total number in this group to 19 (Fig. 1A). A second cohort initially shaped to learn to pull the lever bar at low force, before performing a low force high repetition (Low-ForceHR) task at similar timing ($n = 23$). The remaining food restricted rats did not undergo shaping or task performance and were considered control (C) rats ($n = 27$). The individuals carrying out all tissue analyses were blinded to treatment.

2.2. Task apparatuses, shaping and task paradigm

Operant behavioral apparatuses were as previously described [29]. Briefly, rats reached through a shoulder height portal and pulled on a vertical 1.5 mm metal bar, positioned 2.5 cm outside of the chamber wall, attached to a load cell (Futek Advanced Sensor Technology, Irvine, CA) (see Supplemental Movie). The load cell was interfaced with custom written Force-Lever software that allowed us to choose a required force level for provision of a food reward (Med Associates, St. Albans, VT). Light and auditory indicators (Med Associates) lasting 500 milliseconds (msec) cued the animal to attempt a reach every 15 s.

Rats were first shaped to learn a reaching and lever-pulling task during a 6-wk period for 10 min/day, 5 days/wk, in which they ramped upwards from naïve towards high force or low force pulling (Fig. 1A), as previously described [29,32]. Briefly, rats learned to reach for a lever bar at increasing pulling forces, without any specified repetition rate, for a food reward. By the end of shaping week 6, rats randomly chosen to be High-ForceHR task rats were required to pull at 130 g of force (gf; 1.27 Newtons), estimated to be 50% of their maximum pulling force, without any specified repetition rate, for a food reward. They then moved on to the High-ForceHR task. Rats randomly chosen to be Low-ForceHR task rats were required to pull at 17 g of force (0.17 Newtons; 6% of their maximum pulling force), without any specified repetition rate, for a food reward, by the end of shaping period. They then moved on to the Low-ForceHR task.

The mean maximum voluntary pulling force of rats was determined on the last day of shaping by requiring the rat to pull at increasing levels for a food reward until their maximum level was reached. The maximum voluntary pulling force was 260 ± 7.02 (mean ± SEM) grams, which is 2.45 ± 0.07 Newtons.

The High-ForceHR task consisted of pulling the lever bar at a rate of 4 reaches/min, and at a graded force effort of 50% ± 5% (mean ± SEM) of their maximum pulling force, for 2 h/day, 3 days/wk for 18 weeks. The Low-ForceHR task had the same reach rate and work/rest hrs, but had to pull on the lever bar at a graded force effort of 6% ± 5% of their

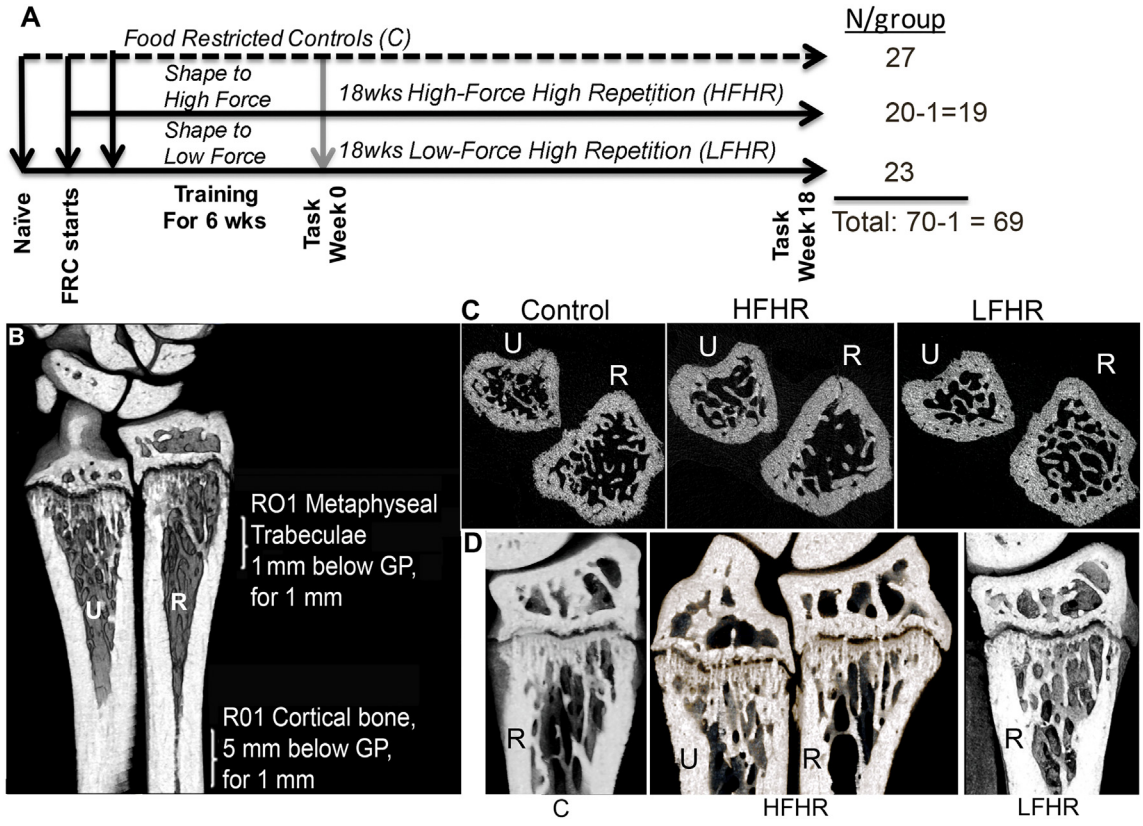

Fig. 1. Design and microCT images. (A) Young adult (2.5 months at onset) Sprague-Dawley rats were randomly assigned as food-restricted control (C) rats, rats that performed a high force high repetition task (High-ForceHR) for 18 weeks, or rats that performed a low force high repetition task (Low-ForceHR) for 18 weeks. Numbers per group shown at right. (B) Regions of interest (ROI) in radius (R) and ulnar (U) analyzed using micro-computerized tomography. (C) Upper row: Representative transaxial 2D image slices of distal ulnar and radial metaphyses. Lower row: Representative longitudinal 3D images of the distal radius. The ulna is also shown for a HFHR rat.

maximum pulling force. Each daily task was divided into four 30 min sessions separated by 1.5 h each, to avoid satiation. If the above criteria were met within a 5 s cueing period, a 45 mg food pellet reward was dispensed into a trough located at floor height for the animal to lick up. Rats were not prevented from reaching at a higher or lower force than their target force; however, if they either undershot the minimum criterion, or overshot the maximum criterion, no food reward was delivered (Supplemental Fig. 1). Rats were allowed to use their preferred limb to reach.

2.3. Determination of reach performance behaviors in task rats

Force lever data were recorded continuously during each task session for later calculation of the dependent variables (mean reaches/session, reaches/min, reaches/day, reach force and grasp time) via a custom written and automated script (MATLAB, MathWorks®, Natick, MA) that translated the Force Lever Program data into Excel spreadsheets. Reach force was the mean recordable reach force (in gf) applied to the force lever bar for all reaches across a given day. Grasp time was the mean average time (in msec) that the rats spent grasping and pulling on the lever bar for all recordable reaches. Mean reach force and grasp time were calculated over the interval that ended when the force fell below 2.5% of baseline. Mean reach impulse was calculated for each rat by multiplying the mean reach force in Newton's by the mean duration of grasp in msec. The percent duty cycle (the percent of time the rats were engaged in the reaching efforts) was calculated, as suggested for ergonomic reaching and grasping studies [40,41]: ((number of reaches/cycle × grasp time/reach) / 60 s per cycle) × 100. Data for each variable was calculated on the last day of task weeks 1, 3, 6, 12 and 18 for 15 Low-ForceHR rats and 12 High-ForceHR rats. The total number of reaches, total volume of grasping the lever bar, and the total volume of loading (total reaches × total msec of grasping × mean force per grasp) across all weeks were estimated from these times points. These data could not be generated for control rats, as they did not perform the task.

2.4. Tissue collection

Animals were anesthetized with 5% isoflurane using oxygen as a carrier, and euthanized by cardiac puncture for blood collection using an 18-gauge needle at 36 h after their last task session. Blood was kept on ice for 30 min, and allowed to clot before being centrifuged. Serum was harvested and frozen at −80 °C until use. Thereafter, subcohorts of rats per group were perfused transcardially with 0.9% saline and then fixed with 4% paraformaldehyde in 0.1 M PO_4 buffer, pH 7.4, for serum analyses (n = 8–15/group), forelimb bone (radius and ulna) micro-computerized tomography (microCT, n = 5–14/group), en bloc basic fucshin staining and microcrack analysis (3 control and 3 High-ForceHR rat bones), bone static histomorphometry (n = 6–12/group) and/or TUNEL staining (n = 4–7/group), bone immunohistochemistry (n = 5–7/group), muscle histomorphometry (n = 5–6/group), or void analysis on radial and ulnar bones (n = 6–9/group). Bones, forelimb flexor muscles and tendons were collected from other subcohorts of rats, flash frozen and used for mRNA (n = 4–6/group) or protein assays (n = 4–6/group).

2.5. MicroCT imaging and analysis

After fixation, as described above, forelimb bones were collected, cleaned of soft tissues, and stored in phosphate buffered saline (PBS) with sodium azide until microCT analysis of the radius (n = 5–14/group) using a Skyscan 1172, 12 megapixel, high-resolution cone-

beam microCT scanner (Bruker, Kontich, Belgium), using the following settings: a pixel resolution size of 5.89 μm, x-ray source spot size of 300 nm, Al 0.5 mm filter, voltage of 59 kV, current of 167 μA, rotation step of 0.40°, frame averaging of 5. Skyscan volume rendering software (CTVox) and analysis software (CTAn) was used to render 3D models of longitudinal sections (Fig. 1C). MicroCT analysis was performed, as previously described [30] in metaphyseal and diaphyseal regions of the radius and ulna (Fig. 1B).

2.6. Histomorphometry of bone and muscle

Bones of rats assayed for microCT and from additional rats (in order to reach n = 6–12/group) were used for histomorphometry using published guidelines [42,43]. Calcein (i.p., 10 mg/kg body weight) had been previously injected at 9 and 2 days before euthanasia. Subcohorts of bones (n = 4–5/gp) were processed and embedded in methyl methacrylate resin (MMA, Osteo-Bed Bone Embedding Kit, Polysciences, Warrington, PA), and sectioned into 5 μm longitudinal sections and placed on charged slides. Unstained plasticized longitudinal sections were used to measure the fluorochrome label. Histomorphometry for dynamic parameters of trabecular bone formation was then performed in the distal metaphyseal radius, as previously described [30]. Sections were then stained with Masson's Trichrome or TRAP5b and used for histomorphometry for static parameters of trabecular bone microarchitecture, as previously described [30] using an image analysis program (Osteo 2017, Bioquant, Nashville, TN). The remaining forelimb bones were paraffin-embedded (n = 5–7/group), after decalcification in a 14% acid free EDTA solution. The paraffin-embedded sections were used for TUNEL and immunohistochemical staining (described below). The percentage of empty lacunae was determined in H&E stained bones by counting the number of empty osteocyte lacunae and then dividing by the total number of lacunae with or without evidence of cells, in 3 sections per rat radius (same metaphyseal and mid-diaphyseal regions as assayed with microCT). Void areas within the marrow areas of all bones were also qualitatively assessed during this scoring.

Flexor digitorum muscles were dissected off the radial and ulnar bones prior to microCT analyses, equilibrated in 30% sucrose in phosphate buffer (pH 7.4; n = 5–6/group), and then cryosectioned at the mid-region of the muscle (at its widest point) into cross-sections of 12 μm thick each. These sections were mounted on slides, dried and stained with hematoxylin and eosin. An image analysis program was used (Bioquant) to measure the cross-sectional area (CSA) of the entire flexor digitorum muscle belly in mm^2.

2.7. TUNEL staining in radius

Paraffin-embedded bone sections were deparaffinized with xylene (three times, for 45 min at 37 °C, each), rehydrated in alcohol washes, and then washed in a 0.9% NaCl solution, followed by a PBS wash. Sections were permeabilized with a proteinase K buffer, followed by a rTdT enzyme, nucleotide mix and equilibration buffer solution incubation for 60 min at 37 °C protected from light (G3250, Promega DeadEnd Fluorometric, Madison, WI, USA). Sections were batched stained to reduce variability. Positive control staining was achieved by pre-treating one tissue section with DNAse to generate DNA fragments. For negative controls, the rTdT enzyme was omitted during incubation. Slides were coverslipped with Vectashield + DAPI (4′,6-diamidino-2-phenylindole, H-1200, Vector Lab, Burlingame, CA, USA). The number of TUNEL-positive and DAPI-stained osteocytes was counted in metaphyseal trabecular and mid-diaphyseal cortical regions of the radius. Two sections were counted in the preferred reach limbs of 4–7 rats/group. Percent of TUNEL positive osteocytes per area was determined by dividing the number of TUNEL-positive osteocytes by the total number of DAPI-stained osteocytes, and multiplying by 100.

2.8. Immunohistochemistry

Immunohistochemistry for sclerostin and RANKL was performed on paraffin-embedded bone sections (n = 5–7/group), after deparaffinization with xylene and rehydration through a series of alcohol washes, 0.5% pepsin antigen retrieval and blocking steps (4% goat serum in PBS, 30 min). Primary antibodies used were anti-Sclerostin (SostDC1, ab99340, Abcam, Cambridge, MA) and anti-RANKL (sc-7628, Santa Cruz Biotechnology, Santa Cruz, CA), at 1:200 and 1:400 dilutions, respectively, in PBS, for 24 h at room temperature. Appropriate secondary antibodies (Jackson Immuno Research Labs, West Chester, PA) tagged with horseradish peroxidase were used (1:100 dilution in PBS for 2 h at room temperature) and visualized using diaminobenzidine (SigmaFast D0426, Sigma-Aldrich, St. Louis, MO). Sections were batched stained to reduce variability. Preabsorption controls were performed to demonstrate specificity of RANKL and sclerostin antibodies using recombinant RANKL protein (ab9958, Abcam) and SOSTDC1 peptide (ab119134, Abcam). A two-fold excess of purified protein or peptide was pre-incubated with the matching antibody overnight at 4 °C, the mixture centrifuged, and the pre-absorbed antibody supernatant then incubated with tissues (after pepsin and goat serum treatment) for 2 h, before washing and incubation with secondary antibodies; no labeling was observed (data not shown). Negative control staining was performed by omitting either the primary or secondary antibody; no labeling was observed in any case (data not shown). Sclerostin and RANKL immunoexpression was quantified as percent area of tissue with immunostaining per area, using previously described methods [44], using a Nikon microscops (E800) linked to a digital camera (Q-Imaging Retiga camera) and a computer with image analysis software (Osteo II, Bioquant). Cells within the marrow area were excluded from these analyses. At least 3 adjacent trabecular regions (at 1.5 mm below the center of the epiphyseal plate) and mid-diaphyseal cortical regions were quantified per rat bone.

2.9. Microcrack staining and analysis

Bones of six additional rats (3 contols and 3 High-ForceHR rats) were used for en bloc basic fuchsin staining, using previously described methods [45,46]. Specimens of the radius and ulna (still attached via their interosseous membrane) were placed in 70% ethanol, then bulk stained in 1% basic fuchsin in a graded series of alcohols (80, 90 and 100%) under vacuum of 20 mm Hg for 24 h before being embedded without decalcification in MMA. Specimens were cut into 80 μm transverse sections using a diamond blade saw at the level of the metaphyseal regions (trabeculae and cortical bone included) and mid-diaphysis regions. Cross-section were mounted on slides and linear microcracks were counted at 400× magnification using a light microscope (Nikon E600) interfaced with a Nikon camera (DS-Ri2) and NIS-Elements. In vivo microcracks were defined as open cracks that were intensely stained with basic fuchsin, having a certain depth of field, and a surrounding halo of increased basic fucshin stain [47]. Linear microcrack density (Cr.Dn = Cr.N/B.Ar, #/mm^2) was then measured. Data from several sections of radial and ulnar bones were summarized.

2.10. qPCR analysis

Forelimb bones (radius and ulnar together) were collected from 6 Controls and 4 High-ForceHR rats (without flushing the marrow area), divided into distal (metaphysis and epiphysis combined) and mid-diaphysis using sharp scissors, flash frozen separately and stored at −80 °C until use. After thawing on ice, the bones regions were powdered, keeping distal and mid-diaphyseal regions separate, using liquid nitrogen and a mortar and pestle, and RNA isolated using Trizol (15596-026, Life Technologies, Grand Island, NY, USA) and chloroform, before precipitating with 2-propanol. RNA was quantified using a Beckman spectrophotometer (Beckman Coulter, Jersey City, NJ, USA). cDNA was

then synthesized using a cDNA kit (A-B1453/A, Thermo Scientific Verso, Pittsburgh, PA, USA) and a GeneAmp PCR 9700 system (Applied Biosystem, Grand Island, NY, USA). Quantification was achieved by Real Time PCR using SYBR Green PCR Master Mix (4309155, Applied Biosystems), ran in duplicate using a Real-Time PCR 7500 Instrument and analyzed with sequence detection software (V:1.2.3) from Applied Biosystems. Beta-actin was selected as the housekeeping gene. Primer's sequences used are provided in Supplemental Table 1. Values reported are fold difference compared to Beta-actin using the $2^{-\Delta\Delta CT}$ method.

2.11. ELISAs

Serum was collected from n = 8–15/group and assayed using commercially available ELISA kits for levels of osteocalcin (AC-12F1, Rat-MID Osteocalcin EIA, Immunodiagnostic Systems, Tyne & Wear, UK), CTX-1 (AC-06F1, RatLaps EIA, Immunodiagnostic Systems), RANKL (RRNKLMAG-31K-01, Millipore Corporation, Billerica, MA), and sclerostin (MSST00, R&D Systems) following manufacturer protocols. For the RANKL assay, each sample was run in duplicate and analyzed using a Bio-Rad Bio-Plex System with a Bioplex manager 4.0 software (Hercules, CA). Forelimb bones (radius and ulnar together) of subsets of rats (n = 4–6/group) were collected and divided into distal metaphyseal and mid-cortical regions, stored at −80 °C until homogenized individually, as previously described [48], and analyzed for RANKL and sclerostin using the same ELISAs kits as for serum. Bones were also analyzed for osteoactivin using a commercially available DuoSet ELISA Development kit (DY2330, R&D Systems) onto which an anti-osteoactivin antibody was added (1:350, custom made anti-chicken OA; produced and verified for specificity, as previously described [49]). Flexor muscles of the forelimb (flexor digitorum, flexor carpi ulnaris and flexor carpi radialis) and flexor digitorum tendons were also collected from 4 to 6 rats/group and analyzed for osteoactivin levels using ELISA. Results were analyzed using a VersaMax microplate reader and SoftmaxPro Version 5 software (Molecular Devices LLC, Sunnyvale, CA). ELISA data (pg cytokine protein) were normalized to μg total protein, which was determined using a bicinchoninic acid (3225, Pierce BCA Protein assay, Thermo Fisher Scientific, Waltham, MA). Each sample was run in duplicate in a blinded manner.

2.12. Western blot analysis

Bone homogenates from above were also assayed using 4–12% Tris-Glycine gels (Novex, XP04122BOX, Thermo Fisher Scientific) and then Western Blot analysis methods for TNFalpha levels using a specific anti-TNFalpha antibody (1:1000 dilution, ab6671, Abcam) and visualized using Licor imaging methods. GAPDH (glyceraldehyde-3-phosphate dehydrogenase) and/or Beta-actin were used as loading controls and were detected using specific antibodies (anti-GAPDH, 1:500 dilution, sc32233, Santa Cruz; anti-Beta-actin, 1:300 dilution, A1978, Sigma). Densitometry was performed using myImageAnalysis version 1.1 (Thermo Fisher Scientific). Western blots were repeated at least three times.

2.13. Statistical analyses

Graphpad Prism 7 was used for the statistical analyses. p values of <0.05 were considered as statistically significant. Data are expressed as mean ± standard error of the mean (SEM). Two-way ANOVAs were used to determine: 1) differences in task parameters between High-ForceHR versus Low-ForceHR rats using the factors group and time (week of task performance); 2) differences in microCT and histomorphometry outcomes using the factors group and bone (radius versus ulna); 3) differences in mRNA expression levels, and sclerostin and RANKL protein levels that were assayed via ELISA, using the factors group and region (distal versus proximal); and 4) differences in sclerostin and RANKL protein levels that were assayed immunohistochemically, using the factors group and bone (radius versus ulna). One-way ANOVAs were used to determine differences in serum protein levels between the three groups (High-ForceHR, Low-ForceHR and control rats). ANOVAs were followed by Tukey posthoc tests (for one-way ANOVAs) or Sidak posthoc tests (for two-way ANOVAs) to determine differences. Two-tailed *t*-tests were used when only two groups were compared.

3. Results

3.1. Reach performance across the 18 weeks

We first investigated the consistency of performance of the operant High-ForceHR and Low-ForceHR tasks by the task rats. Each group learned to perform their respective task appropriately by task week 3 (Fig. 2A–D). The High-ForceHR rats performed the task at or near 4 reaches/min in task weeks 3 through 12, although below target levels in weeks 1 and 18 (Fig. 2A), matching past findings of symptoms of forepaw discomfort in High-ForceHR 18 week rats [34]. The Low-ForceHR rats had a tendency to overreach, particularly in task week 1, yet neared target levels in weeks 12 and 18. Each task group met their target mean reach force consistently in weeks 3 through 18 (Fig. 2B). The High-ForceHR rats had higher, yet consistent mean grasp durations and reach impulses levels than Low-ForceHR rats, in weeks 3 through 18 (Fig. 2C,D), and worked at a significantly higher percent duty cycle than Low-ForceHR rats in weeks 3–18 (Fig. 2E). The mean % duty cycle of the High-ForceHR rats was 0.98%, and 0.79% for the Low-ForceHR rats calculated from the formula as suggested by Potvin [41,50], for repetitive upper extremity tasks [41,50] (see Materials and methods). During individual sessions, High-ForceHR rats had ranging grasp force levels around their target level, with many reaches within maximum and minimum range levels, but a few reaches above or below required force thresholds, for which they received no food reward (Fig. 2F; Supplemental Fig. 1). Thus, despite the voluntary nature of the task, the rats performed each task fairly consistently, while still maintaining some dynamic properties of pulling and tissue loading. Low-ForceHF rats showed similar dynamic loading within sessions (data not shown).

The Low-ForceHR rats had a higher total number of reaches across the 18 weeks of task performance than High-ForceHR rats, due to the former's tendency to overreach (Table 1). Yet, the total grasp time and the total volume of lever bar grasping and loading across the 18 weeks (total reaches × total msec of grasping × mean force per grasp) were higher in High-ForceHR rats than in Low-ForceHR rats (Table 1).

The rats also showed variations in the style of pulling with continued task performance. The Low-ForceHR rats maintained a fairly isometric style of lever pull across weeks of task performance, although the number of digits used to pull might vary (Supplemental Fig. 2A,B). High-ForceHR showed increasing tendencies towards supinated or twisted forelimb and forepaw positions, as show in Supplemental Fig. 2C, and as previously reported [34,51].

3.2. Distal metaphyseal trabecular bone

We next examined the impact of performance of the tasks for 18 weeks on trabecular bone microarchitecture in the distal metaphyseal region of the radius and ulna using microCT (Table 2). Fig. 1C shows representative two-dimensional (2D) and 3D images of each group. Two-way ANOVAs showed several significant differences by group and between the radius and ulna bones. Distal metaphyseal trabeculae in the radius showed reduced % BV/TV and Tb.N in High-ForceHR rats, compared to controls, as well as increased Tb.Sp and degree of anisotropy (DA). In contrast, trabeculae in this same region in Low-ForceHR rats showed increased BV/TV and Tb.Th, and a decrease in DA, compared to controls. Microarchitectural changes induced by the tasks differed in the ulna, with High-ForceHR rats showing

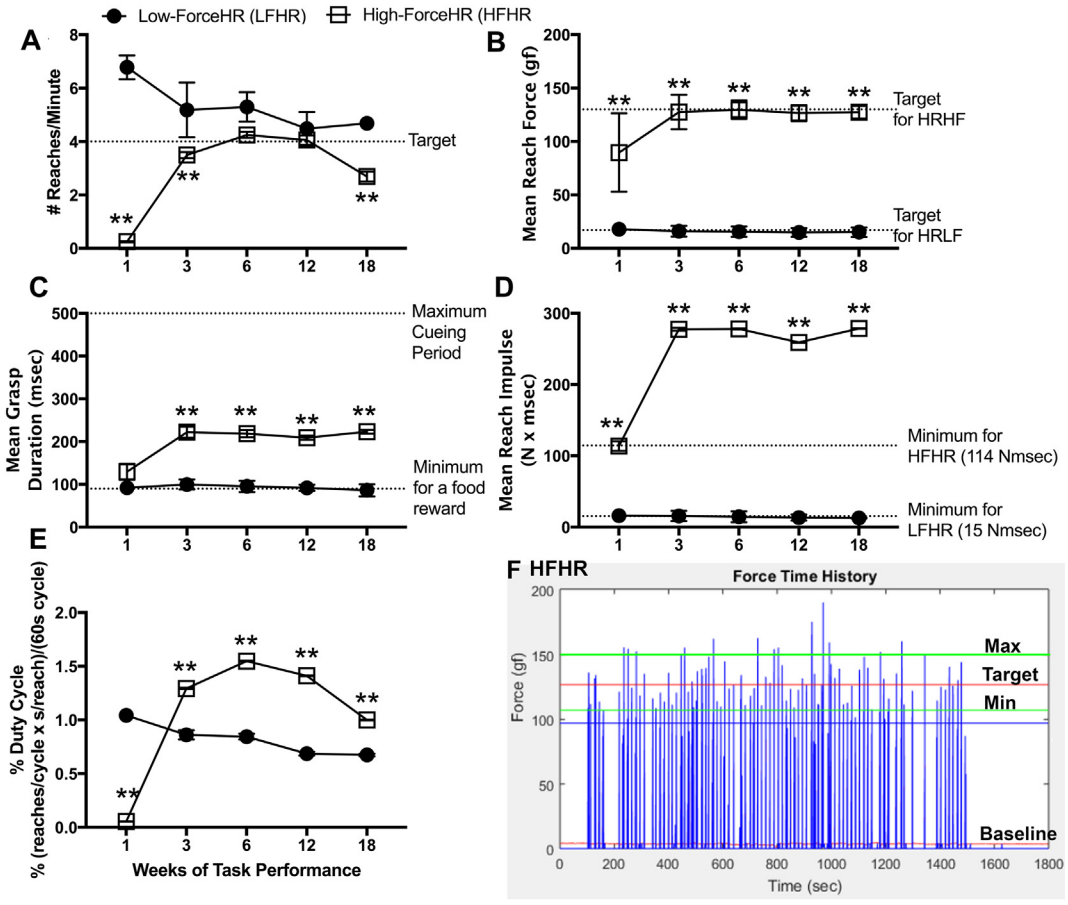

Fig. 2. Reach parameters in High-ForceHR (HFHR) and Low-ForceHR (LFLR) rats across weeks of task performance (n = 12 and 15/gp, respectively). (A) Number of reaches per minute; the target was 4 reaches/min (dashed line). (B) Mean reach force on the lever bar (grams force, gf). Target for HFHR rats was 130 grams of force (gf); target for LFLR rats was 17 gf. (C) Mean duration of grasping the lever bar (msec) per reach. The minimum duration required for a food reward was 90 msec. (D) Mean Reach Impulse (Nmsec), defined as mean reach force (N) multiplied by grasp duration (msec). (E) Percent Duty Cycle, defined as reaches/cycle multiplied by grasp duration (in seconds (s)) on the lever bar per reach, divided the cycle time (60 s), and then multiplied by 100. (F) Representative graph of force time history of one 30 minute session (1800 s) by a High-ForceHR rat, extracted from Force Lever program files using a custom-written MATLAB program. The vertical blue lines indicate a pull on the force lever bar; the horizontal red line indicates the target of 130 gf; the green lines indicate the minimum (110 gf) and maximum (150 gf) thresholds of force. Baseline as indicated. Mean ± SEM is shown; **p < 0.01, compared to LFLR rats.

decreases in their ulnar metaphyseal trabecular % BV/TV that did not reach significance, compared to controls, although they did have significantly decreased Tb.N and increased Tb.Sp and Tb.Th (the latter an adaptive change that apparently prevented the loss of overall trabecular bone volume in High-ForceHR rats' ulnas). Low-ForceHR rats' ulnas showed only an increase in metaphyseal Tb.Th, compared to controls.

3.3. Mid-diaphyseal cortical bone

We then examined the mid-diaphyseal cortical bone of the radius and ulna using microCT (Table 3). Two-way ANOVAs showed several significant differences by group and between the radius and ulna bones. Specifically, analyses of mid-diaphyseal cortical bone of the radius in High-ForceHR rats revealed only a small increase in cortical area fraction, compared to controls. In contrast, the Low-ForceHR rats showed increased total cross-sectional thickness and cortical area, and decreased cortical area fraction in the mid-diaphysis of the radius, compared to controls. In further contrast, there were no significant changes in the ulna's mid-diaphyseal cortical bone in High-ForceHR rats, and Low-ForceHR rats only showed an increased total cross-sectional area in this same region of the ulna, compared to controls.

Table 1
Estimated total volume of loading across 18 weeks.

Reach parameter	HFHR (n = 12)	LFHR (n = 9)
	Mean ± SEM	Mean ± SEM
Total volume of reaches (total reaches)	19,105 ± 795*	34,252 ± 3724
Total grasp time of lever bar (msec)	3605 ± 178**	1676 ± 213
Mean Grasp Force (N)	1.18 ± 0.08**	0.16 ± 0.01
Total volume of loading (total reaches × total msec grasping × mean force per grasp)	81,266,234 ± 11,333**	9,187,665 ± 7938

* and **: p < 0.05 and p < 0.01, compared to LFHR.

3.4. Histomorphometry of distal metaphyseal trabeculae

Static histomorphometry of the distal metaphyseal trabeculae showed several significant differences by group and between the radius and ulna bones (Table 4). Specifically, in this region of the radius, there were decreased numbers of osteoblasts per bone surface (N.Ob/BS) in High-ForceHR rats, yet increased N.Ob/BS and osteoid volume per bone volume (% OV/BV) in Low-ForceHR rats, compared to controls. The percent osteoid surface (% OS/BS) was also increased in Low-ForceHR rats, compared to High-ForceHR rats. Also in this region of the radius, the number of osteoclasts per bone perimeter (N.Oc/B.Pm) and percent osteoclast surface to total bone surface (Oc.S/BS) were considerably increased in High-ForceHR rats, compared to control and Low-ForceHR rats. Most of these attributes were unchanged in this same region of the ulna of both High-ForceHR and Low-ForceHR rats, compared

Table 2
MicroCT results for distal metaphyseal trabeculae in radius and ulna in response to 18 weeks of High-Force High Repetition (HFHR) or Low-Force High Repetition (LFHR) task, compared to age-matched control rats (C).

Radial distal metaphysis		C	HFHR	HFHR/C	LFHR	LFHR/C	Two-way ANOVAs
Trabecular bone		n = 14	n = 8 reach limbs	% diff[a]	n = 7 reach limbs	% diff[a]	Radius vs Ulna[b]
Bone volume fraction	BV/TV (%)	37.35 ± 2.26	**32.30 ± 1.29***	**86%**	**45.16 ± 3.19 *,††**	**121%**	Gp p = 0.005, Bone p < 0.0001
Trabecular number	Tb.N (1/mm)	5.27 ± 0.23	**4.58 ± 0.29***	**87%**	**6.08 ± 0.35†**	115%	Gp p = 0.002, Bone p < 0.0001
Trabecular thickness	Tb.Th (mm)	0.07 ± 0.001	0.07 ± 0.001	100%	**0.08 ± 0.004***	**114%**	Interaction p = 0.04
Trabecular separation	Tb.Sp (mm)	0.12 ± 0.006	**0.15 ± 0.01***	**125%**	0.12 ± 0.009	100%	n.s.
Degree of anisotropy, 0 = isotropic	DA	0.47 ± 0.03	**0.56 ± 0.03***	**119%**	**0.34 ± 0.04**,††**	**72%**	n.s.
Ulnar distal metaphysis		C	HFHR	HFHR/C	LFHR	LFHR/C	
Trabecular bone		n = 8	n = 7 reach limbs	% diff[a]	n = 5 reach limbs	% diff[a]	
Bone volume fraction	BV/TV (%)	27.62 ± 2.65	24.23 ± 1.57	88%	29.1 ± 3.28	104%	
Trabecular number	Tb.N (1/mm)	3.76 ± 0.30	**2.50 ± 0.18****	**67%**	3.34 ± 0.42	88%	
Trabecular thickness	Tb.Th (mm)	0.08 ± 0.001	**0.09 ± 0.002****	**112%**	**0.09 ± 0.002****	**112%**	
Trabecular separation	Tb.Sp (mm)	0.18 ± 0.01	**0.24 ± 0.02***	**133%**	0.22 ± 0.02	122%	
Degree of anisotropy	DA	0.49 ± 0.02	0.46 ± 0.06	94%	0.45 ± 0.06	92%	

* and ** p < 0.05 and p < 0.01, compared to age-matched C rats; † and ††: p < 0.05 and p < 0.01, compared to HFHR rats.
[a] % difference between means; means ± SEM shown.
[b] Two way ANOVA results using the factors group (gp) and bone. n.s. = not significant.

to control rats, with the exception of increases in both osteoblast and osteoclast numbers in High-ForceHR rats. Void areas were also assessed in all stained bone sections; no differences were seen when comparing any group or bone.

Based on the above, dynamic histomorphometry of distal metaphyseal radial trabeculae was examined and showed a reduced bone formation rate (BFR) in High-ForceHR rats, compared to controls, yet increases in Low-ForceHR rats (as well an increased mineral apposition rate, MAR), compared to both control and High-ForceHR rats (Fig. 3A,B). The distal radial trabeculae of control rats showed the presence of double-labeled calcein lines, as did Low-ForceHR rats (Fig. 3C). In contrast, distal radial trabeculae of High-ForceHR rats showed more sites with woven bone and single-labeled calcein lines (Fig. 3C).

Serum osteocalcin, a marker of bone formation throughout the body, was increased only in Low-ForceHR rats compared to the other groups (Fig. 3D). Serum CTX1, a biomarker of bone degradation, was altered only in Low-ForceHR rats (decreased), compared to control and High-ForceHR rats (Fig. 3E).

3.5. Apoptosis in distal metaphyseal trabeculae of the radius

When examining radial bone sections, we noticed that High-ForceHR rats had more empty osteocyte lacunae in distal metaphyseal trabeculae than controls (Fig. 4A–C). Histomorphometry confirmed this finding (Fig. 4D). In contrast, the mid-diaphyseal radial cortical bone did not show such increases (see Fig. 6H for an example), nor did any region of the radius in Low-ForceHR rats, compared to controls (Fig. 4D; mid-diaphyseal data not shown). Both regions of the ulna in each group also lacked this increase in empty osteocyte lacunae (data not shown).

To determine if the High-ForceHR task induced osteocyte apoptosis, we performed TUNEL staining and quantification. High-ForceHR had increased numbers of TUNEL-positive osteocytes in distal metaphyseal trabeculae of the radius, compared to controls (Fig. 4E). Such increases were neither observed in Low-ForceHR rat bones, nor in the mid-diaphysis of either group of task rats (Fig. 4F). Representative images of TUNEL stained distal radial trabeculae are shown in Fig. 4G.

Table 3
MicroCT results for mid-diaphyseal cortical bone in radius and ulna in response to 18 weeks of High-Force High Repetition (HFHR) or Low-Force High Repetition (LFHR) task, compared to age-matched control rats (C).

Radial mid-diaphyseal		C	HFHR	HFHR/C	LFHR	LFHR/C	Two-way ANOVAs
Cortical bone		n = 14	n = 8 reach limbs	%	n = 6 reach limbs	% diff[a]	Radius vs Ulna[b]
Total cross-sectional area	Tt.Ar (mm^2)	1.56 ± 0.06	1.50 ± 0.03	96%	**1.92 ± 0.002**,††**	**123%**	Gp p = 0.009, Bone p < 0.0001
Cortical bone area	Ct.Ar (mm^2)	1.46 ± 0.06	1.45 ± 0.02	99%	**1.76 ± 0.02**,††**	**121%**	Gp p = 0.009, Bone p < 0.0001
Cortical area fraction	Ct.Ar/Tt.Ar (%)	94.86 ± 1.21	**96.66 ± 0.30***	**102%**	**91.62 ± 0.83*,††**	**96%**	Interaction p = 0.03
Marrow area	Ma.Ar (mm^2)	0.10 ± 0.02	0.12 ± 0.45	120%	0.15 ± 0.02	150%	n.s.
Mean cortical thickness	Ct.Th (mm)	0.17 ± 0.02	0.17 ± 0.01	100%	0.18 ± 0.03	106%	n.s.
Closed cortical porosity	Po(cl) (%)	0.83 ± 0.17	0.69 ± 0.14	83%	0.70 ± 0.19	84%	n.s.
Ulnar mid-diaphyseal		C	HFHR	HFHR/C	LFHR	LFHR/C	
Cortical bone		n = 7	n = 8 reach limbs	%	n = 5 reach limbs	% diff[a]	
Total cross-sectional area	Tt.Ar (mm^2)	1.19 ± 0.04	1.27 ± 0.13	114%	**1.45 ± 0.07***	**122%**	
Cortical bone area	Ct.Ar (mm^2)	1.19 ± 0.04	1.28 ± 0.13	108%	1.38 ± 0.04	116%	
Cortical area fraction	Ct.Ar/Tt.Ar (%)	99.81 ± 0.20	99.72 ± 0.71	100%	99.78 ± 0.30	96%	
Marrow area	Ma.Ar (mm^2)	0.002 ± 0.0001	0.003 ± 0.0002	150%	0.003 ± 0.0005	150%	
Mean cortical thickness	Ct.Th (mm)	0.17 ± 0.01	0.18 ± 0.005	106%	0.19 ± 0.004	112%	
Cortical porosity	Ct.Po (%)	0.34 ± 0.05	0.39 ± 0.12	114%	0.33 ± 0.05	97%	

* and ** p < 0.05 and p < 0.01, compared to age-matched C rats; † and ††: p < 0.05 and p < 0.01, compared to HFHR rats.
[a] % difference between means; means ± SEM shown.
[b] Two way ANOVA results using the factors group (gp) and bone. n.s. = not significant.

Table 4
Static histomorphometry of metaphyseal trabecular bone in radius and ulna in response to 18 weeks of High-Force High Repetition (HFHR) or Low-Force High Repetition (LFHR) task, compared to age-matched control rats (C).

Radial distal metaphysis		C	HFHR	HFHR/C	LFHR	LFHR/C	Two-way ANOVAs
Trabecular bone		n = 7	n = 8 reach limbs	%	n = 6 reach limbs	% diff[a]	Radius vs Ulna[b]
Osteoblast surface	N.Ob/BS, (mm^{-1})	2.25 ± 0.66	**0.99 ± 0.19***	**44%**	**4.63 ± 0.64*,††**	**206%**	Interaction p = 0.02
Osteoid volume	OV/BV (%)	0.007 ± 0.002	0.003 ± 0.0007	43%	**0.05 ± 0.006*,†**	**714%**	Group p = 0.049
Osteoid surface	OS/BS (%)	0.04 ± 0.01	0.02 ± 0.005	50%	**0.05 ± 0.009†**	96%	n.s.
Osteoclast Number	N.Oc/BS (mm^{-1})	0.33 ± 0.05	**1.62 ± 0.21****	**490%**	**0.62 ± 0.25††**	188%	Group p < 0.0001
Osteoclast Surface	Oc.S/BS (%)	0.02 ± 0.005	**0.14 ± 0.02****	**700%**	**0.04 ± 0.02††**	200%	Interaction p = 0.04

Ulnar distal metaphysis		C	HFHR	HFHR/C	LFHR	LFHR/C
Trabecular bone		n = 5	n = 5 reach limbs	%	n = 5 reach limbs	% diff[a]
Osteoblast surface	N.Ob/BS, (mm^{-1})	3.04 ± 0.54	**3.80 ± 0.95***	**125%**	3.26 ± 0.90	107%
Osteoid volume	OV/BV (%)	0.007 ± 0.001	0.004 ± 0.0007	57%	0.005 ± 0.001	72%
Osteoid surface	OS/BS (%)	0.05 ± 0.007	0.05 ± 0.01	100%	0.05 ± 0.01	100%
Osteoclast number	N.Oc/BS (mm^{-1})	0.21 ± 0.17	**1.16 ± 0.28***	**552%**	0.36 ± 0.12	171%
Osteoclast surface	Oc.S/BS (%)	0.02 ± 0.006	0.06 ± 0.01	300%	0.03 ± 0.02	150%

* and ** p < 0.05 and p < 0.01, compared to age-matched C rats; † and ††: p < 0.05 and p < 0.01, compared to HFHR rats.
[a] % difference between means; means ± SEM shown.
[b] Two way ANOVA results using the factors group (gp) and bone. n.s. = not significant.

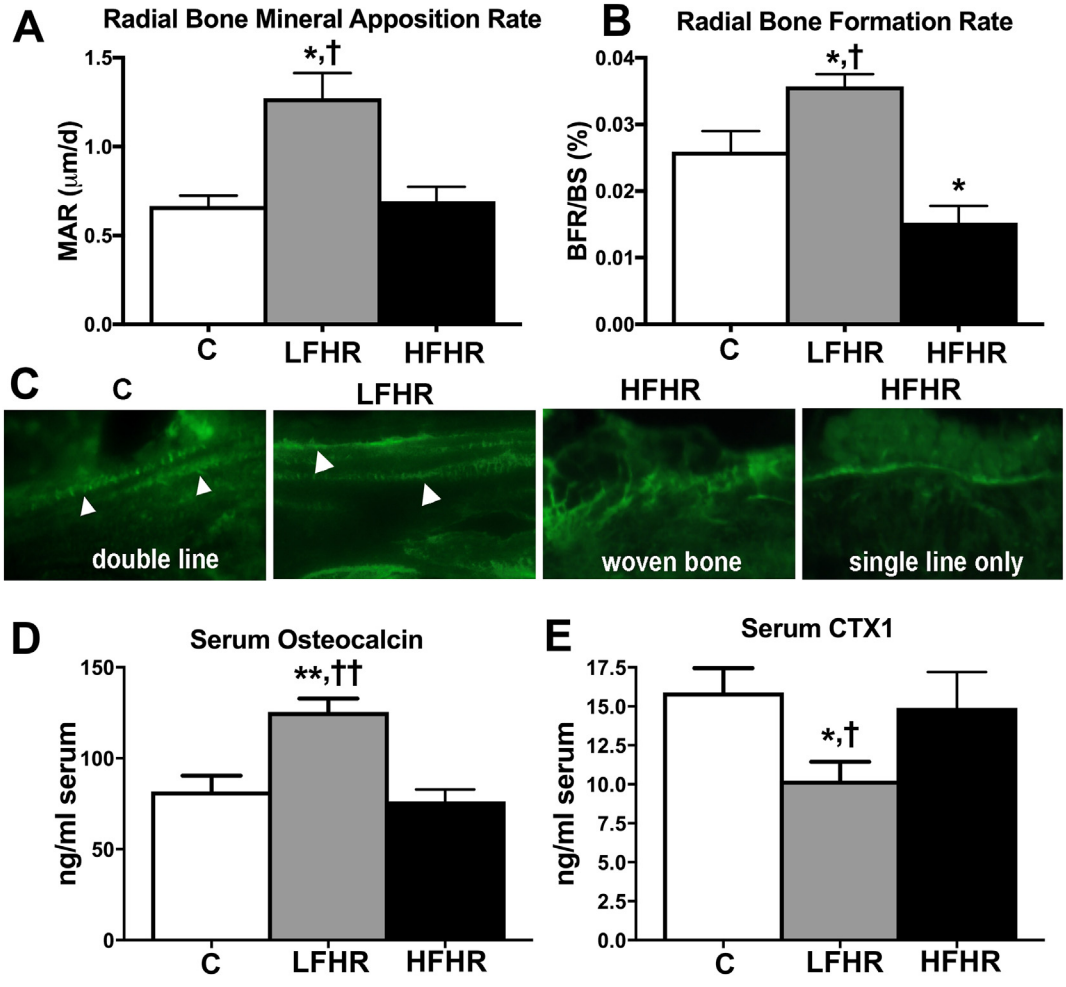

Fig. 3. Dynamic histomorphometry in distal radial metaphyseal trabeculae (n = 6–12/gp) and serum biomarkers of bone formation and turnover (n = 8–12/gp). (A) Mineral apposition rate (MAR). (B) Bone formation rate (% BFR/BS). (C) Calcein incorporation in C and LFLR rats was observed as double-labeled lines (arrowheads) in distal radial trabeculae, while calcein incorporation in HFHR rats was observed only as woven bone or single-labeled lines. (D) Serum levels of osteocalcin (a biomarker of bone formation). (E) Serum levels of CTX1 (a biomarker of bone degradation). Magnification 400×. Mean + SEM shown. * and **: p < 0.05 and p < 0.01, compared to control rats; † and ††: p < 0.05 and p < 0.01, compared to High-ForceHR rats.

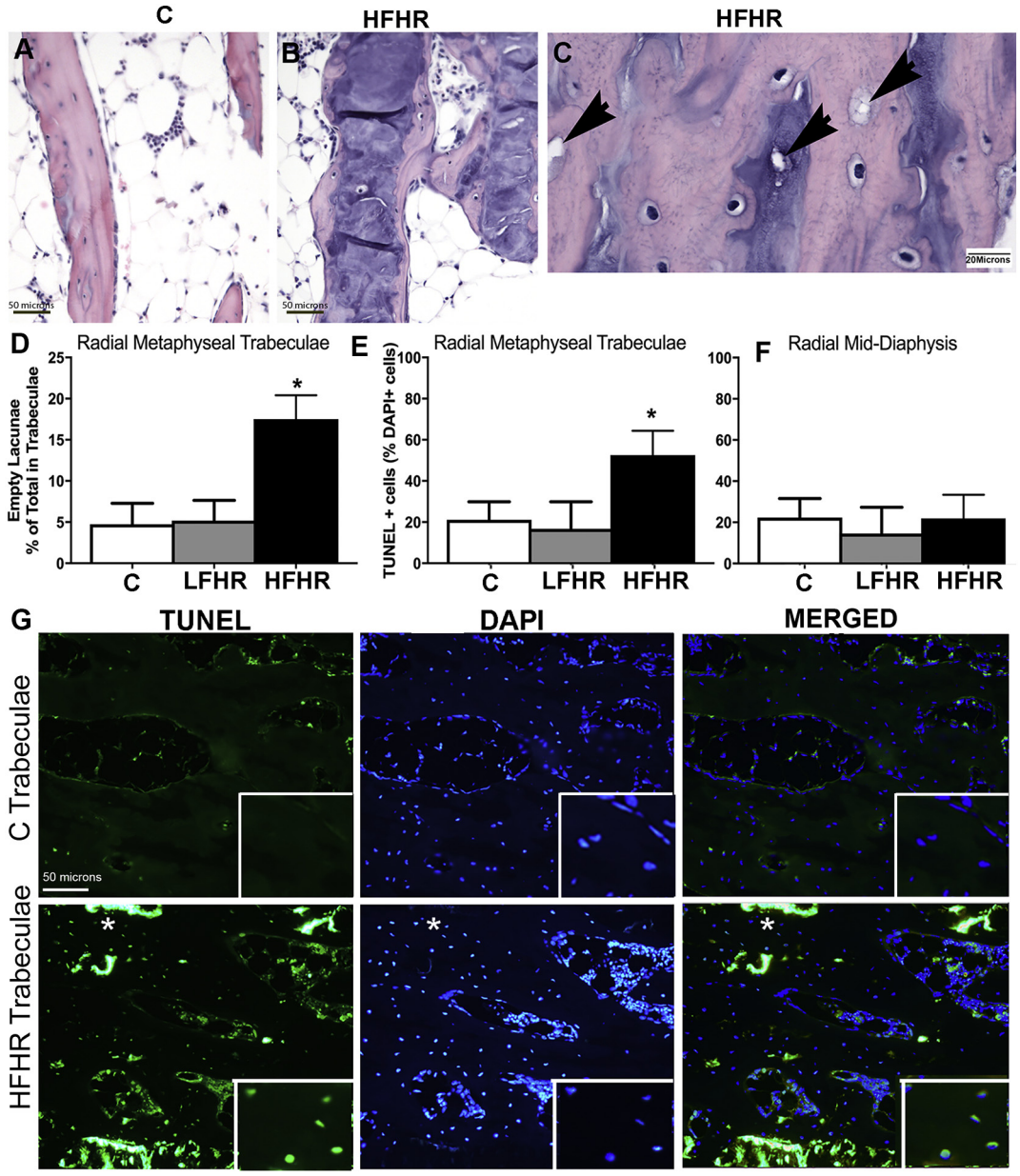

Fig. 4. Increased empty lacunae and TUNEL stained cells in distal radial metaphyseal trabeculae (n = 4–7/gp). (A–C) Representative distal radial trabeculae stained with H&E showing disrupted organization and increased empty lacunae (arrows in B and C) in High-ForceHR (HFHR) rats, relative to a Control rat (C). (D) Percentage of empty lacunae to all lacunae. (E and F) Percentage of TUNEL positive cells as a ratio of all DAPI stained cells in radial metaphyseal trabeculae and mid-diaphyseal cortical bone. (G) TUNEL stained cells (green), DAPI stained cells (blue) and merged representative images in C and HFHR rats. Asterisks indicate an area in the lower panels that are enlarged in the insets, showing examples of cells double-labeled with both TUNEL and DAPI. Mean ± SEM shown. *: $p < 0.05$, compared to C rats.

3.6. Microdamage analysis

Since apoptosis of osteocytes has been associated with presence of microdamage [26], we next assayed radial and ulnar bones of High-ForceHR and control rats for presence of linear microcracks (Fig. 5A–E). Linear microcracks were visible in distal metaphyseal trabeculae (some in association with resorptive spaces; Fig. 5A), and distal metaphyseal interstitial cortical bone regions of both bones in High-ForceHR rats (Fig. 5B–D). Quantification of Cr.Dn revealed higher numbers in metaphyseal trabecular and metaphyseal cortical bone regions of the radius in High-ForceHR rats, compared to controls (Fig. 5E). The number of microcracks in the ulna did not reach significance, and no microcracks were found in mid-diaphyseal bone regions of either bone in High-ForceHR or control rats.

3.7. Sclerostin protein levels

Since apoptosing osteocytes have been shown to increase their release of sclerostin [26], we next examined sclerostin protein levels in distal versus mid-diaphyseal regions of the radius and ulna (distal epiphyseal and metaphyseal regions of the radius and ulna were homogenized together, as were diaphyseal regions of the radius and ulna). ELISA revealed increased levels of sclerostin protein in distal regions of these forelimb bones in High-ForceHR rats, compared to control rats, but not in mid-diaphyseal regions, and not in either region in Low-ForceHR rats (Fig. 6A). Immunohistochemistry confirmed the increase in sclerostin protein in distal regions of the radius and ulna of High-ForceHR rats, compared to control rats, although a slightly higher level in the distal radius than distal ulna of High-ForceHR rats (Fig. 6B).

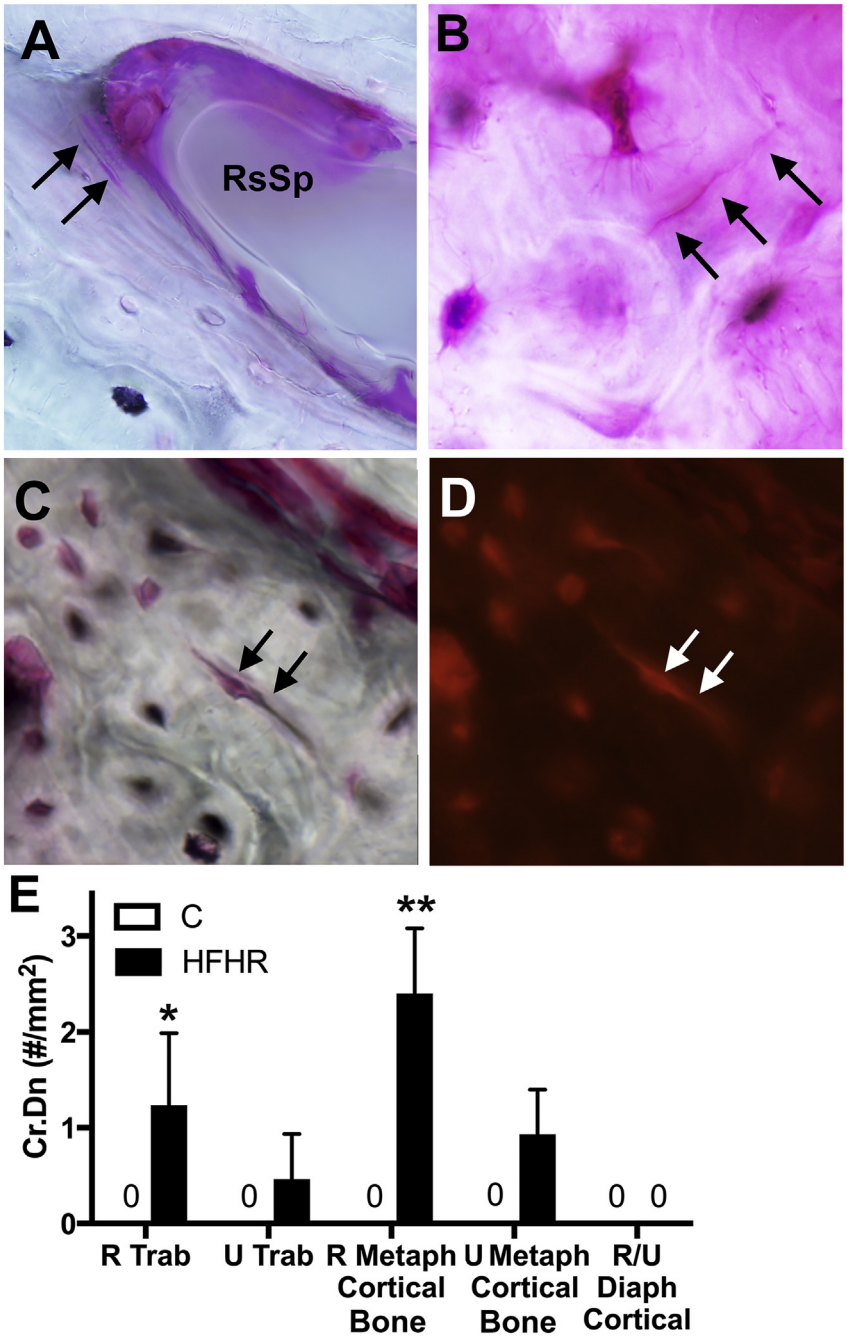

Fig. 5. Microcracks in radius bones. (A) Small linear microcracks in a trabeculae adjacent to a resorptive space (RsSp). (B-D) Examples of microcracks in interstitial bone of the metaphyseal radius cortical shell. Panel D shows same crack as in panel C using orange fluorescence. (E) Crack density (Cr.Dn) quantification, n = 3/gp. 400× magnification. Mean ± SEM shown. * and **: $p < 0.05$ and 0.01, compared to same region in control rats.

Sclerostin immunostaining was localized to osteocytes in trabecular and cortical bone regions of control rats (in both the radius and ulna), yet there was only low to no immunoexpression in the bone matrix in these regions in control rat bones (Fig. 6C,E,F). Small rounded cells adjacent to the trabecular bone also showed immunostaining for sclerostin (Fig. 6E); closer examination showed that these cells were not osteoblasts or osteoclasts. In contrast, High-ForceHR rats showed clear increases in sclerostin immunostaining within radial bone matrices (Fig. 6D,G,H). The High-ForceHR rats typically had no stained osteocytes in distal metaphyseal trabeculae of the radius (Fig. 6D,G), yet a mix of stained and unstained osteocytes in mid-diaphyseal cortical bone of the radius (Fig. 6H). Bone lining cells also showed increased sclerostin immunostaining in High-Force HR rats (Fig. 6H). Serum levels of sclerostin showed no significant differences ($p = 0.10$) between the groups (FRC: 348 ± 22.5, n = 15; High-ForceHR: 285 ± 16.51, n = 9; Low-ForceHR: 386 ± 36.36, n = 9).

3.8. RANKL levels

Since RANKL is also a signal released by apoptotic osteocytes following loading-induced microdamage [17], and known to promote osteoclast activity [22], we next examined RANKL levels using qPCR and ELISA methods (for each subcohort of bones, distal epiphyseal and metaphyseal regions of the radius and ulna were homogenized

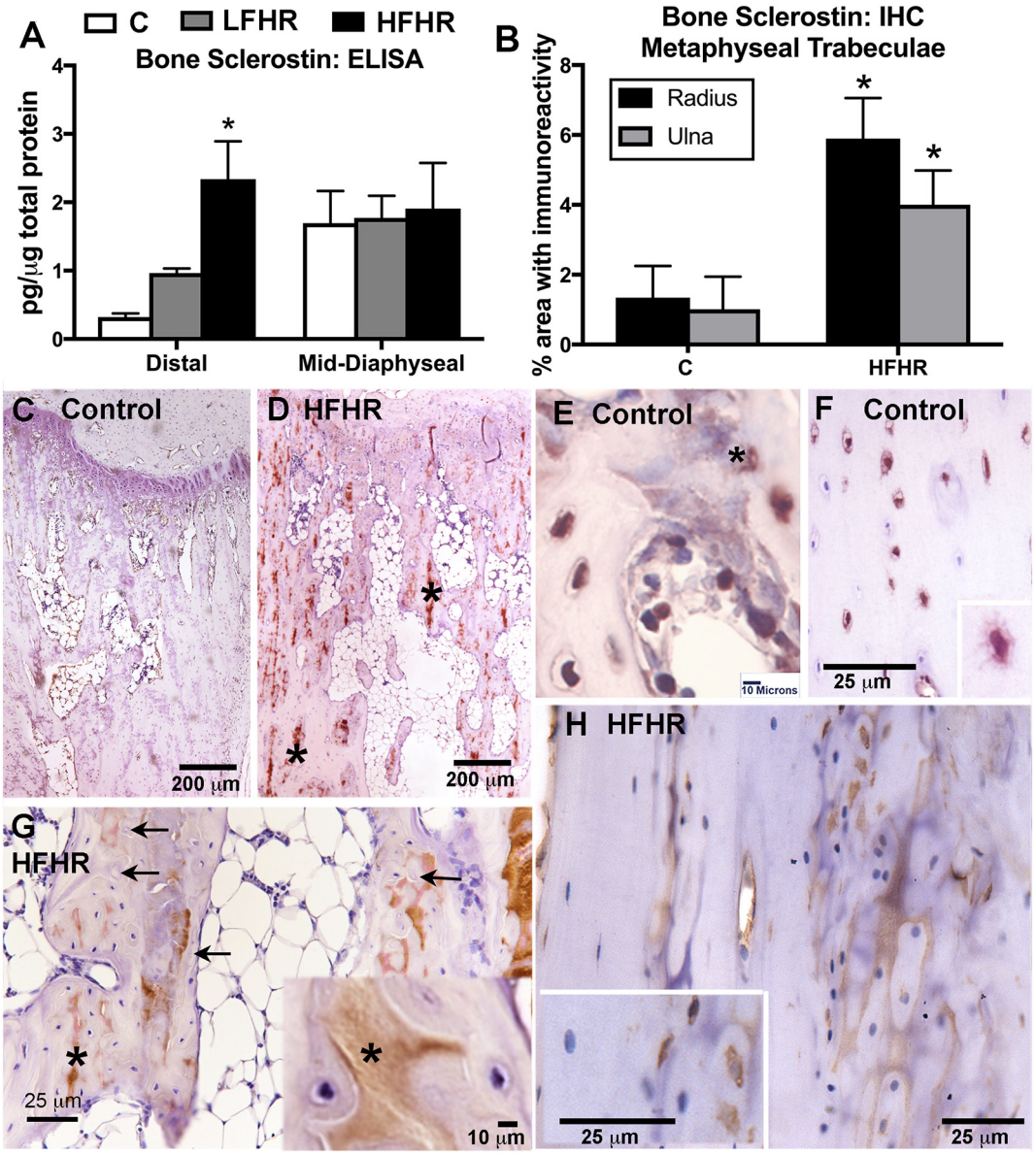

Fig. 6. Sclerostin expression in forelimb bones. (A) Sclerostin protein levels in forelimb bones assayed using ELISA (n = 4–6/gp). Distal region included radial and ulnar metaphyses and epiphyses; mid-diaphyseal region included the radial and ulnar diaphyses. (B) Quantification of sclerostin immunoexpression in distal metaphyseal trabeculae of the radius and ulna (n = 4–7/gp). (C and D) Representative low power images of sclerostin immunostaining (brown) in osteocytes and matrix (asterisks) of a control (C) and a High-ForceHR (HFHR) rat, respectively. (E and F) Representative higher power images showing sclerostin immunostaining in a C rat's trabecular and mid-diaphyseal cortical bone, respectively. (G and H) Representative higher power images showing sclerostin immunostaining in a HFHR rat's trabecular and mid-diaphyseal cortical bone, respectively. Small arrows indicate empty lacunae observed in HFHR 18 W rats' trabecular bone. Asterisks indicate an area in panel G enlarged in the inset. Bones in panels C–H were counterstained lightly with H&E. Mean + SEM shown. *$p < 0.05$, compared to C rats.

together, as were diaphyseal regions of the radius and ulna). Increased mRNA expression of RANKL was observed in distal radius and ulna regions of High-ForceHR rats, compared to controls (Fig. 7A; Low-ForceHR bones were not examined using qPCR), as was mRNA expression of its receptor, RANK (Fig. 7B). Osteoprotegerin (OPG) mRNA levels did not differ significantly by region or group (Fig. 7C). However, the ratio of RANKL mRNA expression to OPG mRNA expression increased in distal regions of the radius and ulna in High-ForceHR rats, compared to controls (Fig. 7D). No significant increases in mRNA expression of any analyte were observed in the mid-diaphysis regions (Fig. 7A–D).

Increased RANKL mRNA expression was matched by increased RANKL protein levels in the distal radius and ulna regions of High-ForceHR, compared to control rats, but not in the mid-diaphyseal regions (Fig. 7E). In contrast, RANKL protein levels were decreased in both of the radius and ulna in Low-ForceHR rats, compared to controls (Fig. 7E), and distally compared to High-ForceHR rats. Quantification of RANKL immunoexpression in distal metaphyseal trabeculae showed increased levels of RANKL in High-ForceHR rat radial bones, compared to control rat radii and High-ForceHR rat ulna bones, although these latter bones also showed increased RANKL immunoexpression, compared to control rat ulna bones (Fig. 7G). Immunohistochemistry was also used to identify RANKL producing cells and location and showed RANKL immunoexpression in osteocytes and bone lining cells, but not in osteoclasts, of controls (Fig. 7G). In High-ForceHR rats, the relative number of osteocytes expressing RANKL appeared higher than in controls, and the bone matrix of the distal radial trabeculae showed

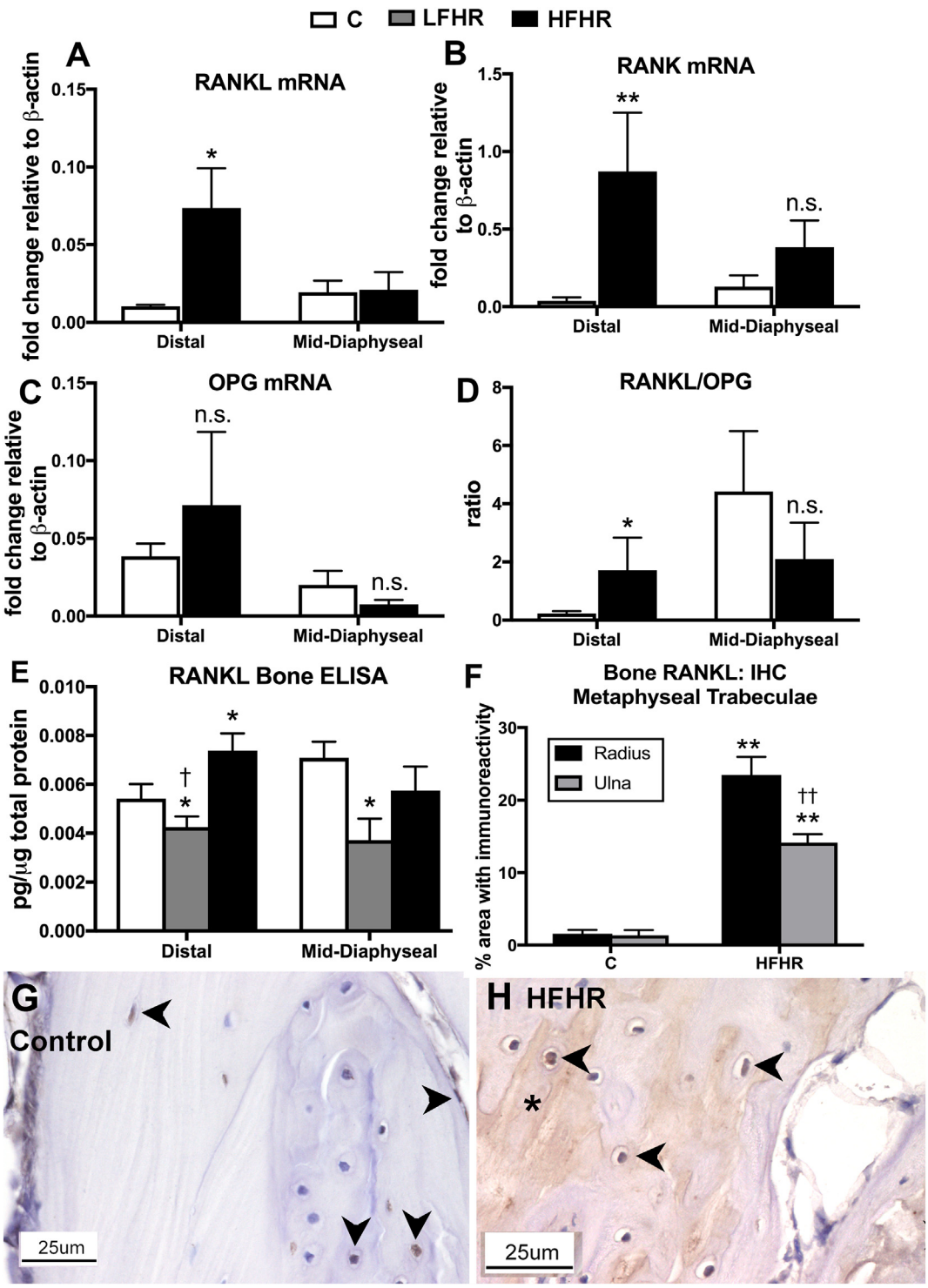

Fig. 7. RANKL, RANK and OPG analyses. (A–C) qPCR quantification of RANKL, RANK and OPG mRNA in forelimb bones (bones and regions as described in Fig. 7 legend). Fold changes compared to housekeeping gene beta-actin are reported. (D) The ratio of RANKL mRNA levels to OPG mRNA levels. (E and F) RANKL protein levels in forelimb bones, assayed using ELISA and immunohistochemical methods (n = 4–7/gp). (G and H) Representative images showing RANKL immunostaining (brown staining) in distal radial trabeculae of control (C) and High-ForceHR (HFHR) rats, respectively. Arrowheads indicate RANKL immunostained cells; asterisk indicates RANKL immunoreactive matrix. Sections were counterstained lightly with hematoxylin. Mean + SEM shown. Symbols as in Fig. 3's legend; n.s. = not significant.

increased RANKL immunostaining (Fig. 7H). Matrix RANKL staining was not present in control rats (Fig. 7G) or Low-ForceHR rats (data not shown). Serum levels of RANKL showed no significant differences ($p = 0.15$) between the groups (FRC: 10.26 ± 2.63, n = 8; High-ForceHR: 16.61 ± 5.18, n = 9; Low-ForceHR: 14.43 ± 1.96, n = 12).

3.9. Investigation of other possible contributors of observed bone differences

Radius and ulna bone levels of osteoactivin, a bone anabolic growth factor [49], were assayed using ELISA and showed decreased levels ($p = 0.02$) in High-ForceHR rats (0.14 ± 0.001, n = 7), compared to controls

(0.19 ± 0.01, n = 7) Since osteoactivin is also considered a potential "myometabokine" (a substance secreted by skeletal muscles that effects metabolism in other tissues including bone) [52], we also examined its levels in flexor muscles and flexor digitorum tendons. Using ELISA, we observed decreased levels ($p = 0.03$) in flexor forearm muscles (flexor digitorum, flexor carpi ulnaris and flexor carpi radialis muscles combined) of High-ForceHR rats (0.18 ± 0.02, n = 6), compared to controls (0.26 ± 0.02, n = 5). No group differences were observed in the flexor digitorum tendons (0.13 ± 0.009 in controls, versus 0.14 ± 0.006 in High-ForceHR rats, $p = 0.48$).

We also examined TNFalpha protein levels in distal regions of the radius and ulna (homogenized together) since it can stimulate osteoclastogenesis [53] and may serve as a mediator of increased sclerostin expression [54]. We have also observed increased TNFalpha levels in 6- and 12-week High-ForceHR rat forelimb bones in association with increased osteoclast numbers [29,33]. We observed no differences in TNFalpha levels in distal regions of control versus 18-week High-ForceHR rat radial and ulnar bones, using Western blot analysis (Supplemental Fig. 3), matching prior results of resolution of inflammatory responses in forearm muscles and serum of 18-week High-ForceHR rats [34].

To make sure that muscle atrophy was not contributing to bone catabolism, we examined for changes in the cross-sectional area of the flexor digitorum muscle, a key muscle involved in performing the High-ForceHR task and therefore bone loading. The cross-sectional area of the flexor digitorum muscle was 50.84 ± 3.12 mm^2 (mean ± SEM) in controls (n = 6), 49.73 ± 2.10 mm^2 in Low-ForceHR rats (n = 12), and 41.99 ± 2.76 mm^2 in High-ForceHR rats (n = 6). Although being lower in High-ForceHR rats, these differences were not significant.

Lastly, we tracked body weight across time and investigated serum estrogen levels at the time of euthanasia. No significant differences were observed between the groups, matching past findings for body weights and estrogen levels for 12- and 18-week Low-ForceHR rats, and 12-week High-ForceHR rats [30,32,55].

Thus, weight changes, differences in estrogen levels, potential muscle atrophy, or inflammatory responses at the time of tissue collection were ruled out as possible contributors to the observed bone changes. However, muscle changes in osteoactivin levels and past inflammatory changes [29,33] may be potential contributors.

4. Discussion

This is the first study, to our knowledge, to show clear support of the Damage Repair Theory response in trabecular bone when loaded at high force levels, rather than just positive adaptive changes in response to prolonged muscle contraction-induced loading. Prolonged high force loading was a key factor driving radial bone microarchitecture and cellular responses. Rats performing a High-ForceHR task for 18 weeks showed several catabolic indices trabeculae in their distal radial metaphyses, including decreased trabecular bone volume and osteoblasts, increased osteoclasts, microcracks and osteocyte apoptosis, as well as increased sclerostin and RANKL protein levels, compared to control rats. The mid-diaphyseal cortical bone of the radius showed few microarchitecture differences in High-ForceHR rats, compared to control rats, and unchanged apoptosis, sclerostin and RANKL protein levels. In contrast, the 18-week Low-ForceHR task induced many indices of positive adaptation in both distal metaphyseal trabeculae and mid-diaphyseal cortical bone of the radius, as well as decreased RANKL levels, and no apoptosis or changes in sclerostin levels, compared to control rats. Interestingly, in general, changes in the ulna bone of each task group were significantly less than in the radius, indicating that this reaching and grasping of a lever bar task results in more loading of the radial bone than the ulna. Thus, prolonged performance of an upper extremity reaching and grasping task is loading-, region-, and bone-dependent, as discussed further below.

In each task group, we observed small variations in the within session force-time history that are plausible reasons for the continued response of trabecular bone to either task since dynamic loads are thought to determine the osteogenic response [39]. We also observed that both task groups were able to maintain their target maximum voluntary pulling force and reach impulse levels in task weeks 3–18, meaning that each group's forelimb bones were loaded fairly consistently across time, according to their target requirements. Thus, as intended, the High-ForceHR rats maintained higher reach force, reach impulse levels and duty cycles than Low-ForceHR rats (despite the higher reaches/min in the latter group).

Duty cycle is the frequency of effort duration (percent time) an individual worker is engaged in a repetitive task [40,41,50]. Demands of a particular task are specific with regards to required grasp, load distributions on tissues, force requirements, and so on [56]. Maximum acceptable efforts (MAE) and maximum acceptable forces (MAF) of a job task on tissues are better predicted by force and duty cycle, than force and repetition, although all three are important [41,50]. If we first calculate the MAE for our two tasks, performed voluntarily by rats according to the expectations for psychophysical methodology [57], using an equation suggested by Potvin ($MAE = 1 - DC^{0.24}$) [41,50], we can predict that the MAE for High-ForceHR rats is 0.67, and 0.69 for Low-ForceHR rats. Calculation of the MAF by multiplying MAE by the rats' mean maximum voluntary force (2.45 N; see Materials and methods for determination) [41,50], shows that the predicted MAF is 1.64 N and 1.69 N for the High-ForceHR and Low-ForceHR tasks, respectively. The target grasp force of the High-ForceHR rats was 50% of their maximum voluntary force (1.27 N), easily below the predicted MAF. Yet, they developed bone microcracks and small muscle tears (reported previously [34]). We suggest that these equations over estimate the MAF on these tissues by 1.3 fold (1.64/1.27). These equations were developed from 69 short-term psychophysical data tasks (each <4 weeks in duration) and using physiological data from 6 studies demonstrating muscle fatigue after only 1 h [41,50]. As acknowledged by their creator, corrections are needed to accommodate longer endurance times, changes in worker performance, and very low duty cycles as limited data was available for validation. Since we observed increased radial trabecular bone volume in Low-ForceHR rats in this 18 week study, and previously in young adult rats performing at 15% of their maximum voluntary force and a similar duty cycle of 0.79% for 12 weeks [29,30], perhaps 15% is the MAF for prolonged performance of this task when performed at 4 reaches/min. Lowering force levels from 50% to 15% of maximum in task weeks 5–12, as a type of ergonomic intervention, rescues the loss of radial trabecular bone volume [58], further supporting high force as a key risk factor. Rest allowances, e.g., lowering duty cycles, may increase MAF and enhance tissue recovery [41,50,59]. Previously, we reduced the duty cycle to 0.66% by lowering the repetition rate to 2 reaches/min, yet maintained the same high force requirement (50% of maximum) in order to examine the effects of a 12-week High-Force Low-Repetition task; no significant losses were observed in radial trabecular bone volume, yet also no gains [29]. Increasing periods of complete relaxation between work cycles can also reduce health risks [60,61]. For the tasks reported here, periods of complete relaxation included the 1.5 h between the 30-minute work sessions, and the time between the Monday, Wednesday and Friday workdays. We are currently exploring the effectiveness of longer rest periods in our model.

The observed reductions in distal metaphyseal trabecular BV/TV and Tb.N, increased Tb.Sp, and woven bone seen in radii of 18-week High-ForceHR rats are indicators of reduced trabecular bone volume and quality in this bone region [62–65]. These changes could make the trabeculae at this site more brittle, increasing fracture risk [64,65]. The increase in degree of anisotropy (DA) in distal metaphyseal trabeculae of High-ForceHR radial bones may have also contributed to the microcracks and osteocyte apoptosis in this bone region, since a disorganized trabecular pattern would increase stress in the trabeculae [66]. These results are consistent with prior studies from our lab in

which 12-week High-ForceHR rats showed similar losses in bone volume in distal radial trabeculae, although empty osteocyte lacunae were not observed in those shorter studies [29,32,58]. The loss of trabecular bone volume in the distal metaphysis of the radius in High-ForceHR rats indicates that a pure mechanostat theory in which bones adapt to mechanical loads [35,67] does not apply to prolonged High-ForceHR loading of trabeculae. The various rest periods (discussed above) were apparently not often enough or long enough to allow for sufficient removal of the damaged bone and repair. This would be consistent with the Damage Repair Theory suggested previously for cortical bone [37,38] and with the Fatigue-Failure Theory for musculoskeletal disorder injuries [29,68].

In contrast to the distal trabeculae, the mid-diaphyseal cortical bones of both the radius and ulna remained relatively unchanged in High-ForceHR rats. There were no significant changes of mediators of either bone formation or resorption, and no induction of osteocyte apoptosis, in the mid-diaphyses. This finding of fewer changes in mid-diaphyseal regions of the radius and ulna than in their distal regions is consistent with prior findings from young adult rats performing either a negligible force repetitive reaching task for 8 weeks or the Low-ForceHR task for 12 weeks [30,69]. Our findings also match those by Tu et al. showing the cortical bone exhibits lower remodeling rates than trabecular bone [70]. It is also likely the interosseous membrane, which is attached to both the radius and ulna, equalized the peak strain magnitudes by the mid-diaphysis level, as shown previously using a mouse radius-ulna compression loading model [71].

Our data differs from those of ulna end-loading compression models, in which the ulnar bone shows more involvement than the radius and significant changes in the mid-diaphysis region [71–74]. We postulate that this is because our model is an operant reach and grasping model in which the forelimb is used as a freelimb. The increased degradative changes in distal metaphyseal trabeculae of the radius versus ulna of High-ForceHR rats is likely a result of repeated high force compressive forces from muscles involved in performing this lever pulling task [75]. Enthesis attachments to bones (both fibrocartilagenous and fibrous muscle-to-tendon-to-bone insertions) are known to drive changes in the underlying bone, including trabecular bone [76–78]. In our model, such entheses would include the brachioradialis muscle inserting on the distal epiphyseal radius, the pronator quadratus muscle inserting on the distal metaphyseal radius, and the pronator teres and supinator muscles inserting on proximal-to-mid regions of the radius. The ulna bone lacks such muscle insertion entheses, which may also contribute to fewer changes in the ulna than the radius. A number of static and dynamic loading experiments using human wrists/forearms in cadaveric studies, or models, have examined force distributions across the wrist joint to forelimb bones using sensors [79–85]. Results show that the wrist is extended and ulnarly deviated when in a neutral position, and that applied muscle-tendon loading while in this neutral position leads to force transmissions across carpal joints to the radius than through the triangular cartilage to the ulna (Erhart et al. reported a ratio of force transmission of 77:23, radius versus ulna, for example) [79,81–84]. During power gripping, there is even a greater ulnar deviation that rotates the proximal row of carpal bones dorsally, and extends the lunate and translates it radially, so that the force-transmission increases even further to the radius and decreases to the ulna [79,81]. Both Low-ForceHR and High-ForceHR rats used isometric-like pulls [29], although increasing incidence supinated/twisted power grip pulls in the High-ForceHR rats with continued task performance (see Supplemental Fig. 2 and previously reported results for High-ForceHR rats [34,51]). These findings combined also help explain the greater changes in radial versus ulnar architecture in the 18 week High-ForceHR rats.

Findings in the Low-ForceHR rats differ considerably from those in High-ForceHR rats. The increased anabolic indices in metaphyseal trabecular and mid-diaphyseal cortical bone in 18-week Low-ForceHR rats is consistent with studies showing that physical activity increases bone adaptation in response to loading [35,75]. Furthermore, the continued osteogenic response of the radius to Low-ForceHR loading is consistent with current evidence in human bones suggesting that there is no "lazy zone", and that bone can continue to adapt to imposed loads [31]. Note though, that these results pertain only to young adult rats. Aged rats performing this same Low-ForceHR for 12 weeks developed many signs of trabecular and cortical bone degradation that appeared to be due to increased systemic and tissue inflammatory cytokine responses occurring as consequences of both aging and continued loading, as well as reduced osteoblastic responses [30,86].

To return to the responses in High-ForceHR rats, increased empty lacunae were observed, as were increased numbers of TUNEL-positive osteocytes in distal radial bone trabeculae, compared to control rats. Findings of microcracks and apoptotic osteocytes in High-ForceHR metaphyseal trabeculae are suggestive of loading-induced microdamage in the bone matrix of the trabeculae through which the osteocytes extend their canaliculi [45,47,87–89]. Osteocyte apoptosis after microcrack damage is known to enhance the release of sclerostin and RANKL [26], which then increase bone catabolism and osteoclast activity [21,90].

Sclerostin production typically decreases with physiological bone loading and increases with bone unloading [19,70,91–93,108]. Although no decrease in sclerostin levels was seen in either task group, only prolonged performance of the High-ForceHR task was associated with significantly increased sclerostin bone protein levels, compared to control rats. Immunohistochemistry also showed enhanced sclerostin production in the remaining osteocytes surrounding empty lacunae and deposition in the radial bone trabeculae of High-ForceHR rats, findings not present in control or Low-ForceHR rats (data not shown for the latter group). A proposed mathematical model using an inhibitory protein mechanism suggests that a reduction in osteocyte numbers by apoptosis should result in a decline in sclerostin production [94]. Instead, our results are similar to those reporting that osteocyte apoptosis increases sclerostin secretion into the bone matrix [26]. The increase of sclerostin in distal bones in this current study was paralleled by decreased bone formation, which is interesting in light of studies indicating that sclerostin is a negative regulator of bone formation [89,95]. Recombinant sclerostin upregulates RANKL production and increases osteoclast formation [22], changes that enhance bone resorption. A key point to make is that the bones in this study were loaded continuously for 18 weeks after the shaping period, in which there was also increasing loading with each week (thus, 24 total weeks). No prior experimental study has examined sclerostin in bones after this length of loading time. Lastly, serum levels of sclerostin were unchanged from control levels in High-ForceHR rats, matching the mid-diaphyseal results (and likely levels in other bones throughout the body) rather than the distal metaphyseal results. This is consistent with a recent study indicating that serum levels of sclerostin may not reflect local levels [96].

RANKL immunoexpression was primarily seen in osteocytes in this study, matching recent reports that osteocytes are the primary source of RANKL post-embryogenesis [18,24,97]. It has been suggested that production and activity of RANKL and OPG, its receptor decoy, is dictated by the severity of the damage (i.e., microcracks, stress fractures), disrupting the osteocytic network [98]. Osteocytes in proximity to the damage site undergo apoptosis, while neighboring cells increase their production of RANKL, a response believed to encourage removal of the damaged matrix by osteoclasts [17,18,21,99]. The increase in RANKL mRNA and protein expression in distal forelimb bone regions of High-ForceHR rats, combined with the presence of microcracks, is suggestive of loading-induced matrix microdamage that was disruptive to the osteocytes, leading to their apoptosis, and triggering an increase in RANKL production by neighboring cells and then osteoclastogenesis [17,45,87,98,99].

We also attempted to investigate a muscle-bone interaction by examining osteoactivin levels in multiple forelimb tissues. Osteoactivin is an osteoblast-related glycoprotein and bone anabolic growth factor

[49,100–102], as well as a potential "myometabokine" that can affect metabolism in bone [52]. The decreased osteoactivin protein levels in both forelimb flexor muscles and bones of High-ForceHR rats could be contributing to the decreased osteoblast activity. We have reported an increase of osteoactivin in flexor forelimb muscles of rats that had performed a related Low-ForceHR task for 8 weeks [100,101]. Although more research is needed on this topic, perhaps the increased muscle osteoactivin contributed to bone anabolism in Low-ForceHR rats, and muscle reductions contributed to lowered metabolic responses in the underlying bone of High-ForceHR rats, as suggested in the literature for myometabokines [52,75,103].

Regarding possible contributions from underlying inflammatory responses, we have not yet assessed inflammatory cytokine responses occurring between 12 and 18 weeks of task performance in either task group [34,55]. However, we have reported that inflammatory cytokine levels in serum and forelimb muscles were highest immediately after training to high force levels or in task week 6 of High-ForceHR rats, and then declined progressively and significantly in task weeks 12 and 18, compared to post-training or task week 6 levels [34]. By week 18, serum and muscle inflammation appears resolved in serum and muscle of High-ForceHR rats [34], findings further confirmed here in bone. That said, the prior inflammatory cytokine responses likely contributed to the bone microarchitecture changes observed by week 18, since we have previously found that reducing this inflammation using ibuprofen beginning in task week 5 and continuing to week 12, prevented High-ForceHR induced trabecular bone loss.

We have several limitations in this study, including that serum levels of osteocalcin, CTX-1, RANKL and sclerostin are representative of changes occurring in all bones involved in performing the task, such as the humerus and scapula. The serum changes should be interpreted with that in mind. For mRNA and bone protein level analyses, we collected and homogenized both ulna and radial bones together after separating them into distal and mid-diaphyseal regions. Therefore, these latter data are representative of changes in distal versus mid-diaphyseal regions of both bones. Quantification of immunohistochemical expression of these proteins in radial versus ulna bones was used to reduce this limitation. Lastly, although we were able to rule out flexor muscle mass, weight and circulating estrogen level differences as potential contributors, median nerve pathology in the form of both irritative (inflammatory) and compressive injury (increased collagen deposition) is present in High-ForceHR rats that performed the task for 12 weeks [32,104]. Such median nerve pathology may be contributing to radial bone loss in High-ForceHR rats, although it would be more likely to affect carpal or phalangeal bones than the radius since the latter receives its primary input from branches of the radial nerve [105]. Future studies should attempt to determine if median nerve pathology is causing a general permissive effect on bone turnover, as suggested in a recent review [75].

5. Conclusion

It is commonly assumed that bone mass increases with vigorous exercise and decreases as a result of unloading or reduced mechanical stimulation. We observed different remodeling responses when using a similar repetition rate yet two different stress magnitudes (Low-Force versus High-Force). Performance of a Low-ForceHR task for 18 weeks was matched by positive bone adaptation in both distal trabecular and mid-diaphyseal cortical bone of the radius (and somewhat in the ulna of these rats), matching most theories of loading-induced bone anabolism. In contrast, 18 weeks of performance of a High-ForceHR task for 2 h/day, in 30 min intervals separated by 1.5 h rest periods, 3 days/week, for 18 weeks, was demanding enough to increase many indices of bone degradation consistent with damage repair and fatigue in the radius. The ulna bone showed fewer loading effects, in line with other studies showing that in muscular loading of forelimb bones in both neutral and ulnar deviated positions (such as used in power grip) that the radius is the primary bone receiving force transmission [79,81]. Perhaps high demand repetitive tasks or movements are contributing to the increasing prevalence of distal radial fractures in pediatric and elderly populations [14]. Upon diagnosis of long-term upper extremity overuse injuries perhaps bone scans of the distal forelimb should become part of clinical testing. We also suggest from these data that prolonged performance of highly repetitive upper extremity tasks (> 2 reaches/min) [106,107] should not be performed at force loads >15% of the maximum voluntary force for this particular task, and/or that future studies should investigate the effectiveness of longer rest/recovery periods when performing such tasks.

Supplementary data to this article can be found online at https://doi.org/10.1016/j.bone.2018.02.014.

Acknowledgements

Research reported in this publication was supported by the National Institute of Arthritis and Musculoskeletal and Skin Diseases of the National Institutes of Health under Award Number AR056019 to MFB. This study utilized services offered by core facilities of the Center for Substance Abuse Research (Grant Number DA013429), the MicroCT and Imaging Core at Temple University School of Medicine, and Bioquant Image Analysis Corporation. We would also like to thank Vicki Kalscheur at the School of Veterinary Medicine, University of Wisconsin-Madison, for her help with part of the basic fuchsin staining and sectioning. The content is solely the responsibility of the authors and does not necessarily represent the official views of the National Institutes of Health.

Note: Vicky Massicotte is recently deceased (Feb 2017). She was a key contributor to the microCT analyses and previously gave permission for co-authorship.

Competing interests

None of the authors have any competing interests to declare.

References

[1] S.N. Blair, H.W. Kohl, N.F. Gordon, R.S. Paffenbarger Jr., How much physical activity is good for health? Annu. Rev. Public Health 13 (1992) 99–126.
[2] E.A. Clark, A.E. Goodship, L.E. Lanyon, Locomotor bone strain as the stimulus for bone's mechanical adaptability, J. Physiol. 245 (2) (1975) (57 PP.).
[3] M. Kivimaki, M. Jokela, S.T. Nyberg, A. Singh-Manoux, E.I. Fransson, L. Alfredsson, J. B. Bjorner, M. Borritz, H. Burr, A. Casini, E. Clays, D. De Bacquer, N. Dragano, R. Erbel, G.A. Geuskens, M. Hamer, W.E. Hooftman, I.L. Houtman, K.H. Jockel, F. Kittel, A. Knutsson, M. Koskenvuo, T. Lunau, I.E. Madsen, M.L. Nielsen, M. Nordin, T. Oksanen, J.H. Pejtersen, J. Pentti, R. Rugulies, P. Salo, M.J. Shipley, J. Siegrist, A. Steptoe, S.B. Suominen, T. Theorell, J. Vahtera, P.J. Westerholm, H. Westerlund, D. O'Reilly, M. Kumari, G.D. Batty, J.E. Ferrie, M. Virtanen, I.P.-W. Consortium, Long working hours and risk of coronary heart disease and stroke: a systematic review and meta-analysis of published and unpublished data for 603,838 individuals, Lancet 386 (10005) (2015) 1739–1746.
[4] Bureau of Labor Statistics (2016). Nonfatal Occupational Injuries and Illnesses Requiring Days Away From Work, 2015. https://www.bls.gov/news.release/pdf/osh2.pdf. U. S. D. o. Labor. www. bls.gov/iif/oshcdnew.htm, iifstaff@bls.gov.
[5] S. Villotte, D. Castex, V. Couallier, O. Dutour, C.J. Knusel, D. Henry-Gambier, Enthesopathies as occupational stress markers: evidence from the upper limb, Am. J. Phys. Anthropol. 142 (2) (2010) 224–234.
[6] J. Hlavkova, T. Lebeda, T. Tichy, P. Gadourek, P. Urban, M. Nakladalova, A. Lastovkova, Z. Fenclova, P. Ridzon, E. Ehler, M. Richter, L. Pesakova, D. Pelclova, Evaluation of lumbar spine load by computational method in order to acknowledge low-back disorders as occupational diseases, Cent. Eur. J. Public Health 24 (1) (2016) 58–67.
[7] A. Seidler, A. Bergmann, M. Jager, R. Ellegast, D. Ditchen, G. Elsner, J. Grifka, J. Haerting, F. Hofmann, O. Linhardt, A. Luttmann, M. Michaelis, G. Petereit-Haack, B. Schumann, U. Bolm-Audorff, Cumulative occupational lumbar load and lumbar disc disease—results of a German multi-center case-control study (EPILIFT), BMC Musculoskelet. Disord. 10 (2009) 48.
[8] H. Vanharanta, M. Heliovaara, J. Korpi, J.D. Troup, Occupation, work load and the size and shape of lumbar vertebral canals, Scand. J. Work Environ. Health 13 (2) (1987) 146–149.
[9] A.M. Dale, D. Ryan, L. Welch, M.A. Olsen, B. Buchholz, B. Evanoff, Comparison of musculoskeletal disorder health claims between construction floor layers and a general working population, Occup. Environ. Med. 72 (1) (2015) 15–20.

[10] H. Ding, S. Solovieva, T. Vehmas, E.P. Takala, P. Leino-Arjas, Hand osteoarthritis and pinch grip strength among middle-aged female dentists and teachers, Scand. J. Rheumatol. 39 (1) (2010) 84–87.
[11] S. Solovieva, T. Vehmas, H. Riihimaki, K. Luoma, P. Leino-Arjas, Hand use and patterns of joint involvement in osteoarthritis. A comparison of female dentists and teachers, Rheumatology (Oxford) 44 (4) (2005) 521–528.
[12] T. Vehmas, S. Solovieva, H. Riihimaki, K. Luoma, P. Leino-Arjas, Hand workload and the metacarpal cortical index. A study of middle-aged teachers and dentists, Osteoporos. Int. 16 (6) (2005) 672–680.
[13] J.W. Karl, P.R. Olson, M.P. Rosenwasser, The epidemiology of upper extremity fractures in the United States, 2009, J. Orthop. Trauma 29 (8) (2015) e242–244.
[14] K.W. Nellans, E. Kowalski, K.C. Chung, The epidemiology of distal radius fractures, Hand Clin. 28 (2) (2012) 113–125.
[15] NIOSH, National Manufacturing Agenda - June 2010Retrieved October 23, 2011, from http://www.cdc.gov/niosh/nora/comment/agendas/manuf/ 2011.
[16] D.M. Findlay, G.J. Atkins, Relationship between serum RANKL and RANKL in bone, Osteoporos. Int. 22 (10) (2011) 2597–2602.
[17] O.D. Kennedy, D.M. Laudier, R.J. Majeska, H.B. Sun, M.B. Schaffler, Osteocyte apoptosis is required for production of osteoclastogenic signals following bone fatigue in vivo, Bone 64 (2014) 132–137.
[18] K. Matsuo, Osteocytes Communicate with Osteoclast Lineage Cells Via RANKL IBMS BoneKEy **9**(February 2012), 2012.
[19] A.G. Robling, P.J. Niziolek, L.A. Baldridge, K.W. Condon, M.R. Allen, I. Alam, S.M. Mantila, J. Gluhak-Heinrich, T.M. Bellido, S.E. Harris, C.H. Turner, Mechanical stimulation of bone in vivo reduces osteocyte expression of Sost/sclerostin, J. Biol. Chem. 283 (9) (2008) 5866–5875.
[20] T.M. Skerry, L. Bitensky, J. Chayen, L.E. Lanyon, Early strain-related changes in enzyme activity in osteocytes following bone loading in vivo, J. Bone Miner. Res. 4 (5) (1989) 783–788.
[21] S.A. Al-Dujaili, E. Lau, H. Al-Dujaili, K. Tsang, A. Guenther, L. You, Apoptotic osteocytes regulate osteoclast precursor recruitment and differentiation in vitro, J. Cell. Biochem. 112 (9) (2011) 2412–2423.
[22] A.R. Wijenayaka, M. Kogawa, H.P. Lim, L.F. Bonewald, D.M. Findlay, G.J. Atkins, Sclerostin stimulates osteocyte support of osteoclast activity by a RANKL-dependent pathway, PLoS One 6 (10) (2011), e25900.
[23] B.F. Boyce, L. Xing, Biology of RANK, RANKL, and osteoprotegerin, Arthritis Res. Ther. 9 (Suppl. 1) (2007) S1.
[24] T. Nakashima, M. Hayashi, T. Fukunaga, K. Kurata, M. Oh-Hora, J.Q. Feng, L.F. Bonewald, T. Kodama, A. Wutz, E.F. Wagner, J.M. Penninger, H. Takayanagi, Evidence for osteocyte regulation of bone homeostasis through RANKL expression, Nat. Med. 17 (10) (2011) 1231–1234.
[25] M.E. Brunkow, J.C. Gardner, J. Van Ness, B.W. Paeper, B.R. Kovacevich, S. Proll, J.E. Skonier, L. Zhao, P.J. Sabo, Y. Fu, R.S. Alisch, L. Gillett, T. Colbert, P. Tacconi, D. Galas, H. Hamersma, P. Beighton, J. Mulligan, Bone dysplasia sclerosteosis results from loss of the SOST gene product, a novel cystine knot-containing protein, Am. J. Hum. Genet. 68 (3) (2001) 577–589.
[26] G. Mabilleau, A. Mieczkowska, M.E. Edmonds, Thiazolidinediones induce osteocyte apoptosis and increase sclerostin expression, Diabet. Med. 27 (8) (2010) 925–932.
[27] C. Lin, X. Jiang, Z. Dai, X. Guo, T. Weng, J. Wang, Y. Li, G. Feng, X. Gao, L. He, Sclerostin mediates bone response to mechanical unloading through antagonizing Wnt/beta-catenin signaling, J. Bone Miner. Res. 24 (10) (2009) 1651–1661.
[28] L.F. Bonewald, Osteocyte messages from a bony tomb, Cell Metab. 5 (6) (2007) 410–411.
[29] M.F. Barbe, S. Gallagher, V.S. Massicotte, M. Tytell, S.N. Popoff, A.E. Barr-Gillespie, The interaction of force and repetition on musculoskeletal and neural tissue responses and sensorimotor behavior in a rat model of work-related musculoskeletal disorders, BMC Musculoskelet. Disord. 14 (1) (2013) 303.
[30] V.S. Massicotte, N. Frara, M.Y. Harris, M. Amin, C.K. Wade, S.N. Popoff, M.F. Barbe, Prolonged performance of a high repetition low force task induces bone adaptation in young adult rats, but loss in mature rats, Exp. Gerontol. 72 (2015) 204–217.
[31] P. Christen, K. Ito, R. Ellouz, S. Boutroy, E. Sornay-Rendu, R.D. Chapurlat, B. van Rietbergen, Bone remodelling in humans is load-driven but not lazy, Nat. Commun. 5 (2014) 4855.
[32] N.X. Jain, A.E. Barr-Gillespie, B.D. Clark, D.M. Kietrys, C.K. Wade, J. Litvin, S.N. Popoff, M.F. Barbe, Bone loss from high repetitive high force loading is prevented by ibuprofen treatment, J. Musculoskelet. Neuronal Interact. 14 (1) (2014) 78–94.
[33] S. Rani, M.F. Barbe, A.E. Barr, J. Litivn, Role of TNF alpha and PLF in bone remodeling in a rat model of repetitive reaching and grasping, J. Cell. Physiol. 225 (1) (2010) 152–167.
[34] P.W. Fisher, Y. Zhao, M.C. Rico, V.S. Massicotte, C.K. Wade, J. Litvin, G.M. Bove, S.N. Popoff, M.F. Barbe, Increased CCN2, substance P and tissue fibrosis are associated with sensorimotor declines in a rat model of repetitive overuse injury, J. Cell Commun. Signal. 9 (1) (2015) 37–54.
[35] H.M. Frost, Wolff's Law and bone's structural adaptations to mechanical usage: an overview for clinicians, Angle Orthod. 64 (3) (1994) 175–188.
[36] H. Li, J. Li, Z. Zou, A.S. Fok, Fracture simulation of restored teeth using a continuum damage mechanics failure model, Dent. Mater. 27 (7) (2011) e125–133.
[37] J. Li, H. Li, L. Shi, A.S. Fok, C. Ucer, H. Devlin, K. Horner, N. Silikas, A mathematical model for simulating the bone remodeling process under mechanical stimulus, Dent. Mater. 23 (9) (2007) 1073–1078.
[38] P.J. Prendergast, D. Taylor, Prediction of bone adaptation using damage accumulation, J. Biomech. 27 (8) (1994) 1067–1076.
[39] K.G. Avin, S.A. Bloomfield, T.S. Gross, S.J. Warden, Biomechanical aspects of the muscle-bone interaction, Curr. Osteoporos. Rep. 13 (1) (2015) 1–8.
[40] V.M. Ciriello, S.H. Snook, B.S. Webster, P. Dempsey, Psychophysical study of six hand movements, Ergonomics 44 (10) (2001) 922–936.
[41] J.R. Potvin, An equation to predict maximum acceptable loads for repetitive tasks based on duty cycle: evaluation with lifting and lowering tasks, Work 41 (Suppl. 1) (2012) 397–400.
[42] D.W. Dempster, J.E. Compston, M.K. Drezner, F.H. Glorieux, J.A. Kanis, H. Malluche, P.J. Meunier, S.M. Ott, R.R. Recker, A.M. Parfitt, Standardized nomenclature, symbols, and units for bone histomorphometry: a 2012 update of the report of the ASBMR Histomorphometry Nomenclature Committee, J. Bone Miner. Res. 28 (1) (2013) 2–17.
[43] A.M. Parfitt, M.K. Drezner, F.H. Glorieux, J.A. Kanis, H. Malluche, P.J. Meunier, S.M. Ott, R.R. Recker, Bone histomorphometry: standardization of nomenclature, symbols, and units. Report of the ASBMR Histomorphometry Nomenclature Committee, J. Bone Miner. Res. 2 (6) (1987) 595–610.
[44] T. Al-Shatti, A.E. Barr, F.F. Safadi, M. Amin, M.F. Barbe, Increase in inflammatory cytokines in median nerves in a rat model of repetitive motion injury, J. Neuroimmunol. 167 (1–2) (2005) 13–22.
[45] S.A. Colopy, J. Benz-Dean, J.G. Barrett, S.J. Sample, Y. Lu, N.A. Danova, V.L. Kalscheur, R. Vanderby Jr., M.D. Markel, P. Muir, Response of the osteocyte syncytium adjacent to and distant from linear microcracks during adaptation to cyclic fatigue loading, Bone 35 (4) (2004) 881–891.
[46] P. Muir, S.J. Sample, J.G. Barrett, J. McCarthy, R. Vanderby Jr, M.D. Markel, L.J. Prokuski, V.L. Kalscheur, Effect of fatigue loading and associated matrix microdamage on bone blood flow and interstitial fluid flow, Bone 40 (4) (2007) 948–956.
[47] T.E. Wenzel, M.B. Schaffler, D.P. Fyhrie, In vivo trabecular microcracks in human vertebral bone, Bone 19 (2) (1996) 89–95.
[48] M.F. Barbe, M.B. Elliott, S.M. Abdelmagid, M. Amin, S.N. Popoff, F.F. Safadi, A.E. Barr, Serum and tissue cytokines and chemokines increase with repetitive upper extremity tasks, J. Orthop. Res. 26 (10) (2008) 1320–1326.
[49] S.M. Abdelmagid, M.F. Barbe, I. Arango-Hisijara, T.A. Owen, S.N. Popoff, F.F. Safadi, Osteoactivin acts as downstream mediator of BMP-2 effects on osteoblast function, J. Cell. Physiol. 210 (1) (2007) 26–37.
[50] J.R. Potvin, Predicting maximum acceptable efforts for repetitive tasks: an equation based on duty cycle, Hum. Factors 54 (2) (2012) 175–188.
[51] G.M. Bove, M.Y. Harris, H. Zhao, M.F. Barbe, Manual therapy as an effective treatment for fibrosis in a rat model of upper extremity overuse injury, J. Neurol. Sci. 361 (2016) 168–180.
[52] C. Tagliaferri, Y. Wittrant, M.J. Davicco, S. Walrand, V. Coxam, Muscle and bone, two interconnected tissues, Ageing Res. Rev. 21 (2015) 55–70.
[53] R. Guo, M. Yamashita, Q. Zhang, Q. Zhou, D. Chen, D.G. Reynolds, H.A. Awad, L. Yanoso, L. Zhao, E.M. Schwarz, Y.E. Zhang, B.F. Boyce, L. Xing, Ubiquitin ligase Smurf1 mediates tumor necrosis factor-induced systemic bone loss by promoting proteasomal degradation of bone morphogenetic signaling proteins, J. Biol. Chem. 283 (34) (2008) 23084–23092.
[54] B.J. Kim, S.J. Bae, S.Y. Lee, Y.S. Lee, J.E. Baek, S.Y. Park, S.H. Lee, J.M. Koh, G.S. Kim, TNF-alpha mediates the stimulation of sclerostin expression in an estrogen-deficient condition, Biochem. Biophys. Res. Commun. 424 (1) (2012) 170–175.
[55] H.G. Gao, P.W. Fisher, A.G. Lambi, C.K. Wade, A.E. Barr-Gillespie, S.N. Popoff, M.F. Barbe, Increased serum and musculotendinous fibrogenic proteins following persistent low-grade inflammation in a rat model of long-term upper extremity overuse, PLoS One 8 (8) (2013), e71875.
[56] J.R. Potvin, I.C. Calder, J. Cort, M.J. Agnew, A. Stephens, Maximal acceptable forces for manual insertions using a pulp pinch, oblique grasp and finger press, Int. J. Ind. Ergon. 36 (2006) 779–787.
[57] S.H. Snook, C.H. Irvine, Maximum frequency of lift acceptable to male industrial workers, Am. Ind. Hyg. Assoc. J. 29 (6) (1968) 531–536.
[58] M.F. Barbe, N.X. Jain, V.S. Massicotte, S.N. Popoff, A.E. Barr-Gillespie, Ergonomic task reduction prevents bone osteopenia in a rat model of upper extremity overuse, Ind. Health 53 (3) (2015) 206–221.
[59] W. Rohmert, Problems in determining rest allowances part 1: use of modern methods to evaluate stress and strain in static muscular work, Appl. Ergon. 4 (2) (1973) 91–95.
[60] G. Sjogaard, L.V. Jorgensen, D. Ekner, K. Sogaard, Muscle involvement during intermittent contraction patterns with different target force feedback modes, Clin. Biomech. (Bristol, Avon) 1 (15 Suppl) (2000) S25–29.
[61] G. Sjogaard, U. Lundberg, R. Kadefors, The role of muscle activity and mental load in the development of pain and degenerative processes at the muscle cell level during computer work, Eur. J. Appl. Physiol. 83 (2–3) (2000) 99–105.
[62] B. Borah, T. Dufresne, J. Nurre, R. Phipps, P. Chmielewski, L. Wagner, M. Lundy, M. Bouxsein, R. Zebaze, E. Seeman, Risedronate reduces intracortical porosity in women with osteoporosis, J. Bone Miner. Res. 25 (1) (2010) 41–47.
[63] D.B. Burr, M.R. Forwood, D.P. Fyhrie, R.B. Martin, M.B. Schaffler, C.H. Turner, Bone microdamage and skeletal fragility in osteoporotic and stress fractures, J. Bone Miner. Res. 12 (1) (1997) 6–15.
[64] Y. Jiang, J. Zhao, E.Y. Liao, R.C. Dai, X.P. Wu, H.K. Genant, Application of micro-CT assessment of 3-D bone microstructure in preclinical and clinical studies, J. Bone Miner. Metab. 23 (Suppl) (2005) 122–131.
[65] C.H. Turner, Biomechanics of bone: determinants of skeletal fragility and bone quality, Osteoporos. Int. 13 (2) (2002) 97–104.
[66] M. Ding, A. Odgaard, I. Hvid, Changes in the three-dimensional microstructure of human tibial cancellous bone in early osteoarthritis, J. Bone Joint Surg. (Br.) 85 (6) (2003) 906–912.
[67] J. Klein-Nulend, R.G. Bacabac, A.D. Bakker, Mechanical loading and how it affects bone cells: the role of the osteocyte cytoskeleton in maintaining our skeleton, Eur. Cell. Mater. 24 (2012) 278–291.
[68] S. Gallagher, M.C. Schall Jr., Musculoskeletal disorders as a fatigue failure process: evidence, implications and research needs, Ergonomics 60 (2) (2017) 255–269.

[69] A.E. Barr, F.F. Safadi, I. Gorzelany, M. Amin, S.N. Popoff, M.F. Barbe, Repetitive, negligible force reaching in rats induces pathological overloading of upper extremity bones, J. Bone Miner. Res. 18 (11) (2003) 2023–2032.
[70] X. Tu, Y. Rhee, K.W. Condon, N. Bivi, M.R. Allen, D. Dwyer, M. Stolina, C.H. Turner, A. G. Robling, L.I. Plotkin, T. Bellido, Sost downregulation and local Wnt signaling are required for the osteogenic response to mechanical loading, Bone 50 (1) (2012) 209–217.
[71] G. Thiagarajan, Y. Lu, M. Dallas, M.L. Johnson, Experimental and finite element analysis of dynamic loading of the mouse forearm, J. Orthop. Res. 32 (12) (2014) 1580–1588.
[72] Y.F. Hsieh, M.J. Silva, In vivo fatigue loading of the rat ulna induces both bone formation and resorption and leads to time-related changes in bone mechanical properties and density, J. Orthop. Res. 20 (4) (2002) 764–771.
[73] S.P. Kotha, Y.F. Hsieh, R.M. Strigel, R. Muller, M.J. Silva, Experimental and finite element analysis of the rat ulnar loading model-correlations between strain and bone formation following fatigue loading, J. Biomech. 37 (4) (2004) 541–548.
[74] H. Matsuzaki, G.R. Wohl, D.V. Novack, J.A. Lynch, M.J. Silva, Damaging fatigue loading stimulates increases in periosteal vascularity at sites of bone formation in the rat ulna, Calcif. Tissue Int. 80 (6) (2007) 391–399.
[75] M.R. Laurent, V. Dubois, F. Claessens, S.M. Verschueren, D. Vanderschueren, E. Gielen, F. Jardi, Muscle-bone interactions: from experimental models to the clinic? A critical update, Mol. Cell. Endocrinol. 432 (2016) 14–36.
[76] J. Apostolakos, T.J. Durant, C.R. Dwyer, R.P. Russell, J.H. Weinreb, F. Alaee, K. Beitzel, M.B. McCarthy, M.P. Cote, A.D. Mazzocca, The enthesis: a review of the tendon-to-bone insertion, Muscles Ligaments Tendons J. 4 (3) (2014) 333–342.
[77] M. Benjamin, H. Toumi, J.R. Ralphs, G. Bydder, T.M. Best, S. Milz, Where tendons and ligaments meet bone: attachment sites ('entheses') in relation to exercise and/or mechanical load, J. Anat. 208 (4) (2006) 471–490.
[78] M. Benjamin, H. Toumi, D. Suzuki, S. Redman, P. Emery, D. McGonagle, Microdamage and altered vascularity at the enthesis-bone interface provides an anatomic explanation for bone involvement in the HLA-B27-associated spondylarthritides and allied disorders, Arthritis Rheum. 56 (1) (2007) 224–233.
[79] S. Erhart, W. Schmoelz, R. Arora, M. Lutz, The biomechanical effects of a deepened articular cavity during dynamic motion of the wrist joint, Clin. Biomech. (Bristol, Avon) 27 (6) (2012) 557–561.
[80] K.J. Fischer, J.E. Johnson, A.J. Waller, T.E. McIff, E.B. Toby, M. Bilgen, MRI-based modeling for radiocarpal joint mechanics: validation criteria and results for four specimen-specific models, J. Biomech. Eng. 133 (10) (2011), 101004.
[81] T. Hara, E. Horii, K.N. An, W.P. Cooney, R.L. Linscheid, E.Y. Chao, Force distribution across wrist joint: application of pressure-sensitive conductive rubber, J. Hand. Surg. [Am.] 17 (2) (1992) 339–347.
[82] J.E. Johnson, T.E. McIff, P. Lee, E.B. Toby, K.J. Fischer, Validation of radiocarpal joint contact models based on images from a clinical MRI scanner, Comput. Methods Biomech. Biomed. Engin. 17 (4) (2014) 378–387.
[83] K. Marquez-Florez, E. Vergara-Amador, E.B. de Las Casas, D.A. Garzon-Alvarado, Theoretical distribution of load in the radius and ulna carpal joint, Comput. Biol. Med. 60 (2015) 100–106.
[84] D.A. Rikli, P. Honigmann, R. Babst, A. Cristalli, M.M. Morlock, T. Mittlmeier, Intra-articular pressure measurement in the radioulnocarpal joint using a novel sensor: in vitro and in vivo results, J. Hand. Surg. [Am.] 32 (1) (2007) 67–75.
[85] F.W. Werner, A.K. Palmer, J.H. Somerset, J.J. Tong, D.B. Gillison, M.D. Fortino, W.H. Short, Wrist joint motion simulator, J. Orthop. Res. 14 (4) (1996) 639–646.
[86] D.L. Xin, M.Y. Harris, C.K. Wade, M. Amin, A.E. Barr, M.F. Barbe, Aging enhances serum cytokine response but not task-induced grip strength declines in a rat model of work-related musculoskeletal disorders, BMC Musculoskelet. Disord. 12 (2011) 63.
[87] O.D. Kennedy, B.C. Herman, D.M. Laudier, R.J. Majeska, H.B. Sun, M.B. Schaffler, Activation of resorption in fatigue-loaded bone involves both apoptosis and active pro-osteoclastogenic signaling by distinct osteocyte populations, Bone 50 (5) (2012) 1115–1122.
[88] B. Noble, Microdamage and apoptosis, Eur. J. Morphol. 42 (1–2) (2005) 91–98.
[89] A.G. Robling, K.S. Kang, W.A. Bullock, W.H. Foster, D. Murugesh, G.G. Loots, D.C. Genetos, Sost, independent of the non-coding enhancer ECR5, is required for bone mechanoadaptation, Bone 92 (2016) 180–188.
[90] K. Hoshi, H. Kawaki, I. Takahashi, N. Takeshita, M. Seiryu, S.A. Murshid, T. Masuda, T. Anada, R. Kato, H. Kitaura, O. Suzuki, T. Takano-Yamamoto, Compressive force-produced CCN2 induces osteocyte apoptosis through ERK1/2 pathway, J. Bone Miner. Res. 29 (5) (2014) 1244–1257.
[91] J. Nguyen, S.Y. Tang, D. Nguyen, T. Alliston, Load regulates bone formation and sclerostin expression through a TGFbeta-dependent mechanism, PLoS One 8 (1) (2013), e53813.
[92] S.E. Papanicolaou, R.J. Phipps, D.P. Fyhrie, D.C. Genetos, Modulation of sclerostin expression by mechanical loading and bone morphogenetic proteins in osteogenic cells, Biorheology 46 (5) (2009) 389–399.
[93] J. Spatz, R. Ellman, A. Cloutier, L. Louis, M. van Vliet, L. Suva, D. Dwyer, M. Stolina, H. Ke, M. Bouxsein, Sclerostin antibody inhibits skeletal deterioration due to reduced mechanical loading, J. Bone Miner. Res. 28 (4) (2011) 865–874.
[94] R.F. van Oers, B. van Rietbergen, K. Ito, P.A. Hilbers, R. Huiskes, A sclerostin-based theory for strain-induced bone formation, Biomech. Model. Mechanobiol. 10 (5) (2011) 663–670.
[95] K.E. Poole, R.L. van Bezooijen, N. Loveridge, H. Hamersma, S.E. Papapoulos, C.W. Lowik, J. Reeve, Sclerostin is a delayed secreted product of osteocytes that inhibits bone formation, FASEB J. 19 (13) (2005) 1842–1844.
[96] J. Delgado-Calle, A.Y. Sato, T. Bellido, Role and mechanism of action of sclerostin in bone, Bone 96 (2017) 29–37.
[97] J. Xiong, C.A. O'Brien, Osteocyte RANKL: new insights into the control of bone remodeling, J. Bone Miner. Res. 27 (3) (2012) 499–505.
[98] L.E. Mulcahy, D. Taylor, T.C. Lee, G.P. Duffy, RANKL and OPG activity is regulated by injury size in networks of osteocyte-like cells, Bone 48 (2) (2011) 182–188.
[99] C.A. O'Brien, T. Nakashima, H. Takayanagi, Osteocyte control of osteoclastogenesis, Bone 54 (2) (2013) 258–263.
[100] N. Frara, S.M. Abdelmagid, G.R. Sondag, F.M. Moussa, V.R. Yingling, T.A. Owen, S.N. Popoff, M.F. Barbe, F.F. Safadi, Transgenic expression of osteoactivin/gpnmb enhances bone formation in vivo and osteoprogenitor differentiation ex vivo, J. Cell. Physiol. 231 (1) (2016) 72–83.
[101] N. Frara, S.M. Abdelmagid, M. Tytell, M. Amin, S.N. Popoff, F.F. Safadi, M.F. Barbe, Growth and repair factors, osteoactivin, matrix metalloproteinase and heat shock protein 72, increase with resolution of inflammation in musculotendinous tissues in a rat model of repetitive grasping, BMC Musculoskelet. Disord. 17 (2016) 34.
[102] F.M. Moussa, I.A. Hisijara, G.R. Sondag, E.M. Scott, N. Frara, S.M. Abdelmagid, F.F. Safadi, Osteoactivin promotes osteoblast adhesion through HSPG and alphavbeta1 integrin, J. Cell. Biochem. 115 (7) (2014) 1243–1253.
[103] K.K. Baskin, B.R. Winders, E.N. Olson, Muscle as a "mediator" of systemic metabolism, Cell Metab. 21 (2) (2015) 237–248.
[104] B.D. Clark, T.A. Al-Shatti, A.E. Barr, M. Amin, M.F. Barbe, Performance of a high-repetition, high-force task induces carpal tunnel syndrome in rats, J. Orthop. Sports Phys. Ther. 34 (5) (2004) 244–253.
[105] M.E. Tageldin, M. Alrashid, A.A. Khoriati, S. Gadikoppula, H.D. Atkinson, Periosteal nerve blocks for distal radius and ulna fracture manipulation—the technique and early results, J. Orthop. Surg. Res. 10 (2015) 134.
[106] N.A. Nelson, R.M. Park, M.A. Silverstein, F.E. Mirer, Cumulative trauma disorders of the hand and wrist in the auto industry, Am. J. Public Health 82 (11) (1992) 1550–1552.
[107] B.A. Silverstein, L.J. Fine, T.J. Armstrong, Hand wrist cumulative trauma disorders in industry, Br. J. Ind. Med. 43 (11) (1986) 779–784.
[108] A.G. Robling, T. Bellido, C.H. Turner, Mechanical stimulation in vivo reduces osteocyte expression of sclerostin, J. Musculoskelet. Neuronal Interact. 6 (4) (2006) 354.

Calcif Tissue Int (2011) 89:396–410
DOI 10.1007/s00223-011-9531-z

ORIGINAL RESEARCH

Abrogation of Cbl–PI3K Interaction Increases Bone Formation and Osteoblast Proliferation

Tracy Brennan · Naga Suresh Adapala · Mary F. Barbe · Vanessa Yingling · Archana Sanjay

Received: 2 March 2011 / Accepted: 30 August 2011 / Published online: 28 September 2011

Abstract Cbl is an adaptor protein and E3 ligase that plays both positive and negative roles in several signaling pathways that affect various cellular functions. Tyrosine 737 is unique to Cbl and phosphorylated by Src family kinases. Phosphorylated CblY737 creates a binding site for the p85 regulatory subunit of phosphatidylinositol 3 kinase (PI3K) that also plays an important role in the regulation of bone homeostasis. To investigate the role of Cbl–PI3K interaction in bone homeostasis, we examined knock-in mice in which the PI3K binding site on Cbl was ablated due to the substitution of tyrosine 737 to phenylalanine ($Cbl^{YF/YF}$, YF mice). We previously reported that bone volume in these mice is increased due to decreased osteoclast function (Adapala et al., J Biol Chem 285:36745–36758, 19). Here, we report that YF mice also have increased bone formation and osteoblast numbers. In ex vivo cultures bone marrow-derived YF osteoblasts showed increased Col1A expression and their proliferation was also significantly augmented. Moreover, proliferation of MC3T3-E1 cells was increased after treatment with conditioned medium generated by culturing YF bone marrow stromal cells. Expression of stromal derived factor-1 (SDF-1) was increased in YF bone marrow stromal cells compared to wild type. Increased immunostaining of SDF-1 and CXCR4 was observed in YF bone marrow stromal cells compared to wild type. Treatment of YF condition medium with neutralizing anti-SDF-1 and anti-CXCR4 antibodies attenuated MC3T3-E1 cell proliferation. Cumulatively, these results show that abrogation of Cbl–PI3K interaction perturbs bone homeostasis, affecting both osteoclast function and osteoblast proliferation.

Keywords Osteoblast · Cbl · PI3K · Proliferation · SDF-1

A Sanjay has received funding from the NIH. All other authors have stated no conflict of interest.

Electronic supplementary material The online version of this article (doi:10.1007/s00223-011-9531-z) contains supplementary material, which is available to authorized users.

T. Brennan · N. S. Adapala · M. F. Barbe · A. Sanjay
Department of Anatomy and Cell Biology,
Temple University School of Medicine,
Philadelphia, PA, USA

N. S. Adapala · A. Sanjay (✉)
Department of Orthopaedic Surgery, New England Musculoskeletal Institute, 263 Farmington Avenue, Farmington, CT, USA
e-mail: asanjay@uchc.edu

V. Yingling
Department of Kinesiology, Temple University School of Medicine, Philadelphia, PA, USA

A. Sanjay
Sol Sherry Thrombosis Research Center, Temple University School of Medicine, Philadelphia, PA, USA

Bone is a dynamic organ that provides support and protection to vital organs. Bone also plays a role in the regulation of calcium homeostasis. The effects of two cell types, osteoblasts and osteoclasts, are critical for maintaining proper bone mass and shape. Osteoclasts are a member of the monocyte/macrophage family, while osteoblasts are of mesenchymal origin and responsible for mineralizing bone matrix [1].

Cbl and Cbl-b are highly homologous members of a family of adaptor proteins that promote assembly of signaling complexes downstream of several receptors [2]. Both function as E3 ubiquitin ligases that regulate

ubiquitylation of proteins. Cbl proteins are known to participate in growth factor, cytokine, and integrin-mediated signaling pathways in various cell types. Tyrosine phosphorylation of Cbl upon receptor activation is one of the most common signaling phenomena shown to promote both its E3 ubiquitin ligase activity and adaptor function [2].

Despite the marked effect of mutating Cbl [3, 4] or reducing its expression in vitro to affect osteoclast activity [5], $Cbl^{-/-}$ mice have a mild bone phenotype manifested primarily during endochondral bone formation [6]. In contrast, absence of Cbl-b protein in mice results in osteopenia due to osteoclast hyperactivity [7]. In spite of significant homology between Cbl and Cbl-b proteins, single knockouts of Cbl and Cbl-b have distinct bone phenotypes, suggesting specific roles for each protein in bone homeostasis. However, Cbl/Cbl-b double knockout mice die in utero around E10.5 [8], suggesting that Cbl and Cbl-b also have overlapping functions. The major structural difference that could contribute to the unique function(s) of Cbl proteins includes a tyrosine present only in Cbl (CblY737), which when phosphorylated binds to the SH2 domain of the p85 subunit of phosphatidylinositol 3 kinase (PI3K) [9–11]. Other investigators have shown that Tyr^{737} is among several Tyr residues that are phosphorylated by Src family kinases [12] and that when phosphorylated binds to the SH2 domain of the regulatory p85 subunit of PI3K [10, 11]. The absence of this residue in Cbl-b highlights a potential divergence in the role and mode of action of these two highly similar regulatory proteins, although this has not been examined with respect to osteoclast or osteoblast biology.

PI3Ks are a class of enzymes that phosphorylate phosphatidylinositol and its derivatives and regulate cell growth, the cytoskeleton, and cell survival [13]. PI3K activation in various cell types, including osteoblasts, is often associated with increased tyrosine phosphorylation induced by growth and differentiation factors. The importance of PI3K in osteoblast function has been established [14, 15]. In several cell types, Cbl is known to be a major protein that interacts with PI3K and regulates its activity [11, 16]. Downregulation of Cbl induced by twist haploinsufficiency in Saethre-Chotzen syndrome results in increased PI3K/AKT signaling and osteoblast proliferation [17]. In humans, osteoblasts expressing mutated FGFR2 levels of PI3K are decreased. The decreased PI3K signaling in response to FGFR2 activation is due to increased Cbl–PI3K molecular interaction mediated by the Cbl Y731 residue, which results in increased PI3K ubiquitylation and proteasome degradation [18]. We recently reported that, on the one hand, the Cbl–PI3K complex negatively regulates osteoclast differentiation and survival while, on the other hand, it positively influences osteoclast function [19].

In this report, we continued to study the role of Cbl–PI3K interaction in the skeletal system. Our results indicated that abrogation of the Cbl–PI3K interaction resulted in increased bone mass and increased trabecular and cortical bone volumes. The altered geometry of bone due to increased volume also resulted in increased mechanical properties. While osteoblast numbers were increased in mice, ex vivo differentiation and survival of the YF osteoblast was not significantly affected. Analysis of the conditioned medium derived from culturing YF bone marrow stromal cells, as well as the expression analysis of cells, showed increased expression of stromal cell derived factor-1 (SDF-1) and its receptor, CXCR4. Antibody-mediated ablation of SDF-1 activity attenuated cell proliferation. Taken together, these data and our previously published work suggest that abrogation of Cbl–PI3K interaction perturbs bone homeostasis, affecting both osteoclast function and osteoblast proliferation.

Materials and Methods

Mice Colony

The generation of CblY737F mice has been previously described [20]. Mice were maintained in a mixed C57BL/6 × 129SvJ background, and experiments were performed in compliance with the Institutional Animal Care and Use Committee at Temple University.

Histological Analysis

To label the skeleton, calcein (i.p., 10 mg/kg body weight) was injected 9 and 2 days before death. After death, tibiae and femora of 12-week-old male mice were excised and cleaned of soft tissue. Bones were processed as previously described [21]. Longitudinal sections (5 μM) were used to measure the fluorochrome label and then deplasticized and stained with Masson trichrome, as described previously [21]. Histomorphometry was performed on three tissue sections per limb using a Nikon 800 fluorescence microscope linked to a Bioquant Osteo II system (R&M Biometrics, Nashville, TN). Dynamic parameters of bone formation were collected using unstained sections from the trabecular surface in a defined region of interest (100 μM below the growth plate and 50 μM in from the cortical bone) using a ×20 objective. Bone formation rate (BFR) was assessed by measuring single-labeled surface for single perimeter (sL.Pm), double-labeled surface (dL.Pm), and the interlabel distance in the dL.Pms. The same sections were then evaluated under polarized white light after Masson's trichrome staining to determine static parameters of bone formation: bone surface (BS), osteoid volume

(OV), and osteoblast number (Ob.N). The following were then calculated: mineralizing surface (MS/BS, %), mineral apposition rate (MAR, mM/day), BFR (BFR/BS, MAR × [MS/BS]), OV (OV/BS), and (Ob.N/BS), as described previously [22].

Immunohistochemistry

Alternate sections of the above bones were deplasticized, rehydrated, and then stained for SDF-1 and CXCR4 using previously described methods for detecting tissue cytokines [23]. Specific antibodies for SDF-1 (rabbit SDF-1α, 1:250 dilution in PBS; Abcam, Cambridge, MA) and CXCR4 (rabbit CXCR4, 1:250 dilution in PBS; Abcam) were used. Primary antibodies were detected using anti-rabbit secondary antibodies tagged with Cy2 (green), Cy3 (red), or HRB (brown after enzymatic reaction with DAB). Sections were counterstained with DAPI or hematoxylin.

Micro-CT Analysis

High-resolution images of long bones from age-matched male mice were acquired using a Skyscan 1172, 12 MPix model (Microphotonics, Allentown, PA). Proximal tibiae and distal femora were scanned with the source voltage 59 kV, a source current of 167, and an isotropic voxel size of 6 μm. Imaging started at the distal end of the femur or the proximal end of the tibiae and included approximately 7 mm (1,335 slices) of the total bone length. After scanning, 3D image data were reconstructed using Sykscan (Aartselaar, Belgium) NRecon software; structural indices were calculated using the Skyscan CT Analyzer (CTAn) software. Using the CTAn software, trabecular bone was separated from cortical bone with a region of interest tool. Trabecular morphometric traits were computed from binarized images using direct 3D techniques that do not rely on prior assumptions from the underlying structures. The volume of interest for trabecular microarchitectural variables was bounded to the endocortical margin, starting 1.9 mm from the proximal tibial condyles, 0.2 mm distal to the growth plate, in the direction of the metaphysis, and then extending from this position for 100 slices (0.6 mm). Upper and lower thresholds of 255 and 80 were used to delineate each pixel as "bone" or "nonbone," and trabecular bone volume per total volume (BV/TV), BS (BS/TV), mean trabecular thickness (Tb.Th), mean trabecular number (Tb.N), and mean trabecular separation (Tb.Sp) indices were computed. For the analysis of cortical parameters, the mid-shaft of the femur was determined as 40% of the entire length of the bone. The cortical region of interest began at the mid-shaft and extended 100 slices (0.6 mm) toward the femoral head. Using upper and lower thresholds of 255 and 80, total area (T.Ar), periosteal perimeter (Ps.Pm), endosteal area (En.Ar), endosteal perimeter (En.Pm), cortical bone area (Ct.Ar), cortical thickness (Ct.Th), and relative cortical area (RCA) were computed.

Mechanical Testing

Breaking strength of the right femur was measured under three-point bending using a material testing machine (ElectroForce Systems Group, Bose, Eden Prairie, MN) fitted with a 1,000 N load cell as previously described [24, 25]; to minimize the effect of shear loading, the distance between the lower support points was maximized. Femora were placed on the loading fixture anterior side down and loaded in the anterior–posterior plane at a span length of 19.26 mm. Prior to testing, bones were thawed in saline at room temperature to ensure hydration. Femora were loaded to failure at a rate of 0.05 mm/s, during which displacement and force were collected (100 Hz). Force and displacement values were normalized using terms derived from engineering analysis of three-point bending. Bending moments were calculated from the force (F) data ($M = FL/4$) (Nmm). Displacement data were divided by $L^2/12$ (mm/mm^2), where L is the distance between the lower supports (19.26 mm). Whole-bone mechanical properties were then determined from the moment versus normalized displacement curves, including peak moment (Nmm, ultimate load the specimen sustained), yield moment (Nmm), stiffness (Nmm^2, the slope of the initial linear portion of the moment–displacement curve), yield displacement (mm/mm^2, displacement at the yield point), postyield displacement (mm/mm^2), work to failure (Nmm-mm/mm^2, the area under the moment–displacement curve before failure), and work to failure postyield (Nmm-mm/mm^2). The yield point was calculated as the point where a 10% change in the slope of the moment versus normalized displacement curve occurred.

Cell Culture

Calvarial osteoblasts were obtained from pups 3–5 days old as previously described [26]. Typically, cells from three calvaria were plated in T-75 flasks in medium supplemented with 10% FBS. Culture medium was changed every third day until cells reached confluence. Cells were harvested and frozen until further use. For osteoblast differentiation in a typical experiment, 5×10^5 cells were plated in a 6 cm dish and cultured in the presence of 10% fetal bovine serum (FBS; Thermo Fisher Scientific, Pittsburg, PA). "Complete medium" is 10% FBS containing α-MEM. Differentiation of cells in the above medium was initiated by adding 50 mM ascorbic acid and 5 mM glycerophosphate (Sigma, St. Louis, MO). Osteogenic medium

was changed every third day. On day 14 osteoblasts were stained for alkaline phosphatase (ALP) and assessed for ALP activity according to the manufacturer's protocol (Sigma). ALP activity was normalized to the total protein content of cell lysates. Protein concentrations were quantified by a BCA protein assay (Pierce, Rockford, IL). On day 21 osteoblasts were stained with alizarin red, and staining was quantified using the Bioquant Osteo II (Nashville, TN) program.

Bone marrow stromal cells were isolated from the hind limbs of mice aged 6–8 weeks. The proximal and distal ends of the hind limbs were cut to allow the marrow to be flushed with complete medium. Bone marrow cells were filtered through a 70 μ nylon mesh filter (BD, Falcon, Oxnard, CA). Following lysis of RBCs using ammonium chloride lysis buffer, cells were collected by centrifugation and resuspended in complete medium. Cells (25 to 30×10^7) were plated into T-75 tissue culture flasks. Nonadherent cells were removed after 16–18 h. Adherent cells were cultured until they became 70–80% confluent. Cell culture was treated with 0.025% trypsin containing 0.02% EDTA for 2 minutes at room temperature. To generate conditioned medium, cells (1×10^7) were seeded in a 6 cm dish and cultured in the presence of complete medium for 5 days at 37°C, 5% CO_2. On the fifth day, medium was removed, centrifuged at 1,500 rpm for 5 min, filtered through 22 μ filters, and either used immediately or stored at −80°C. Cells were harvested for analysis in protein markers by real-time PCR as described below. For colony-forming unit (CFU) assay, bone marrow-derived cells were used as previously described [27]. Briefly, bone marrow cells (1.5×10^5 cells cm^{-2}) were plated in complete medium and cultured for 5 days. Then, one-third of the medium was replaced with complete medium every third day. After 20 days, cells were fixed with 3.7% formaldehyde and stained with KaryoMax Giemsa stain or ALP (Sigma) according to the manufacturer's protocol. Cells were visualized using an E300 microscope at 10× magnification to count the number of colonies. Cells in clusters of 20 or more were counted as one colony.

For the proliferation assay, 10,000 cells were plated/well in a 96-well plate in quadruplets. After 18–20 h in culture in complete medium, cells were washed with serum-free medium and then incubated with appropriate medium or growth factors. After 72 h, cells were washed three times with cold PBS. A proliferation assay was performed using the Cyquant Cell Proliferation Kit (Molecular Probes, Eugene, OR) per the manufacturer's protocol. Fluorescence was measured using a Wallac 1420 fluorometer (Perkin-Elmer and Analytical Sciences, Turku, Finland), and cell proliferation was expressed as a percent of proliferation in 10% FBS-containing medium. In some experiments, prior to addition to cells, conditioned medium was treated with appropriate antibodies (10 μg/ml) and this solution was mixed end on end for 1 h at 4°C. In other experiments, cells were incubated with antibodies (10 μg/ml) for 1 h at 37°C prior to the addition of condition medium. Cell lysates were prepared in mRIPA lysis buffer (50 mM Tris-HCl [pH 8.0], 150 mM NaCl, 0.5% NP40, 0.25% sodium deoxycholate, protease inhibitors, 1 mM PMSF, 1 mM Na_2VO_3, 50 mM NaF) and lysates were processed for electrophoresis and Western blotting analysis as previously described [19].

Real-Time PCR Analysis

The expression levels of osteoblast markers were analyzed by quantitative real-time PCR. RNA isolation was performed using TRIzol reagent (Invitrogen, Carlsbad, CA) according to the manufacturer's protocol. RNA (1 μg) was transcribed using Super Script II reverse transcriptase (Invitrogen), following the manufacturer's protocol. Oligo(dT) and dNTPs were purchased from Promega (Madison, WI). Quantitative real-time PCR was performed using 1 μl of cDNA and SYBR Green PCR master mix (Applied Biosystems, Foster City, CA) on an Applied Biosystems 7500 real-time PCR system. Gene expression levels were normalized to GAPDH and calculated using the ΔΔCt method. Primers were designed using mRNA sequences obtained from Mouse Genomics Informatics and the Primer3 program (http://sourceforge.net/projects/primer3/). The following primers were used: SDF-1, AGTAGTGGCTCCC CAGGTTT (sense) and GAGACAGTCTTGCGGACACA (antisense); CXCR4, TCAGTGGCTGACCTCCTCTT (sense) and TTTCAGCCAGCAGTTTCCTT (antisense); Col1A, TGAACGTGACCAAAAACCAA (sense) and GCA GAAAAGGCAGCATTAGG (antisense); RUNX2, CCCA GCCACCTTTACCTACA (sense) and TATGGAGTGCTG CTGGTCTG (antisense); BSP, AAAGTGAAGGAAAGCG ACGA (sense) and GTTCCTTCTGCACCTGCTTC (antisense); GAPDH, AACTTTGGCATTGTGGAAGG (sense) and ACACATTGGGGGTAGGAACA (antisense).

Analysis of Cytokines

Conditioned medium from bone marrow stromal cells was generated as described above and then sent for analysis to Searchlight Aushon Bio Systems (Billerica, MA) to determine the presence of cytokines and chemokines. Briefly, a multiplex ELISA was performed using the conditioned medium and the antibody to the protein of interest. Samples were diluted 1:2, 1:50, and 1:1,000 and tested in duplicate. A standard curve was established from the dilutions of the samples. Then, a mean value for the cytokine of interest was determined from the standard curve and reported as picograms per milligram total

protein. Protein estimation of the conditioned medium was performed using the BCA kit. The results of the cytokine assays were normalized to the protein concentration for each sample.

Statistics

All experiments were performed at least three times, and differences between wild type (WT) and YF were determined using Student's *t* test. All statistics were generated from Prism 4.0 program (GraphPad, San Diego, CA). Differences were considered significant at $P < 0.05$, and all data are represented as means ± SEM. For mechanical testing, body weights of mice in each group were normalized with a linear regression–based correction as previously described [28].

Results

Abrogation of Cbl–PI3K Interaction Results in Increased Cortical and Trabecular Bone

To understand the role of the Cbl–PI3K interaction in skeletal remodeling, we employed knock-in mice (CblY737F/Y737F, henceforth YF mice) in which the PI3K binding site on Cbl was ablated. Gross analysis revealed that YF mice were smaller in size and had decreased body weight compared to control pups (Fig. 1a, b). The delayed growth was first apparent 3 days after birth (data not shown) and continued for 9–18 days. The delay in growth occurred simultaneously with a lag in the growth of long bones (Fig. 1c). Histological analysis of bones from 9-day-old YF pups showed a significant delay in the formation of secondary spongiosa (data not shown). Histological analysis of tibial sections from 12-week-old mice stained with von Kossa showed that cancellous bone was increased in YF relative to age-matched control mice (Fig. 1d). However, weight and total tibial length were comparable between 12-week-old WT and YF mice (Fig. 1e, f). YF mice had a slight but significant decrease in body length from tail to snout (Fig. 1g). This matches prior reports of short stature on postnatal day 9, decreased bone length, and delayed formation of secondary ossification centers in $Cbl^{-/-}$ mice [6], although adult $Cbl^{-/-}$ mice do not exhibit any overt skeletal phenotype. We also examined bone architecture of 12-week-old mice by micro-CT analysis (Fig. 2a, b) and, in agreement with our histological analysis, found increased trabecular bone volume in YF mice (Table 1). Similarly, Ct.Ar was significantly increased due to the increased Ps.Pm and Ct.Th in YF mice (Table 1). Taken together, these results suggest that lack of interaction between Cbl and PI3K results in increased bone volume.

Static and Dynamic Parameters of Bone Formation are Increased in YF Mice

We recently reported that although YF osteoclasts are unable to resorb bone in vivo, their numbers are significantly increased in YF mice [19]. Given that bone volume can also be increased due to increased osteoblast numbers, we examined osteoblasts in YF and WT mice. Histological analysis of tibiae stained with Masson trichome (Fig. 3a) revealed a significant increase in osteoblast numbers and a 63% increase in osteoid (unmineralized bone) in YF sections (Fig. 3b, c). Histomorphometric analysis of calcein-labeled sections indicated that the normalized MS/BS, MAR, and BFR/BS were significantly increased in YF samples (Fig. 3d–g). Taken together, the above results indicate that in the absence of Cbl–PI3K interaction increased bone volume in mice is due not only to the decreased osteoclast-mediated bone resorption reported previously by our group [19] but also to increased bone formation by osteoblasts.

Lack of Cbl–PI3K Interaction Confers Increased Bone

While structural changes in bone are most likely to be detected in trabecular bone, we also observed structural changes in cortical bone in YF mice. A significant increase in total bone area ($P < 0.05$ vs. WT) as well as increased Ps.Pm, En.Pm, and En.Ar ($P < 0.05$ vs. WT, each) led to an increase in overall size of the cortical bone (Table 1). In addition, polar moment of inertia was significantly greater in YF mice. The RCA did not change between groups, although there was an overall increase in cortical thickness (Table 1). Imbalances between bone resorption and bone formation can affect bone geometry, affecting its ability to resist damage (fracture). Given that YF mice have increased cancellous bone (Fig. 1d; Table 1) and increased cortical bone size (Table 1), we examined the mechanical properties of the long bones using a three-point bending assay, as previously described [24, 25]. There was a significant increase in peak moment and yield displacement in YF mice compared to WT, but no differences were observed in the other parameters listed in Table 2. These data suggest that the structural and geometric changes in YF bones could potentially be a compensatory mechanism to maintain bone strength since both size and the quality of the bone contribute to whole-bone strength.

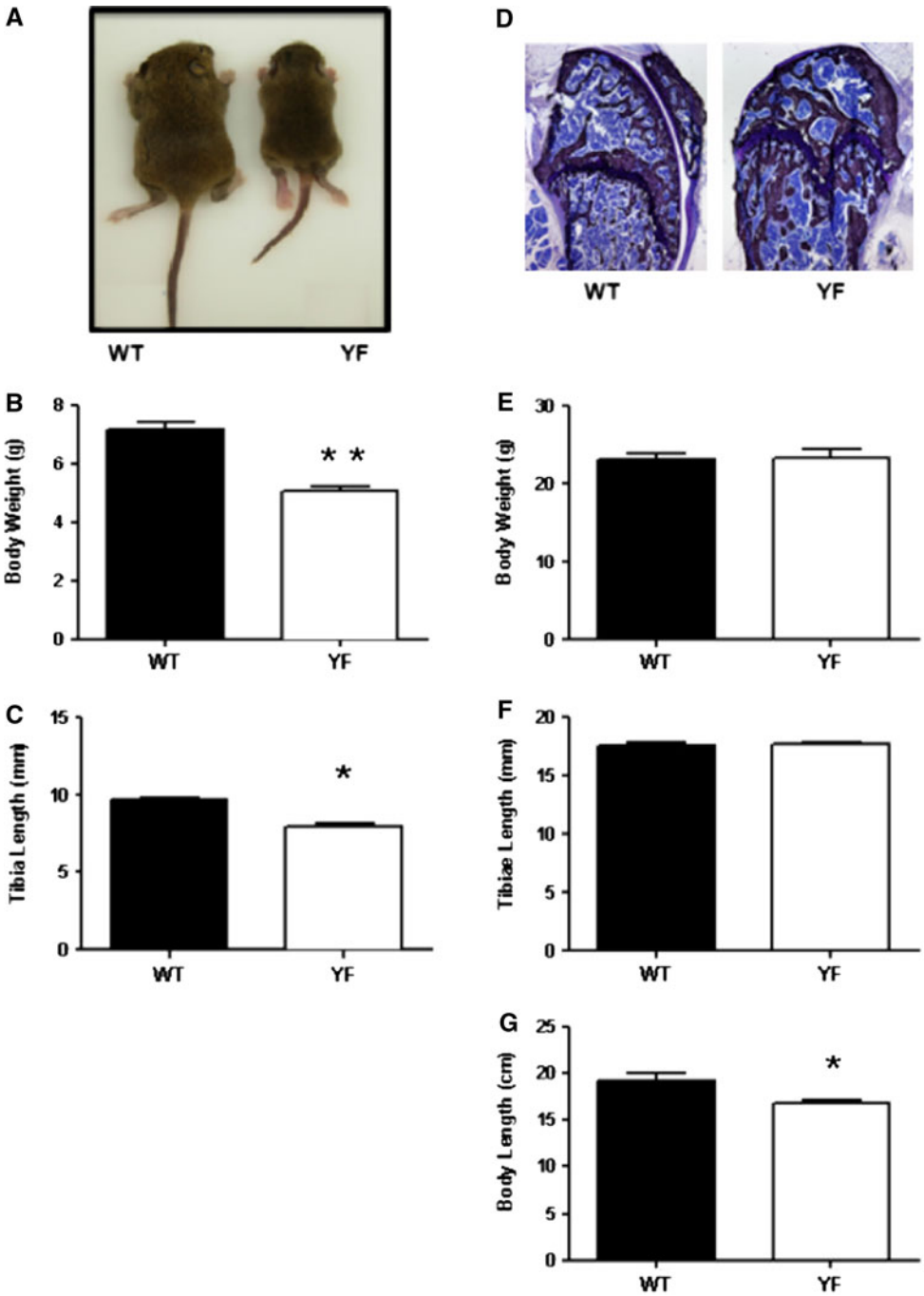

Fig. 1 Disruption of Cbl–PI3K interaction results in a growth delay in young mice. **a** At 9 days old, YF mice are smaller than their counterpart WT mice. Delayed growth in 9-day-old YF mice resulted in decreased total body weight (**b**) and decreased tibial length (**c**). **d** Representative histological sections of proximal tibiae of 12-week-old WT and YF mice stained with von Kossa and counterstained with toluidine blue show increased mineralized bone in YF mice. Images were taken using a 10× objective. Twelve-week-old male WT and YF mice have similar weights (**e**) and tibial lengths (**f**). **g** Twelve-week-old YF mice have shorter body lengths. $n = 8$ mice per genotype. Mean ± SEM. $^*P < 0.05$ compared to WT

In the Absence of Cbl–PI3K Interaction Bone Marrow-Derived Osteoblasts Show Increased Col1A Expression

We previously reported that YF mice have increased osteoclast numbers and enhanced differentiation [19]. Given that the numbers of osteoblasts are also significantly increased in YF mice (Fig. 3b), we next examined if similar increases in numbers were seen in ex vivo culture conditions. To assess the ability of osteoblasts to differentiate in vitro, calvarial osteoblasts or bone marrow stromal cells from WT and YF mice were treated with osteogenic media for 14 or 21 days. No appreciable differences were observed in the expression levels of Col-1A, BSP, and Runx2 between WT- and YF-derived calvarial osteoblasts and no significant differences were observed in ALP and von Kossa staining (Fig. 4a–c and data not shown). In contrast, in YF bone marrow stromal cell cultures, expression levels of Col1A were significantly increased during differentiation compared to WT samples (Fig. 4d), while expression levels of BSP and Runx2 were

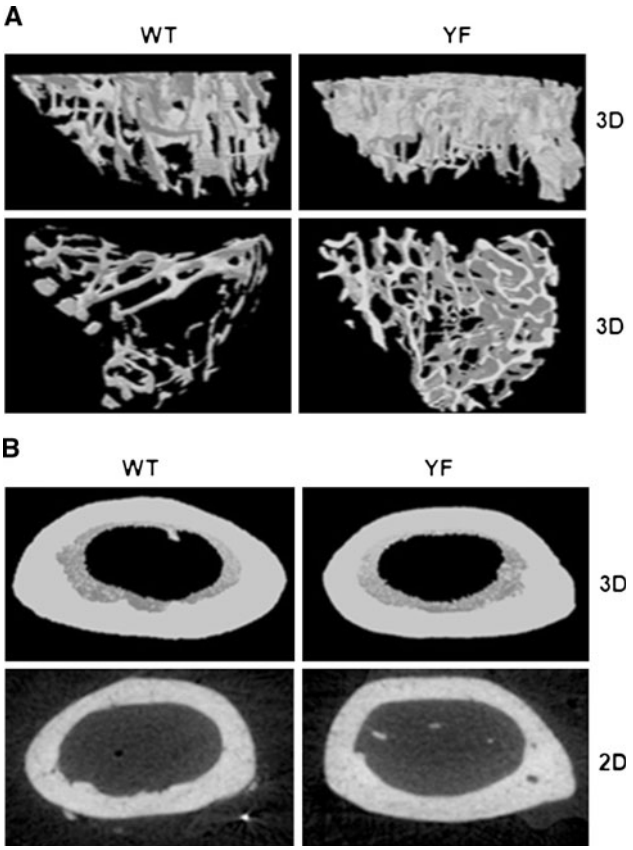

Fig. 2 Disruption of Cbl–PI3K interaction in mice perturbs trabecular and cortical bone architecture. **a** The trabecular region of proximal tibiae was scanned starting at the proximal end and included approximately 7 mm (1,335 slices) of the total bone length. *Top* and *bottom panels* represent a 3D reconstruction of trabecular bone. **b** The cortical bone analysis began at 40% from the distal end of the femur and included 100 sections proximal from that point. *Top panel* represents a 3D reconstruction of the cortical bone at mid-shaft. *Bottom panel* represents a 2D section of the cortical bone, taken 0.3 mm (50 slices) from the mid-shaft toward the femur. Micro-CT was performed on six mice per genotype. Representative scanned images are shown

Table 1 Analysis of trabecular and cortical bone parameters from 12-week-old WT and YF mice

	WT	YF
Trabecular bone		
Bone volume/tissue volume (BV/TV, %)	9.27 ± 1.69	14.36 ± 1.51*
Bone surface/tissue volume (BS/TV, %)	9.29 ± 1.11	11.73 ± 0.36*
Trabecular thickness (Tb. Th., mm)	0.047 ± 0.001	0.056 ± 0.003*
Trabecular number (Tb. N., 1/mm)	2.00 ± 0.32	2.80 ± 0.17*
Trabecular separation (Tb. Sp., mm)	0.230 ± 0.021	0.189 ± 0.004*
Cortical bone		
Total area (T.Ar, mm^2)	1.50 ± 0.09	1.77 ± 0.08*
Periosteal perimeter (Ps.Pm (mm)	4.82 ± 0.14	5.18 ± 0.12*
Endosteal area (En.Ar, mm^2)	0.75 ± 0.04	0.88 ± 0.03*
Endosteal perimeter (En.Pm, mm)	3.26 ± 0.06	3.50 ± 0.09*
Cortical bone area (Ct.Ar, mm^2)	0.82 ± 0.06	0.95 ± 0.05*
Cortical thickness-2D (Ct.Th, mm)	0.183 ± 0.006	0.200 ± 0.003**
Relative cortical area (RCA)	0.55 ± 0.02	0.54 ± 0.01
Polar moment of inertia (J, mm^4)	0.313 ± 0.041	0.424 ± 0.039*

Table represents the parameters of trabecular and cortical bone obtained through micro-CT analysis. $n = 10$ mice/genotype. Mean ± SEM

* $P < 0.05$, ** $P < 0.01$ compared to WT, respectively

not appreciably altered (Fig. 4e, f). Histochemical analysis of in vitro cultures demonstrated comparable levels of ALP and alizarin red activity between WT and YF samples (Fig. 4g–j). Taken together, these data suggest that, unlike YF osteoclasts, which exhibit enhanced differentiation due to the upregulation of transcription factors NFATc1 and NFκB [19], for the most part ex vivo osteoblast differentiation and the expression of transcription factor that regulates osteoblastogenesis are not significantly affected in the absence of Cbl–PI3K interaction.

Osteoblast Proliferation is Upregulated in the Absence of Cbl–PI3K Interaction

Trabecular and endocortical bone formation are directly correlated with the number of marrow-derived osteoprogenitors. Histological analysis of long bones indicated that in the absence of Cbl–PI3K interaction there is a twofold increase in osteoblast numbers (Fig. 3b) and increased MAR (Fig. 3f). Also, in contrast to calvarial cells, there was a significant increase in the expression of Col-1A when YF bone marrow-derived stromal cells were cultured in osteogenic medium (Fig. 4d). These data suggest that in the absence of Cbl–PI3K interaction, there might be increased potential for the bone marrow precursors to differentiate into osteoblasts and/or that osteoblasts have augmented proliferative capacity. To determine if the numbers of osteoblast progenitors were affected in YF mice, the number of CFUs was determined from bone marrow-derived cells. Although, the total numbers of marrow cells were comparable between the WT and YF mice (data not shown), there was a significant increase in CFUs for YF samples (Fig. 5a) and the potential of these cells to proliferate was increased compared to WT cells (Fig. 5b). We also observed a slight, but not statistically significant, increase in the proliferation rate of YF calvarial osteoblasts (data not shown).

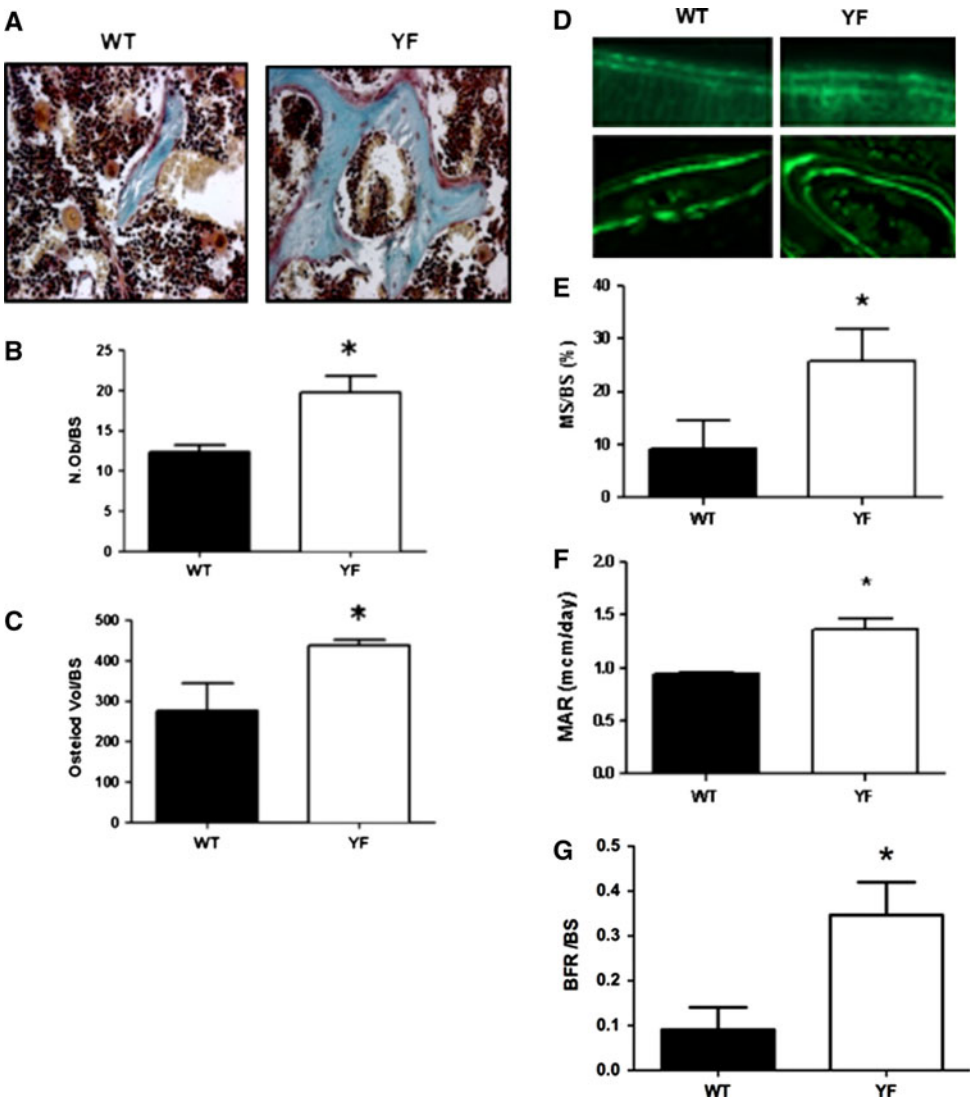

Fig. 3 Bone formation is increased in YF mice. **a** Tibial sections from 12-week-old WT and YF were stained with Masson's trichrome (400× magnification). Quantification of osteoblasts/bone surface (N.Ob/BS) (**b**) and osteoid/BS (**c**). **d** Dynamic parameters of bone formation were assessed using tibiae harvested from 12-week-old WT and YF that were injected with calcein as described in Materials and Methods. Representative photomicrographs of calcein double labeling (40×) in WT and YF in cortical bone (*upper panels*) and in trabeculae (*lower panels*) are shown. **e** Mineralized surface/bone surface (MS/BS, %). **f** Mineral apposition rate (MAR, μm^2/day). **g** Bone formation rate/bone surface (BFR/BS, μm^2/μm/day). $n = 6$ mice per genotype. Mean ± SEM. *$P < 0.05$, compared to WT

Table 2 Mechanical properties of bone from 12-week-old WT and YF mice

	WT	YF
Peak moment (Nmm)	32.30 ± 1.23	38.24 ± 2.75*
Yield moment (Nmm)	28.78 ± 1.41	31.49 ± 2.70
Stiffness (Nmm^2)	1222 ± 74.1	1209 ± 124.4
Yield displacement (mm/mm^2)	0.02 ± 0.001	0.05 ± 0.01*
Postyield displacement (mm/mm^2)	0.004 ± 0.001	0.002 ± 0.002
Work to failure ($Nmm*mm/mm^2$)	0.61 ± 0.07	0.76 ± 0.16
Work to failure postyield ($Nmm*mm/mm^2$)	0.18 ± 0.04	0.22 ± 0.08

Femora were placed on the prongs of a materials testing machine. A constant load of 0.05 mm/s was applied to femora until bone failure, during which displacement and force were collected at 100 Hz. Force and displacement values were normalized using terms as described in Materials and Methods. Whole-bone mechanical properties were determined from the moment vs. normalized displacement curves. $n = 10$ mice/genotype. Mean ± SEM

* $P < 0.05$ compared to WT

PI3K is known to regulate cell survival, and we previously reported that abrogation of Cbl–PI3K resulted in enhanced osteoclast survival [19]; however, no differences were observed between the survival of WT and YF bone marrow-derived stromal cells (Supplementary Fig. 1). We also examined whether increased proliferation in YF osteoblasts was influenced by extracellular growth factors known to influence osteoblast proliferation. Treatment with several growth factors resulted in a similar level of proliferation in both WT and YF cells (Supplementary Fig. 2a). In response to addition of EGF, FGF, IGF, and PDGF to the cultures, phosphorylation of p85 and AKT was comparable in WT and YF samples (Supplementary Fig. 2b).

In addition to their resorptive activity, osteoclasts are known to secrete factors that promote anabolic activity [29, 30]. Since YF mice had increased numbers of osteoblasts and osteoclasts (Fig. 3b and [19]), we next examined the possibility that osteoclast-dependent secretory factors may promote increased YF osteoblast proliferation. WT

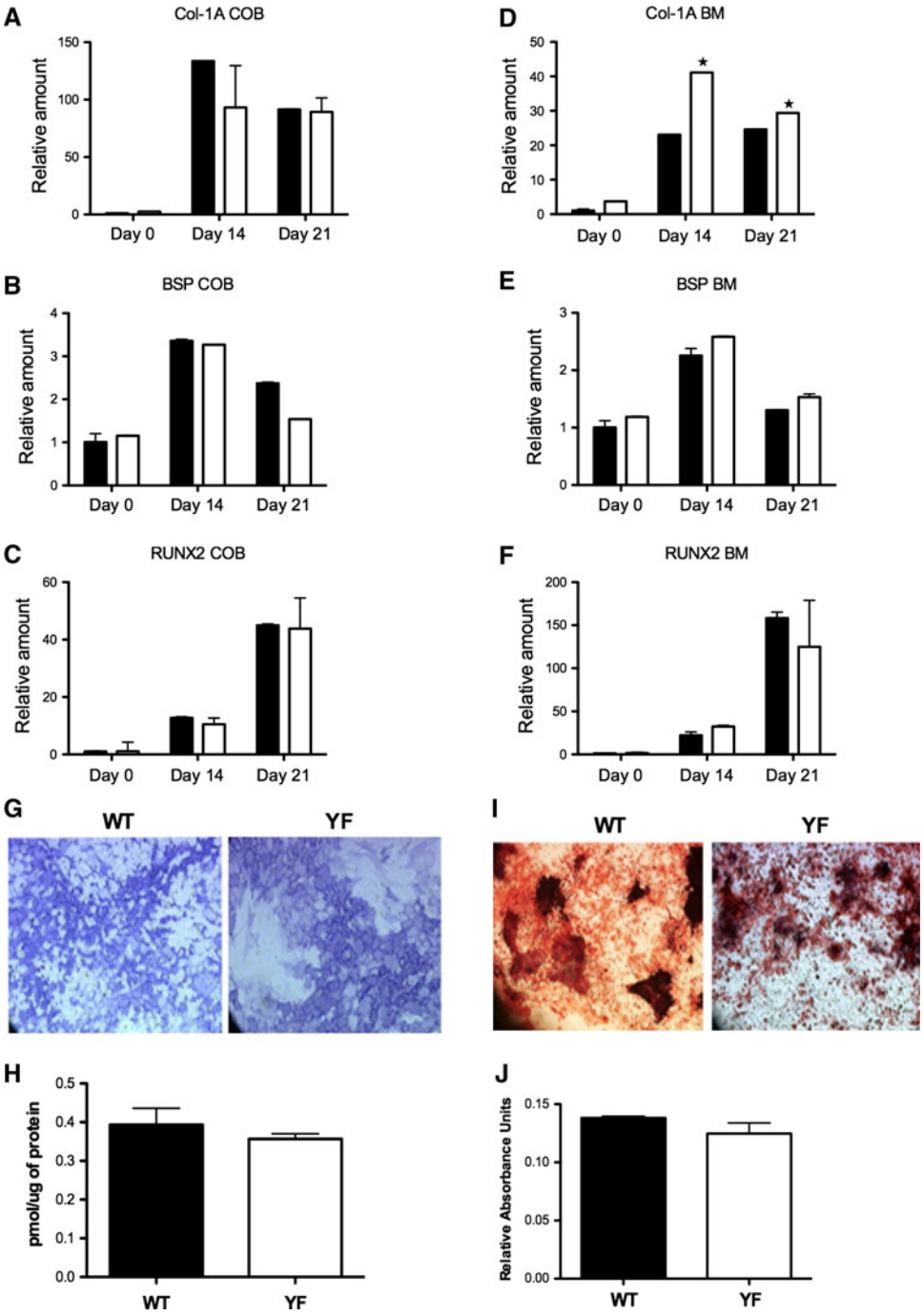

Fig. 4 Differentiation of calvarial and bone marrow stromal cells in ex vivo culture. **a–f** WT and YF primary calvarial or bone marrow stromal cells were differentiated in osteogenic media for 0, 14, or 21 days, as indicated. Osteogenic medium was changed every third day. Expression levels of Col-1A (**a**, **d**), BSP (**b**, **e**), and Runx-2 (**c**, **f**) were analyzed by real-time PCR in calvarial osteoblasts (COB) and bone marrow stromal cells (BM). **g** Bone marrow stromal cells stained for ALP activity. **h** ALP activity. **i** Bone marrow stromal cells stained with alizarin red S to assess calcium deposition. **j** Alizarin red S stain was released from the cell matrix and quantified. All experiments were performed three times. A representative sample of three experiments is shown. Mean ± SEM. $*P < 0.05$ compared to WT

and YF osteoclasts were generated in ex vivo cultures as previously described [19] and the culture medium on day 5 of differentiation was collected. To analyze if the factors secreted from osteoclasts promote proliferation, MC3T3-E1 cells were grown in the osteoclast-derived culture medium. No significant differences were observed in the proliferation rate when cells were cultured in WT osteoclast-conditioned medium versus YF osteoclast-conditioned medium (Fig. 5c). This result suggests that, under these experimental conditions, factors secreted by YF osteoclasts may not contribute to the observed enhanced YF osteoblast proliferation.

Increased Levels of SDF-1 in YF Bone Marrow

The bone marrow niche contains a variety of cell types in various stages of maturation/differentiation. Many of these cell types secrete factors that can affect osteoblast proliferation. Therefore, we next examined if other factor(s) secreted by resident bone marrow cells could influence osteoblast

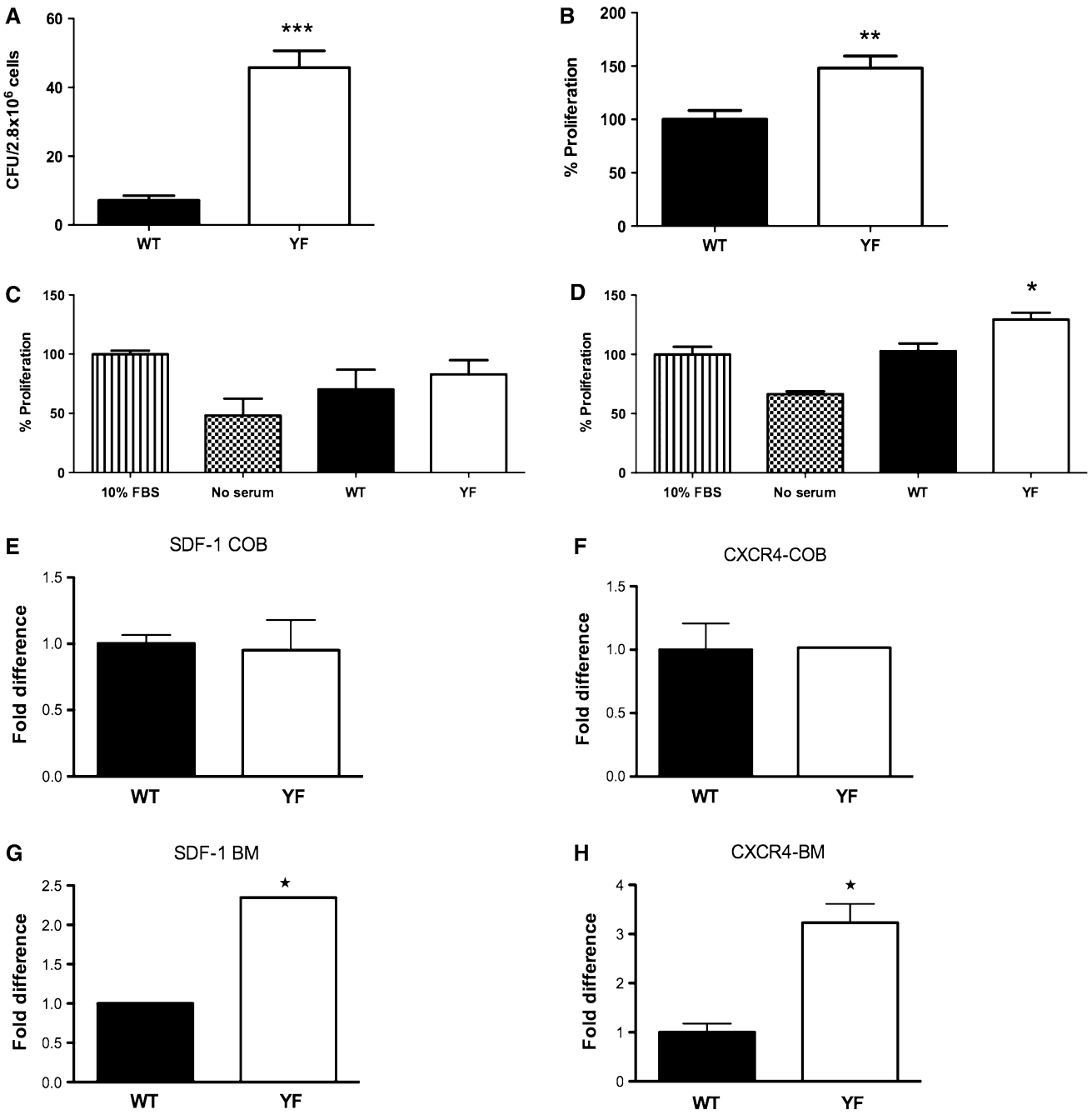

Fig. 5 Proliferation of YF osteoblasts is increased. **a** Bone marrow stromal cells were cultured for 20 days in 10% FBS-containing medium. Cells were fixed and stained with Giemsa; clusters of 20 or more cells were counted as a colony. **b** Bone marrow stromal cells from WT and YF were seeded in a 96-well plate in complete medium for 72 h, and proliferation was assessed by the Cyquant method, as described in Materials and Methods. **c** MC3T3-E1 cells were cultured in the presence of serum-free medium, 10% FBS, or osteoclast-conditioned medium derived from WT or YF osteoclasts. Cell proliferation was assessed as described above. **d** MC3T3-E1 were treated with serum-free medium, 10% FBS, or bone marrow conditioned medium derived from WT or YF bone marrow cultures. Cell proliferation was assessed as described above. **e**–**h** Calvarial and bone marrow stromal cells were cultured in complete medium for 5 days. Expression levels of SDF-1 (**e**, **g**) and CXCR4 (**f**, **h**) were measured by quantative real-time PCR. Data are presented as fold difference of expression between WT and YF culture. All experiments were performed three times, and a representative is shown. Mean ± SEM. $^*P < 0.05$ compared to WT

proliferation. For this experiment, bone marrow stromal cells from WT and YF mice were cultured in the presence of 10% FBS-containing medium for 5 days. The resulting supernatant was used as the bone marrow conditioned medium. Proliferation of MC3T3-E1 cells was examined in response to WT and YF conditioned media. Compared to

WT, treatment with YF conditioned medium induced increased proliferation of MC3T3-E1 cells (Fig. 5d), suggesting that a factor(s) present in the YF bone marrow-derived medium might contribute to the increased cell proliferation.

Analysis of the conditioned media using multiplex ELISAs indicated that the levels of IL-1β, IL-18, MCP-1, RANTES, and TGF-1β were comparable in WT and YF samples (Table 3). Only levels of SDF-1, a chemokine known to be present in the bone marrow milieu, were significantly increased in the YF bone marrow conditioned medium (Table 3). We next determined mRNA expression levels of SDF-1 and its receptor, CXCR4, in calvarial osteoblasts and bone marrow stromal cells. For these experiments, cells were cultured in the presence of 10% FBS for 5 days before harvesting. RT-PCR analysis showed that SDF-1 and CXCR4 levels were comparable in WT and YF calvarial cells (Fig. 5e, f). In contrast, compared to expression levels in WT bone marrow stromal cells, YF bone marrow stromal cells showed $\sim$2.5- and 3.5-fold increases in the expression levels of SDF-1 and CXCR4, respectively (Fig. 5g, h). This expression was then verified by immunohistochemistry. Staining of YF tibial sections with anti-SDF-1 antibodies showed enhanced staining in many bone stromal cells but no staining in mature osteoblasts adjacent to the trabeculae (Fig. 6b, c, i). Both stromal cells and osteocytes in sections from YF samples demonstrated increased CXCR4 staining compared to WT samples (Fig. 6f, j, h, l). For validation, bone marrow proliferation assays were performed using neutralizing antibodies against SDF-1 or CXCR4. Enhanced proliferation of MC3T3-E1 cells in response to YF conditioned medium was significantly decreased in the presence of neutralizing antibodies (Fig. 7). Taken together, these data suggest that in YF mice cell proliferation is increased, at least in part, due to increased SDF-1 present in the bone marrow milieu. However, our results do not eliminate the possibility that other factors may also contribute to the increased osteoblast proliferation.

Table 3 Expression of cytokines in WT and YF bone marrow-derived conditioned medium

	WT	YF
IL-1β	0.003 $\pm$ 0.0005	0.004 $\pm$ 0.0005
IL-18	0.02 $\pm$ 0.007	0.02 $\pm$ 0.005
MCP-1	1.48 $\pm$ 0.80	1.11 $\pm$ 0.83
RANTES	0.01 $\pm$ 0.009	0.008 $\pm$ 0.002
TGF-β1	4.44 $\pm$ 0.70	4.71 $\pm$ 1.54
SDF-1	0.04 $\pm$ 0.01	0.10 $\pm$ 0.03*

Table represents levels for each protein tested using a multiplex ELISA. The concentration of each factor was normalized to the total amount of protein present in the conditioned medium for each sample and expressed as picograms of cytokine per micrograms of protein. Mean $\pm$ SEM

* $P < 0.05$ compared to WT

Discussion

Cbl proteins are known to play a role in osteoclast migration and function as well as in osteoblast differentiation downstream of the FGF pathway by ubiquitylating and degrading the Src family kinases Lyn and Fyn [31, 32]. However, loss of Cbl protein in adult mice did not result in an overt skeletal phenotype [6]. On the other hand, absence of Cbl-b, another member of the Cbl family, resulted in decreased bone volume [7]. These findings suggest that although Cbl and Cbl-b proteins share significant homologies and identical domain organization [2], they have different effects on cells that regulate bone mass. One major difference between the two proteins is the absence of Y737 in Cbl-b. Cbl protein phosphorylation of Y737 has been shown to recruit PI3K and regulate PI3K activity [16]. Studies on osteoblast cell lines have established that PI3K plays an important role in osteoblast function [15, 33, 34]. In an immortalized human osteoblast cell line, FGFR2–Cbl interaction in lipid rafts resulted in attenuation of PI3K signaling and osteoblast survival [18]. We recently reported that the lack of Cbl–PI3K interaction promotes decreased osteoclast function while increasing their survival [19]. In this report, we examined if the lack of this molecular interaction also had an effect on osteoblast differentiation and function.

Cbl is a major PI3K binding protein in several cell types. With a Y > F mutation on the Cbl–PI3K binding site, the expectation is that loss of this interaction would perturb PI3K-mediated signaling and cell survival. In thymocytes loss of Cbl–PI3K results in decreased AKT phosphorylation [35], whereas in osteoclasts abrogation of this interaction results in increased AKT phosphorylation, leading to enhance survival [19]. Others have shown that in human osteoblast cells that express mutated forms of FGFR2 FGFR2–Cbl interaction in lipid rafts triggers attenuation of PI3K/AKT signaling and osteoblast survival [18]. On the other hand, stimulation of growth factor receptors in YF osteoblasts did not modulate proliferation or PI3K-mediated signaling (Supplementary Fig. 2a, b). Thus, it appears that Cbl–PI3K interaction plays distinct roles in different cell types. In YF osteoblasts, the lack of impact on PI3K-mediated signaling suggests that Cbl-b and/or other proteins (e.g., Src) that are capable of interacting with PI3K might be able to compensate for the lack of Cbl–PI3K interaction and preserve the signaling. It is also likely that another SH2 domain-containing protein

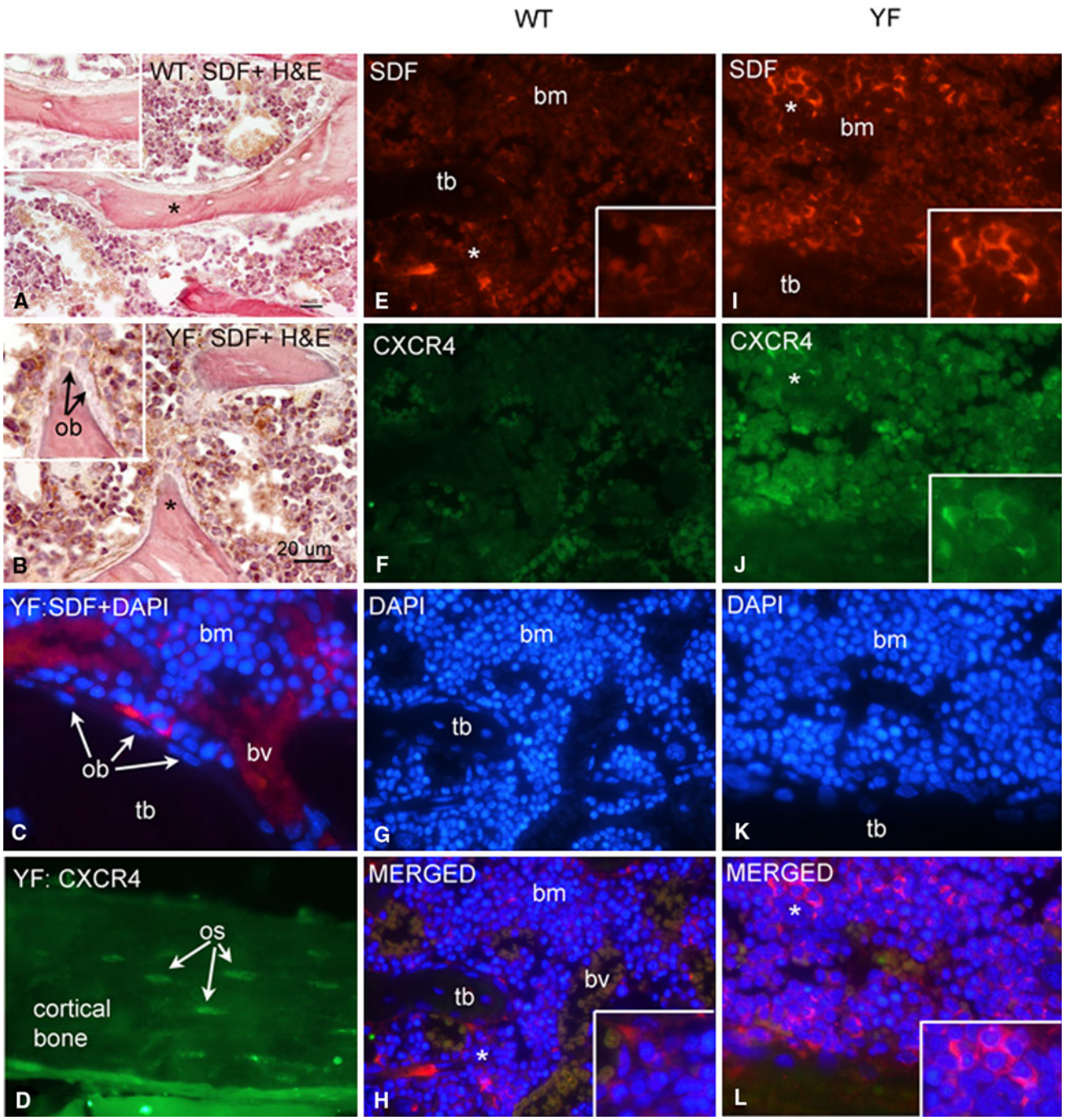

might interact with phosphorylated Y737 Cbl and that the observed effects in the YF mice are a consequence of loss of that interaction.

Histological and micro-CT analysis of bones from YF mice indicated that there was an increase in trabecular bone volume (Fig. 2; Table 1), osteoblast numbers (Fig. 3b), BFR, mineralizing surface, and MAR compared to WT mice (Fig. 3e–g). Also, culturing YF bone marrow stromal cells resulted in increased numbers of CFUs and increased proliferation (Fig. 5a, b). The increase in Col1A expression during differentiation of YF bone marrow cells (Fig. 4d) suggests that the increase in MAR is driven at least in part by increased matrix protein production. However, other markers of differentiation were unaffected in YF bone marrow cells (Fig. 4). These combined data suggest that the increased numbers of YF osteoblasts in bone marrow may be in part also due to a secondary effect.

The increased bone volume and increased numbers of nonresorbing osteoclasts and osteoblasts are indicative of an osteopetrotic phenotype in YF mice (Fig. 2 and

◀ **Fig. 6** Bone marrow stromal cells from YF mice show enhanced SDF-1 and CXCR4 expression. Representative sections of proximal tibiae from 12-week-old WT and YF immunostained with either anti-SDF-1α (HRP-DAB or secondary antibody tag), anti-CXCR4, or DAPI. In all images, area indicated with *asterisk* is enlarged in inset. **a** WT tibial section showing only low-level SDF-1 staining in bone marrow stromal cells. *Inset* shows an absence of SDF-1 staining in osteocytes or quiescent bone lining cells on trabecular bone. **b** YF tibial section showing SDF-1 staining in many bone stromal cells. *Inset* shows SDF-1 staining in many stromal cells, including cells surrounding the trabecular bone, but no staining in osteoblasts (ob). Sections in **a** and **b** are lightly counterstained with hematoxylin and eosin (H&E). **c** YF tibial section with SDF and DAPI labeling showing SDF-1-stained cells in the bone marrow (bm) but not in cells lining the trabecular bone (tb). **d** YF tibial cortical bone showing increased numbers of osteocytes (os) expressing CXCR4. **e** WT tibial section showing SDF-1 staining in only a few of bone marrow cells but no staining in trabecular bone. *Inset* shows SDF-1 staining in only a few stromal cells. **f** Same section as shown in **e** showing an absence of CXCR4 staining. **g** Same section showing DAPI staining. **h** Merged **e**–**g** panels. *Inset* shows a low number of SDF + DAPI-stained stromal cells. **i** YF tibial section showing high levels of SDF-1 staining in many bone marrow stromal cells but none in trabecular bone. *Inset* shows SDF-1 in the cytoplasm of these cells. **j** Same section as in **i** showing increased CXCR4 staining in several stromal cells. Some, but not all, of the CXCR4-stained cells are double-labeled with SDF-1. *Inset* shows CXCR4 staining in the same cells as shown in inset in **i**. **k** Same section showing DAPI staining. **l** Merged **i**–**k** panels. *Inset* shows SDF + DAPI-stained stromal cells. All images were taken using a 40× objective. *Scale bar* in **l** = 20 μm. bv, blood vessel

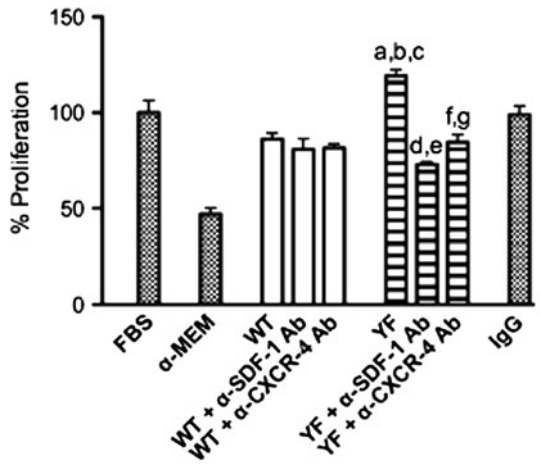

Fig. 7 Increased proliferation of cells in YF conditioned medium is mediated by SDF-1. MC3T3-E1 cells were cultured in the presence of serum-free medium, 10% FBS, or condition medium derived from WT or YF bone marrow cells. To assess the effect of SDF-1, 10 μg/ml of neutralizing anti-SDF-1 antibodies or isotype control antibodies was added to the conditioned medium. To determine the role of CXCR4, MC3TC-E1 cells were pretreated with 10 μg/ml neutralizing anti-CXCR4 antibodies. The cell proliferation assay was performed as described above. Cell proliferation is expressed as a percent of control (10% FBS-treated cells). Mean ± SEM. Symbols indicate $P < 0.05$ for the following comparisons: *a* FBS versus YF, *b* WT versus YF, *c* YF versus IgG, *d* YF versus YF + α-SDF-1, *e* IgG versus YF + α-SDF-1, *f* YF versus YF + α-CXCR4, *g* IgG versus YF + α-CXCR4

[19, 36]). In several osteopetrotic mouse models where bone resorption is compromised due to the absence of osteoclast (c-Fos$^{-/-}$) [37] or due to impaired osteoclast function (e.g., Src$^{-/-}$ [38] and Pyk2$^{-/-}$ [39]), bone formation is also impaired due to a cell autonomous defect in osteoblast activity [37, 40, 41]. In v-ATPase knockout mice, in which osteoclasts are incapable of degrading the bone matrix, both bone formation and osteoblast numbers increase due to uncoupling [42]. Osteoclast activity has been regarded as restricted to bone resorption; however, recent studies have suggested that osteoclasts might release anabolic signals that are not linked to their resorption activity [29, 30]. Our results indicate that cell proliferation was not significantly affected when cells were grown in conditioned medium generated from YF osteoclasts (Fig. 5c). This could be due to several possibilities. First, in an ex vivo culture system, a secreted factor(s) may not be in sufficient quantity or concentration to influence cell proliferation. Second, cell–cell contact between osteoclasts and osteoblasts may be required for the desired effect on proliferation since direct contact of osteoblasts with the bone marrow precursors is a prerequisite for the generation of mature osteoclasts and to facilitate interaction of the membrane-bound RANKL on osteoblasts with RANK on osteoclasts [43]. Furthermore, recent studies have indicated that the interaction between the transmembrane ephrinB2 ligand that is present on osteoclasts mediates anabolic signals via the ephB4 receptor present on osteoblasts [44]. Given that YF osteoclasts are not functional in in vivo and in vitro cultures [19], we could not test the possibility that a bone matrix-derived factor(s) could influence increased proliferation of osteoblasts in vivo. Given this scenario, it is not likely that YF osteoclasts modulate enhanced proliferation of YF osteoblasts, although more studies are needed to explore this further.

Bone marrow contains several different types of hematopoietic and stromal cells that secrete a variety of growth factors and cytokines that can influence the properties of cells residing in the marrow space [45, 46]. Our result show that there was a significant increase in the rate of proliferation of MC3T3-E1 cells cultured in YF conditioned medium compared to WT conditioned medium (Fig. 5d). Comparative analysis of WT and YF condition media showed that the level of the chemokine SDF-1 was elevated in the YF conditioned medium (Table 3). SDF-1, also known as CXCL2, is produced in bone marrow stromal cells and directs the migration of hematopoietic cells to the bone marrow during development [47]. The SDF-1/CXCR4 signaling axis is essential for several normal physiological functions, including bone remodeling [48]. For example, SDF-1 has been implicated as a regulator of bone resorption [49]. SDF-1 also regulates BMP2-mediated osteogenic differentiation in mesenchymal cell lines [50].

More recently, it has been demonstrated that conditional inactivation of CXCR4 in osteoblast precursors reduces postnatal bone formation due to impaired osteoblast development [51]. Our results show that expression of both SDF-1 and CXCR4 was substantially increased in YF bone marrow stromal cells (Fig. 6). In contrast, SDF-1 was not increased in mature osteoblast and bone lining cells (Fig. 6c, d). Interestingly, the increased expression was restricted to the YF bone marrow milieu since expression levels of SDF-1 and CXCR4 were comparable in WT and YF calvarial cells (Fig. 5e, f). It is likely that increased SDF-1 in the YF bone marrow environment promotes osteoblast proliferation since both Cbl [52] and PI3K [53] are known to participate in SDF-1-mediated signaling. Further studies are needed to specifically analyze the role of Cbl–PI3K interaction in the effects of SDF-1-mediated signaling events that induce proliferation, attachment, and migration of bone marrow stromal cells.

In conclusion, our studies establish that abrogation of Cbl–PI3K interaction results in increased bone volume. While our past studies show that this is primarily due to defective osteoclast function, these new data also suggest that the increased numbers of osteoblasts in vivo and increased proliferation of osteoblasts are due to a secondary effect probably mediated by factors in the marrow cavity, such as SDF-1.

Acknowledgements This study was supported by National Institutes of Health grant AR055601 (to A. S.). The authors also thank Ms. Mamta Amin for performing the immunohistochemical staining of the bone sections.

References

1. Sims N, Baron R (2000) Bone cells and their function. In: Canalis E (ed) Skeletal growth factors. Lippincott Williams and Wilkins, Philadelphia, pp 1–16
2. Swaminathan G, Tsygankov AY (2006) The Cbl family proteins: ring leaders in regulation of cell signaling. J Cell Physiol 209:21–43
3. Miyazaki T, Sanjay A, Neff L, Tanaka S, Horne WC, Baron R (2004) SRC kinase activity is essential for osteoclast function. J Biol Chem 279:17660–17666
4. Sanjay A, Miyazaki T, Itzstein C, Purev E, Horne WC, Baron R (2006) Identification and functional characterization of an Src homology domain 3 domain-binding site on Cbl. FEBS J 273:5442–5456
5. Tanaka S, Amling M, Neff L, Peyman A, Uhlmann E, Levy JB, Baron R (1996) c-Cbl is downstream of c-Src in a signalling pathway necessary for bone resorption. Nature 383:528–531
6. Chiusaroli R, Sanjay A, Henriksen K, Engsig MT, Horne WC, Gu H, Baron R (2003) Deletion of the gene encoding c-Cbl alters the ability of osteoclasts to migrate, delaying resorption and ossification of cartilage during the development of long bones. Dev Biol 261:537–547
7. Nakajima A, Sanjay A, Chiusaroli R, Adapala NS, Neff L, Itzsteink C, Horne WC, Baron R (2009) Loss of Cbl-b increases osteoclast bone-resorbing activity and induces osteopenia. J Bone Miner Res 24:1162–1172
8. Naramura M, Jang I-K, Kole H, Huang F, Haines D, Gu H (2002) c-Cbl and Cbl-b regulate T cell responsiveness by promoting ligand-induced TCR down-modulation. Nat Immunol 3:1192–1199
9. Feshchenko EA, Shore SK, Tsygankov AY (1999) Tyrosine phosphorylation of C-Cbl facilitates adhesion and spreading while suppressing anchorage-independent growth of V-Abl-transformed NIH3T3 fibroblasts. Oncogene 18:3703–3715
10. Hunter S, Burton EA, Wu SC, Anderson SM (1999) Fyn associates with Cbl and phosphorylates tyrosine 731 in Cbl, a binding site for phosphatidylinositol 3-kinase. J Biol Chem 274:2097–2106
11. Ueno H, Sasaki K, Honda H, Nakamoto T, Yamagata T, Miyagawa K, Mitani K, Yazaki Y, Hirai H (1998) c-Cbl is tyrosine-phosphorylated by interleukin-4 and enhances mitogenic and survival signals of interleukin-4 receptor by linking with the phosphatidylinositol 3′-kinase pathway. Blood 91:46–53
12. Feshchenko EA, Langdon WY, Tsygankov AY (1998) Fyn, Yes, and Syk phosphorylation sites in c-Cbl map to the same tyrosine residues that become phosphorylated in activated T cells. J Biol Chem 273:8323–8331
13. Vanhaesebroeck B, Ali K, Bilancio A, Geering B, Foukas LC (2005) Signalling by PI3K isoforms: insights from gene-targeted mice. Trends Biochem Sci 30:194–204
14. Dufour C, Holy X, Marie PJ (2007) Skeletal unloading induces osteoblast apoptosis and targets alpha5beta1-PI3K-Bcl-2 signaling in rat bone. Exp Cell Res 313:394–403
15. Ghosh-Choudhury N, Abboud SL, Nishimura R, Celeste A, Mahimainathan L, Choudhury GG (2002) Requirement of BMP-2-induced phosphatidylinositol 3-kinase and Akt serine/threonine kinase in osteoblast differentiation and Smad-dependent BMP-2 gene transcription. J Biol Chem 277:33361–33368
16. Meng F, Lowell CA (1998) A β_1 integrin signaling pathway involving Src-family kinases, Cbl and PI-3 kinase is required for macrophage spreading and migration. EMBO J 17:4391–4403
17. Guenou H, Kaabeche K, Dufour C, Miraoui H, Marie PJ (2006) Down-regulation of ubiquitin ligase Cbl induced by twist haploinsufficiency in Saethre-Chotzen syndrome results in increased PI3K/Akt signaling and osteoblast proliferation. Am J Pathol 169:1303–1311
18. Dufour C, Guenou H, Kaabeche K, Bouvard D, Sanjay A, Marie PJ (2008) FGFR2–Cbl interaction in lipid rafts triggers attenuation of PI3K/Akt signaling and osteoblast survival. Bone 42:1032–1039
19. Adapala NS, Barbe MF, Langdon WY, Nakamura MC, Tsygankov AY, Sanjay A (2010) The loss of Cbl–phosphatidylinositol 3-kinase interaction perturbs RANKL-mediated signaling, inhibiting bone resorption and promoting osteoclast survival. J Biol Chem 285:36745–36758
20. Molero JC, Turner N, Thien CB, Langdon WY, James DE, Cooney GJ (2006) Genetic ablation of the c-Cbl ubiquitin ligase domain results in increased energy expenditure and improved insulin action. Diabetes 55:3411–3417
21. Sims NA, Clement-Lacroix P, Da Ponte F, Bouali Y, Binart N, Moriggl R, Goffin V, Coschigano K, Gaillard-Kelly M, Kopchick J, Baron R, Kelly PA (2000) Bone homeostasis in growth hormone receptor-null mice is restored by IGF-I but independent of Stat5. J Clin Invest 106:1095–1103

22. Parfitt AM, Drezner MK, Glorieux FH, Kanis JA, Malluche H, Meunier PJ, Ott SM, Recker RR (1987) Bone histomorphometry: standardization of nomenclature, symbols, and units. Report of the ASBMR Histomorphometry Nomenclature Committee. J Bone Miner Res 2:595–610
23. Al-Shatti T, Barr AE, Safadi FF, Amin M, Barbe MF (2005) Increase in inflammatory cytokines in median nerves in a rat model of repetitive motion injury. J Neuroimmunol 167:13–22
24. Yingling V, Elle Saine M, Joshi R (2009) Hypothalamic suppression decreases bone strength before and after puberty in a rat model. Calcif Tissue Int 84:485–493
25. Yingling VR (2009) A delay in pubertal onset affects the covariation of body weight, estradiol, and bone size. Calcif Tissue Int 84:286–296
26. Sabatakos G, Davies GE, Grosse M, Cryer A, Ramji DP (1998) Expression of the genes encoding CCAAT-enhancer binding protein isoforms in the mouse mammary gland during lactation and involution. Biochem J 334:205–210
27. Hankenson KD, Bain SD, Kyriakides TR, Smith EA, Goldstein SA, Bornstein P (2000) Increased marrow-derived osteoprogenitor cells and endosteal bone formation in mice lacking thrombospondin 2. J Bone Miner Res 15:851–862
28. Di Masso RJ, Font MT, Capozza RF, Detarsio G, Sosa F, Ferretti JL (1997) Long-bone biomechanics in mice selected for body conformation. Bone 20:539–545
29. Karsdal MA, Martin TJ, Bollerslev J, Christiansen C, Henriksen K (2007) Are nonresorbing osteoclasts sources of bone anabolic activity? J Bone Miner Res 22:487–494
30. Karsdal MA, Neutzsky-Wulff AV, Dziegiel MH, Christiansen C, Henriksen K (2008) Osteoclasts secrete non-bone derived signals that induce bone formation. Biochem Biophys Res Commun 366:483–488
31. Kaabeche K, Guenou H, Bouvard D, Didelot N, Listrat A, Marie PJ (2005) Cbl-mediated ubiquitination of alpha5 integrin subunit mediates fibronectin-dependent osteoblast detachment and apoptosis induced by FGFR2 activation. J Cell Sci 118:1223–1232
32. Kaabeche K, Lemonnier J, Le Mee S, Caverzasio J, Marie PJ (2004) Cbl-mediated degradation of Lyn and Fyn induced by constitutive fibroblast growth factor receptor-2 activation supports osteoblast differentiation. J Biol Chem 279:36259–36267
33. Lai C-F, Cheng S-L (2002) Signal transductions induced by bone morphogenetic protein-2 and transforming growth factor-β in normal human osteoblastic cells. J Biol Chem 277:15514–15522
34. Stains JP, Civitelli R (2005) Gap junctions regulate extracellular signal-regulated kinase signaling to affect gene transcription. Mol Biol Cell 16:64–72
35. Thien CB, Dagger SA, Steer JH, Koentgen F, Jansen ES, Scott CL, Langdon WY (2010) c-Cbl promotes TCR-induced thymocyte apoptosis by activating the PI3K/Akt pathway. J Biol Chem 285:10969–10981
36. Adapala NS, Barbe MF, Langdon WY, Tsygankov AY, Sanjay A (2010) Cbl-phosphatidylinositol 3 kinase interaction differentially regulates macrophage colony-stimulating factor-mediated osteoclast survival and cytoskeletal reorganization. Ann NY Acad Sci 1192:376–384
37. Wang Z-Q, Ovitt C, Grigoriadis AE, Mohle-Steinlein U, Ruther U, Wagner EF (1992) Bone and haematopoietic defects in mice lacking *c-fos*. Nature 360:741–745
38. Soriano P, Montgomery C, Geske R, Bradley A (1991) Targeted disruption of the *c-src* proto-oncogene leads to osteopetrosis in mice. Cell 64:693–702
39. Gil-Henn H, Destaing O, Sims NA, Aoki K, Alles N, Neff L, Sanjay A, Bruzzaniti A, De Camilli P, Baron R, Schlessinger J (2007) Defective microtubule-dependent podosome organization in osteoclasts leads to increased bone density in Pyk2$^{-/-}$ mice. J Cell Biol 178:1053–1064
40. Buckbinder L, Crawford DT, Qi H, Ke HZ, Olson LM, Long KR, Bonnette PC, Baumann AP, Hambor JE, Grasser WA 3rd, Pan LC, Owen TA, Luzzio MJ, Hulford CA, Gebhard DF, Paralkar VM, Simmons HA, Kath JC, Roberts WG, Smock SL, Guzman-Perez A, Brown TA, Li M (2007) Proline-rich tyrosine kinase 2 regulates osteoprogenitor cells and bone formation, and offers an anabolic treatment approach for osteoporosis. Proc Natl Acad Sci USA 104:10619–10624
41. Marzia M, Sims NA, Voit S, Migliaccio S, Taranta A, Bernardini S, Faraggiana T, Yoneda T, Mundy GR, Boyce BF, Baron R, Teti A (2000) Decreased c-Src expression enhances osteoblast differentiation and bone formation. J Cell Biol 151:311–320
42. Lee SH, Rho J, Jeong D, Sul JY, Kim T, Kim N, Kang JS, Miyamoto T, Suda T, Lee SK, Pignolo RJ, Koczon-Jaremko B, Lorenzo J, Choi Y (2006) v-ATPase V0 subunit d2-deficient mice exhibit impaired osteoclast fusion and increased bone formation. Nat Med 12:1403–1409
43. Teitelbaum SL, Ross FP (2003) Genetic regulation of osteoclast development and function. Nat Rev Genet 4:638–649
44. Zhao C, Irie N, Takada Y, Shimoda K, Miyamoto T, Nishiwaki T, Suda T, Matsuo K (2006) Bidirectional ephrinB2–EphB4 signaling controls bone homeostasis. Cell Metab 4:111–121
45. Mendez-Ferrer S, Michurina TV, Ferraro F, Mazloom AR, Macarthur BD, Lira SA, Scadden DT, Ma'ayan A, Enikolopov GN, Frenette PS (2010) Mesenchymal and haematopoietic stem cells form a unique bone marrow niche. Nature 466:829–834
46. Winkler IG, Sims NA, Pettit AR, Barbier V, Nowlan B, Helwani F, Poulton IJ, van Rooijen N, Alexander KA, Raggatt LJ, Levesque JP (2010) Bone marrow macrophages maintain hematopoietic stem cell (HSC) niches and their depletion mobilizes HSCs. Blood 116:4815–4828
47. Nagasawa T, Hirota S, Tachibana K, Takakura N, Nishikawa S, Kitamura Y, Yoshida N, Kikutani H, Kishimoto T (1996) Defects of B-cell lymphopoiesis and bone-marrow myelopoiesis in mice lacking the CXC chemokine PBSF/SDF-1. Nature 382:635–638
48. Yu X, Huang Y, Collin-Osdoby P, Osdoby P (2003) Stromal cell-derived factor-1 (SDF-1) recruits osteoclast precursors by inducing chemotaxis, matrix metalloproteinase-9 (MMP-9) activity, and collagen transmigration. J Bone Miner Res 18:1404–1418
49. Wright LM, Maloney W, Yu X, Kindle L, Collin-Osdoby P, Osdoby P (2005) Stromal cell-derived factor-1 binding to its chemokine receptor CXCR4 on precursor cells promotes the chemotactic recruitment, development and survival of human osteoclasts. Bone 36:840–853
50. Zhu W, Boachie-Adjei O, Rawlins BA, Frenkel B, Boskey AL, Ivashkiv LB, Blobel CP (2007) A novel regulatory role for stromal-derived factor-1 signaling in bone morphogenic protein-2 osteogenic differentiation of mesenchymal C2C12 cells. J Biol Chem 282:18676–18685
51. Zhu W, Liang G, Huang Z, Doty SB, Boskey AL (2011) Conditional inactivation of the CXCR4 receptor in osteoprecursors reduces postnatal bone formation due to impaired osteoblast development. J Biol Chem 286:26794–26805
52. Okabe S, Tauchi T, Ohyashiki K, Broxmeyer HE (2006) Stromal-cell-derived factor-1/CXCL12-induced chemotaxis of a T cell line involves intracellular signaling through Cbl and Cbl-b and their regulation by Src kinases and CD45. Blood Cells Mol Dis 36:308–314
53. Sotsios Y, Whittaker GC, Westwick J, Ward SG (1999) The CXC chemokine stromal cell-derived factor activates a Gi-coupled phosphoinositide 3-kinase in T lymphocytes. J Immunol 163: 5954–5963

J Musculoskelet Neuronal Interact 2014; 14(1):78-94

Original Article

Hylonome

Bone loss from high repetitive high force loading is prevented by ibuprofen treatment

N.X. Jain[1], A.E. Barr-Gillespie[2], B.D. Clark[3], D.M. Kietrys[4], C.K. Wade[5], J. Litvin[1], S.N. Popoff[1], M.F. Barbe[1]

[1]Department of Anatomy and Cell Biology, Temple University School of Medicine, 3500 North Broad St., Philadelphia, PA 19140; [2]College of Health Professions, Pacific University, 190 SE 8th Avenue, Hillsboro, OR 97123; [3]Department of Neurobiology and Anatomy, Drexel University College of Medicine, 2900 Queen Lane, Philadelphia, PA 19129; [4]Department of Rehabilitation and Movement Sciences, Rutgers School of Health Related Professions, 40 E. Laurel Rd, Stratford, NJ, 08084; [5]Department of Physical Therapy, Thomas Jefferson University, Philadelphia, PA, 19107, USA

Abstract

We examined roles of loading and inflammation on forearm bones in a rat model of upper extremity overuse. Trabecular structure in distal radius and ulna was examined in three groups of young adult rats: 1) 5% food-restricted that underwent an initial training period of 10 min/day for 5 weeks to learn the repetitive task (TRHF); 2) rats that underwent the same training before performing a high repetition high force task, 2 hours/day for 12 weeks (HRHF); and 3) food-restricted only (FRC). Subsets were treated with oral ibuprofen (IBU). TRHF rats had increased trabecular bone volume and numbers, osteoblasts, and serum osteocalcin, indicative of bone adaptation. HRHF rats had constant muscle pulling forces, showed limited signs of bone adaptation, but many signs of bone resorption, including decreased trabecular bone volume and bone mineral density, increased osteoclasts and bone inflammatory cytokines, and reduced median nerve conduction velocity (15%). HRHF+IBU rats showed no trabecular resorptive changes, no increased osteoclasts or bone inflammatory cytokines, no nerve inflammation, preserved nerve conduction, and increased muscle voluntary pulling forces. Ibuprofen treatment preserved trabecular bone quality by reducing osteoclasts and bone inflammatory cytokines, and improving muscle pulling forces on bones as a result of reduced nerve inflammation.

Keywords: Repetitive Loading, Work-related Musculoskeletal Disorders, Radius, Ulna, Inflammatory Cytokines, Carpal Tunnel Syndrome

Introduction

Work-related musculoskeletal disorders (WMSDs) are also known as occupational overuse injuries, or repetitive strain injuries. They account for 33% of all lost workday illnesses, and WMSDs of the hand and wrist are associated with the greatest work absences[1,2]. Epidemiological studies have linked upper extremity WMSDs with occupational physical activities involving repetitive arm motions and other risk factors (including force, duration, and female gender)[3-5]. The combined effects of force and repetition are associated with the greatest risks, via accumulated loading and gradual reduction of tissue tolerance[6-8].

Cyclical loading and high force loads are known to affect bone quality[9-12]. However, only a few studies have examined changes occurring in upper extremity bones as a consequence of prolonged performance of occupational tasks. A few studies have shown that occupational tasks increase the incidence of hand osteoarthritis[13-15]. Bone scan studies of patients with upper extremity MSDs show increased blood flow and pooling (suggestive of inflammation) in affected bones, although the sensitivity and accuracy of the results were variable across studies[16-18]. A loss of bone mineral density (BMD) was reported in metacarpal bones and distal radius and ulna of patients with long-term carpal tunnel syndrome[19], a condition of reduced conduction velocity of the median nerve that is under the um-

The authors have no conflict of interest.

Corresponding author: Mary F. Barbe, PhD, Department of Anatomy and Cell Biology, Temple University School of Medicine, 3500 North Broad St., Philadelphia, PA 19140, USA
E-mail: mary.barbe@temple.edu

Edited by: S. Warden
Accepted 6 January 2014

brella of WMSDs. Surgical release treatment for carpal tunnel syndrome rescues this decline in distal forearm BMD[20]. These authors hypothesized that nerve-compression induced muscle weakness led to bone loss as a consequence of reduced muscular loading on the bone[19], since the muscles involved in performing hand grip actions produce forces on forearm bones[21,22].

However, several factors contribute to bone density and quality, including the magnitude, frequency and duration of loading, and overload-induced increases in inflammatory cytokines[9-12,23,24]. Increased interleukin-1 alpha (IL-1alpha), IL-1beta and tumor necrosis factor alpha (TNF-alpha), or their receptors, have been reported in serum of human subjects with upper extremity WMSDs[25-28]. Since these same inflammatory cytokines promote osteoclast activity and bone resorption[29-31], it is plausible that systemic or local inflammatory responses are contributing to pathological bone changes occurring with occupational physical activities.

We have developed a unique, voluntary rat model of repetitive reaching and pulling that permits the examination of responses of upper limb tissues to cumulative muscular loads and naturally occurring inflammation *in vivo*[32-37]. Rats are trained to voluntarily reach for and pull on a lever, with reach rate and force controlled operantly by food reward criteria. We have shown exposure-dependent declines in median nerve conduction velocity and increased forepaw hypersensitivity, establishing this as a model of carpal tunnel syndrome[36,38-41]. We have also observed that performance of a high-repetition high-force task (HRHF; 8 reaches/min at force loads of 60% maximum isometric pulling force) initially induces increases in serum osteocalcin (in weeks 3-9 of the HRHF task), suggestive of bone formation, but cortical bone thinning, increased osteoclasts, and increased serum Trap5b (a biomarker of osteoclast activity and bone resorption) by week 12 of HRHF task performance, suggestive of bone catabolism[35-37]. We have yet to determine if the HRHF load-induced increases of osteoclasts and serum biomarkers of bone resorption correspond to alterations of trabecular morphology and bone loss, or if the shorter duration loading occurring during the initial training period (the TRHF period) induces to bone formation, which forms the basis for this study.

Our primary aim was to use our rat model to examine the effects of performing a reaching and grasping task for a short time period at progressively increasing force loads, versus the effects of prolonged performance (12 weeks) of a high repetition high force (HRHF) reaching and grasping task on forearm trabecular bone microarchitecture and bone mineral density. For the short time period, we examined tissues from trained-only rats (TRHF rats) that had undergone initial training for 10 min/day, 5 days/week, for 5 weeks, at progressively increasing force loads, until they had learned the HRHF task; these rats euthanized immediately after this training period. For the prolonged task, we examined tissues from rats that had performed the HRHF task for 2 hours/day, 3 days/week, for 12 weeks (HRHF rats), after the earlier training period. We hypothesized that the initial training period would induce increased osteoblasts and bone adaptive changes in the TRHF rats due to the short-term progressive nature of this training regimen (described further in the methods), and that long-term performance of the HRHF task would induce bone resorptive changes in the HRHF rats due to an inflammatory response induced by prolonged bone loading at high cyclical rates and high force loads. To test this hypothesis, we treated subsets of rats daily with anti-inflammatory doses of oral ibuprofen with the hopes of shifting the balance of bone turnover away from inflammation-induced net bone resorption towards bone maintenance and perhaps even adaptation, despite continued bone loading at high force loads. We also examined other factors suggested in the literature as contributors to bone changes, including nerve compression and dysfunction, and muscle injury and weakness. This study will elucidate the extent of forearm trabecular bone changes occurring as a consequence of a high demand upper extremity occupational tasks, and the contributions of load versus inflammation.

Materials and methods

Animals and overview

All experiments were approved by the Temple University Institutional Animal Care and Use Committee and were in compliance with NIH guidelines for humane care and use of laboratory animals. A total of 113 young adult, female, Sprague-Dawley rats (2.5 months of age at onset of experiments) were used. All were food-restricted to body weights of 5% less than age-matched normal controls (the latter were used for weight-matching purposes only). These rats were randomly divided into groups as shown in Figure 1A: 1) food-restricted rats that underwent an initial training period for 10 min/day, 5 days/week, for 5 weeks to learn a high repetition high force reaching and pulling task (TRHF rats); 2) food restricted rats that trained to learn the task and then performed the high repetition high force task for 2 hours/day, 3 days/week, for 12 weeks (HRHF rats); and 3) food-restricted control rats that did not undergo training or task performance (FRC). Subsets were treated with oral ibuprofen: HRHF+IBU, TRHF+IBU and FRC+IBU. All rats were housed in a central animal facility in separate cages with a 12 hour light:dark cycle, and free access to water and environment enrichment toys. In addition to 45 mg food pellet rewards (a 1:1 mix of purified grain and banana flavored pellets; Bioserve, NJ, USA), all rats received Purina rat chow daily (i.e. same food reward and chow rations). Since rats were 2.5 months of age at onset, and 4 or 7 months of age at the point of tissue collection (TRHF were 4 mo, and FRC and HRHF were 7 mo of age at euthanasia), all were allowed to gain weight as a consequence of normal growth (Figure 1B).

Adult female rats were used in this study for several reasons: (1) Human females have a higher incidence of work-related musculoskeletal disorders than males[4,5,42]; (2) human females are three times more likely to have carpal tunnel syndrome than males[43], although the Bureau of Labor Statistics has determined that carpal tunnel syndrome is less likely to be captured on OSHA logs and reported in the Survey of Occupational Injuries and Illnesses (SOII) than other work place injuries and is there-

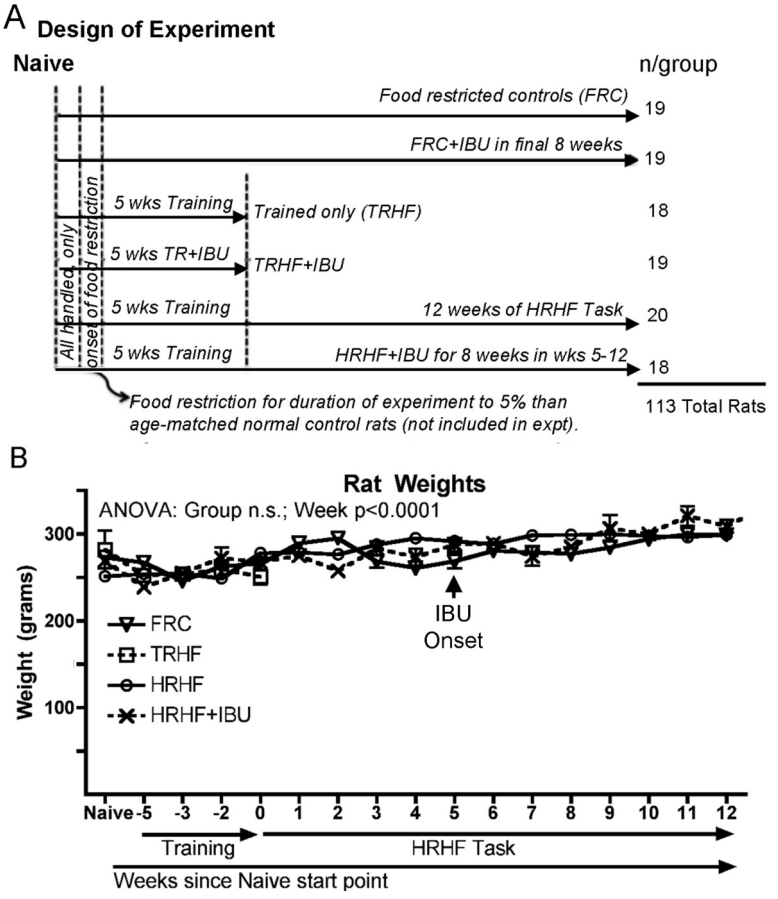

Figure 1. Experimental design and rat body weights over time. (A). Experimental design showing onset of food restriction following a 1 week period of daily handling. All rats were food restricted to 5% less than weights of age-matched normal controls rats. Food-restricted control (FRC) rats rested until euthanasia at matched time points as HRHF rats. Trained and task rats underwent a 5 week training period (rats reached the HRHF level by last week of training). Trained only rats (TRHF) were euthanized after training. Task rats performed a high repetition high force (HRHF) task for 12 weeks. FRC+IBU rats received daily ibuprofen (IBU) treatment in final 8 weeks, as did HRHF+IBU rats (arrow indicates onset of ibuprofen treatment). TRHF+IBU rats received ibuprofen treatment prophylactically during training. Number/group shown at far right. (B) Rats were weighed weekly from the naïve time point to euthanasia, and showed an increase in weight across weeks of experiment. No differences in weight were observed between groups at matched time points (n.s.= not significant).

fore under-estimated[44]; and (3) for comparison to data from our past studies on female rats using this model.

Behavioral apparatuses, training and task regimens

The custom-designed behavioral apparatuses used were as previously described and depicted[38,45]. The rats reached through a shoulder height portal and then isometrically pulled on a 1.5 mm metal bar, termed a force lever, that is attached to a load cell (Futek Advanced Sensor Technology, Irvine, CA) positioned 2.5 cm outside of the chamber wall. The bar was oriented vertically. The load cell output was interfaced with a signal conditioner (Analog Devices, Norwood, MA), which amplified and filtered the signal before it was sampled digitally at 100 Hz with Force Lever software (Med Associates, St. Albans, VT). The load cell was interfaced with custom written Force-Lever software that allowed us to choose a set force level before a food reward was provided (version 1.03.02, Med Associates, St. Albans, VT). Every 15 seconds, a series of auditory indicators (Stimulus Clicker; Med Associates, St. Albans, VT) lasting 5 seconds cued the animal to attempt a reach. During this period, the animal was trained to grasp the force lever bar and pull toward the chamber wall with a graded effort of a percentage of the maximum grip strength of control rats (rats not included in this study) for at least 50 milliseconds[38,46]. If reach and force criteria (defined below) were met within a 5 second cueing period, a 45 mg food pellet was dispensed into a trough located at floor height for the animal to lick up.

Prior to the initiation of the experiments, all rats were handled for 10 minutes/day for 1 week. All 113 rats were initially food-restricted for 7 days to no more than 10-15% less than their naive weight to initiate interest in the food reward pellets (a 1:1 mix of grain-based and banana-flavored pellets). After

that week, they were given extra rat chow to gain weight quickly back to only 5% less than age-matched normal control rats. Rats were weighed weekly, maintained at 5% less than age-matched normal controls until euthanasia, and allowed to gain weight during the study since they were young adult rats. Thirty-eight of the food-restricted rats were randomly chosen as food-restricted controls (FRC) that rested until euthanasia at time points matched to the HRHF rats (Figure 1A). The remaining food-restricted rats were randomly chosen to be TRHF or HRHF rats.

With regard to the initial training period, seventy-five food-restricted rats were trained to learn the HRHF reaching and lever-pulling task during a 5-week period of 10 min/day, 5 days/wk. During this period, the rats moved through several stages of training. First, in week 1 of training, they were placed in a plastic box outfitted with a piece of Plexiglas with a portal located at shoulder height connected to a small plastic trough. In this chamber, the rats were introduced to the 45 mg food pellets that served as food reward (a 1:1 mix of grain-based and banana-flavored food pellets). Using calibrated force transducers, we estimate that retrieval of the 45 mg food pellets required a negligible amount of force (<5% of the rats' maximum grasping force). When the rats learned to reach (without a specified reach rate) into a trough for the food pellets, a time period of typically 3 days, they were moved to the custom-designed operant conditioning chambers (Med Associates, St. Albans, VT), depicted previously[45]. In the operant chambers, rats learned with the aid of auditory and light cueing to reach through a shoulder-height portal within the apparatus to isometrically pull the force lever attached to a force transducer. Using a magazine style training, in which the force lever started within the chamber for the remainder of week 1, the rats learned to grasp the force lever bar and exert an isometric pull of approximately 1% of their maximum voluntary force, without any specified repetition rate for a food reward. In week 2, the force lever bar was moved to 2.5 cm outside of the chamber and the rats were required to grasp the force lever and exert an isometric pull of 0.10 Newton's (11 grams; approximately 5% of their maximum voluntary pulling force) without any specified repetition rate for a food reward. In week 3, they were required to pull at 0.29 Newton's (30g; approximately 15% of their maximum voluntary pulling force), without any specified repetition rate for a food reward, and in week 4, at 0.58 Newton's (60g; approximately 30% of their maximum voluntary pulling force). By the end of the 5 week training period, the rats were able to perform the HRHF task of four reaches/min at 1.93 Newton's (11g; approximately 60% of their maximum voluntary force). The TRHF rats reached this HRHF level only during the last days of their 5th week of training. After training, rats were randomly divided into TRHF only rats (n=37) and HRHF (n=38). TRHF rats were euthanized at this point (Figures 1A,B).

The remaining trained rats went on to perform the HRHF task regimen (the 38 HRHF rats) for 2 hrs/day, 3 days/wk for up to 12 weeks. The daily task was divided into four 30-minute sessions separated by 1.5 hrs each in order to avoid satiation. HRHF rats were cued to reach at a rate of 8 reaches/min and to grasp the force lever bar at a target force effort of 60% ± 5% of the mean maximum pulling force (which equals 120 to 128 grams, or 1.17 to 1.25 Newton's). HRHF rats had to grasp the force lever bar and exert an isometric pull at the target level for at least 50 milliseconds to receive a food reward.

Limb dominance was not evident until after the training period, but was evident during the task regimen, and was recording thereafter. Rats were allowed to use their preferred limb to reach (the ''reach'' limb), and their contralateral limb as support against the operant chamber wall while pulling (the "support" limb), as described and depicted previously[45]. For the purpose of this study, tissues were collected and assayed from only the dominant, preferred, reach limb, since our purpose was to assess the effects of reaching and grasping repetitively on bones.

Ibuprofen treatment

At the end of the 4th week of task performance, 18 HRHF rats were administered ibuprofen (Children's Motrin Grape Flavored, Johnson & Johnson) in drinking water daily (45 mg/kg body weight), and are termed HRHF+IBU rats, as described previously[35]. Nineteen FRC rats received oral ibuprofen in their final 8 weeks (FRC+IBU); 19 TRHF rats received ibuprofen beginning at the onset of training (TRHF+IBU). Ibuprofen dosing was tracked as 48.8±6.3 mg/kg body weight for each rat by measuring the difference between the initial and final volume of suspended solution daily, and by assaying serum levels of ibuprofen (National Medical Services, Willow Grove, PA). The dose used was lower than the maximum limit for gastrointestinal toxicity in rats, yet was a dose shown to be effective in reducing chronic inflammation[35,47]. No adverse changes in behavior suggestive of abdominal discomfort or pain were observed in the ibuprofen-treated rats (such as hunching or licking of their abdomen, or reduced food intake). Stomachs were collected from five of the HRHF+IBU rats, and examined histologically. No evidence of thinning of the stomach lining was observed.

Voluntary pulling force

Force lever data were recorded continuously during each task session for latter calculation of the pulling force by the custom written Force-Lever software (version 1.03.02, Med Associates) during each task session for later calculation of voluntary pulling force via an automated script (MatLab; Mathworks, Natick, MA). Mean voluntary grasp force was the average force (in grams) applied to the force lever bar during a reach. Voluntary grasp force data were obtained from: 26 HRHF animals at week 1, 18 rats in weeks 3 and 6, and 10 rats in week 12; and 10 HRHF+IBU animals in weeks 1, 3, 6 and 12. Week 1 of the HRHF task was used as the baseline for grasp force since that was the first week that task rats actually performed the task regimens.

MicroCT analysis of the distal radius and ulna

Animals were euthanized by lethal overdose (Nembutal, 120 mg/kg body weight) at 18 hours after the last task session in

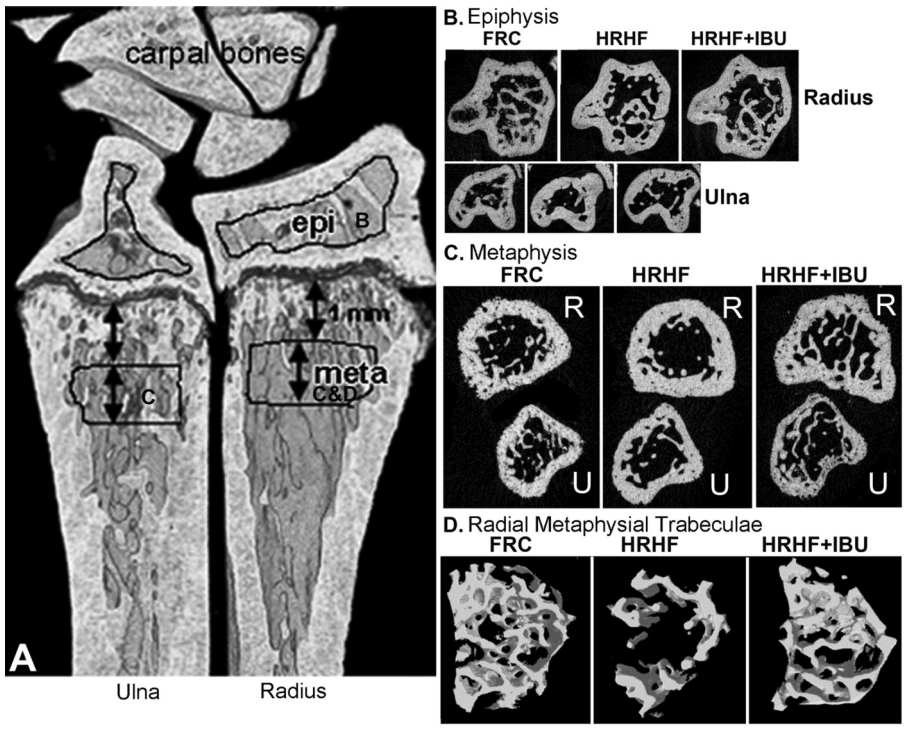

Figure 2. MicroCT images of distal radius and ulna. (A) A representative 3D model of the distal radius and ulna, cut sagittally, showing the site of the epiphyseal (epi) and metaphyseal (meta) analyses (encircled by black lines), and the sites of the images shown in panels B-D, as indicated by the letters B, C and D. (B) Representative transaxial microCT slices of the epiphysis of the radius and ulna (at 27 slices, 243 micrometers from the proximal edge of their respective growth plates) from a food restricted control (FRC), a 12-week high repetition high force (HRHF), and 12-week HRHF rat treated with ibuprofen for 8 weeks (HRHF+IBU). (C) Representative transaxial microCT slices of the metaphysis of the radius and ulna (at 166 slices, 1.5 millimeters from the distal edge of their respective growth plate) from a FRC, HRHF, and HRHF+IBU rat. (D) Representative 3D models of transaxial microCT slices through the metaphyseal region of the left radius (R) of a FRC, HRHF, and HRHF+IBU rat, with the surrounding cortical bone segmented away from the cortical bone in order to show the trabecular architecture. The transaxial reconstructions are located from 1.0 to 2.0 mm proximal to the respective growth plates, and are viewed from the bottom looking towards the growth plate. Increased separation and loss of trabeculae are seen in the HRHF rats, changes not present in FRC or HRHF+IBU rats (panel D).

order to avoid exercise-induced changes in serum cytokines. Serum collected for biochemical assays (described more below), then perfused transcardially with 4% paraformaldehyde in 0.1M PO_4 buffer (pH 7.4). For this assay, forelimb bones were collected, cleaned of soft tissues, and washed in phosphate buffered saline, from the reach limbs of TRHF (n=6), TRHF+IBU (n=7), 12 wk HRHF (n=8), and 12 wk HRHF+IBU (n=5) rats; as well as limbs of FRC (n=7) and FRC+IBU (n=6) rats. A Skyscan 1172, 12 MPix model, microCT scanner (Bruker-microCT, Kontich, Belgium) was used to image a 6 mm length of the distal radial and ulna bones (1000 slices), using a modification of previously described methods[48-50]: an isotropic voxel resolution size of 9 μm, source voltage of 59 kV, source current of 167 μA, Al 0.5 mm filter, rotation step of 0.40°, frame averaging of 4, ring artifact correction of 10, and beam hardening correction of 60%. After scanning, 3D image data were reconstructed using Skyscan NRecon software. Using Skyscan CTAn software, the volume of interest for trabecular microarchitectural variables was bounded to the endocortical margin. For the epiphyseal trabeculae, morphological traits were assessed starting 0.2 mm distal to the growth plates, and then extending from this position distally for 0.50 mm (56 slices, or until the edge of the subchondral cortical bone was reached; Figure 2A), as described in Bouxsein, 2010[51]. For the distal metaphyseal trabeculae, morphological traits were assessed starting 1 mm proximal to the growth plates, and then extending proximally from this position for 1 mm (112 slices; Figure 2A). Upper and lower thresholds of 255 (max) and 75 were used to delineate each pixel as "bone" or "nonbone". Trabecular morphometric traits were computed from binarized images using direct 3D techniques that do not rely on prior assumptions on underlying structures, and trabecular bone volume per total volume (BV/TV), mean trabecular thickness (Tb.Th.), mean trabecular number (Tb.N.), and mean trabecular separation (Tb.Sp.) indices were computed.

For assay of bone mineral density (BMD), a set of 3 calcium hydroxyapatite phantoms of rat bones was scanned (partially in air; partially in water) using the same settings as for the bones. Houndsfield units for the phantoms, air and water were calculated and then used to compute columetric BMD of the

segmented metaphyseal trabeculae with surrounding marrow space for the radius of animal analyzed using microCT.

Histomorphometry of the distal radius metaphysis

Subcohorts of the above bones were then used for histomorphometry: FRC (n=5), FRC+IBU (n=6), TRHF (n=6), TRHF+IBU (n=6), 12 wk HRHF (n=9), and 12 wk HRHF+IBU (n=9) rats (reach limbs were used for the TRHF and HRHF rats). Bones from all rats but 3 of the 12 wk HRHF and 3 of the HRHF+IBU were processed and embedded in methyl methacrylate (MMA), sectioned into 3 μm thick longitudinal sections and mounted onto slides, as described previously[35]. The remaining bones (3 HRHF and 3 HRHF+IBU) were processed and embedded in paraffin, sectioned into 5 μm thick longitudinal sections and mounted onto slides, as a consequence of other experiments in which immunohistochemical probing of the bones was needed. Slides were stained with Goldner's Trichrome for counting osteoblasts, or immunohistochemically for Trap5 and ED1 for counting osteoclasts (ED1 is a marker of osteoclasts, macrophages and their progenitors; only multinucleated ED1+ cells were counted in this study), as described previously[34]. Numbers of cells per bone surface (N.Ob./BS and N.Oc./BS) were counted in the same region as assayed using microCT using a Nikon E800 microscope interfaced with a Q-Imaging digital camera, and an image analysis system (Bioquant Osteo 2012, v12.1). The person carrying out the histomorphometry was blinded to treatment.

Muscle histomorphometry

Flexor digitorum muscles were collected from the same rats as for microCT. After transcardial fixation and then immersion fixation for at least 24 hours, a 3 mm thick cross-sectional piece of the flexor digitorum muscle was cut, with a scalpel, from the proximal end of the muscle mass. The muscles were cryosectioned into 12 μm sections, placed onto charged and coated slides (Fisher Scientific, Tissue Path Superfrost Plus Gold Slides), dried, and stained with Hematoxylin and Eosin (H&E). The cross-sectional area (CSA) of each myofiber fascicle was quantified using a Nikon microscope interfaced with a digital camera and image analysis system (Bioquant Osteo 2012, v12.1), as described previously[52]. An average of 82 fascicles were counted per muscle. The individual measuring the areas was blinded to group assignment. The muscle sections were also examined for signs of histopathological changes after staining with the ED1 antibody. Muscles were defined as having microdamage by the presence of atrophied myofibers and the presence of ED1+ macrophages within myofibers (internal) in the same tissue section, as described previously[53]. The number of ED1+ macrophages within atrophied myofibers (internal) were counted in the mid-belly region of the flexor digitorum longus, using previously described semi-automated quantification methods and an image analysis system (Bioquant) connected to a Nikon E800, at three microscope field locations per rat[54].

Histomorphometry of median nerve inflammation

To examine the median nerve inflammation, flexor forelimb tissues were collected from the same rats and limbs as above as a flexor mass, postfixed "en bloc" (nerves still intact) by immersion overnight, cryosectioned, immunostained on slides for ED1+ macrophages, as described previously[55]. The number of ED1+ macrophages were quantified in 3 regions and sections per nerve using a Nikon E800 microscope linked to an image analysis system, as described previously[39]. Adjacent sections were stained with Hematoxylin and Eosin (H&E) and examined for peripheral nerve pathology, such as increased extraneural collagen deposition (indicative of extraneural nerve fibrosis), presence of axonal swelling (indicative of axonal compression), myelin degradation visible using H&E, and visible signs of nerve disruption and nerve compression.

Biochemical analyses of serum, radius and ulna

To study serum biomarkers of bone turnover, animals were euthanized with an overdose of sodium pentobarbital (Nembutal; 120 mg/kg body weight) at 18 hours after completion of the final task session to avoid exercise induced increases in inflammatory cytokines. Blood was collected by cardiac puncture using a 23-gauge needle from: FRC (n=6), FRC+IBU (n=6), TRHF (n=9), TRHF+IBU (n=9), 12 wk HRHF (n=6), and 12 wk HRHF+IBU (n=6) rats. Blood was centrifuged at 1,800 g for 20 min at 4ºC, serum collected and flash-frozen, and stored at -80ºC until analyzed using commercially available ELISA kits for: Trap5b (band 5 tartrate-resistant acid phosphatase; a biomarker of osteoclast activity and bone resorption; Immunodiagnostic systems, Fountain Hills, AZ; #SB-TR102), CTX1 (the C-terminal telopeptide of Collagen type I cleaved by osteoclasts during bone resorption; Immunodiagnostic systems, RatLaps, # AC-06F1), osteocalcin (a non-collagenous protein secreted by osteoblasts; Nordic Bioscience Diagnostics, Herlev, Denmark, #Rat-MIDTM Osteocalcin). Two pro-inflammatory cytokines, interleukin (IL) beta and tumor necrosis factor alpha (TNF-alpha) were assayed using ELISA kits from (Aushon, Pierce), as described previously[33]. Serum samples were tested in duplicate and presented as pg of protein per ml of serum.

Radius and ulna bones were collected for biochemical assays from: FRC (n=6), FRC+IBU (n=5), TRHF (n=5), TRHF+IBU (n=4), 12 wk HRHF (n=5), and 12 wk HRHF+IBU (n=6) rats. Reach limbs were used for the TRHF and HRHF rats. Distal regions (which included the epiphysis, growth plate and metaphysis) and diaphyseal regions were combined and the bones were assessed for IL-1beta and TNF-alpha using commercially available ELISA kits (BioSourceTM, Invitrogen Life Sciences, CA), as described previously[33]. ELISA assay data (pg cytokine protein) were normalized to μg total protein, determined using a bicinchoninic acid protein assay kit.

Electrophysiological testing of median nerve conduction velocity (NCV)

In order to test focal slowing of conduction, NCV was determined for the segment of the median nerve that passes beneath the transcarpal ligament in the preferred reach limbs of anesthetized rats: HRHF (n=7) and HRHF+IBU (n=6) rats. NCV was also determined bilaterally in FRC (n=6), FRC+IBU

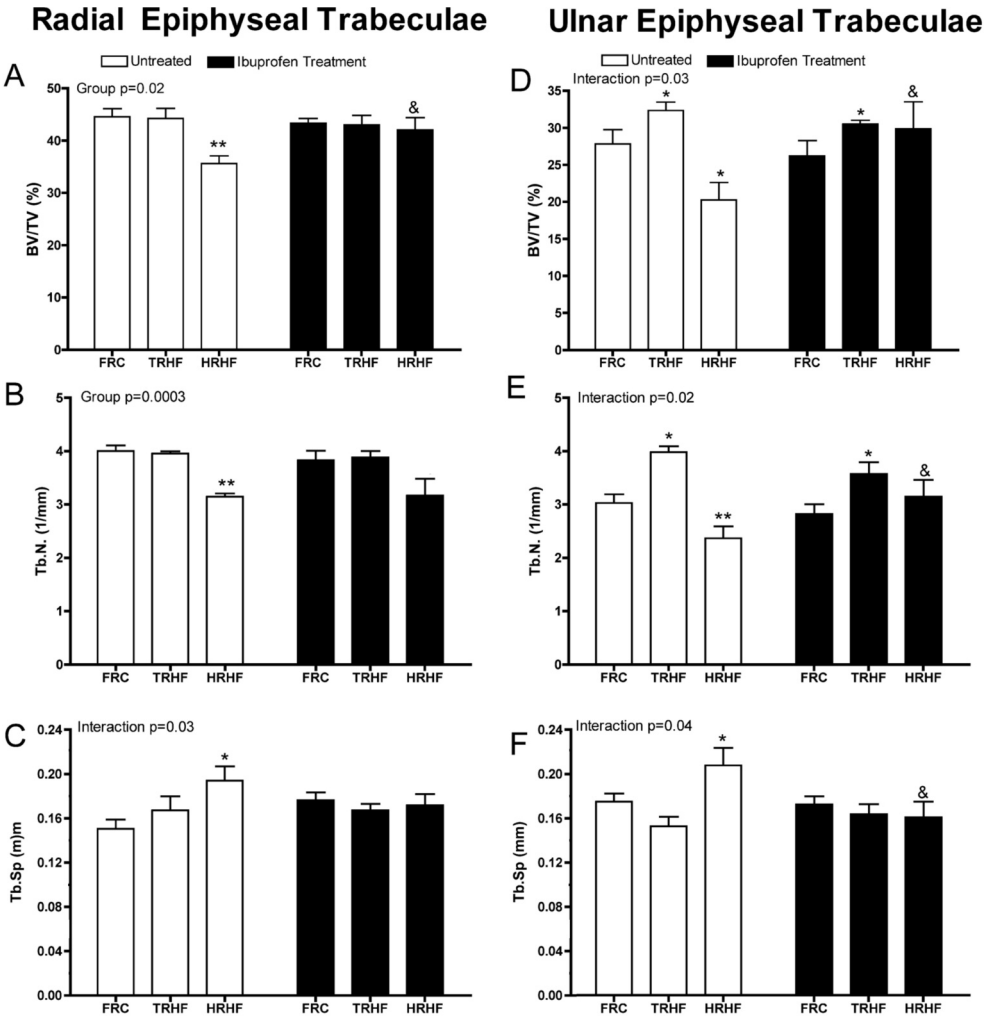

Figure 3. MicroCT analysis of trabeculae of distal radial (A-D) and ulnar epiphyses (E-H). Results for trabecular bone volume (BV/TV), trabecular number (Tb.N.), and trabecular separation (Tb.Sp.) are shown. Significant 2-way ANOVA findings shown in individual panels and hereafter. Symbols: *:p<0.05 and **:p<0.01, compared to FRC rats; &: p<0.05, compared to untreated HRHF rats.

(n=9), TR-HF (n=7) and TR+IBU (n=8) rats. The method for measurement of NCV of the median nerve in rats matched that described previously[41]. Both the surgeon and the person carrying out the recordings and data analysis were blinded to rat treatment. Serum was not collected from rats that underwent the NCV testing to avoid confounding interpretation of results by changes induced by this surgical procedure.

Statistical analyses

To determine differences in weight, grasp force and grip strength, a mixed-model, two-way ANOVA was used with the factors: week of task performance (weekly weights from naïve to euthanasia) and group. For bone microCT variables, cell counts, cytokine data, and electrophysiological variables, two-way ANOVAs were used with the factors: group and treatment (untreated versus ibuprofen). A one-way ANOVA was used to compare BMD changes to FRC rats. For each, the Bonferroni post-hoc method for multiple comparisons was used, with comparisons to FRC or FRC+IBU data, as appropriate for the treatment group. Adjusted p-values are reported, and after adjustment, a p value of <0.05 was considered statistically different. All data are expressed as mean ± standard error (SEM).

Results

Rat weights

A two-way ANOVA indicated that there were no significant differences in weight between the trained or task groups, compared to FRC rats (not significant). All rats gained weight in a consistent manner across the weeks of the experiment (week p<0.0001) (Figure 1B). Thus, any changes observed in bone structure were not due to changes in body weight.

Short-term loading leads to bone adaptation (TRHF rats), while long term loading at HRHF leads to bone resorption in distal epiphyseal trabeculae

Changes in trabecular microarchitecture that could be caused by increased bone adaptation was observed in the distal ulna of TRHF rats, and changes that could be caused by bone resorption were detected in the distal radial and ulnar epiphyses of 12-week HRHF rats (Figures 2A,B & Figure 3; significant 2-way ANOVA findings are indicated in figures). Specifically, increased trabecular bone volume density (BV/TV) and trabecular number (Tb.N.) were observed in the ulna epiphysis of TRHF rats (rats that underwent training only), compared to FRC rats (Figures 3D,E; post hoc findings are indicated in figures), indicative of bone adaptation. In contrast, both radial and ulnar epiphyses of 12-week HRHF rats show decreased trabecular BV/TV and Tb.N., and increased trabecular separation (Tb.Sp.), compared to FRC rats (Figures 3 A-C,F), indicative of bone resorptive changes. Ibuprofen treatment did not improve the ulnar epiphyseal adaptive changes in TRHF rats, but did prevent bone resorptive changes in the radius and ulna epiphyses of HRHF+IBU rats (Figures 3 A-F). The preventive effects of ibuprofen treatment are also indicated by the significant group x treatment interactions in radial Tb.Sp. (Figure 3C), and ulnar BV/TV, Tb.N., and Tb.Sp. (Figures 3D-F). Trabecular thickness was not affected by training, task performance or ibuprofen treatment (data not shown). Thus, bone adaptation was observed in ulnar epiphyses of untreated TRHF rats; however, resorptive changes were observed in radial and ulnar epiphyses of untreated HRHF rats, changes prevented by ibuprofen treatment.

Trabecular resorption and limited adaptation in distal metaphyseal trabeculae with HRHF loading

No significant changes were observed in the distal metaphyseal trabeculae of TRHF rats. In contrast, high force loading-induced resorptive changes were apparent in radial and ulnar metaphyseal trabeculae of HRHF rats (Figures 2A,C,D; Figures 4A-E,G,H), yet there were also limited signs of bone adaptation in the radial metaphysis in the HRHF rats (Figure 4B). Specifically, in the distal radial metaphysis, HRHF rats had decreased trabecular BV/TV and Tb.N., as well as increased Tb.Sp, compared to FRC rats (Figures 4A,C,D), indicative of bone resorptive changes. The distal ulnar metaphysis of HRHF rats had similar changes, with decreased trabecular BV/TV and Tb.N., and increased Tb.Sp., compared to FRC rats (Figures 4E,G,H). Bone adaptive changes were also present in HRHF rats, in the form of increased Tb.Th. in the distal radial metaphysis (Figure 4B). Bone resorptive changes were not present in HRHF+IBU rats (Figures 4A,C-E,G,H). Ibuprofen treatment prevented BV/TV and Tb.Sp. declines in the distal radial metaphysis (Figures 4A,D), and enhanced Tb.Th. in the distal ulna metaphysis (Figure 4F). The radius of HRHF+IBU rats showed a similar increase in Tb.Th. as that of untreated HRHF rats (Figure 4B). The preventive effects of ibuprofen treatment are further indicated by the significant effects of treatment on radial BV/TV (Figure 4A), and on the ulnar Tb.Th. (Figure 4F). Thus, bone resorptive changes were observed in radial and ulnar metaphyses of untreated HRHF rats, changes prevented by ibuprofen treatment in HRHF+IBU rats.

Loading-induced increases in osteoclasts and osteoblasts

We next investigated the metaphyseal radius in sectioned bones for changes in osteoclast and osteoblast numbers. Osteoclast numbers were highest in HRHF rats, compared FRC (Figure 5A), an increase prevented by Ibuprofen treatment of TRHF+IBU and HRHF+IBU rats (a finding further bolstered by a significant group x treatment interaction effect on osteoblast numbers). Osteoblasts numbers were increased in TRHF and HRHF rats, compared FRC, and similarly in TRHF+IBU and HRHF+IBU rats, compared to FRC+IBU (Figure 5B), but no additional effect from ibuprofen treatment. Thus, ibuprofen treatment reduced osteoclast numbers in HRHF+IBU, but did not affect osteoblast numbers.

Bone mineral density decreased in HRHF rats

Bone mineral density (BMD) was decreased in radial metaphyseal trabeculae of HRHF rats, compared to FRC rats (Figure 5C). This decline was prevented by ibuprofen treatment (HRHF+IBU).

Serum biomarkers indicate bone formation with training, but bone resorption with HRHF task

To confirm the micro-CT results, serum biomarkers of bone turnover were analyzed (Figures 5D-F). With regard to indicators of bone resorption, Trap 5b increased significantly in serum of HRHF rats (Figure 5D), while CTX1 increased in both TRHF and HRHF rats (Figure 5E), compared to FRC rats. Ibuprofen treatment prevented the loading induced increase in serum TRAP5b in these rats (Figure 5C). The 4 week treatment of TRHF rats with ibuprofen (TRHF+IBU rats) did not alter their increase in CTX-1 (Figure 5E); in contrast, the 8 week treatment of HRHF+IBU rats prevented an increase of serum CTX-1 in these latter rats. Serum osteocalcin, a marker of bone formation, increased only in TRHF and TRHF+IBU rats, compared to FRC and FRC+IBU rats, respectively (Figure 5F). Thus, training, with or without ibuprofen, induced increased serum biomarkers of both bone formation and resorption; in contrast, HRHF-induced increases of serum biomarkers of bone resorption were prevented by ibuprofen treatment.

Voluntary lever pulling is highest in HRHF+IBU rats

Since a relationship between voluntary grip strength and radial bone mineral density has been established in humans[21,56-60], we next examined mean voluntary lever pulling force data collected during task performance as a proxy for muscle loading levels (Figure 6A). The untreated HRHF rats consistently pulled at a high force level of around 92 grams (92.97±2.59, mean±SEM, which is still a high force task as this is approximately 40% of their maximum pulling force, although lower than their target of 120 grams) (Figure 6A). In contrast, vol-

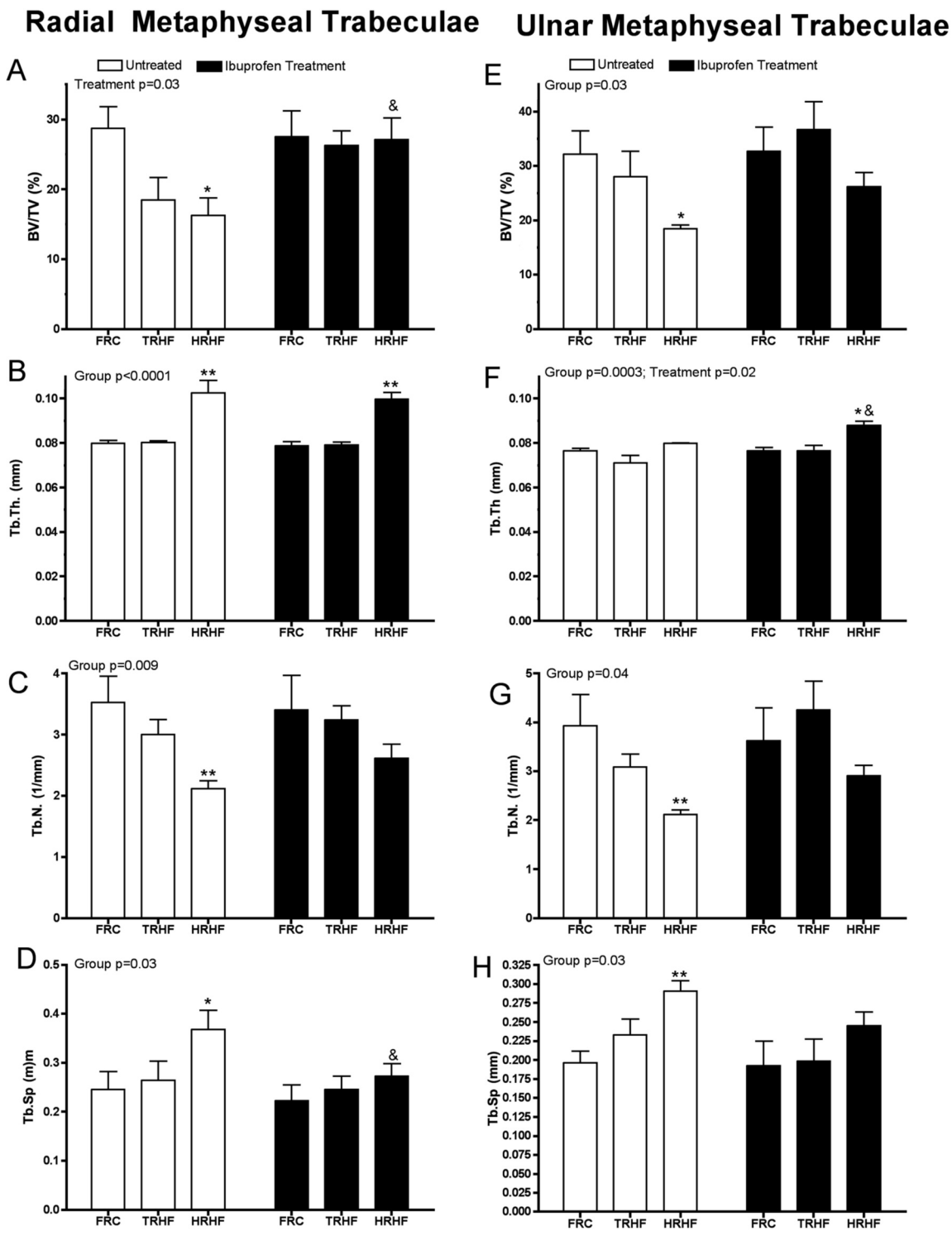

Figure 4. MicroCT analysis of trabeculae of the distal radial (A-D) and ulnar metaphysis (E-H). Results for trabecular bone volume (BV/TV), trabecular number (Tb.N.), trabecular separation (Tb.Sp.) and trabecular thickness (Tb.Th.) are shown. Symbols: *:p<0.05 and **:p<0.01, compared to FRC rats; &: p<0.05, compared to untreated HRHF rats.

untary pulling force increased to target levels in 6- and 12-week HRHF+IBU rats, significantly higher than force levels reached before this treatment. Thus, since HRHF rats had consistent pulling forces across the 12 weeks of task performance, declines in bone structure in these rats were not the result of changes in muscle function. However, the anti-inflammatory effect by ibuprofen enhanced the rats' voluntary pulling force and likely contributed to bone homeostasis in HRHF+IBU rats.

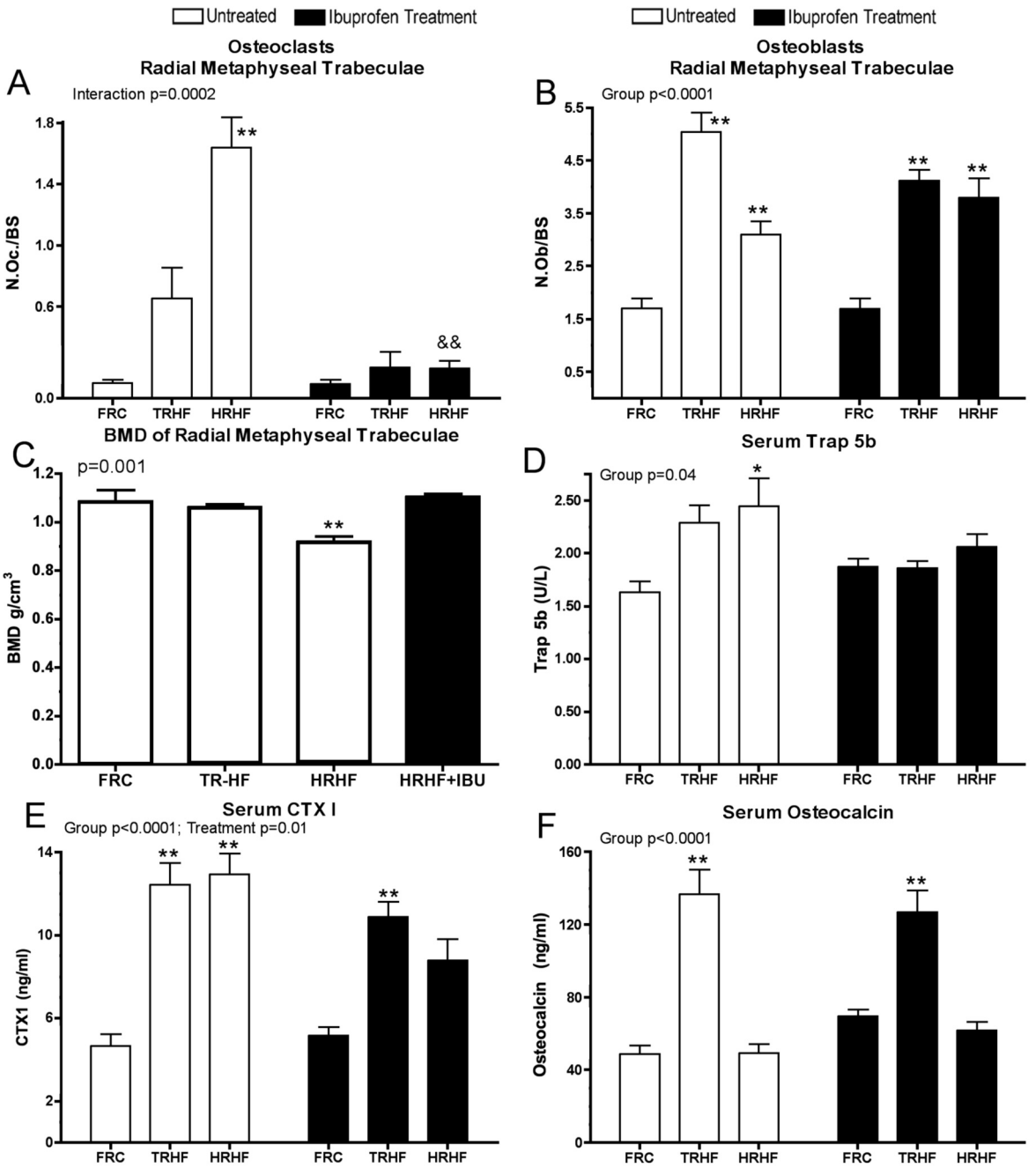

Figure 5. Bone cell histomorphometry and bone mineral density in distal radial trabeculae, and serum bone turnover markers. (A-B) Density of osteoclasts (N.Oc.) and osteoblasts (N.Ob.), normalized to bone surface (BS), of distal radial metaphyseal trabeculae. (C) Bone mineral density (BMD) of radial metaphyseal trabeculae. (D-F) Serum levels of Trap 5b, CTX1 and osteocalcin, assayed using ELISA. Symbols: *:p<0.05 and **:p<0.01, compared to FRC rats; &&:p<0.01, compared to untreated HRHF rats.

HRHF loading, with and without ibuprofen, increases in both cross-sectional myofiber area and subdegenerative myofiber numbers

Exercise-induced changes in muscle are postulated to lead to proportional changes in bone mass[61]. Also, repeated small amplitude contractions of muscles with incomplete recovery time between bouts of loading can lead to subdegenerative muscle injury[62]. Therefore, we first investigated the cross sectional area of myofiber fascicles in flexor digitorum muscles (Figure 6B). Myofiber cross sectional areas were increased similarly in TRHF, HRHF and HRHF+IBU rats, compared to FRC or FRC+IBU rats (Figure 6B), although the range in fiber sizes was much greater in the HRHF and HRHF+IBU rats. Ten percent of the myofibers in the HRHF and HRHF+IBU rats cross sectional areas in the 300 micrometer^2 range (minimum=

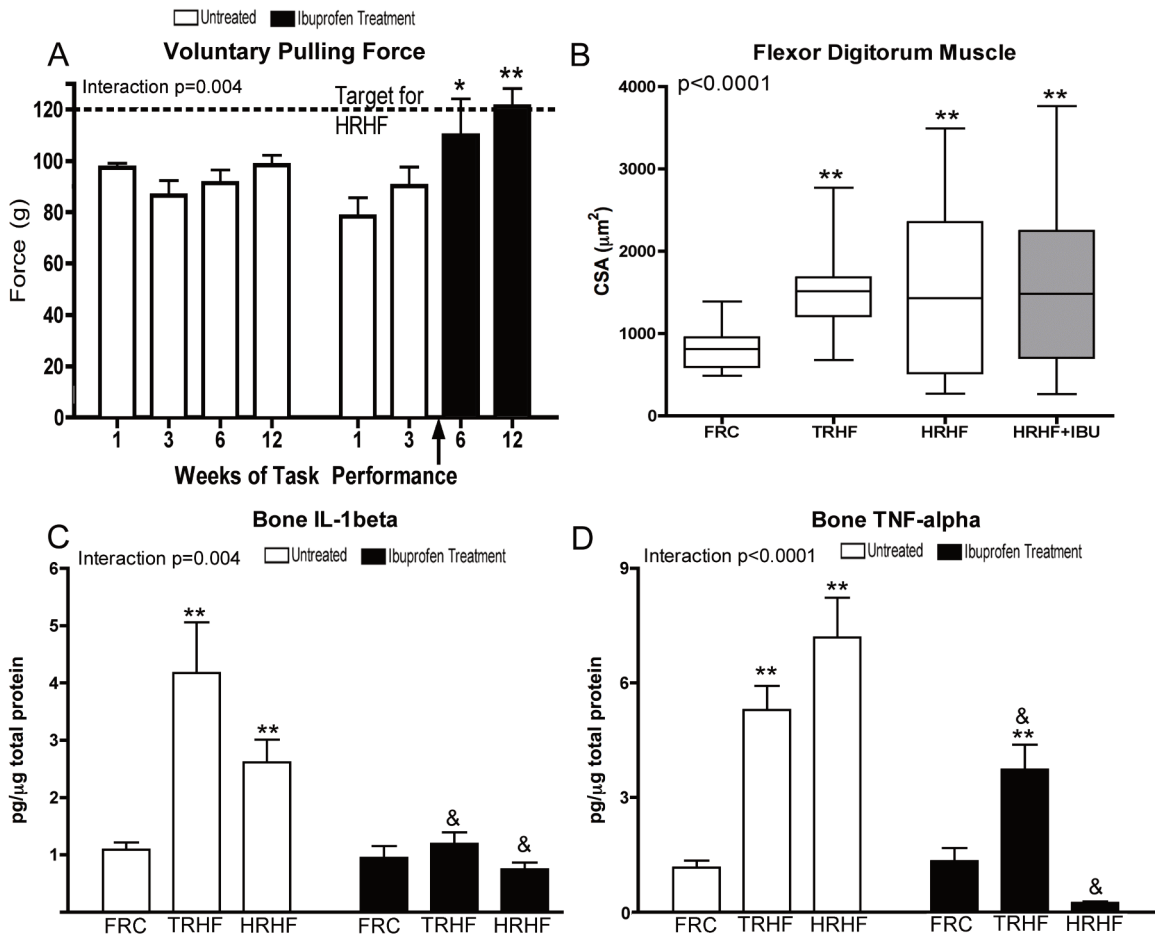

Figure 6. Mean voluntary pulling force, muscle cross sectional area, and bone cytokine levels (serum cytokine levels are provided in the text). (A) Mean voluntary pulling force on the lever bar used for the reaching and grasping task, in grams. Arrow indicates onset of ibuprofen treatment. (B) Mean cross-sectional area of myofibers in flexor digitorum muscle, quantified at mid-muscle level. (C&D) IL-1beta and TNF-alpha in forelimb bones, tested using ELISA. Symbols: *:p<0.05 and **:p<0.01, compared to FRC rats; &:p<0.05, compared to untreated HRHF rats.

264.7 micrometers^2 in HRHF rats; minimum= 303.4 micrometers^2 in HRHF+IBU rats), compared to the mean in HRHF of 1705±91.29 SEM, and the mean in HRHF+IBU rats of 1670±80.41. We next counted the number of degenerating myofibers (presence of macrophages within atrophying myofibers). HRHF and HRHF+IBU flexor digitorum muscles had 17±1.0 and 15.85±1.3, respectively, ED1 immunoreactive cells/mm^2 within atrophying myofibers at the mid flexor digitorum muscle belly, compared to none in the other groups, indicative of a low level of loading-induced myofiber degeneration in each group. Since similar changes in muscle morphology were observed in both the HRHF and HRHF+IBU rats, changes in muscle morphology were not contributing factors to the observed bone changes.

Bone and serum IL-1beta and TNF-alpha increased with HRHF loading; decreased with ibuprofen

Since IL-1beta and TNF-alpha are potent stimulators of bone resorption[63,64], and since we have previously observed increases of both in our model in musculoskeletal tissues and serum with this HRHF task and other task demands[33,36,40], their levels were assayed in bone and serum. IL-1beta and TNF-alpha levels were increased in forelimb bones of TRHF and HRHF rats, compared to FRC rats (Figures 6C,D). These increases were prevented by ibuprofen treatment (Figures 6C,D), as indicated by the group x treatment interaction effects of p=0.004 and p<0.0001 respectively. Serum levels of IL-1beta were significantly increased in HRHF rats (107.5±11.04 (mean±SEM)), compared to TRHF and FRC rats (undetectable in each group), an increase prevented by the ibuprofen treatment (IL-1beta was undetectable in TRHF+IBU and HRHF+IBU rats, p<0.01 each; the group x treatment interaction effect was p<0.0001). Serum TNF-alpha was also significantly increased in HRHF rats (645.7±267.8; mean±SEM), compared to FRC rats (3.92±3.92). This increase was prevented by ibuprofen treatment (serum TNF-alpha was 22.66±7.02 in HRHF+IBU rats, p<0.01; the group x treatment interaction effect was p=0.0004). These results indicate that TRHF and HRHF task performance induces

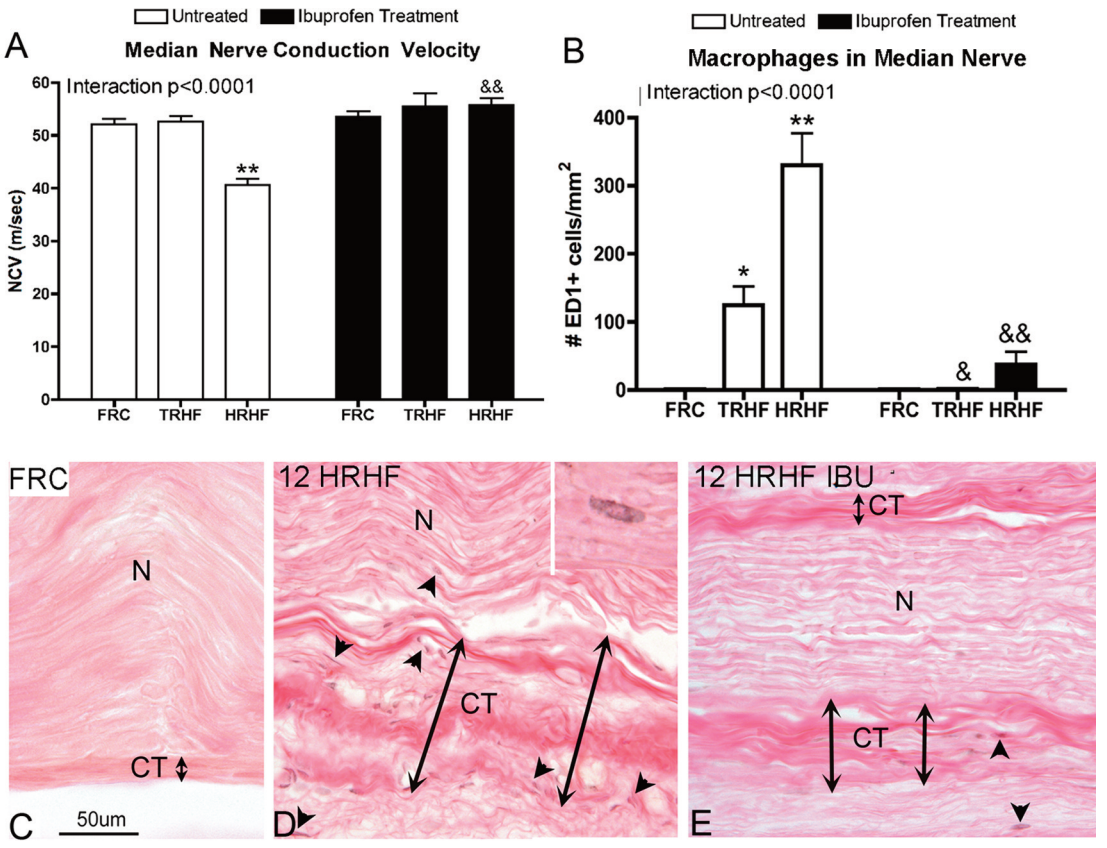

Figure 7. Changes in the median nerve in the carpal tunnel. (A) Nerve conduction velocity (NCV) in meters/second (m/sec), measured electrophysiologically. (B) Mean number of ED1+ in media nerve at the level of the wrist. (C-E) Representative microscopic photos showing width of epineurial connective tissues (CT) located around median nerve (N) at wrist level (double arrows). Arrowheads indicate ED1+ macrophages (detected immunohistochemically). Eosin counterstain. Each photo in C-E was taken at same magnification; thus, the scale bar is the same for panels C through E. Symbols: *:p<0.05 and **:p<0.01, compared to FRC rats; &:p<0.05 and &&:p<0.01, compared to untreated HRHF rats.

production of these inflammatory cytokines both locally in loaded bones, and systemically in serum; these increases were prevented by ibuprofen treatment in the HRHF rats, despite continued task performance, as supported by the significant interaction effects.

Evidence of carpal tunnel syndrome with HRHF task

Next, we examined TRHF and HRHF rats for indicators of carpal tunnel syndrome, since we have previously observed reduced conduction velocity in the median nerve with associated increases in pain behaviors[38-41]. We observed a low-grade decline of 15% in median nerve conduction velocity (NCV) in HRHF rats that was attenuated by ibuprofen treatment (Figure 7A; the interaction effect was p<0.0001). Ibuprofen treatment also reduced a task-induced increase in the number of ED1+ macrophages in both TRHF+IBU and HRHF+IBU rats, compared to untreated HRHF rats (Figures 7B-E; the interaction effect was p<0.0001). A mild level of extraneural neural connective tissue was evident in HRHF rats (Figure 7D), compared to FRC rats (Figure 7C). This increase was only partially attenuated in the HRHF+IBU, (compare Figures 7E to 7D). No axonal swellings, myelin degradation visible using H&E staining, or visible nerve disruption, were observed in the median nerves of any group (Figures 7C-D), indicating that frank axonal damage was not present at the time of tissue collection. These results combined with the muscle findings indicate that the 15% reduction in nerve conduction was not great enough to reduce muscle function in HRHF rats (Figure 6A), although the reduced nerve inflammation shown in Figures 7B and E) likely reduced discomfort, and increased voluntary muscle pulling force in HRHF+IBU rats (Figure 6A).

Discussion

In this study, several indicators of trabecular bone adaptation in forelimb bones and increased serum osteocalcin in TRHF rats were observed, indicating that short time periods of progressively increased loading to high force levels by week 5 induced net bone adaptation. In contrast, performance of a HRHF task for 12 weeks (in which voluntary muscle pulling forces remained constant in untreated HRHF rats) led to reduced trabecular bone quality and bone mineral density in dis-

tal forelimb bones, and a net loss of bone. Systemic anti-inflammatory treatment with ibuprofen prevented these bone catabolic changes. Ibuprofen treatment also prevented HRHF-induced increases in bone and serum inflammatory cytokines, osteoclast numbers, and nerve inflammation, as well as HRHF-induced declines in median nerve conduction velocity. The mean voluntary pulling force was increased in the HRHF+IBU rats, compared to FRC+IBU rats. In contrast, morphological changes in the flexor digitorum muscle were similar in both HRHF and HRHF+IBU rats, with each showing similar mean increases in myofiber cross-sectional areas and low numbers of atrophied myofibers with internal macrophages. No groups showed visible signs of median nerve injury, or differences in weight loss. The similar changes in muscle and nerve morphology, and body weight in the HRHF and HRHF+IBU rats rules out these as contributing factors to the observed changes in bone structure. Furthermore, the constant level of pulling forces in the untreated HRHF rats, rules out muscle function as a contributing factor to the observed changes in bone structure in untreated HRHF rats. Since there were many significant effects of group x treatment, these results suggest that bone catabolism in the untreated HRHF rats was the results of increased osteoclasts and inflammatory cytokines. Eight weeks of continual ibuprofen treatment prevented this catabolism, by reducing, nerve and bone inflammatory responses, and by reducing osteoclast numbers and activity, despite continued task performance. The improved muscle pulling forces and preservation of nerve conduction velocity in HRHF+IBU rats were not due to HRHF specific morphological changes in muscle or nerve, but were likely related to the prevention of median nerve inflammatory responses in HRHF+IBU rats.

It was interesting to see that short-term loading in the TRHF rats induced bone adaptation; evident as increased trabecular bone volume and number in the distal ulna epiphysis, increased osteoblasts in the distal radial metaphysis, and increased serum osteocalcin. In contrast, only a few indices of bone resorptive changes were observed in the TRHF rats (increased osteoclasts and serum CTX1). Thus, bone adaptive responses were concomitant with resorptive responses, with the former being greater, by the end of the training period in TRHF rats. During training, rats work for 10 min/day, 5 days/week, for 5 days to learn the HRHF task, which translates as ramping upwards from no reaching at all initially, to first 1% maximum pulling force by the end of week 1, 5% (0.1 Newton's) by the end of week 2, 15% (0.29 Newton's) by the end of week 3, 30% (0.58 Newton's) by the end of week 4, and 60% maximum pulling force (1.93 Newton's) by the end of week 5. This progressive level of activity was apparently enough to stimulate net bone formation, despite the increase in bone inflammatory cytokines observed in TRHF rats after the training period. These results match our prior findings of increased production of a matrix protein (periostin-like-factor) associated with tissue repair concomitant with bone adaptation in TRHF rats and with 3 to 9-weeks of HRHF loading[37], although this protein decreased coincident with prolonged high levels of several inflammatory cytokines and increased serum TRAP5b in 12-week HRHF rats[35,65]. We have also observed qualitative signs of bone adaptation in rats performing a moderate demand task of high repetition and low force for 12 weeks[34]. Collectively, these results from our model indicate that performance of moderate demand occupational tasks for 12 weeks, or high demand tasks for short time periods, leads to bone adaptation.

In contrast, we observed only limited adaptation in the 12-week HRHF rats (only increased trabecular thickness and osteoblasts in the distal radial metaphysis), rats that were performing a high force loading task of 42% of their maximum pulling force (high force loading being defined as >30% of maximum pulling forces[6,66]). Instead, many indicators of bone resorption were observed in the HRHF rats, including decreased trabecular bone volume density in the radial and ulnar epiphyses and metaphyses, increased osteoclasts and decreased bone mineral density in the distal radius, increased serum Trap5b and CTX1, and increased inflammatory cytokines both locally (in these bones) and systemically. Thus, indices of osteoclast-related bone resorption were greater than adaptive changes in the untreated 12-week HRHF rats, leading to net bone resorption.

Results of this study are consistent with these past studies, and support a cumulative overload hypothesis in bones leading to a reduction of tissue tolerance with continued overloading[6,7,67-69]. Bone is known to respond to loading along a continuum ranging from anabolism to catabolism, depending on the magnitude, frequency and duration of loading[9-11,70-72]. Repetitive loading conditions, such as in studies of rats running on treadmills, performing repetitive jumping, and performing repetitive loading at high force loads, show that increasing the intensity of weight-bearing or muscle loading exercise/activities may be associated with diminishing returns in bone morphology, such as declines in bone mass and quality[12,37,73-76].

Increased levels of bone IL-1beta and TNF-alpha, such as seen in this study, are known to stimulate osteoclastogenesis and activity[23,24]. A strong role for task-induced inflammatory processes in muscle and bone tissues is supported in our model. We have previously shown that a 2-week treatment with anti-rat TNFalpha or an 8-week treatment with ibuprofen reduces a HRHF-induced increase in bone inflammatory cytokines, and enhances voluntary muscle loading (i.e., the voluntary pulling forces, as shown here)[35,36,46]. The ibuprofen treatment also preserved articular cartilage integrity at radiocarpal joints, despite continued bone loading at high cyclical high force loads[35]. In this study, ibuprofen treatment preserved trabecular microarchitecture and bone mineral density, and enhanced trabecular thickness in the distal ulna epiphyses. These findings match results by others showing that non-steroidal anti-inflammatory drug treatment inhibits bone resorption and aids bone healing[77-79].

Declines in bone structure in untreated HRHF rats were not due to declines in muscle function, since they pulled consistently across the 12 weeks of task performance. However, the ibuprofen treatment improved voluntary pulling force in HRHF+IBU rats. In fact, the highest voluntary pulling forces were observed in week 12 HRHF+IBU rats. These latter find-

ings are suggestive of task-induced discomfort occurring as a result of increased inflammatory cytokines in the flexor digitorum muscles, findings reported previously[36]. We have reported that ibuprofen treatment of HRHF rats improved reflexive grip strength, as did treatment of rats with an anti-TNFalpha antibody[36,46,67], further supportive of an inflammatory component to muscle function with repetitive tasks. Thus, muscular function appear to be influenced by inflammatory responses occurring in tissues and perhaps also in sera, as shown previously[33,67].

Myofiber size increased with training, and with HRHF task performance (in both the HRHF and HRHF+IBU groups). HRHF and HRHF+IBU rat muscles also had low increases of atrophied myofibers containing internal macrophages, indicative of subdegenerative muscle changes. Since these changes were occurring in both groups, these subdegenerative muscle changes are likely due to fatigue failure effects[7,8]. Because muscle and bone are biomechanically linked[70,80], it is often assumed that greater physical strength is associated with a greater load on the bone, and corresponding increases in bone mass[81,82]. A few studies have shown site-specific correlations between grip strength and bone mineral density in the radius of non-athletic women[58], young athletes (wrestlers and basketball players)[83], and males[56]. However, one study showed that factors other than muscle size accounted for 12-16% of the variance in differences in bone traits, such as bone mass[81]. These authors concluded that other factors associated with loading that are distinct from muscle size contribute to bone adaptive responses. Since similar changes in muscle morphology were observed in the HRHF and HRHF+IBU rats, our results also indicate that other factors contribute to changes in bone mass, in our case, osteoclast activity and inflammatory changes occurring in not only bone but also in muscles and nerves.

The early onset and then eight weeks of ibuprofen treatment prevented the development of nerve inflammation and declines in conduction velocity in the HRHF+IBU, and partially attenuated nerve fibrosis in these rats. We have previously reported signs and symptoms of carpal tunnel syndrome in our model, with declines in nerve conduction velocity, and increased nerve inflammation and pain behaviors in 12-week HRHF rats[38]. A two week treatment of ibuprofen reduced fibrogenic proteins levels and fibrosis in flexor digitorum muscles of HRHF rats[67], supportive of an inflammatory mechanism to the nerve fibrosis observed in this study. We can rule out a contribution from nerve injury, since no signs of axonal swelling, myelin degradation, or gross nerve disruption were observed in the median nerves of any group.

Lastly, the observed differences between the ulna and radius are likely due to anatomical differences, since the radius has a direct articulation with the carpal bones, whereas the forces applied to the ulna are transmitted and distributed across the interosseus membrane to the radius. We should also note that the observed increases in serum osteocalcin and CTX-1 could be occurring at any bone site involved in task performance, such as the metacarpal bones, diaphysis of forelimb bones, or humerus. Therefore, one limitation of this study is that we did not examine other bony sites of the upper extremity for either adaptive or resorptive bone changes. This should be a topic of future studies, since prior studies by Kuiper and colleagues has shown that serum levels of biomarkers of collagen type I turnover, including CTX1, alter with prolonged occupational loading at high physical demands, and are associated with vertebral column shrinkage[84,85]. Another limitation of this study is its length of 5 weeks of training and then 3 months of task performance. This time frame allowed us to determine the effects of inflammation early in the process of upper extremity overuse injury with nerve involvement. However, patients treated for carpal tunnel syndrome typically have had symptoms for years, and have sometimes reached the state of muscle atrophy and wasting by the time of surgical intervention. Thus, our findings of the usefulness of ibuprofen treatment should be considered in that light.

In conclusion, trabecular bone adaptation was observed in TRHF rats, despite increased levels of bone inflammatory cytokines, indicative of a muscle loading mechanism with short-term duration loading at progressively increasing high force loads. In contrast, 12 weeks of HRHF task-induced declines in trabecular bone volume and structure was linked to inflammatory mechanisms in the form of increased inflammatory cytokines and increased osteoclast numbers and activity, but not muscle loading as that was constant in the untreated HRHF rats across the 12 weeks of task performance. We were also able to rule out changes in muscle and nerve morphology, or weight loss as contributing factors to the observed changes in bone structure. Provision of a non-steroidal anti-inflammatory drug during weeks 5-12 of this 12 week task preserved trabecular bone volume and structure, and even allowed for increase in trabecular thickness in the ulnar metaphysis (although no net bone formation in the form of increased bone volume). Thus in our model, bone structure is maintained and may even exhibit some adaptation when inflammatory processes were suppressed, despite continued bone loading at high repetition high force loads in this task paradigm.

Acknowledgements

Research reported in this publication was supported by the National Institute of Arthritis and Musculoskeletal and Skin Diseases of the National Institutes of Health under Award Number AR056019 to MFB and AR051212 to AEB. The content is solely the responsibility of the authors and does not necessarily represent the official views of the National Institutes of Health. We would like to thank Michelle Harris for her contribution to the animal training and testing, Shreya Amin for sectioning the tissues, and Mamta Amin for performing the ELISA assays.

References

1. Bureau of Labor Statistics. Nonfatal ocupational injuries and illnesses requiring days away from work, 2011. http://www.bls.gov/news.release/osh2.nr0.htm. News Release USDL-12-2204, November 8, 2012.
2. Werner RA, Franzblau A, Gell N, Ulin SS, Armstrong TJ. Predictors of upper extremity discomfort: a longitudinal

study of industrial and clerical workers. Journal of occupational rehabilitation 2005;15(1):27-35.
3. Bernard B. Musculoskeletal disorders and workplace factors. NIOSH Report 97-141, National Institute for Occupational Safety and Health, Cincinatti, Ohio, USA, 1997.
4. Srilatha MAG, Bhat V, Sathiakumar N. Prevalence of Work-Related Wrist and Hand Musculoskeletal Disorders (WMSD) among Computer Users, Karnataka State, India. Journal of Clinical and Diagnostic Research 2011; 5(3):605-607.
5. Ratzlaff CR, Gillies JH, Koehoorn MW. Work-related repetitive strain injury and leisure-time physical activity. Arthritis and rheumatism 2007;57(3):495-500.
6. Silverstein BA, Fine LJ, Armstrong TJ. Hand wrist cumulative trauma disorders in industry. British journal of industrial medicine 1986;43(11):779-784.
7. Gallagher S, Heberger JR. Examining the interaction of force and repetition on musculoskeletal disorder risk: a systematic literature review. Human factors 2013; 55(1):108-124.
8. Barbe MF, Gallagher S, Massicotte VS, Tytell M, Popoff SN, Barr-Gillespie AE. The interaction of force and repetition on musculoskeletal and neural tissue responses and sensorimotor behavior in a rat model of work-related musculoskeletal disorders. BMC Musculoskelet Disord 2013;14(1):303.
9. Rubin C, Turner AS, Muller R, et al. Quantity and quality of trabecular bone in the femur are enhanced by a strongly anabolic, noninvasive mechanical intervention. Journal of bone and mineral research : the official journal of the American Society for Bone and Mineral Research 2002; 17(2):349-357.
10. Gross TS, Srinivasan S. Building bone mass through exercise: could less be more? British journal of sports medicine 2006;40(1):2-3; discussion 2-3.
11. Srinivasan S, Weimer DA, Agans SC, Bain SD, Gross TS. Low-magnitude mechanical loading becomes osteogenic when rest is inserted between each load cycle. Journal of bone and mineral research : the official journal of the American Society for Bone and Mineral Research 2002;17(9):1613-1620.
12. Bourrin S, Genty C, Palle S, Gharib C, Alexandre C. Adverse effects of strenuous exercise: a densitometric and histomorphometric study in the rat. Journal of applied physiology 1994;76(5):1999-2005.
13. Solovieva S, Vehmas T, Riihimaki H, Luoma K, Leino-Arjas P. Hand use and patterns of joint involvement in osteoarthritis. A comparison of female dentists and teachers. Rheumatology 2005;44(4):521-528.
14. Ding H, Solovieva S, Vehmas T, Takala EP, Leino-Arjas P. Hand osteoarthritis and pinch grip strength among middle-aged female dentists and teachers. Scandinavian journal of rheumatology 2010;39(1):84-87.
15. Kalichman L, Hernandez-Molina G. Hand osteoarthritis: an epidemiological perspective. Seminars in arthritis and rheumatism 2010;39(6):465-476.
16. Amorim BJ, Etchebehere EC, Dalla Torre G, et al. Low sensitivity of three-phase bone scintigraphy for the diagnosis of repetitive strain injury. Sao Paulo medical journal = Revista paulista de medicina 2006;124(3):145-149.
17. al-Nahhas AM, Jawad AS, McCready VR, Kedar R. Detection of increased blood flow to the affected arm in repetitive strain injury with radionuclide and Doppler ultrasound studies. A case report. Clinical nuclear medicine 1995;20(7):615-618.
18. al-Nahhas AM, Jawad AS, Norman A, McCready VR. 99Tcm-MDP blood-pool phase in the assessment of repetitive strain injury. Nuclear medicine communications 1997; 8(10):927-931.
19. Erselcan T, Topalkara K, Nacitarhan V, Akyuz A, Dogan D. Carpal tunnel syndrome leads to significant bone loss in metacarpal bones. Journal of bone and mineral metabolism 2001;19(5):317-320.
20. Schorn D, Hoskinson J, Dickson RA. Bone density and the carpal tunnel syndrome. The Hand 1978;10(2):184-186.
21. Hasegawa Y, Schneider P, Reiners C. Age, sex, and grip strength determine architectural bone parameters assessed by peripheral quantitative computed tomography (pQCT) at the human radius. Journal of biomechanics 2001; 34(4):497-503.
22. Desrosiers J, Hebert R, Bravo G, Rochette A. Age-related changes in upper extremity performance of elderly people: a longitudinal study. Experimental gerontology 1999; 34(3):393-405.
23. Kulkarni RN, Bakker AD, Everts V, Klein-Nulend J. Mechanical loading prevents the stimulating effect of IL-1beta on osteocyte-modulated osteoclastogenesis. Biochemical and biophysical research communications 2012;420(1):11-16.
24. Nanes MS. Tumor necrosis factor-alpha: molecular and cellular mechanisms in skeletal pathology. Gene 2003; 321:1-15.
25. Carp SJ, Barbe MF, Winter KA, Amin M, Barr AE. Inflammatory biomarkers increase with severity of upper-extremity overuse disorders. Clinical science 2007; 112(5):305-314.
26. Rechardt M, Shiri R, Matikainen S, Viikari-Juntura E, Karppinen J, Alenius H. Soluble IL-1RII and IL-18 are associated with incipient upper extremity soft tissue disorders. Cytokine 2011;54(2):149-153.
27. Riondino S, La Farina F, Martini F, Guadagni F, Ferroni P. Functional impairment in video terminal operators is related to low-grade inflammation. International archives of occupational and environmental health 2011; 84(7):745-751.
28. Gold JE, Mohamed FB, Ali S, Barbe MF. Serum and MRI Biomarkers in Mobile Device Texting: A Pilot Study. Human Factors 2013; In Press.
29. Li YP, Stashenko P. Proinflammatory cytokines tumor necrosis factor-alpha and IL-6, but not IL-1, down-regulate the osteocalcin gene promoter. Journal of immunology 1992;148(3):788-794.
30. Gowen M, Wood DD, Ihrie EJ, McGuire MK, Russell RG. An interleukin 1 like factor stimulates bone resorption *in vitro*. Nature 1983;306(5941):378-380.
31. Heath JK, Saklatvala J, Meikle MC, Atkinson SJ,

Reynolds JJ. Pig interleukin 1 (catabolin) is a potent stimulator of bone resorption *in vitro*. Calcified tissue international 1985;37(1):95-97.
32. Barbe MF, Barr AE, Gorzelany I, Amin M, Gaughan JP, Safadi FF. Chronic repetitive reaching and grasping results in decreased motor performance and widespread tissue responses in a rat model of MSD. J Orthop Res 2003; 21(1):167-176.
33. Barbe MF, Elliott MB, Abdelmagid SM, et al. Serum and tissue cytokines and chemokines increase with repetitive upper extremity tasks. J Orthop Res 2008;26(10):1320-1326.
34. Barr AE, Safadi FF, Gorzelany I, Amin M, Popoff SN, Barbe MF. Repetitive, negligible force reaching in rats induces pathological overloading of upper extremity bones. J Bone Miner Res 2003;18(11):2023-2032.
35. Driban JB, Barr AE, Amin M, Sitler MR, Barbe MF. Joint inflammation and early degeneration induced by high-force reaching are attenuated by ibuprofen in an animal model of work-related musculoskeletal disorder. J Biomed Biotechnol 2011;2011:691412.
36. Rani S, Barbe MF, Barr AE, Litivn J. Role of TNF alpha and PLF in bone remodeling in a rat model of repetitive reaching and grasping. Journal of cellular physiology 2010;225(1):152-167.
37. Rani S, Barbe MF, Barr AE, Litvin J. Periostin-like-factor and Periostin in an animal model of work-related musculoskeletal disorder. Bone 2009;44(3):502-512.
38. Clark BD, Al-Shatti TA, Barr AE, Amin M, Barbe MF. Performance of a high-repetition, high-force task induces carpal tunnel syndrome in rats. J Orthop Sports Phys Ther 2004;34(5):244-253.
39. Clark BD, Barr AE, Safadi FF, et al. Median nerve trauma in a rat model of work-related musculoskeletal disorder. J Neurotrauma 2003;20(7):681-695.
40. Elliott MB, Barr AE, Clark BD, Amin M, Amin S, Barbe MF. High force reaching task induces widespread inflammation, increased spinal cord neurochemicals and neuropathic pain. Neuroscience 2009;158(2):922-931.
41. Elliott MB, Barr AE, Clark BD, Wade CK, Barbe MF. Performance of a repetitive task by aged rats leads to median neuropathy and spinal cord inflammation with associated sensorimotor declines. Neuroscience 2010; 170(3):929-941.
42. Gerr F, Marcus M, Ensor C, et al. A prospective study of computer users: I. Study design and incidence of musculoskeletal symptoms and disorders. American journal of industrial medicine 2002;41(4):221-235.
43. Centers for disease control and prevention. Percentage of employed adults* aged 18-64 years who had carpal tunnel syndrome† in the past 12 months, by sex and age group - National Health Interview Survey, 2010. 2011; http://www.cdc.gov/mmwr/preview/mmwrhtml/mm6049a4.htm. Accessed December 16, 2011, December 16, 2011.
44. Bureau of Labor Statistics. Injuries, Illnesses, and Fatalities, 2013. http://www.bls.gov/iif/oshfaq1.htm. News Release 2013.
45. Fedorczyk JM, Barr AE, Rani S, et al. Exposure-dependent increases in IL-1beta, substance P, CTGF, and tendinosis in flexor digitorum tendons with upper extremity repetitive strain injury. Journal of orthopaedic research : official publication of the Orthopaedic Research Society 2010;28(3):298-307.
46. Kietrys DM, Barr AE, Barbe MF. Exposure to repetitive tasks induces motor changes related to skill acquisition and inflammation in rats. Journal of motor behavior 2011; 43(6):465-476.
47. Adams SS, Bough RG, Cliffe EE, et al. Some aspects of the pharmacology, metabolism, and toxicology of ibuprofen. I. Pharmacology and metabolism. Rheumatol Phys Med 1970;10:(Suppl 10):19-26.
48. Brennan T, Adapala NS, Barbe MF, Yingling V, Sanjay A. Abrogation of Cbl-PI3K interaction increases bone formation and osteoblast proliferation. Calcif Tissue Int 2011;89(5):396-410.
49. Joshi RN, Safadi FF, Barbe MF, Del Carpio-Cano F, Popoff SN, Yingling VR. Different effects on bone strength and cell differentiation in pre pubertal caloric restriction versus hypothalamic suppression. Bone 2011; 49(4):810-818.
50. Lambi AG, Pankratz TL, Mundy C, et al. The skeletal site-specific role of connective tissue growth factor in prenatal osteogenesis. Dev Dyn 2012;241(12):1944-1959.
51. Bouxsein ML, Boyd SK, Christiansen BA, Guldberg RE, Jepsen KJ, Muller R. Guidelines for assessment of bone microstructure in rodents using micro-computed tomography. Journal of bone and mineral research : the official journal of the American Society for Bone and Mineral Research 2010;25(7):1468-1486.
52. Delcour M, Russier M, Xin DL, Massicotte VS, Barbe MF, Coq JO. Mild musculoskeletal and locomotor alterations in adult rats with white matter injury following prenatal ischemia. International journal of developmental neuroscience : the official journal of the International Society for Developmental Neuroscience 2011;29(6):593-607.
53. Baker BA, Mercer RR, Geronilla KB, Kashon ML, Miller GR, Cutlip RG. Stereological analysis of muscle morphology following exposure to repetitive stretch-shortening cycles in a rat model. Applied physiology, nutrition, and metabolism = Physiologie appliquee, nutrition et metabolisme 2006;31(2):167-179.
54. Barbe MF, Barr AE, Gorzelany I, Amin M, Gaughan JP, Safadi FF. Chronic repetitive reaching and grasping results in decreased motor performance and widespread tissue responses in a rat model of MSD. J Orthop Res 2003; 21(1):167-176.
55. Bove GM, Weissner W, Barbe MF. Long lasting recruitment of immune cells and altered epi-perineurial thickness in focal nerve inflammation induced by complete Freund's adjuvant. Journal of neuroimmunology 2009; 213(1-2):26-30.
56. Aydin G, Atalar E, Keles I, et al. Predictive value of grip strength for bone mineral density in males: site specific or systemic? Rheumatology international 2006; 27(2):125-129.
57. Tsuji S, Tsunoda N, Yata H, Katsukawa F, Onishi S, Yamazaki H. Relation between grip strength and radial bone

mineral density in young athletes. Archives of physical medicine and rehabilitation 1995;76(3):234-238.
58. Sinaki M, Wahner HW, Offord KP. Relationship between grip strength and related regional bone mineral content. Archives of physical medicine and rehabilitation 1989; 70(12):823-826.
59. Bauer DC, Browner WS, Cauley JA, et al. Factors associated with appendicular bone mass in older women. The Study of Osteoporotic Fractures Research Group. Annals of internal medicine 1993;118(9):657-665.
60. Osei-Hyiaman D, Ueji M, Toyokawa S, Takahashi H, Kano K. Influence of grip strength on metacarpal bone mineral density in postmenopausal Japanese women: a cross-sectional study. Calcified tissue international. Mar 1999;64(3):263-266.
61. Turner CH. Muscle-bone interactions, revisited. Bone 2000;27(3):339-340.
62. Hauret KG, Jones BH, Bullock SH, Canham-Chervak M, Canada S. Musculoskeletal injuries description of an under-recognized injury problem among military personnel. American journal of preventive medicine 2010;38(1 Suppl):S61-70.
63. Gowen M, Mundy GR. Actions of recombinant interleukin 1, interleukin 2, and interferon-gamma on bone resorption *in vitro*. Journal of immunology 1986;136(7):2478-2482.
64. Gowen M, Nedwin GE, Mundy GR. Preferential inhibition of cytokine-stimulated bone resorption by recombinant interferon gamma. Journal of bone and mineral research : the official journal of the American Society for Bone and Mineral Research 1986;1(5):469-474.
65. Rani S, Barbe MF, Barr AE, Litvin J. Induction of periostin-like factor and periostin in forearm muscle, tendon, and nerve in an animal model of work-related musculoskeletal disorder. The journal of histochemistry and cytochemistry: official journal of the Histochemistry Society 2009;57(11):1061-1073.
66. Barr AE, Barbe MF. Pathophysiological tissue changes associated with repetitive movement: a review of the evidence. Phys Ther 2002;82(2):173-187.
67. Abdelmagid SM, Barr AE, Rico M, et al. Performance of repetitive tasks induces decreased grip strength and increased fibrogenic proteins in skeletal muscle: role of force and inflammation. PLoS One 2012;7(5):e38359.
68. Di Domizio J, Keir PJ. Forearm posture and grip effects during push and pull tasks. Ergonomics 2010;53(3):336-343.
69. Barr AE, Barbe MF. Inflammation reduces physiological tissue tolerance in the development of work-related musculoskeletal disorders. Journal of electromyography and kinesiology: official journal of the International Society of Electrophysiological Kinesiology 2004;14(1):77-85.
70. Gross TS, Poliachik SL, Prasad J, Bain SD. The effect of muscle dysfunction on bone mass and morphology. Journal of musculoskeletal & neuronal interactions 2010; 10(1):25-34.
71. Bentley VA, Sample SJ, Livesey MA, et al. Morphologic changes associated with functional adaptation of the navicular bone of horses. Journal of anatomy 2007;211(5):662-672.
72. Danova NA, Colopy SA, Radtke CL, et al. Degradation of bone structural properties by accumulation and coalescence of microcracks. Bone 2003;33(2):197-205.
73. Newhall KM, Rodnick KJ, van der Meulen MC, Carter DR, Marcus R. Effects of voluntary exercise on bone mineral content in rats. Journal of bone and mineral research : the official journal of the American Society for Bone and Mineral Research 1991;6(3):289-296.
74. Raab DM, Smith EL, Crenshaw TD, Thomas DP. Bone mechanical properties after exercise training in young and old rats. Journal of applied physiology 1990;68(1):130-134.
75. Umemura Y, Ishiko T, Yamauchi T, Kurono M, Mashiko S. Five jumps per day increase bone mass and breaking force in rats. Journal of bone and mineral research: the official journal of the American Society for Bone and Mineral Research 1997;12(9):1480-1485.
76. Lacourt M, Gao C, Li A, et al. Relationship between cartilage and subchondral bone lesions in repetitive impact trauma-induced equine osteoarthritis. Osteoarthritis and cartilage / OARS, Osteoarthritis Research Society 2012; 20(6):572-583.
77. O'Connor JP, Lysz T. Celecoxib, NSAIDs and the skeleton. Drugs of today 2008;44(9):693-709.
78. Votta BJ, Bertolini DR. Cytokine suppressive anti-inflammatory compounds inhibit bone resorption *in vitro*. Bone 1994;15(5):533-538.
79. Bertolini DR, Votta B, Hoffman S, Strassmann G. Interleukin 6 production in fetal rat long bone cultures is correlated with PGE2 release and does not correlate with the extent of bone resorption. Cytokine 1994;6(4):368-375.
80. Edwards M, Gregson C, Patel H, et al. Muscle size, strength and physical performance and their associations with bone structure in the Hertfordshire Cohort Study. Journal of bone and mineral research 2013;28(11):2295-304.
81. Daly RM, Saxon L, Turner CH, Robling AG, Bass SL. The relationship between muscle size and bone geometry during growth and in response to exercise. Bone 2004; 34(2):281-287.
82. Schoenau E, Frost HM. The "muscle-bone unit" in children and adolescents. Calcified tissue international 2002; 70(5):405-407.
83. Chan DC, Lee WT, Lo DH, Leung JC, Kwok AW, Leung PC. Relationship between grip strength and bone mineral density in healthy Hong Kong adolescents. Osteoporosis international: a journal established as result of cooperation between the European Foundation for Osteoporosis and the National Osteoporosis Foundation of the USA 2008;19(10):1485-1495.
84. Kuiper JI, van Dieen JH, Everts V, Verbeek JH, Frings-Dresen MH. Associations between serum markers of collagen metabolism and spinal shrinkage. Clinical biomechanics 2004;19(2):209-212.
85. Kuiper JI, Verbeek JH, Everts V, Straub JP, Frings-Dresen MH. Serum markers of collagen metabolism: construction workers compared to sedentary workers. Occupational and environmental medicine 2005;62(6):363-367.

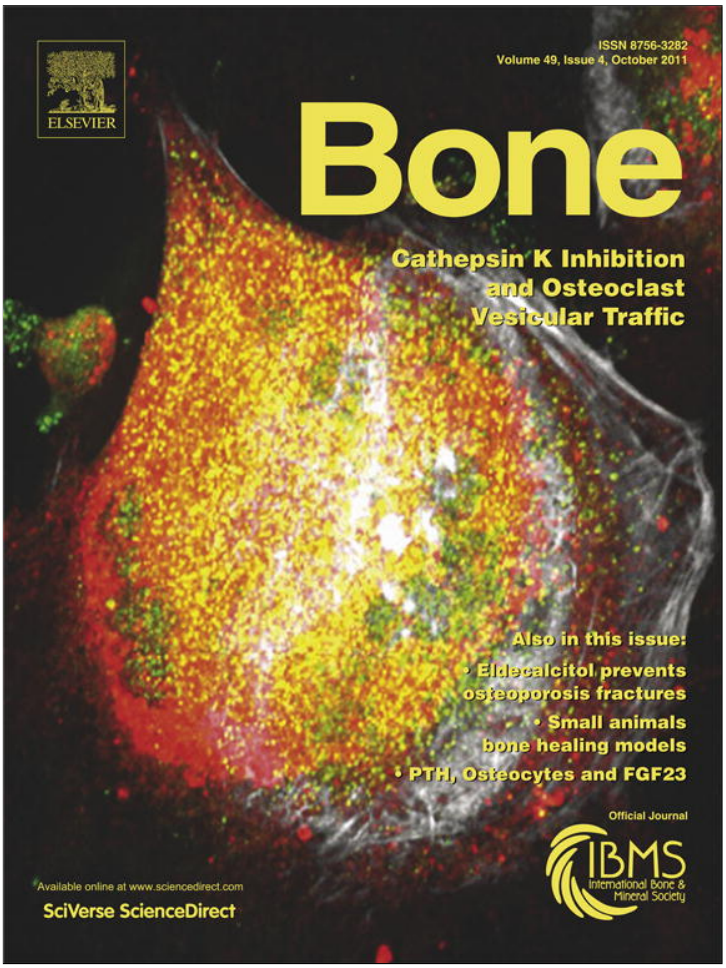

Bone 49 (2011) 810–818

Contents lists available at ScienceDirect

Bone

journal homepage: www.elsevier.com/locate/bone

Different effects on bone strength and cell differentiation in pre pubertal caloric restriction versus hypothalamic suppression☆,☆☆

R.N. Joshi [a], F.F. Safadi [b], M.F. Barbe [b], Fe Del Carpio-Cano [b], S.N. Popoff [b], V.R. Yingling [a,*]

[a] Department of Kinesiology, Temple University, Philadelphia, PA, 19122, USA
[b] Department of Anatomy and Cell Biology, Temple University, Philadelphia, PA, 19140, USA

ARTICLE INFO

Article history:
Received 22 December 2010
Revised 14 June 2011
Accepted 14 July 2011
Available online 23 July 2011

Edited by: Bjorn Olsen

Keywords:
Rodent
Delayed puberty
Caloric restriction
GnRH antagonist
Bone strength

ABSTRACT

Hypothalamic amenorrhea and energy restriction during puberty affect peak bone mass accrual. One hypothesis suggests energy restriction alters hypothalamic function resulting in suppressed estradiol levels leading to bone loss. However, both positive and negative results have been reported regarding energy restriction and bone strength. Therefore, the purpose of this study was to investigate energy restriction and hypothalamic suppression during pubertal onset on bone mechanical strength and the osteogenic capacity of bone marrow-derived cells in two models: female rats treated with gonadotropin releasing hormone antagonists (GnRH-a) or 30% energy restriction. At 23 days of age, female Sprague Dawley rats were assigned to three groups: control group (C, n = 10), GnRH-a group (n = 10), and Energy Restriction (ER, n = 12) group. GnRH-a animals received daily injections for 27 days. The animals in the ER group received 70% of the control animals' intake. After sacrifice (50 days of age), body weight, uterine and muscle weights were measured. Bone marrow-derived stromal cells were cultured and assayed for proliferation and differentiation into osteoblasts. Outcome measures included bone strength, bone histomorphometry and architecture, serum IGF-1 and osteocalcin. GnRH-a suppressed uterine weight, decreased osteoblast proliferation, bone strength, trabecular bone volume and architecture compared to control. Elevated serum IGF-1 and osteocalcin levels and body weight were found. The ER model had an increase in osteoblast proliferation compared to the GnRH-a group, similar bone strength relative to body weight and increased trabecular bone volume in the lumbar spine compared to control. The ER animals were smaller but had developed bone strength sufficient for their size. In contrast, suppressed estradiol via hypothalamic suppression resulted in bone strength deficits and trabecular bone volume loss. In summary, our results support the hypothesis that during periods of nutritional stress the increased vertebral bone volume may be an adaptive mechanism to store mineral which differs from suppressed estradiol resulting from hypothalamic suppression.

Introduction

Pubertal timing is a key factor that contributes to optimal bone accrual and thus bone strength [1,2]. Bone mass doubles during the onset of puberty [3] with more than 90% of peak bone mass accrued by the end of the second decade of life [4]. However, reproductive abnormalities such as delayed puberty (primary amenorrhea) result in suboptimal bone gain and increased incidence of stress fracture [5,6].

Delayed puberty (primary amenorrhea) and/or secondary amenorrhea are highly prevalent in athletes [7–9], dancers [2,10,11] and patients with anorexia nervosa (AN) [12–14]. An association between eating disorders and reproductive abnormalities (amenorrhea) has been established [15]. Energy deficient conditions both in the long term [16,17] and short term [18–21] have been reported to affect reproductive function. Furthermore, disordered eating and menstrual irregularities are associated with decreased estrogen levels [19,22,23] and lower bone mineral density (BMD) [6,24]. A current hypothesis is that energy deficiency results in hypothalamic suppression that can then affect the reproductive axis, estrogen levels and bone accrual [25] and suboptimal bone accrual is a strong risk factor for post menopausal fracture.

An incomplete recovery of bone mass following treatment (estrogen supplementation) in young women with hypothalamic amenorrhea associated with anorexia or exercise suggests that factors other than estrogen suppression may be involved in bone loss [26–28]. Estrogen replacement therapies have been shown to result in weight gain or menses resumption, but do not result in complete bone mass recovery

☆ Funding for this project was provided by College of Health Professions and Social Work Dean's Incentive Research Grant.
☆☆ Presented in part at the, American Society for Bone and Mineral Research ASBMR 30th Annual Meeting, Montreal, QB. September 12–16, 2008. 4th Asia West Pacific regional conference of World Confederation for Physical Therapy (WCPT), Mumbai, India. January 22–25, 2009. American Society for Bone and Mineral Research ASBMR 31st Annual Meeting, Colorado, CO. September 12–16, 2009.
* Correspondence author at: Department of Kinesiology, Temple University, 121 Pearson Hall, Broad Street and Montgomery Avenue, USA. Fax: +1 215 204 4414.
E-mail address: yingling@temple.edu (V.R. Yingling).

8756-3282/$ – see front matter © 2011 Elsevier Inc. All rights reserved.
doi:10.1016/j.bone.2011.07.019

[29]. Nutritional therapy has been used to counter bone loss in anorexic women however in a group regaining 90% of their initial body weight there was still a sub-group of women that did not regain menses or recover their bone mass [28]. A study in humans investigating the interaction of energy restriction and low estrogen included a group of women with low bone mass that were estrogen deficient but energy replete suggesting that estrogen suppression can result from causes other than energy restriction [30]. The interaction of reproductive irregularities, energy restriction and bone accrual is complex and both estrogen dependent [19,22,23] and estrogen independent [31] mechanisms of bone loss have been hypothesized.

Models of energy restriction (ER) have not always had negative consequences on bone mass and structure. Young male rats exposed to 35% food restriction had no change in bone strength when normalized by body weight [32]. Caloric restriction in mice that were older than 1 year may in fact delay age-related bone loss and maintain the proliferative potential of certain cell types [33]. Interestingly caloric restriction in 6 month old male mice resulted in increased trabecular number and lower bone cross-sectional area, a bone phenotype analogous to juvenile mice (3 months old) [34]. Significant decreases in bone mass have resulted from energy restriction models of 40–50% but primarily in older animals ranging from 10 to 17 months of age [35].

Both estrogen suppression and energy restriction affect bone loss, but the mechanisms and interactions of each factor remain elusive. Therefore, the purpose of this study was to investigate energy restriction and estrogen suppression during pubertal onset on bone mechanical strength and the osteogenic capacity of bone marrow-derived cells in two models: female rats treated with gonadotropin releasing hormone antagonists (GnRH-a) or 30% energy restriction. Previous studies have reported that GnRH-a injections have successfully delayed the onset of puberty in female rats and have the advantage that normal hypothalamic–pituitary function was restored after cessation of injections [36–38]. In addition, the GnRH-a injections focus on the mechanisms resulting only from GnRH suppression and avoid confounding results from lower body weights resulting from food restriction. A second model used 30% energy restriction that has also been shown to delay the onset of puberty [39–43].

Materials and methods

Animals

Thirty-two female Sprague Dawley rats (21 days-of-age) were received from Charles Rivers Laboratories, Wilmington, MA, USA and housed individually. All animals received water ad libitum. A 12 h light/dark cycle was maintained at a consistent temperature (21–23 °C) and relative humidity (58%–60%). All procedures were approved by the Institutional Animal Care and Use Committee (IACUC) of Temple University.

Experimental protocol

Animals were randomly assigned to one of three groups; control (C) (n = 10), GnRH-a (n = 10) and Energy Restriction (ER) (n = 12). The control group was given daily injections (0.2 ml) of saline and food ad libitum (AIN-93G). At 23 days of age, animals in the GnRH-a group received intra-peritoneal injections of gonadotropin releasing hormone antagonist (GnRH-a) (Antide, Bachem, Torrance, Ca. USA) daily for 27 days at a dosage of 2.5 mg/kg body mass. The GnRH-a group was pair fed to the ad-lib fed control group. The ER group was fed 70% of the amount of food consumed by control animals (Open Source diet (D07100606)) (Research Diets, New Brunswick, NJ). Food intake for the ER and GnRH-a groups was adjusted daily. The food was a special formulation based on the AIN-93G chow for growing animals that reduced the cornstarch in the food but maintained normal amounts of micronutrients (vitamins and minerals).

Animals were checked daily for vaginal opening to verify the onset of puberty and the first day of estrous was confirmed by cytology analysis of vaginal cells. Body weights were taken every 4 days. Growth rates were calculated for early puberty (body weight at week 3 subtracted from body weight at week 5 divided by 2) and late puberty (body weight at week 5 subtracted from body weight at week 7 divided by 2). All animals were sacrificed on Day 50. Animals were anesthetized by intra-peritoneal injection of ketamine (80 mg/kg) and xylazine (16 mg/kg). Blood was collected via cardiac puncture after which animals were then killed by overdose of pentobarbital. Ovaries, uteri, triceps surae muscle group and retro-peritoneal fat pads were dissected and weighed. The femurs and tibiae were excised, cleaned of soft tissue and measured for length. The right tibiae from six animals per group were flash frozen in liquid nitrogen at −70 °C for RNA analysis. Bone marrow was flushed from tibiae and femurs of two animals per group using a syringe to collect the bone marrow-derived stromal cells. Left femurs and tibiae were tested for mechanical strength and ashed. Right femurs were processed for histomorphometric analysis. Lumbar vertebrae (5–7) were used for trabecular micro-CT analysis.

Blood chemistry

Serum osteocalcin was measured using an immunoenzymometric assay (Rat-MID Osteocalcin EIA, Immunodiagnostic Systems Inc., Fountain Hills, AZ, USA). The sensitivity of the assay was 50 ng/ml. Serum insulin-like growth factor 1 (IGF-1) was measured using an immunoenzymometric assay (Rat/Mouse IGF-1, Immunodiagnostic Systems Inc., Fountain Hills, AZ, USA). The sensitivity of the assay was 63 ng/ml.

RNA isolation, reverse transcription and PCR (qRT-PCR)

Bones were pulverized and then homogenized in Trizol and separated into an organic and aqueous layer by chloroform. RNA was recovered from the aqueous phase by isopropyl alcohol precipitation. The pellet was washed with 70% ethanol and RNA concentration was calculated using spectrophotometer. RNA integrity was evaluated by agarose gel electrophoresis on a 1% agarose/paraformaldehyde minigel stained with ethidium bromide [44]. RNA (1 μg) was reverse transcribed to cDNA and used for qPCR analysis as described previously [44]. qRT-PCR was carried out on an ABI7500 Real-Time PCR system. Reactions were run using Taqman and gene specific primer FAM probe mixes (Applied Biosystems, Foster City, CA). The PCR conditions were standard protocol of ABI Prism 7500 Sequence Detection System. The reactions were run in triplicate and the results were analyzed with SDSv1.3 software that uses the ΔΔCt method for relative quantification [45].

Bone marrow-derived osteoblast differentiation

The epiphyses of two right tibiae and two right femurs from each group were removed. Whole marrow was flushed from the diaphyses and standard culture medium consisting of alpha-MEM (Mediatech cellgro, MT10022CV; Fisher Scientific) supplemented with 10% heat-inactivated Fetal Bovine Serum (FBS) (SH30071.03; Hyclone Laboratories) and penicillin/streptomycin was added to the marrow. The marrow was then passed through a 70-um filter prior to centrifugation at 1150 rpm for 10 min at +4 °C. The supernatant liquid was removed, and the cell pellet was re-suspended in fresh standard medium. Red blood cells were lysed using 2.5% acetic acid. Cells were then washed with fresh standard medium, re-suspended and were counted using a hemocytometer. Cells were diluted to a concentration of 1.8×10^5 cells/ml and plated onto 12-well plastic culture plates at a concentration of 1000 cells/well. These plates were placed in a biological oxygen demand (BOD) incubator with a 5% CO_2 atmosphere at 37 °C. On the third day, non-adherent cells were discarded, and the medium was changed to a standard media supplemented with 13 mM β glycerophosphate (G-9891; Sigma) and 50 mg/l ascorbic acid (A-4544; Sigma). This

osteogenic medium was used throughout the rest of the culture period and was changed completely twice per week.

Cell proliferation assay

Bone marrow derived osteoblast cells were plated in 24-well plates at a density of 1240 cells/well for a period of 4 days. At the end of the culture period, cells were incubated with 50 µl/well MTT (3-[4,5-dimethylthiazol-2-y1]-2,5-diphenyltetrazolium bromide) substrate for 4 h at 37 °C. Cells were then washed with PBS, 500 µl/well solubilizer (20% (w/v) SDS in 50% DMF) was added and samples were read at 570 nm using ELISA plate reader.

Alkaline phosphatase activity and staining measurement

On Day 14, cell layers from each group were rinsed with phosphate buffer saline and extracted in 150 mM Tris pH 9.0/0.1 mM $ZnCl_2$/0.1 mM $MgCl_2$(TZM buffer) with 1% Triton X-100 for 30 min at 37 °C. The cells were then scraped, transferred to eppendorf tubes, vortexed and stored at +4 °C overnight in order to extract alkaline phosphatase (AP) from the cell layer. The following day, cell assay buffer consisting of p-nitrophenol (Sigma P104) substrate in 10× TZM buffer (Sigma) was added to the tubes and the alkaline phosphatase activity was measured in duplicate. AP levels were expressed as nM of p-nitrophenol formed/min and data were normalized for an equivalent amount of protein in each sample. Total protein content was determined from matched cultures using BCA protein assay kit (Pierce).

Alkaline phosphatase staining was performed on cultures at Day 14 using ALP staining kit (Sigma). Cells were counterstained with hematoxylin and allowed to air-dry following which the cells were examined under inverted microscope (E600 Nikon). The pictures from inverted microscope were converted from JPEG to Bioquant readable images and analyzed with Osteo II analysis system (BIOQUANT Image Analysis Corporation, Nashville TN) and quantified for Total Area, AP positive area, AP Optic Density and % positive AP area.

Bone histomorphometry

The right femurs were harvested, de-fleshed and fixed in 10% buffered formalin for 24 h then stored in 70% ethanol. The bones were dehydrated with ethylene glycol monoethyl (Fisher, Fair Lawn, NJ, USA) cleared in methyl salicylate (J.T. Baker, Phillipsburg, NJ, USA), and embedded in methyl methacrylate with 15% dibutyl phthalate (Fisher Scientific). Undecalcified cross-sections (200 µm thickness) were cut at the mid-diaphysis using an Isomet 1000 precision saw with a diamond wafering blade (Buehler, Lake Bluff, IL. USA), polished to a final thickness of 50 µm, and cover slipped for analysis. Histomorphometric measurements were made using the Bioquant Osteo II analysis system (BIOQUANT Image Analysis Corporation, Nashville TN) attached to an epi-flourescence microscope (Nikon E800) and were calculated according to the ASBMR standards [46]. All measurements were made by a single observer who was blinded to the specimen identity. Static histomorphometric indices included total cross-sectional area (T.Ar; mm^2), marrow area (Ma.Ar; mm^2), cortical bone area (Ct.Ar = (T.Ar − Ma.Ar); mm^2), periosteal perimeter (Ps.Pm; mm), endocortical perimeter (Ec.Pm; mm) and relative cortical area (RCA = Ct.Ar/T.Ar).

Cortical bone mechanical strength

Breaking strength of each left femur and tibia was measured under 3-point bending using a material testing machine (ElectroForce Systems Group, Bose Corporation Eden Prairie, MN, USA) fitted with a 1000 N load cell. Femurs were placed on the loading fixture anterior side down and loaded in the anterior–posterior plane at a span length of 12 mm. Tibia were placed medial surface down with a span length of 17 mm. Prior to testing, the bones were thawed in saline at room temperature to ensure hydration. The femurs and tibiae were loaded to failure at a rate of 0.05 mm/s, during which displacement and force were collected (100 Hz). Displacement and force data were normalized using terms derived from engineering analysis of three-point bending [47]. Bending moments were calculated from the force (F) data (M = FL/4) (N mm). Displacement data were divided by ($L^2/12$) (mm/mm^2), where L is the distance between the lower supports. Structural properties were then determined from the moment versus normalized displacement curves; peak moment (N mm), yield-moment (N mm), stiffness (N mm^2), post-yield-displacement (mm/mm^2), and energy to failure (N mm-mm/mm^2). The yield moment was calculated as the point where a 10% change in slope of the moment versus normalized displacement curve occurred [48]. Peak stress was calculated from mechanical and cross-sectional properties (assuming a cylindrical cross section) using the equation:

$$\text{Stress} = \text{Moment}^{*}c / I\left(N / mm^2\right) \times (c \text{ is the distance from the neutral axis to the periosteal surface}).$$

Micro CT

Lumbar vertebrae from C, GnRH-a and ER animals (n = 5/group) were fixed in 10% buffered formalin for 24 h, stored in 70% ethanol, and scanned in an ex-vivo microCT scanner (SkyScan 1172, SkyScan, Aartslaar, Belgium). The SkyScan 1172 has a sealed micro focus X-ray tube which can go from 20 keV–100 keV energy with 10 megapixel (4000×2096) 12-bit cooled CCD-camera. Scanning was performed using a source setting of 60 keV/167 µA with a 0.5 mm Al filter to minimize the beam hardening from the polychromatic nature of the sealed X-ray source. Scans were made with a rotation step of 0.40° through 180° and a pixel size of 7.5 µm. Feldkamp cone-beam reconstruction algorithm was used to reconstruct the 3D cross-sections along with addressing the ring artifact reduction and beam hardening correction. Approximately 400 to 500 slices in the trabecular region of the L5 vertebra were analyzed. Percent bone volume, trabecular thickness, trabecular number, trabecular separation, degree of anisotropy and structural model index (SMI) were measured and all parameters were calculated according to the ASBMR standards [49].

Data analysis

One way analysis of variance testing (ANOVA) with a significance level of 0.05 was used to assess group differences (GraphPad Prism version 5.00 for Windows, GraphPad Software, San Diego California USA, www.graphpad.com). Tukey's honestly significant difference (HSD) post hoc analysis was conducted to determine where significant differences existed. Muscle weights and fat pad weights were calculated as a percent body weight. Mechanical variables were normalized with a linear regression-based correction using body weight [50] since there was a significant difference in body weight between the groups at sacrifice (non-normalized values are also presented). All variables with an R^2 level greater than 0 were normalized to avoid choosing an arbitrary R^2 value as a cut-off for normalization. Linear regression analyses were run for total area and body weight for each group (GraphPad Prism version 5.00 for Windows, GraphPad Software, San Diego California USA, www.graphpad.com).

Results

Suppressed IGF-1 levels in ER group and increased osteocalcin in both GnRH-a and ER groups

Blood serum levels for IGF-1 were significantly lower in the ER group (29%) and significantly higher in the GnRH-a group (13%).

Osteocalcin levels were significantly higher in both groups (ER: 22%, GnRH-a: 18%) (Fig. 1).

Delay in pubertal onset in GnRH-a and ER groups

The day of VO was significantly delayed in the GnRH-a groups (48 days of age) compared to the control group (31 days of age) (Table 1). Eighty percent of the GnRH-a animals never had a vaginal opening during the protocol, therefore 50 days, the day of sacrifice, was the date of vaginal opening used for statistical analysis. The ER had a moderate delay (34 days of age) for VO. Vaginal cytology analysis illustrated variations between the control and ER groups; the percentage of animals in the estrous phase was higher in the control group (81.8%) and the percentage of animals in the pro-estrous phase was higher in the ER group (64.2%).

High growth rates in GnRH-a group and low growth rates in ER group

Pubertal growth can be divided into two phases: an early pubertal (3–5 weeks of age) and a late pubertal (5–7 weeks of age) phase [51]. The growth rate (% growth per week) of the control group was greater early puberty (week 3–5) compared to late puberty (week 5–7). No differences in growth rates were detected between GnRH and control animals during early puberty, however, the growth rate of the GnRH-a group remained elevated during late puberty (Fig. 2). Growth rate during late puberty slows down in control animals (Fig. 2). Growth rate was significantly lower in the ER group compared to the control group. In fact, the ER groups had suppressed growth rates during both early and late puberty compared to control (Fig. 2).

ER resulted in smaller animals compared to GnRH-a with no effect on uterine weight

The GnRH-a group was pair fed to the control group and had similar body weights, muscle weights and retro-peritoneal fat weights at sacrifice (Table 1). Body weight at sacrifice was significantly lower (21%) in the ER group compared to control (Table 1). Muscle weight was significantly lower in the ER group (23%) compared to control (Table 1). After normalizing muscle weight by body weight, there were no differences between the three groups. The retro-peritoneal fat pad weight (Table 1) was significantly lower in the ER group compared to control (65%) and to the GnRH-a group (48%). Retro-peritoneal fat pad weight of the ER group remained significantly lower (55%) than control after normalizing by body weight.

Uterine weight was significantly lower in the GnRH-a group (81%) compared to control (Table 1). There was no difference in uterine weight between the control and ER groups (Table 1). However, ovarian weight (Table 1) was significantly lower in both experimental groups (GnRH-a: 83% and ER: 33%) compared to controls.

Table 1
Summary of group differences for body and tissue weights, femoral bone length and the day of vaginal opening. Values represent means ± standard deviation.

Variables	Control	GnRH-a	ER
Body.wt (g)	191.3 ± 17.7	185.3 ± 6.8	147.2 ± 4.6[a]
Muscle.wt (g)	1.28 ± 0.08	1.28 ± 0.08	0.99 ± 0.07[a]
Muscle.wt/BW (%)	0.72 ± 0.07	0.70 ± 0.04	0.70 ± 0.03
Fat.wt (g)	0.88 ± 0.37	0.73 ± 0.15	0.30 ± 0.08[a]
Fat.wt/BW (%)	0.50 ± 0.18	0.39 ± 0.07	0.22 ± 0.06[a]
Uterine.wt (g)	0.31 ± 0.05	0.06 ± 0.05[a]	0.36 ± 0.14
Ovarian.wt (g)	0.12 ± 0.02	0.02 ± 0.01[a]	0.08 ± 0.01[a]
Tibial.L (mm)	33.1 ± 0.8	33.1 ± 1.2	31.5 ± 0.6[a]
Tibial.L/BW (mm/g)	0.18 ± 0.01	0.18 ± 0.01	0.22 ± 0.01[a]
Femoral ash fraction	0.56 ± 0.06	0.56 ± 0.04	0.57 ± 0.02
Day of VO	30.07 ± 2.86	47.9 ± 7.13[a]	34.41 ± 5.08

BW represents body weight in grams.
[a] Represents a significant difference ($p<0.05$) vs. the control group.

The length of both the tibiae and the femurs was not significantly different between the GnRH-a and the control groups. However, tibial length was significantly decreased (5%) in the ER group compared to both the control and GnRH-a groups. After normalization by body weight, the tibial and femoral lengths were 22% longer in the ER group compared to control. There were no significant differences in the ash fraction between groups for the tibia or femur (Table 1).

In-vitro osteoblast proliferation and differentiation differ between the GnRH-a and ER groups

Bone marrow-derived stromal cell proliferation or viability was expressed as percent of the control group (Fig. 3). Proliferation of the bone marrow-derived osteoblasts was significantly suppressed in GnRH-a group by 41% but the 15% decrease in proliferation in ER group (tibia and femur combined) was not statistically significant. Alkaline phosphatase (AP) activity was decreased by 30% in the GnRH-a group and 64% in the ER group compared to control (only the ER group was statistically significant). However, AP staining was significantly decreased in the GnRH-a group by 46% and by 66% in the ER compared to control suggesting decreased osteoblast differentiation (Fig. 3). No significant differences were found in the relative quantification (RQ) for RUNX2, a transcription factor for osteoblasts.

Body weight predicts total area for ER and control groups

Total subperiosteal area (T.Ar; mm^2), cortical bone area (Ct.Ar; mm^2), and relative cortical area (RCA = Ct.Ar/T.Ar; %) were not significantly different between GnRH-a, ER and control groups. The periosteal and endocortical perimeters were not significantly different between groups. However, body weight predicted total area (T.Ar) for

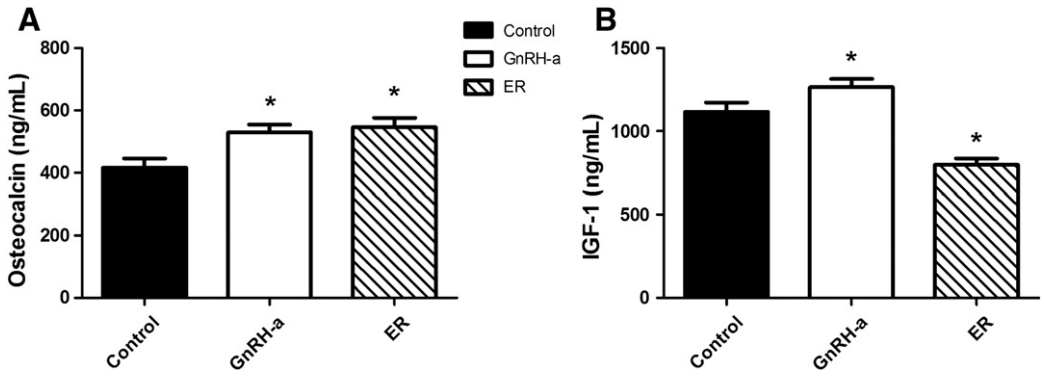

Fig. 1. Serum osteocalcin and IGF-1 levels in the control, GnRH-a and ER groups at 50 days of age. A. Osteocalcin levels (ng/ml) were elevated in both experimental groups (GnRH-a and ER). B. IGF-1 levels (ng/ml) were elevated in the GnRH-a group and suppressed in the ER group. *$p<0.05$ compared to control.

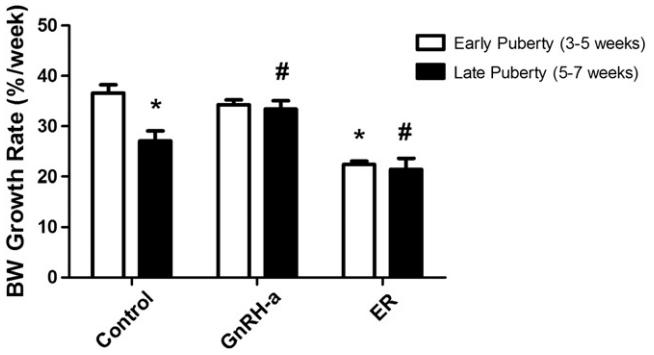

Fig. 2. Growth rate of body weight expressed as the percentage increase during early puberty (3–5 weeks of age) or late puberty (5–7 weeks of age) for the control, GnRH-a and ER groups. *$p<0.05$ compared to control (early puberty). #$p<0.05$ compared to control (late puberty).

the ER and control groups ($r^2=.6811$) but body weight did not predict the T.Ar for the GnRH-a group ($r^2=.2143$) (Fig. 4).

Bone strength relative to body weight is greater in the ER compared to GnRH-a group

Peak moment of the femur was significantly lower in the GnRH-a compared to the control group ($p<0.05$). When normalized using a regression protocol based on body weight, the peak moment of the femur (Fig. 5) remained significantly lower in the GnRH-a group suggesting that body weight had no effect on protecting bone strength. Stiffness ($N\,mm^2$) was significantly lower in the GnRH-a group compared to the control group for the femur (Fig. 5) and tibia. Following normalization, stiffness remained significantly lower in the GnRH-a group for the femur (28.9%) and tibia (17.5%) (Fig. 5).

Tibial and femoral peak moment values in the ER group were not significantly different from control before or after normalization (Fig. 5). Stiffness was significantly lower in the ER group compared to control in the femur by 19% but similar results were not found in the tibia. Normalizing by body weight negated any differences in stiffness in the femur and tibia between the control and the ER groups. Calculated peak stress values were significantly different between groups ($p=0.03$) in particular the GnRH-a group had a significantly lower stress compared to the ER group (Fig. 5).

ER group has increased bone volume in the lumbar spine

The percent bone volume and trabecular number were significantly lower in the GnRH-a group compared to the control group by 20% and 17% respectively (Fig. 6). Trabecular thickness and trabecular separation were not significantly different between the control and the GnRH-a groups (Fig. 6). The structural model index was significantly higher (45%) in the GnRH-a as compared to the control group suggesting an increased rod-like structure in the GnRH-a group. The percent bone volume (BV/TV) was significantly higher in the ER (18.5%) as compared to the control (Fig. 6) as was trabecular thickness (14.3%). However, trabecular number, trabecular separation and structural model index were not significantly affected in the ER group.

Discussion

Previous studies have hypothesized that energy restriction suppresses hormone levels in young female athletes [15,52]. However, energy restriction may also affect bone strength independent of estrogen suppression [31]. The current study results, using two different

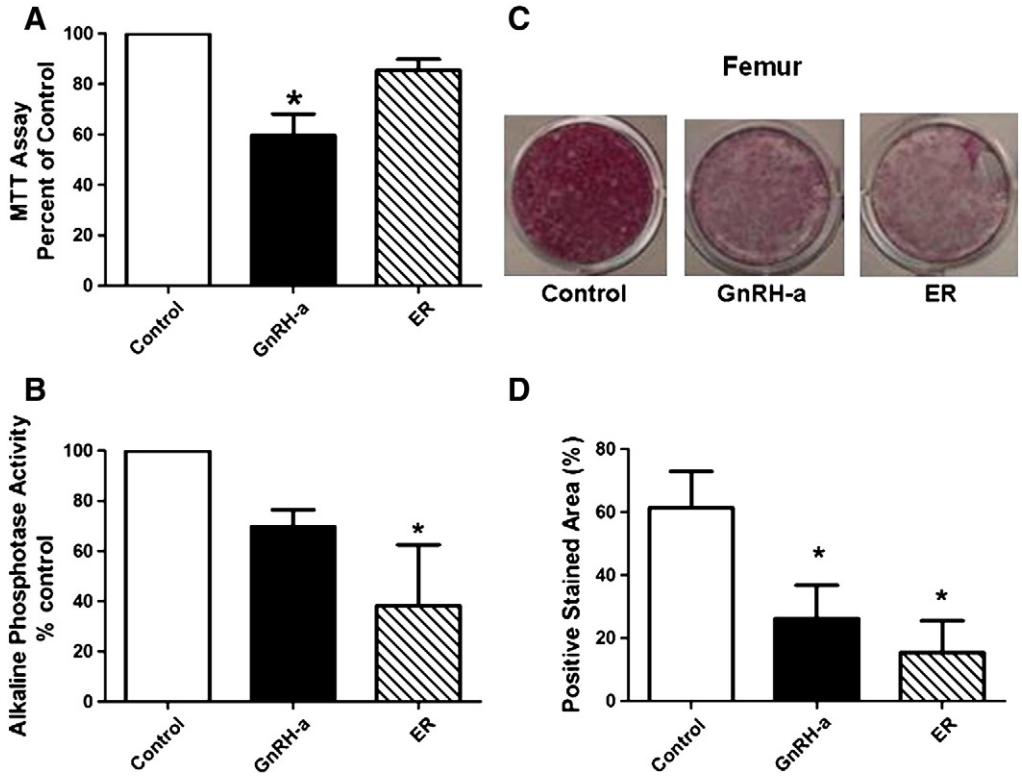

Fig. 3. Bone marrow cell proliferation and alkaline phosphatase activity and stain (Day 14). A. On Day 5 an MTT cell proliferation assay was performed. Results are presented as percent of control and are a combination of assays on the tibia and femur. B. On Day 14, alkaline phosphatase activity was measured and presented as percent of control. Results are both tibia and femur. Activity was measured in nM of p-Nitrophenol/min/ug of protein. C. Sample wells stained for alkaline phosphatase for the control, GnRH-a and ER groups. D. Quantification of the alkaline phosphatase stained percent positive area in each well for the three groups using Osteo II analysis system (BIOQUANT Image Analysis Corporation, Nashville TN). Data presented in A, B and D are the mean ± SD.

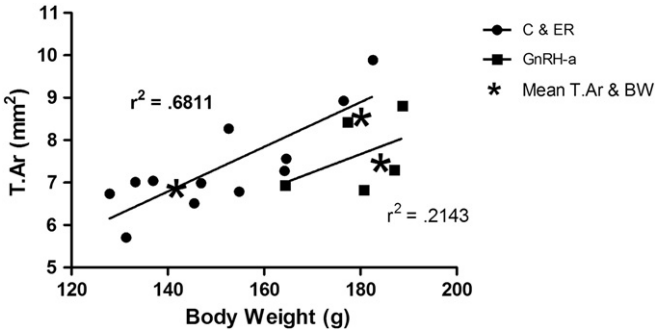

Fig. 4. Linear regression of body weight and total area (T.Ar). There was a significant relationship between body weight and total area in the control and ER groups ($r^2 = .6811$). There was no significant relationship in the GnRH-a group between body weight and total area ($r^2 = .2143$).

models to suppress pubertal development (energy restriction (ER) and hypothalamic suppression (GnRH-a)), demonstrate opposite effects on bone marrow-derived osteoblast proliferation and differentiation and bone strength in female rats. Hypothalamic suppression (GnRH-a) significantly decreased bone strength, trabecular bone volume, and bone marrow-derived cell proliferation accompanied by elevated serum IGF-1 levels and increased body weight. In contrast, the food restriction (ER) failed to reduce bone strength and increased trabecular bone volume in the lumbar spine with decreased marrow-derived cell differentiation and serum IGF-1 levels.

We speculate that our energy restricted animals in the current study had an impaired reproductive axis indicated by a moderate delay in puberty but the impact on the reproductive axis was muted compared to the effect from the GnRH-antagonist injections. Low estradiol levels and delayed puberty are typically associated with energy restriction in a clinical population. Thus a more extreme and prolonged ER protocol including intense exercise, severe food restriction or both may affect estradiol levels resulting in increased resorption and lower trabecular bone volume similar to GnRH-a model. However, the advantage of this experimental approach was that GnRH-a injections suppress estradiol without weight loss and the 30% energy restriction did not have any micronutrient or protein deficits. Yet, the lack of directly measured leptin and bone resorption markers limits this study.

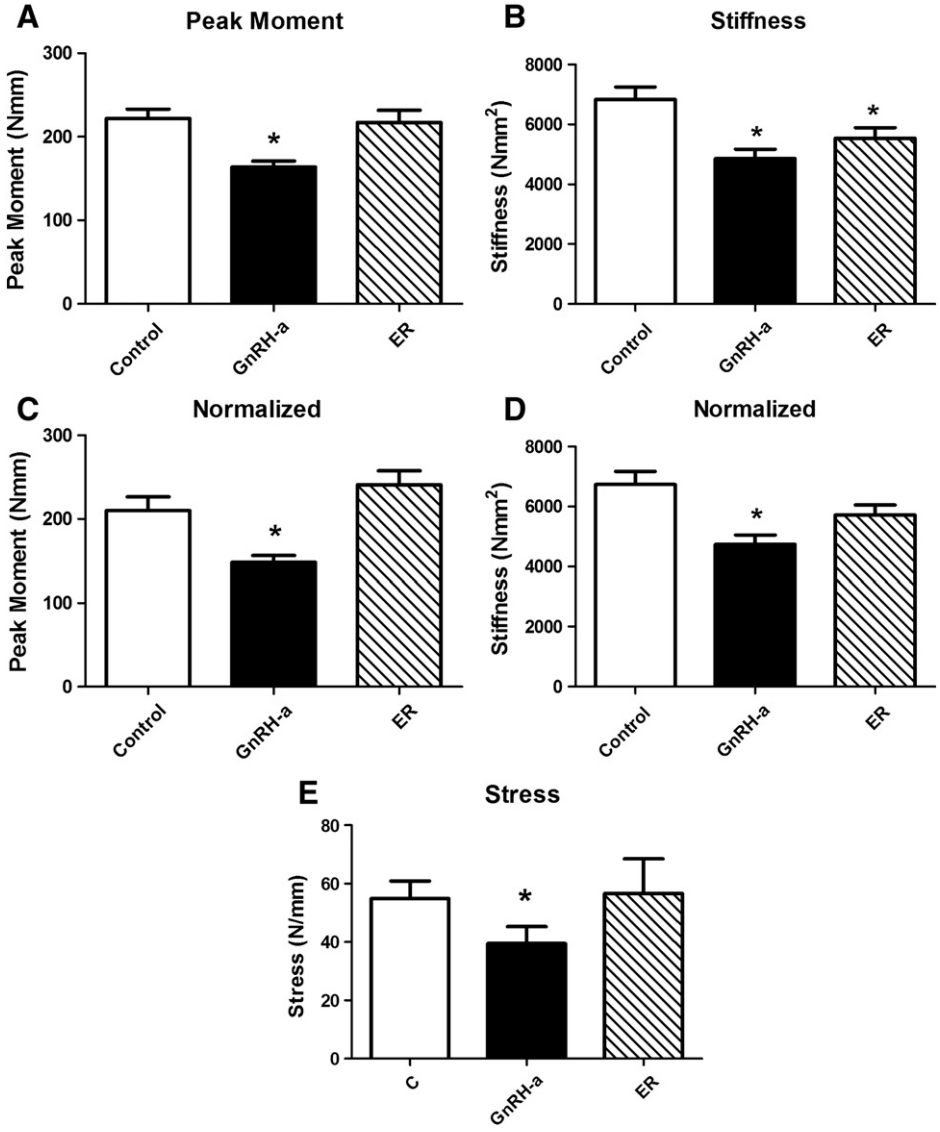

Fig. 5. Bone strength testing using a three-point bending assay on the femur at 50 days of age in the control, GnRH-a and ER groups. Structural properties were measured from moment–displacement curves. A. Peak moment (N mm). B. Stiffness (slope of the moment–displacement curve) (N mm^2). C. Peak moment (N mm) was normalized to body weight using a linear regression based method. D. Stiffness (N mm^2) was normalized to body weight using a linear regression based method. E. Calculated stress Stress = Moment $^*c/I$ (N/mm^2). $^*p<0.05$ compared to control.

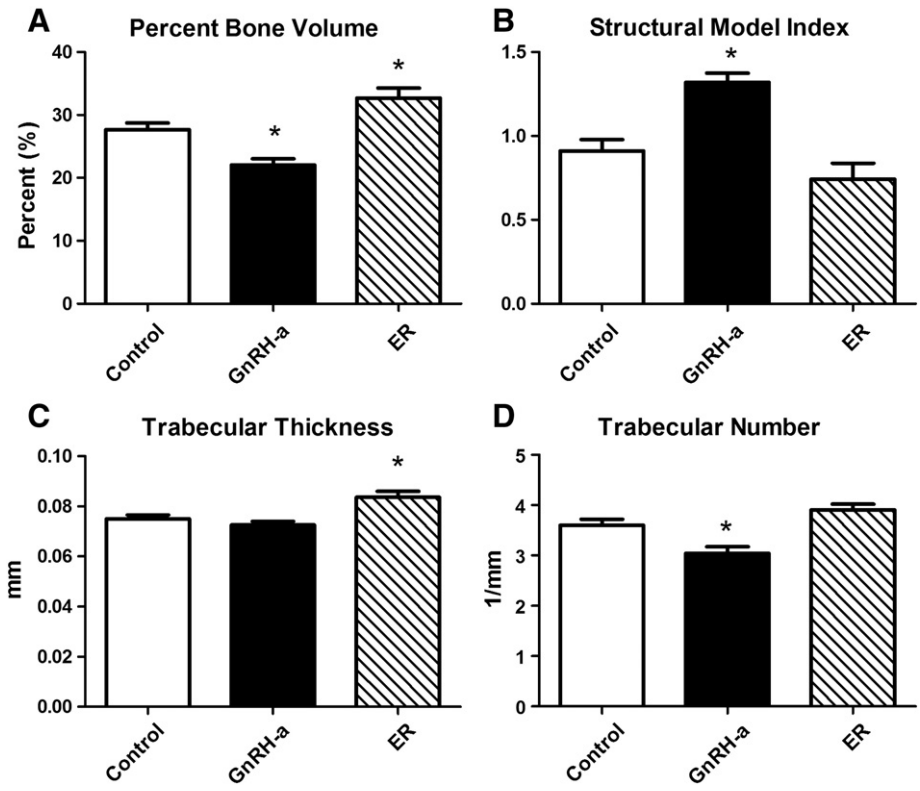

Fig. 6. Micro-CT variables for the trabecular bone of the fifth lumbar vertebra of the control, GnRH-a and ER groups (n = 5). A. Percent bone volume (%). B. Structural model index. C. Trabecular thickness (mm). D. Trabecular number (1/mm). *p<0.05 compared to control.

The increase in vertebral trabecular bone volume and trabecular thickness in the ER group in concert with the decrease in vertebral trabecular bone volume in the GnRH-a group provide a new perspective on the interaction of food restriction and hypothalamic suppression. Our results support the hypothesis that during periods of nutritional stress the increased vertebral bone volume may be an adaptive mechanism to store mineral [34]. Multiple studies of caloric restriction reported increased vertebral trabecula and deficits in the trabecular bone of the femur and tibia [34,53,54]. However, the lower bone volume of the GnRH-a group was consistent with changes reported following ovariectomy surgery (OVX) a common low estrogen model of post menopausal bone loss [55,56]. Decreased serum estrogen is associated with significant decreases in trabecular architecture in both the vertebra and femur. Suppressed levels of the hormone estradiol have been reported following GnRH-a injection protocols [38,57,58] with similar uterine and ovarian tissue atrophies [38,59]. Suppressed leptin levels following energy restriction may provide an explanation for the differing vertebral bone volumes. Leptin levels may play a crucial role in pubertal timing by connecting the gonadotropic and somatotropic axes [34,52,60] and the significantly decreased ovarian weights (33%) and IGF-1 levels in the ER group may be indirect evidence of suppressed leptin levels. Models of hypoleptinemia result in increased vertebral bone volume [61]. Studies of IGF-1 deficient mice [62,63] also reported no change or slightly improved trabecular bone volume along with increased connectivity, increased trabecular number and decreased trabecular spacing in the vertebrae. A recent study in calorie restricted young male mice reported significant decreases in bone volume in the distal femur but no changes in the vertebra [54]. Food restriction and hypothalamic suppression affect axial and appendicular trabecular bone in different ways; bone volume decreases in both weight bearing long bones (tibia and femur) and non weight bearing sites (vertebra) following estradiol suppression but caloric restriction preserves trabecular bone volume in non weight bearing sites (vertebra) with losses in the femur and tibia. In addition, trabecular bone volume and bone architecture measures in the radius, a non weight bearing bone, were similar to controls in human populations practicing long-term calorie restriction [64].

While increased serum osteocalcin was expected with suppressed estradiol levels, serum osteocalcin levels were increased in both models (27% GnRH-a and 31% ER). The unexpected increase in serum osteocalcin in the ER group does not agree with other studies of food restriction [34]. However these results do support, a recent study that showed an increase in serum osteocalcin in humans following a reduction in visceral fat mass after diet combined with exercise [65]. In that study, the authors noted the relationship between increased leg force (muscle function) and serum osteocalcin, suggesting that increased lean mass and decreased fat mass results in increased osteocalcin levels. While the current study did not manipulate exercise, lean mass was preserved. The decreased body weight in the ER group was due to loss of fat mass. The preserved muscle weight of the ER animals may be a result of the moderate level of energy restriction (30%) with a protein replete diet [66].

One could argue that the energy restricted animals may have mechanically sufficient bones for their size based on the strong relationship that exists between bone mineral density and lean mass during the linear growth and development period [67]. The body weights of both the control and ER groups were significantly related to total area in the femoral diaphysis ($r^2 = .6871$). The ER group tended to have a lower body weight and total area overall compared to the control animals even though there were no significant differences between the group means (Fig. 4). In contrast, the GnRH-a animals did not have a significant relationship between body weight and total area ($r^2 = .2143$). GnRH-a animals had lower total area for similar body weights in other words bone size did not increase with body size. Investigators have hypothesized that bone mass of weight bearing bones is determined by body weight [53] and our results, both femoral total area and mechanical strength, support this concept.

The significant increases in body weight and total cortical bone cross sectional area of early puberty compared to late puberty, indicate a growth spurt during early puberty [51]. While the significantly higher growth rate of the control animals during early puberty compared to late puberty reinforced other study results [51], there was no decrease in growth rates during late puberty in the GnRH-a group. The high growth rates associated with the GnRN-a group were consistent with increased growth rates following OVX in two month old animals [68]. One could argue that increased growth rates may result in a greater amount of non-lamellar bone forming on the periosteal surface which in turn decrease material properties of the bone and thus reduce bone strength [48,69]. Furthermore, there were significantly lower growth rates in the ER group compared to the control and the GnRH-a groups yet no decreases in mechanical strength.

Evidence of the effect of growth rates on mechanical strength comes from data using chicks as a model [68]. Fast growing strains of chicks had weaker bones compared to slow growing strains replicating differences observed in mechanical strength results found between the GnRH-a and ER groups. The marrow cell proliferation rates were lower in the fast growing chick strains [68] and similar to the decrease in proliferation in the GnRH-a model with no significant changes in differentiation. The suppression of proliferation in the GnRH-a model may be due to the resulting estrogen suppression based on estrogen's previously documented ability to directly modulate the differentiation of stromal cells into the osteoblast lineage [70]. ER animals exhibited no significant change in proliferation rates compared to controls, but had significantly greater proliferation rates than the GnRH-a group. In addition, the significant suppression of marrow cell differentiation of the ER group was similar to the slow growing chicks. Although these findings may be counter intuitive to the increases in bone volume in the vertebral trabecular bone of the ER animals, the increased mineral apposition rate found in slower growing chicks offers an explanation for the increased bone volume with lower osteoblast differentiation [68,71].

In summary, ER may have an independent mechanism on bone accrual during pre-puberty that differs from suppressed estradiol resultant from hypothalamic suppression. The ER animals were smaller but had cortical bone strength sufficient for their size with an increased vertebral trabecular bone volume. The increased vertebral bone volume may be an adaptive mechanism to store mineral during periods of nutritional stress [34], whereas cortical bone in weight bearing sites is determined by body mass and thus decreases when body mass decreases due to caloric restriction [53]. In contrast, the lowered estradiol levels that follow from hypothalamic suppression reduce bone strength and trabecular bone volume compared to control potentially due to increased bone turnover. The differences during pubertal development may also be in part to growth rate differences. Fast growing chicks had different osteoblast behavior compared to slower growing chicks. Suppressed estradiol accelerates body weight gain in contrast to energy restriction which slows down body weight gain. The opposing effects on the proliferation and differentiation of bone marrow osteoblasts ultimately can affect bone strength in the long bones. Further investigation into the long-term consequences and potential catch-up growth of these models is needed as well as more data on the interaction of these models.

Acknowledgments

Supported by the Dean's Research Incentive Grant, College of Health Professions and Social Work, Temple University. The authors would like to thank M. Alexandra Monroy, PhD for her assistance with the RT-PCR protocol and analysis and to Matthew Seigenfuse for his assistance in data analysis.

Appendix A. Supplementary data

Supplementary data to this article can be found online at doi:10.1016/j.bone.2011.07.019.

References

[1] Bonjour JP, Theintz G, Law F, Slosman D, Rizzoli R. Peak bone mass. Osteoporos Int 1994;4(Suppl 1):7–13.
[2] Warren MP, Brooks-Gunn J, Fox RP, Holderness CC, Hyle EP, Hamilton WG. Osteopenia in exercise-associated amenorrhea using ballet dancers as a model: a longitudinal study. J Clin Endocrinol Metab 2002;87:3162–8.
[3] Katzman DK, Bachrach LK, Carter DR, Marcus R. Clinical and anthropometric correlates of bone mineral acquisition in healthy adolescent girls. J Clin Endocrinol Metab 1991;73:1332–9.
[4] Scheider JE, Wade GN. Inhibition of reproduction in service of energy balance. Reproduction in context: social and environmental influences on reproductive physiology and behaviour. Cambride: The MIT Press; 2000. p. 35–82.
[5] Carbon R, Sambrook PN, Deakin V, et al. Bone density of elite female athletes with stress fractures. Med J Aust 1990;153:373–6.
[6] Warren MP, Brooks-Gunn J, Fox RP, Lancelot C, Newman D, Hamilton WG. Lack of bone accretion and amenorrhea: evidence for a relative osteopenia in weight-bearing bones. J Clin Endocrinol Metab 1991;72:847–53.
[7] O'Donnell E, De Souza MJ. The cardiovascular effects of chronic hypoestrogenism in amenorrhoeic athletes: a critical review. Sports Med 2004;34:601–27.
[8] Hopkinson RA, Lock J. Athletics, perfectionism, and disordered eating. Eat Weight Disord 2004;9:99–106.
[9] Torstveit MK, Sundgot-Borgen J. The female athlete triad: are elite athletes at increased risk? Med Sci Sports Exerc 2005;37:184–93.
[10] Munoz MT, de la Piedra C, Barrios V, Garrido G, Argente J. Changes in bone density and bone markers in rhythmic gymnasts and ballet dancers: implications for puberty and leptin levels. Eur J Endocrinol 2004;151:491–6.
[11] Warren MP, Brooks-Gunn J, Fox RP, et al. Persistent osteopenia in ballet dancers with amenorrhea and delayed menarche despite hormone therapy: a longitudinal study. Fertil Steril 2003;80:398–404.
[12] Roze C, Doyen C, Le Heuzey MF, Armoogum P, Mouren MC, Leger J. Predictors of late menarche and adult height in children with anorexia nervosa. Clin Endocrinol (Oxf) 2007;67:462–7.
[13] Couzinet B, Young J, Brailly S, Le Bouc Y, Chanson P, Schaison G. Functional hypothalamic amenorrhoea: a partial and reversible gonadotrophin deficiency of nutritional origin. Clin Endocrinol (Oxf) 1999;50:229–35.
[14] Baranowska B. Are disturbances in opioid and adrenergic systems involved in the hormonal dysfunction of anorexia nervosa? Psychoneuroendocrinology 1990;15:371–9.
[15] Cobb KL, Bachrach LK, Greendale G, et al. Disordered eating, menstrual irregularity, and bone mineral density in female runners. Med Sci Sports Exerc 2003;35:711–9.
[16] Bullen BA, Skrinar GS, Beitins IZ, von Mering G, Turnbull BA, McArthur JW. Induction of menstrual disorders by strenuous exercise in untrained women. N Engl J Med 1985;312:1349–53.
[17] Williams NI, Caston-Balderrama AL, Helmreich DL, Parfitt DB, Nosbisch C, Cameron JL. Longitudinal changes in reproductive hormones and menstrual cyclicity in cynomolgus monkeys during strenuous exercise training: abrupt transition to exercise-induced amenorrhea. Endocrinology 2001;142:2381–9.
[18] Loucks AB, Heath EM. Dietary restriction reduces luteinizing hormone (LH) pulse frequency during waking hours and increases LH pulse amplitude during sleep in young menstruating women. J Clin Endocrinol Metab 1994;78:910–5.
[19] Loucks AB, Verdun M, Heath EM. Low energy availability, not stress of exercise, alters LH pulsatility in exercising women. J Appl Physiol 1998;84:37–46.
[20] Loucks AB, Thuma JR. Luteinizing hormone pulsatility is disrupted at a threshold of energy availability in regularly menstruating women. J Clin Endocrinol Metab 2003;88:297–311.
[21] Loucks AB, Stachenfeld NS, DiPietro L. The female athlete triad: do female athletes need to take special care to avoid low energy availability? Med Sci Sports Exerc 2006;38:1694–700.
[22] Zanker CL, Swaine IL. The relationship between serum oestradiol concentration and energy balance in young women distance runners. Int J Sports Med 1998;19:104–8.
[23] Zanker CL, Swaine IL. Relation between bone turnover, oestradiol, and energy balance in women distance runners. Br J Sports Med 1998;32:167–71.
[24] Drinkwater BL, Nilson K, Chesnut III CH, Bremner WJ, Shainholtz S, Southworth MB. Bone mineral content of amenorrheic and eumenorrheic athletes. N Engl J Med 1984;311:277–81.
[25] Zanker CL, Swaine IL. Bone turnover in amenorrhoeic and eumenorrhoeic women distance runners. Scand J Med Sci Sports 1998;8:20–6.
[26] Jonnavithula S, Warren MP, Fox RP, Lazaro MI. Bone density is compromised in amenorrheic women despite return of menses: a 2-year study. Obstet Gynecol 1993;81:669–74.
[27] Misra M, Klibanski A. Anorexia nervosa and osteoporosis. Rev Endocr Metab Disord 2006;7:91–9.
[28] Dominguez J, Goodman L, Goodman L, Sen Gupta S, et al. Treatment of anorexia nervosa is associated with increases in bone mineral density, and recovery is a biphasic process involving both nutrition and return of menses. Am J Clin Nutr 2007;86:92–9.
[29] Cobb KL, Bachrach LK, Sowers M, et al. The effect of oral contraceptives on bone mass and stress fractures in female runners. Med Sci Sports Exerc 2007;39:1464–73.
[30] De Souza MJ, Lee DK, VanHeest JL, Scheid JL, West SL, Williams NI. Severity of energy-related menstrual disturbances increases in proportion to indices of energy conservation in exercising women. Fertil Steril 2007;88:971–5.
[31] De Souza MJ, West SL, Jamal SA, Hawker GA, Gundberg CM, Williams NI. The presence of both an energy deficiency and estrogen deficiency exacerbate alterations of bone metabolism in exercising women. Bone 2008;43:140–8.

[32] Lambert J, Lamothe JM, Zernicke RF, Auer RN, Reimer RA. Dietary restriction does not adversely affect bone geometry and mechanics in rapidly growing male Wistar rats. Pediatr Res 2005;57:227–31.
[33] Pendergrass WR, Li Y, Jiang D, Fei RG, Wolf NS. Caloric restriction: conservation of cellular replicative capacity in vitro accompanies life-span extension in mice. Exp Cell Res 1995;217:309–16.
[34] Hamrick MW, Ding KH, Ponnala S, Ferrari SL, Isales CM. Caloric restriction decreases cortical bone mass but spares trabecular bone in the mouse skeleton: implications for the regulation of bone mass by body weight. J Bone Miner Res 2008;23:870–8.
[35] Sanderson JP, Binkley N, Roecker EB, et al. Influence of fat intake and caloric restriction on bone in aging male rats. J Gerontol A Biol Sci Med Sci 1997;52:B20–5.
[36] Roth C, Leonhardt S, Seidel C, Lakomek M, Wuttke W, Jarry H. GnRH antagonist cetrorelix prevents sexual maturation of peripubertal male rats. Exp Clin Endocrinol Diabetes 2000;108:358–63.
[37] Rakover Y, Lu P, Briody JN, et al. Effects of delaying puberty on bone mineralization in female rats. Hum Reprod 2000;15:1457–61.
[38] Yingling VR, Khaneja A. Short-term delay of puberty causes a transient reduction in bone strength in growing female rats. Bone 2006;38:67–73.
[39] Velkoska E, Morris MJ, Burns P, Weisinger RS. Leptin reduces food intake but does not alter weight regain following food deprivation in the rat. Int J Obes Relat Metab Disord 2003;27:48–54.
[40] Bronson FH, Heideman PD. Short-term hormonal responses to food intake in peripubertal female rats. Am J Physiol 1990;259:R25–31.
[41] Messer NA, I'Anson H. The nature of the metabolic signal that triggers onset of puberty in female rats. Physiol Behav 2000;68:377–82.
[42] Engelbregt MJ, van Weissenbruch MM, Popp-Snijders C, Lips P, Delemarre-van de Waal HA. Body mass index, body composition, and leptin at onset of puberty in male and female rats after intrauterine growth retardation and after early postnatal food restriction. Pediatr Res 2001;50:474–8.
[43] Zeinoaldini S, Swarts JJ, Van de Heijning BJ. Chronic leptin infusion advances, and immunoneutralization of leptin postpones puberty onset in normally fed and feed restricted female rats. Peptides 2006;27:1652–8.
[44] Abdelmagid SM, Barbe MF, Arango-Hisijara I, Owen TA, Popoff SN, Safadi FF. Osteoactivin acts as downstream mediator of BMP-2 effects on osteoblast function. J Cell Physiol 2007;210:26–37.
[45] Yuan JS, Reed A, Chen F, Stewart Jr CN. Statistical analysis of real-time PCR data. BMC Bioinformatics 2006;7:85.
[46] Parfitt AM, Drezner MK, Glorieux FH, et al. Bone histomorphometry: standardization of nomenclature, symbols, and units. Report of the ASBMR histomorphometry nomenclature committee. J Bone Miner Res 1987;2:595–610.
[47] Turner CH, Burr DB. Basic biomechanical measurements of bone: a tutorial. Bone 1993;14:595–608.
[48] van der Meulen MC, Jepsen KJ, Mikic B. Understanding bone strength: size isn't everything. Bone 2001;29:101–4.
[49] Bouxsein ML, Boyd SK, Christiansen BA, Guldberg RE, Jepsen KJ, Muller R. Guidelines for assessment of bone microstructure in rodents using micro-computed tomography. J Bone Miner Res 2010;25:1468–86.
[50] Di Masso RJ, Font MT, Capozza RF, Detarsio G, Sosa F, Ferretti JL. Long-bone biomechanics in mice selected for body conformation. Bone 1997;20:539–45.
[51] Callewaert F, Venken K, Kopchick JJ, et al. Sexual dimorphism in cortical bone size and strength but not density is determined by independent and time-specific actions of sex steroids and IGF-1: evidence from pubertal mouse models. J Bone Miner Res 2010;25:617–26.
[52] Dimarco NM, Dart L, Sanborn CF. Modified activity-stress paradigm in an animal model of the female athlete triad. J Appl Physiol 2007;103(5):1469–78.
[53] Brochmann EJ, Duarte ME, Zaidi HA, Murray SS. Effects of dietary restriction on total body, femoral, and vertebral bone in SENCAR, C57BL/6, and DBA/2 mice. Metabolism 2003;52:1265–73.
[54] Devlin MJ, Cloutier AM, Thomas NA, et al. Caloric restriction leads to high marrow adiposity and low bone mass in growing mice. J Bone Miner Res 2010;25:2078–88.
[55] Sheng ZF, Dai RC, Wu XP, Fang LN, Fan HJ, Liao EY. Regionally specific compensation for bone loss in the tibial trabeculae of estrogen-deficient rats. Acta Radiol 2007;48:531–9.
[56] Yao X, Yun X, Chen T, et al. Effects of ovariectomy and estradiol on microarchitecture and biomechanical properties in rat vertebrae. Sheng Wu Yi Xue Gong Cheng Xue Za Zhi 2008;25:626–31 [636].
[57] Roth C, Leonhardt S, Seidel C, Luft H, Wuttke W, Jarry H. Comparative analysis of different puberty inhibiting mechanisms of two GnRH agonists and the GnRH antagonist cetrorelix using a female rat model. Pediatr Res 2000;48:468–74.
[58] Toyama R, Fujimori T, Nabeshima Y, et al. Impaired regulation of gonadotropins leads to the atrophy of the female reproductive system in klotho-deficient mice. Endocrinology 2006;147:120–9.
[59] Yingling VR, Taylor G. Delayed pubertal development by hypothalamic suppression causes an increase in periosteal modeling but a reduction in bone strength in growing female rats. Bone 2008;42:1137–43.
[60] Zeinoaldini S, Swarts JJ, Van de Heijning BJ. Central application of IGF-1 postpones time of vaginal opening in normally fed, but not in food-restricted rats. Horm Res 2006;66:169–74.
[61] Hamrick MW, Pennington C, Newton D, Xie D, Isales C. Leptin deficiency produces contrasting phenotypes in bones of the limb and spine. Bone 2004;34:376–83.
[62] Bikle D, Majumdar S, Laib A, et al. The skeletal structure of insulin-like growth factor I-deficient mice. J Bone Miner Res 2001;16:2320–9.
[63] Yakar S, Canalis E, Sun H, et al. Serum IGF-1 determines skeletal strength by regulating subperiosteal expansion and trait interactions. J Bone Miner Res 2009;24:1481–92.
[64] Villareal DT, Kotyk JJ, Armamento-Villareal RC, et al. Reduced bone mineral density is not associated with significantly reduced bone quality in men and women practicing long-term calorie restriction with adequate nutrition. Aging Cell 2011;10:96–102.
[65] Fernandez-Real JM, Izquierdo M, Ortega F, et al. The relationship of serum osteocalcin concentration to insulin secretion, sensitivity, and disposal with hypocaloric diet and resistance training. J Clin Endocrinol Metab 2009;94:237–45.
[66] Passadore MD, Griggio MA, Nunes MT, Luz J. Effects of ageing on the energy balance of food-restricted rats. Acta Physiol Scand 2004;181:193–8.
[67] Young D, Hopper JL, Macinnis RJ, Nowson CA, Hoang NH, Wark JD. Changes in body composition as determinants of longitudinal changes in bone mineral measures in 8 to 26-year-old female twins. Osteoporos Int 2001;12:506–15.
[68] Rawlinson SC, Murray DH, Mosley JR, et al. Genetic selection for fast growth generates bone architecture characterised by enhanced periosteal expansion and limited consolidation of the cortices but a diminution in the early responses to mechanical loading. Bone 2009;45:357–66.
[69] Tseng KF, Bonadio JF, Stewart TA, Baker AR, Goldstein SA. Local expression of human growth hormone in bone results in impaired mechanical integrity in the skeletal tissue of transgenic mice. J Orthop Res 1996;14:598–604.
[70] Okazaki R, Inoue D, Shibata M, et al. Estrogen promotes early osteoblast differentiation and inhibits adipocyte differentiation in mouse bone marrow stromal cell lines that express estrogen receptor (ER) alpha or beta. Endocrinology 2002;143:2349–56.
[71] Rawlinson SC, Boyde A, Davis GR, Howell PG, Hughes FJ, Kingsmill VJ. Ovariectomy vs. hypofunction: their effects on rat mandibular bone. J Dent Res 2009;88:615–20.

Microcirculation
The Official Journal of the Microcirculatory Society, Inc., the British Microcirculation Society, and the Australia & New Zealand Microcirculation Society

DOI:10.1111/micc.12102

Original Article

Three-Dimensional Reconstruction of Neovasculature in Solid Tumors and Basement Membrane Matrix Using *Ex Vivo* X-ray Microcomputed Tomography

SEUNGHYUNG LEE,*,† MARY F. BARBE,* ROSARIO SCALIA,‡ AND LAWRENCE E. GOLDFINGER*,†,§

*Department of Anatomy & Cell Biology, Temple University School of Medicine, Philadelphia, Pennsylvania, USA; †The Sol Sherry Thrombosis Research Center, Temple University School of Medicine, Philadelphia, Pennsylvania, USA; ‡Department of Physiology and the Cardiovascular Research Center, Temple University School of Medicine, Philadelphia, Pennsylvania, USA; §Cancer Biology Program, Fox Chase Cancer Center, Philadelphia, Pennsylvania, USA

Address for correspondence: Lawrence Goldfinger, Temple University School of Medicine, 3420 N. Broad Street, MRB 219 Philadelphia, PA 19140, USA. *E-mail:* goldfinger@temple.edu

Received 28 June 2013; accepted 22 October 2013.

ABSTRACT

Objective: To create accurate, high-resolution 3D reconstructions of neovasculature structures in xenografted tumors and Matrigel plugs for quantitative analyses in angiogenesis studies in animal models.

Methods: The competent neovasculature within xenografted solid tumors or Matrigel plugs in mice was perfused with Microfil, a radioopaque, hydrophilic polymerizing contrast agent, by systemic perfusion of the blood circulation via the heart. The perfused tumors and plugs were resected and scanned by X-ray micro-CT to generate stacks of 2D images showing the radioopaque material. A nonbiased, precise postprocessing scheme was employed to eliminate background X-ray absorbance from the extravascular tissue. The revised binary image stacks were compiled to reveal the Microfil-casted neovasculature as 3D reconstructions. Vascular structural parameters were calculated from the refined 3D reconstructions using the scanner software.

Results: Clarified 3D reconstructions were sufficiently precise to allow measurements of vascular architecture to a diametric limit of resolution of 3 μm in tumors and plugs.

Conclusions: *Ex vivo* micro-CT can be used for 3D reconstruction and quantitative analysis of neovasculature including microcirculation in solid tumors and Matrigel plugs. This method can be generally applied for reconstructing and measuring vascular structures in three dimensions.

Key words: microcomputed tomography, vascular imaging, tumor angiogenesis, Matrigel plug, microvasculature

Abbreviations used: DMEM, Dulbecco's modified Eagle's medium; FBS, fetal bovine serum; LLC, Lewis lung carcinoma; micro-CT, microcomputed tomography; MVD, mean vessel density; PBS, phosphate-buffered saline; ROI, region of interest; s.c., subcutaneous; SSA, specific surface area; VEGF, vascular endothelial growth factor; VOI, volume of interest; WT, wild type.

Please cite this paper as: Lee S, Barbe MF, Scalia R, Goldfinger LE. Three-dimensional reconstruction of neovasculature in solid tumors and basement membrane matrix using *ex vivo* X-ray microcomputed tomography. *Microcirculation* **21**: 159–170, 2014.

INTRODUCTION

Many imaging modalities exist for visualizing angiogenic responses in animal models [8–10]. A cohort of newer techniques such as contrast-enhanced MRI, marker-based intravital microscopy coupled with optical frequency domain imaging, and both *in vivo* and *ex vivo* X-ray micro-CT have emerged with the promise of providing 3D structural information that previously was inaccessible by standard 2D imaging analysis. A major goal in the development of these techniques is the ability to achieve sufficiently high resolution to visualize the microcirculation [15,30]. Recent studies have used micro-CT to quantify the number of small vessels in lung tumors and to generate 3D vascular reconstructions in other systems [12,16,35,36]. However, a persistent problem is the precise elimination of background absorbance from the scans, which precludes accurate reconstruction and measurements of the vascular structures [10]. We have modified the scanning and image processing to reconstruct and measure neovascular structures including small vessels in carcinomas and melanomas in a knockout mouse model [24].

Neovasculature in tumors is believed to have unique structural properties, reflecting unique functional properties. Blood vessels in tumors are more dynamic, tortuous, and permeable, and perfuse poorly, compared with their normal counterparts in nonpathological settings. Furthermore, the microcirculation in tumors can be heterogeneous and does not resemble the usual hierarchy of arterioles, capillaries, and

venules [3,11,19,22]. Thus, the ability to reconstruct and measure the structure of neovasculature in tumors and other settings is the key to understanding the biological basis for these effects, and to develop targeting strategies [5,9,10,14,15].

Although a variety of *in vivo* and *ex vivo* platforms other than solid tumor models for analyzing angiogenesis exist, s.c. implantation of basement membrane matrices such as Matrigel as a tissue-free receptacle for neovascularization has remained a widely used tool, due in part to its ease of use [32]. Matrigel is a partially defined extract from the Engelbreth-Holm-Swarm tumor, consisting of basement membrane proteins and several growth factors [2,41]. Matrigel from which low molecular mass proteins such as growth factors have been extracted by ammonium sulfate treatment ("growth factor-reduced" Matrigel) is commonly used as a substrate for comixing of defined factors such as VEGF or basic fibroblast growth factor prior to implantation [28,39]. The resulting invasion of endothelial cells from the host animal and subsequent formation of endothelial networks within the Matrigel plugs models angiogenic capillary network formation —albeit in an isolated, tissue-free environment—which is commonly assessed by histological examination of 2D sections from the resected plugs [2,32]. However, this method has eluded standardization, due to heterogeneity of the plug size and composition, as well as sampling variability from 2D sectioning [28,32]. Hence, analysis of *ex vivo* angiogenic platforms such as Matrigel plugs, like solid tumor models, would also benefit from 3D vascular reconstruction.

In this study we have refined a micro-CT-based technique for 3D reconstruction and quantitative analysis of neovasculature in xenografted tumors as well as Matrigel plugs in mice. An isotropic voxel limit of resolution of 3 μm, coupled with thorough depletion of background absorbance using a precise, non-biased image processing scheme, allows for accurate quantitation of vascular architectural parameters, including the microvasculature. We propose that this system will be generally applicable for testing angiogenic responses *ex vivo*.

MATERIALS AND METHODS

Mice

Twenty-four C57BL/6 mice between the ages of six and eight weeks were used for all experiments. For surgical procedures, ketamine-HCl (40 mg/kg) and xylazine (10 mg/kg) (Ketaset) were administered by intraperitoneal injection as anesthetic prior to surgery. All animal experiments followed protocols approved by the Institutional Animal Care and Use Committee (IACUC) at Temple University.

Cell Culture and Inoculation of Tumor Cells *In Vivo*

LLC (LL/2, LLC) cells were obtained from American Type Culture Collection (Rockville, MD, USA). The cells were cultured in DMEM with 10% FBS in a humidified and 5% CO_2 atmosphere at 37°C. LLC cells were harvested by trypsinization, washed and resuspended at 1×10^6 cells/500 μL of DMEM without serum, and this suspension was injected subcutaneously into the flank of six- to eight-week-old C57BL/6 mice. The peripheral circulation was perfused with Microfil and mice were euthanized within 10 days postinjection.

Angiogenesis in Matrigel plugs

The angiogenesis model was based on the use of Matrigel (BD Biosciences, San Jose, CA, USA) implants in C57BL/6 mice. A volume of 500 μL growth factor-reduced Matrigel with or without 100 ng/mL of VEGF was injected s.c. in the mouse flank. After 3, 7, or 10 days the plugs were perfused with Microfil as described below, mice were euthanized and the Matrigel plugs were dissected away from the tissue, photographed, and then fixed with 10% formalin/PBS for 48 hours at room temperature prior to scanning.

Vascular Perfusion with Microfil

A freshly prepared solution of Microfil compound (MV-120; Flow Tech, Inc., South Windsor, CT, USA) was prepared and used immediately, according to the manufacturer recommendations. We used a blue version of Microfil, although other colors are also available. It consisted of 42% of MV-120, 53% of the diluent solution, and 5% of a curing agent. The abdominal cavity and rib cage of each plug- or tumor-bearing mouse were opened under anesthesia. Intracardial cannulation of the left ventricle was done with a 27½g. needle connected to a polyethylene catheter with 1.6 mm tubing while simultaneously nicking the right atrium, and the mouse circulation was perfused with 20 mL of a 0.1% heparinized solution in PBS (heparin; Sigma, H3393, St. Louis, MO, USA) through a pressurized pump (Masterflex System Model 7553-70; Cole Parmer, Vernon Hills, IL, USA) at 2 mL/min, which we found was sufficient for optimal perfusion but did not result in vascular damage. Thereafter, 20 mL of the Microfil mixture was perfused through the same catheter by stopping the pump, moving the back end of the catheter tubing to a 50-mL conical tube containing fresh Microfil solution, and then restarting the pump [16]. Perfusion was allowed to continue for 20 minutes, during which procedure the animal dies under anesthesia. Obvious perfusion in the eyes and tail served as a reliable marker for systemic perfusion of the blood circulation. The neovasculature was also obviously perfused in the LLC tumors and Matrigel plugs (as indicated by blue colored vessels in the tumor and plugs, postperfusion). The Microfil solution was allowed to polymerize at 4°C overnight, after which the tumors or plugs were resected with surgical scissors, and fixed overnight in 10% formalin/PBS.

Scanning

Fixed samples were scanned in a micro-CT system [6]. A Skyscan 1172, 11 MPixel camera model, high-resolution

cone-beam micro-CT scanner (Skyscan, Ltd, Antwerp, Belgium) was used. The specimens were placed inside a 13-mm-diameter ultracentrifuge tube (Nalgene, 3410-1351, Rochester, NY, USA) with the bottom cut off and replaced with a plug of poster putty for placement on the scanner stage. Multiple specimens can be layered within the tube so long as they do not overlap across the horizontal. It is essential to avoid encasing the specimens in wrapping, such as Parafilm, as the wrapping material may absorb X-rays and be visible in the scanned images, which will complicate 3D reconstruction later. The top of the tube was plugged with poster putty to prevent dehydration of the specimens during scanning. The tube was positioned vertically onto the computer-controlled rotation stage of the micro-CT system. Micro-CT scanning and analysis were performed according to recent guidelines [6]. The following settings were used: camera pixel size of 8.75 μm (i.e., the near setting for the camera), image pixel size of 3 μm, source voltage of 60 kV, source current of 130 μA, no filter, frame averaging of 4, and scanned 180° around the vertical axis in rotation steps of 0.28°, one specimen per scan. The average scan duration was 1 hour. These slices were reconstructed into 3D reconstructions using cone-beam reconstruction software (Skyscan NRecon) based on the Feldkamp algorithm, a process that yielded a total of ~3500 image slices per sample that were 3.0 μm thick in the axial plane. The following reconstruction settings were used: a ring artifact correction of 12, a beam hardening correction of 20%, no smoothing, and a postalignment correct of 1.

Summary of 3D Reconstruction, Image Processing, and 3D Analysis

The 3D construction and image processing were performed using the SkyScan accompanying software: NRecon, CTAn, and CTVox [29]. First, the images were resized by ¼, as reconstructed files were very large, which greatly slowed the computer processing. Second, the resized whole image was selected as a ROI, and then saved as a new series of image files. Next, the ROI image series was reloaded onto CTAn. The ROI images were processed from the 2D stack to create a stack of binary images and to eliminate background pixels (voxels in 3D). Once the 2D stack was refined, CTAn 3D analysis was performed to obtain vessel volumes and surface areas. Analyze 10.0 (AnalyzeDirect, Overland Park, KS, USA) was used to generate tree maps and to measure branch angles and segment lengths.

3D Reconstruction with CTVox

1. Reconstruct by SkyScan's volumetric reconstruction software, NRecon.
2. Open NRecon for 3D reconstruction with scanned files.
3. Select the scanned image top and bottom, and then "preview" to make sure the entire specimen is contained in the file series.
4. Set output ranges from 0.0 to 0.1, choose a unique destination folder, and save as a series of 8-bit BMP (bitmap image file format) image files in the new folder.
5. Start the 3D reconstruction (typically overnight).
6. Open the reconstructed files within the CTVox program.
7. Set up log-scale histogram on the channel screen.
8. Slide the histogram bar line to highlight the vessels and deplete the extravascular material from the image, and then save the 3D reconstruction as a single 2D image, as a 3D CTVox image (large file), or as a rotating movie of the 3D reconstruction using the flight recorder.

3D Reconstruction Analysis from Compiled 2D Stacks

1. Open the CTAn program and open the reconstructed files. Optional: resize the files to ¼ of the original size. This step greatly reduces computer processing time for large (~1 cm^3) samples. The reconstructions do not need to be resampled to the original size prior to analysis, as CTAn converts the sample dimensions during the "resize" step. We compared resized (both ¼ and ½ size) with nonresized images followed through the remaining steps, and found the reconstructions and subsequent analysis to yield identical results (not shown).
2. Select ROI by widening an ROI circle around the area including the specimen, but excluding the outer tube. The tube can be seen as a thick circle around the periphery in each image. Although it is not strictly necessary, a tighter fitting VOI can be created by resizing the ROI at multiple image slices within the stack. This will "crop" the VOI and can reduce processing time for the thresholding and despeckling steps later.
3. Save the selected ROI to a new folder as "voi.ROI."
4. Open the ROI files (see example in Figure 2B).
5. Set up and run the following task list:
   a. Thresholding: Mode, Global; Lower gray threshold, 30; Upper gray threshold, 255 (see example in Figure 2C).
   b. Despeckle: remove white speckles/3D space/less than 100 voxels/apply to image (see example in Figure 2D).
   c. Thresholding: Mode, Global; Lower gray threshold, 75; Upper gray threshold, 255 (see example in Figure 2E).Processing at this step can take several hours. The final result will be a series of background-subtracted binarized 2D images with solid white "vessel" sections against a black background. Reconstructions can be visualized using various software packages, such as CTVox or CTVol accompanying software (Figure 3A).
6. Check processed images by reopening the "voi.ROI" files, and then chose the task for "3D analysis."
7. Select "Preferences," set units to μm, and then run the "3D analysis" task.

8. Copy the outputs to a database program such as Microsoft Excel.
9. Tree analysis, as in Figure 4, can also be carried out with the completed reconstructions using Analyze (Analyze-Direct). In our studies, we used Microsoft Excel to compile data from the tree analysis and Kaleidograph to generate dot and box plots.
10. Tortuosity (T_g) was calculated using a surface-based distance metric (Phil Salmon, Bruker-microCT, personal communication). Surface areas (SSA), thickness (vessel diameter, D), and volumes (V) were derived from CTAn as described above. Like the distance metric [7], general tortuosity can be determined as the ratio of surface areas of given vessels to the surface areas of idealized cylinders with the same volume and diameters [1]. Surface area of a cylinder (length × circumference) can be expressed as $(4 \times V)/D$. Hence, we used the following calculation for general tortuosity: $T_g = (\mathrm{SSA} \times D)/(4 \times V)$.

Statistical Analysis

One-way ANOVA followed by Fisher PLSD analysis was used for all statistical data analysis, using StatView (SAS, Cary, NC, USA). A 5% probability was considered significant.

RESULTS

Using Microfil perfusion, micro-CT scanning, and 3D reconstruction of tumor vasculature, we recently determined that angiogenesis in xenografted tumors in mice deleted for the RLIP76 gene was substantially blocked compared with WT [24]. The neovasculature was analyzed days to weeks later, after angiogenesis in the xenografts has occurred. This method relies on the perfusion of competent vessels connected to the peripheral circulation within the tumor, with the hydrophilic, silicon-based polymerizing contrast agent Microfil, perfused via a catheter inserted in the heart [16]. On the basis of these initial results, we sought to refine this method further to be useful as a general tool for *ex vivo* angiogenesis or other vascular studies.

We optimized the perfusion, micro-CT scanning, and image-processing steps to generate 3D reconstructions of the neovasculature in the resected tumors, with an isotropic voxel size of 3 μm (Figures 1 and 2), ensuring inclusion of narrow vessels (capillaries) and minimal background in the reconstructions [24]. We applied this revised method for observing the development of neovascular structures in developing solid tumors in mice over time *ex vivo*. Microfil was perfused at a steady flow rate at 2 mL/min through the left ventricle via a catheter attached to a perfusion pump (Figure 1A,B) in C57Bl/6 mice 7 and 10 days after bolus injection of LLC cells. The dark blue Microfil suspension perfused the peripheral circulation quickly, as within seconds, blood vessels could clearly be seen to fill with the blue Microfil throughout peripheral tissues, including the spleen, colon, and other organs (Figure 1C), and upon later inspection, blood vessels in the brain were also perfused (results not shown). By seven days and later at 10 days, discrete solid neoplasias had formed, and these were deeply perfused with the Microfil solution, which included small diameter vessels (Figure 3A). Tumor volumes at 7 and 10 days averaged 466 and 568 mm^3, respectively. Gross examination indicated little, if any, leakage of the Microfil from the blood circulation into the surrounding tissue (Figure 1D), indicating that in this system, perfusion did not rupture most vessels, and the perfused vessels were impermeable to the compound, which is a large polymer.

We next imaged the neovasculature by micro-CT scanning of the Microfil-perfused, resected tumors at 3 μm isotropic voxel resolution, using a Skyscan micro-CT scanner (Figure 2A; see Materials and Methods) (SkyScan, Kontich, Belgium). The scanner created a stack of 2D images that could then be compiled into a 3D reconstruction. However, to reconstruct the Microfil-perfused vasculature accurately—particularly the microvasculature—it was essential to eliminate the background X-ray absorbance, representing the surrounding tumor tissue as well as the tube in which the samples were placed, from the 2D images before 3D compiling (Figure 2B), while simultaneously preserving the regions of the image which represented the Microfil vascular casts in each image. Therefore, we developed a simple yet precise, nonbiased, threshold-based, image-processing scheme using the accompanying software to apply to the image stacks, which yielded a stack of 2D binary images for each sample representing only the radioopaque regions, corresponding to the perfused vessels (Figure 2E,F; see Materials and Methods) An initial threshold step with a lower gray value of 30 (using a 1-255 LUT) was determined empirically, using 30 randomly selected fields, to be the minimum level to reduce background tissue absorbance to be low enough for subtraction in subsequent steps, while maintaining pixels (representing voxels) derived from Microfil X-ray absorbance (cf. Figure 2B,C). Next, the despeckle function was applied in 3D to subtract background absorbance voxels; again the minimal voxel size (100) was determined empirically to eliminate nonvessel voxels, well below a threshold for microvessels, for which even the shortest vessels corresponded to several hundred voxels (Figure 2D). Finally, a second threshold was applied with a slightly higher minimum gray value, which we determined resulted in nearly complete elimination of spurious absorbance pixels without altering or deleting pixels derived from vessel casts (Figure 2E). Manual inspection of the raw and processed image stacks confirmed that the processing scheme selectively preserved the Microfil absorbance, including small voxels representing the microvasculature, and effectively deleted the background material (Figure 2B–F)

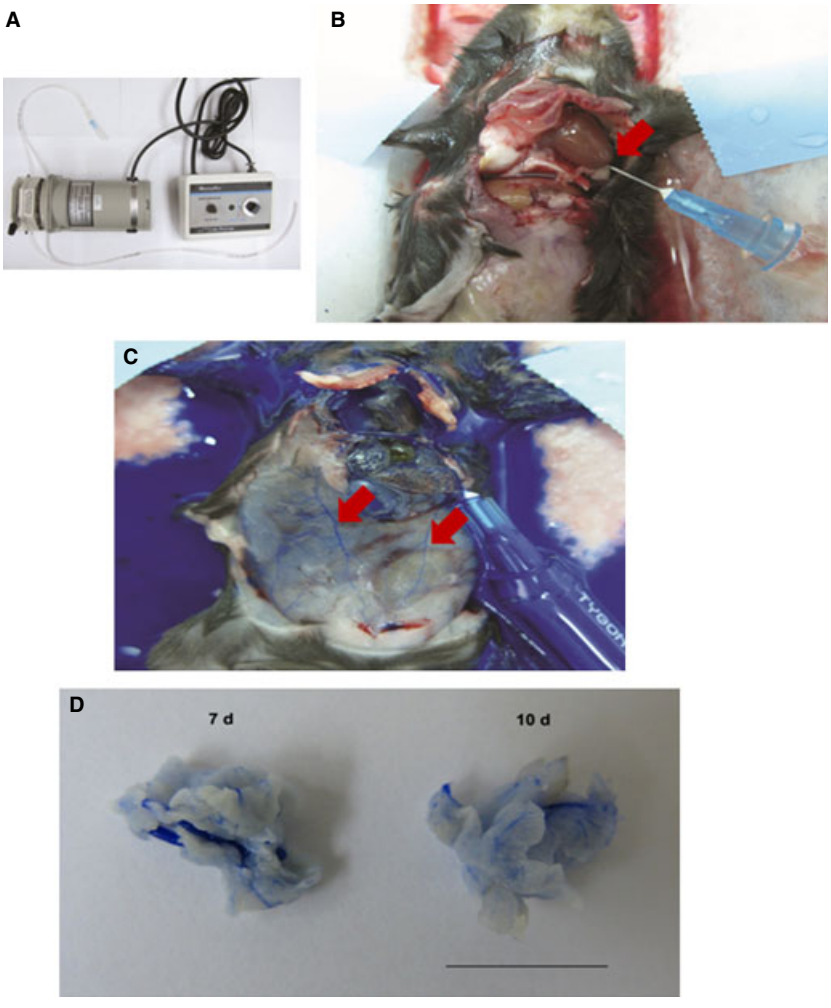

Figure 1. Perfusion of peripheral blood circulation and xenografted tumors with heparin and Microfil. (**A**) Tubing and pump (pump speed, 2 mL/min). (**B**) Catherization in left ventricle, for exsanguination with 0.1% heparinized solution. The right atrium is nicked when the catheter is inserted (arrow). (**C**) Microfil perfusion through the same catheter after heparin treatment. Arrows point to Microfil perfused in peripheral blood vessels. (**D**) Macroscopic appearance of Microfil-perfused LLC carcinomas derived from a bolus injection of 1×10^6 tumor cells in the mouse flanks at seven days (left) and 10 days (right). Bar, 10 mm.

From the scans we generated 3D reconstructions of the neovasculature as binarized images that included small vessels and minimal background voxels (Figure 3A, top row). Skeletonized images can also be generated from these reconstructions (Figure 3A, bottom row). We also generated movies to visualize the 3D reconstructions in full rotation (movie clips S1, S2). These reconstructions not only offered new views of the tumor vasculature, but allowed us to measure the vascular geometries, including total and individual vessel volumes, and individual vessel diameters at the widest points (presumed to be the branch points). Measurements of total vessel volumes of each structure complemented visual inspection of the reconstructions and confirmed the progressive neovascularization in the developing tumors (Figure 3B and Table 1). From the 3D reconstructions we also calculated individual vessel diameters and volumes. Figure 3C shows the range of vessel diameters as a frequency function of the total vascular volumes at 7 and 10 days, and Figure 3D shows the distribution of vessel volumes as a function of vessel diameters. These reconstructions included vessels with diameters in the range 3–14 μm, indicating capillaries, and volumes of these individual small vessels could be calculated. By 10 days there was a broader distribution of vessel volumes, thicknesses, and by extension, vessel lengths in the tumors. Vascular-specific surface area (SSA, Figure 3E) and microvascular density (MVD, Figure 3F) determinations showed a trend toward increased SSA and MVD in the 10 days tumors (although these differences were not significant), confirming the volume and diameter measurements and indicating an increase in abundance of smaller vessels in the 10 days tumors (see also Table 1).

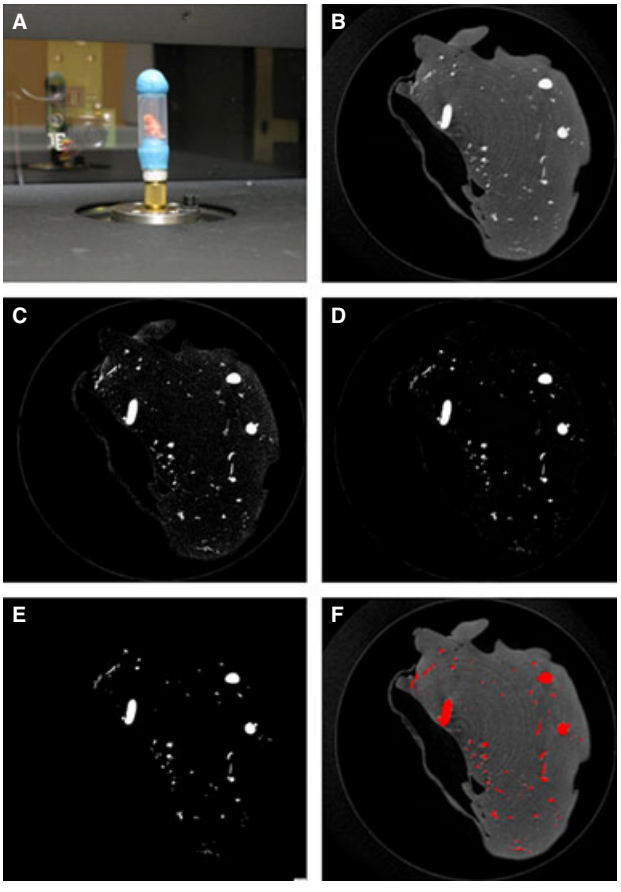

Figure 2. MicroCT scanning setup; raw and thresholded images. (**A**) A perfused tumor specimen (with orange-colored Microfil solution) prepared for X-ray scanning. The specimen was held in place in a polyethylene tube with poster putty (blue) on top and bottom, and the assembly was fixed onto a brass spigot in the SkyScan scanner. (**B**) Example of a raw. BMP reconstructed image slice (3 μm thick) from a scanned LLC tumor sample including the polyethylene tube, before reconstruction. Small and large vessels are seen in cross section as bright gray regions, within the darker gray surrounding tissue, which weakly absorbed the X-rays. The tube, which weakly absorbs X-rays, can usually be seen around the periphery (*). (**C**) The same cross section from (**B**) after the first thresholding step (lower limit 75, upper limit 225) using the CTAn task list. (**D**) Image from (**C**) after despeckling. (**E**) The final cross section converted into a binarized image after a second threshold step (lower limit 105, upper limit 225). This series of steps preserves small diameter vessels, seen here as small white dots, while eliminating background pixels from the surrounding tissue and the tube. (**F**) Overlay of binarized final image from (**E**), pseudocolored red, with raw reconstruction scan from (**B**). Note the absence of background pixels in the final processed image (**E**), which otherwise can create background voxels in the 3D models that would also be included in the analysis. Bar, 400 μm.

The apparently high connectivity in the reconstructions allowed us to convert the 3D images into segmented tree structures for further analysis of the vascular architecture including segment length and branching structure. Representative analysis is shown in Figure 4. Each new branch in the tree map (Figure 4A) represented either a side branch or bifurcation from the parent vessel. Branch angles in both the 7 and 10 days reconstructions showed a broad distribution with a nearly identical median, demonstrating no significant median difference in branch angles at the two time points (Figure 4B and Table 1). Segment lengths also varied greatly in tumors at both 7 and 10 days; however, the median segment lengths were identical (Figure 4C and Table 1). The segment length measurements represent distances between branches or bifurcations; thus, there was no difference in the overall distribution of vessel branching in the more mature tumors. However, these analyses revealed several differences in vascular architecture in the 7 and 10 days tumors, as implicated by vessel volume and diameter measurements (Figure 3). As shown in Figure 4B, branch angle measurements of 0° (empty columns along the abscissa) indicate vessels with no branches or bifurcations. Notably, there was a higher concentration of nonbranched vessels furthest from the root in the 7-day tumors than in the 10-day tumors (right side of the histograms), indicating extensive branching throughout the larger vascular tree in the more mature tumors. Similarly, as shown in Figure 4C, whereas the median length and overall distribution of segments were the same between these tumors, there was a ~30% increase in the total number of segments at 10 days compared with seven days, confirming the presence of longer vessels (i.e., more segments, given a similar distribution of branches). The longer vessels also correlated with an overall increase in tortuosity. Ratios of vessel length to the minimal linear distance between endpoints (e.g., of cylinders) rose from 1.25 ± 0.31 at seven days, to 2.63 ± 0.67 at 10 days, indicating an increase in vascular curvature over time in the tumors (Table 1; see Materials and Methods). Together, these metrics corroborate the reconstructions showing a more extensive tree structure at 10 days.

We next extended the 3D vascular reconstruction approach to analyze neovasculature in Matrigel plugs in the absence of tumor cells. We used growth factor-reduced Matrigel plugs (500 mm^3) $\pm$ 100 ng/mL VEGF, injected into the mouse flanks, and perfused with Microfil at 3, 7, or 10 days for micro-CT scanning. The plugs showed progressive neovascularization over time, with or without VEGF, based on the presence of Microfil and apparent enrichment of the plugs with blood. Thus, Matrigel plugs support infiltration of competent vessels which can be perfused from the peripheral circulation. Gross observations of the Microfil-perfused plugs, facilitated by the translucency of the plugs and opacity of the Microfil, suggested that most of the neovasculature was localized to the periphery of the plugs, even after 10 days (Figure 5A). Plugs scanned at three days showed no apparent X-ray absorbance over background, indicating that substantial angiogenesis did not occur until at least three days after implantation (results not

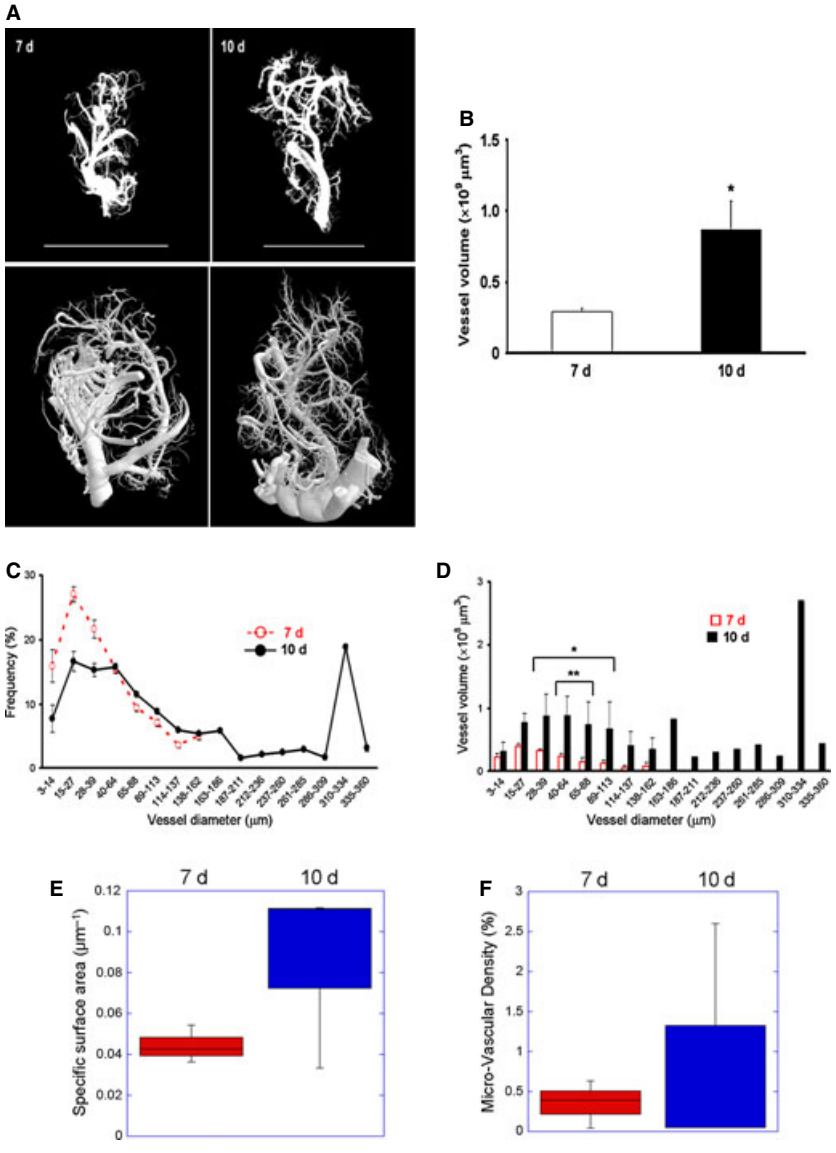

Figure 3. Tumor neovasculature 3D modeling and analysis by X-ray μCT scanning in WT C57Bl/6 mice. (**A**) Sample images of 3D reconstructions of neovasculature in LLC tumors (left, 7 days; right, 10 days) acquired by X-ray μCT scanning of tumors derived as in Figure 1D at 3 μm voxel resolution, followed by postscan processing and 3D reconstruction. Top row, reconstruction view in CTVol; bottom row, using CTVox (different samples). Bars, 10 mm. (**B**) Total vessel volumes in 3D reconstructed vascular models from tumors derived in WT mice. $n = 3$, * $p < 0.01$. (**C**) Frequency distribution of the vascular diameters in LLC tumors at seven days (dotted red line) and 10 days (solid black line). (**D**) Individual vessel volumes plotted against vascular diameters from (C) (* $p < 0.05$, ** $p < 0.01$). (**E**) Vascular-specific surface area in 7- and 10-day tumors determined by the ratio of total vascular surface area to volume. (**F**) Microvascular densities in 7- and 10-day tumors determined as the percentage of total tumor volume occupied by the vascular casts.

shown). However, we were able to generate 3D vascular reconstructions as early as seven days after implantation, as well as in 10 days plugs. We then scanned the plugs by micro-CT and generated 3D reconstructions using the same parameters as for the resected tumors (Figure 5B). The 3D reconstructions recreated "vessels" which closely resembled the overall appearance of the perfused plugs (cf. Figure 5A, B), indicating that the same scanning and reconstruction parameters used for tumors will also reproduce accurate 3D vascular reconstructions from Matrigel plugs. From these we calculated vessel volumes (Figure 5C) and vessel diameters measured at the widest points (Figure 5D,E). These parameters corroborated the visual inspection, such that total vessel volumes increased over time (Figure 5C), with larger diameter vessels appearing later (Figure 5D,E), indicating vessel maturation. As expected, the addition of VEGF was

Table 1. Structural comparisons of tumor vasculature at 7 and 10 days

Time	Total vascular volume ($\times 10^8$ μm^3)	SSA (μm^2)	MVD (%)	Branch angle (°)	Segment length (μm)	T_g (ratio)
7 d	2.9±0.78	0.044±0.005	0.35±0.002	116.5±34.5	31.25±1.69	1.25±0.31
10 d	8.7±0.6	0.085±0.025	0.90±0.008	114.5±35.5	31.49±1.53	2.63±0.67

Total vascular volume, specific surface area (SSA), mean vessel density (MVD), branch angle, segment length, and tortuosity (T_g) are shown ± SEM for data compiled from tumor vessels at seven days and 10 days.

associated with an increase in all these parameters. Thus, new blood vessel formation in Matrigel plugs can be monitored dynamically by micro-CT scanning, 3D reconstruction, and quantitative analysis.

DISCUSSION

We have refined a generalizable method of *ex vivo* X-ray micro-CT scanning and computer-assisted 3D reconstruction of Microfil-perfused vascular structures, including microvasculature, which can be applied to studying formation and topological features of neovasculature in normal and pathological angiogenesis in animal models. The 3-μm-resolution, lower limit of the scans (lower than the 15–16 μm isotropic voxel size from several previous studies [12,16,36]) ensured inclusion of the capillary structures within the 3D reconstructions. Importantly, thorough depletion of background absorbance using a precise, nonbiased, threshold-based image-processing scheme (see Materials and Methods) allowed for accurate reconstruction and subsequent quantitation of vascular volumes, diameters, branch angles, segment lengths, and other morphological parameters from the resultant 3D reconstructions which included microvasculature [12].

This system offers more thorough structural characterization of vasculature than 2D image analysis such as in histological sections and several other intravital imaging methods, in roughly the same amount of analysis time [9,14]. The time for the overall procedure (starting with the day of perfusion, i.e., after angiogenesis has been induced) can range from a few days up to one week, depending on several factors, including the size of each specimen, the perfusion efficiency, and the processing speed of the computer running the software. Micro-CT scanning can be left to run overnight, and using our scanning parameters, takes approximately 3–4 hours for a sample diameter of ~1 cm. Up to three samples can be placed in the scanner for a single (partitioned) scanning procedure which can be run overnight. 3D reconstruction, which occurs after the scanning step, can also be run overnight, but must be run separately for each specimen and takes ~3 hours per specimen. Postreconstruction quantitative analysis can be completed within a few hours.

Perfusion with Microfil relies on the competency of the vessels within the structure of interest. Thus, we have also confirmed that vessels in Matrigel plus can be perfused, resulting in accurate vascular casting in the plugs [17,34]. The apparent restriction of the neovasculature to the plug peripheries may reflect angiogenesis initiating from multiple points in the host vasculature and invading the plug from many directions, in contrast to the more tree-like structures in the tumors. Alternatively, "dead end" vessels could represent sealed or damaged vessels, or could also reflect limited perfusion due to localized fluctuations in perfusion pressure. Similarly, tumor vessels with low patency may be missed with micro-CT casting approaches.

Micro-CT cast analysis does not rely on expression of specific vascular cell markers (e.g., CD31 or smooth muscle actin), on the selectivity of marker expression under particular conditions, or on the ability of tracer probes to access those markers by any labeling methods. However, radioopaque tracers designed to absorb X-rays are conceivable [8,10,19,33]. We have found that using the heart catheter, the Microfil compound readily perfused and formed a cast of the complete blood circulation, including within the brain (not shown), and perfusion was rapid in mice. These results suggest that this method may also be applicable to studies in larger animal models, without the Microfil hardening too quickly. It should be noted that contrast agents such as Microfil in vascular reconstructions may not be as useful in more advanced tumors, or in other model systems in which vessel permeability may be high and the agent can leak through weak and damaged parts of the vessel wall [22]. However, Microfil is a large polymer and may not be useful by itself for assaying vascular permeability, although it has been combined with other contrast agents for this purpose [23].

Accurate 3D reconstructions of neovascular structures derived by this method can be used to assess multiple morphological features with implications for the unique properties of the vasculature in pathological settings. For example, tumor neovasculature is believed to be more tortuous and less hierarchically organized than normal blood vessels, and we have found that tortuosity increased in the

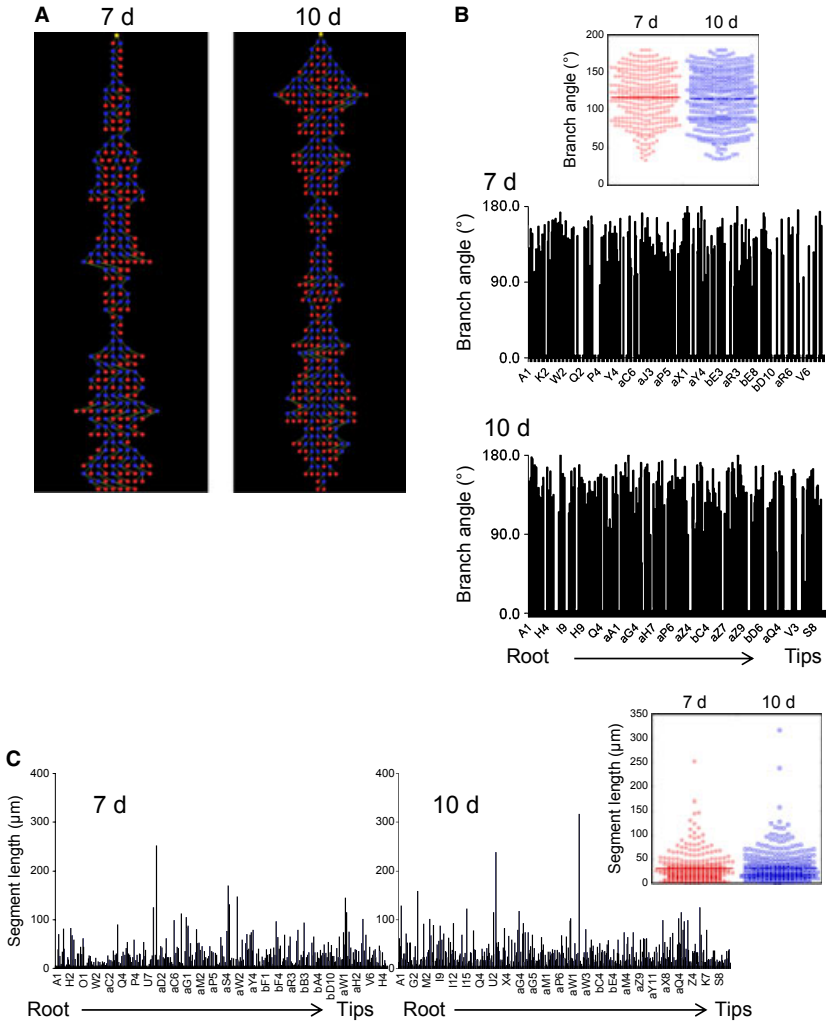

Figure 4. Tree analysis of LLC tumor neovasculature. (**A**) Representative tree structures determined from micro-CT vascular reconstructions in xenografted LLC tumors at seven days (left) and 10 days (right) postimplantation. Yellow nodes represent the tree root, blue nodes indicate branch or bifurcation points, and red nodes indicate branch termini. (**B**) Branch angle measurements are shown for each tree segment from (**A**), beginning with "A1" as the root segment. Seven days, top; 10 days, bottom. Inset, dot plot of branch angles at 7 and 10 days, excluding angles of 0° from nonbranched segments. Medians are shown with a horizontal line in each case. (**C**) Segment length measurements from the tree analysis. Seven days, left; 10 days, right. Inset, dot plot of all segment lengths at 7 and 10 days. Medians are shown with a horizontal line in each case.

tumor vasculature over time in the carcinoma xenografts. Our results closely match those found in gliomas [7]. Other morphological measurements, including branch angles and segment lengths, provide an indication of the distribution of vessels in the tree structure and also can indicate hemodynamic properties [3,5,11,19,25,26,38]. In our reconstructions of tumor neovasculature in LLC xenografts in mouse flanks, we found a broad distribution of branch angles but a narrow distribution of segment lengths between branch points throughout the tree structure, with no distinct changes in patterns of segment length across vessel generations from the root to the tips of the tree (Figure 4). These findings are in contrast to previous studies using maceration casts and other modeling techniques in other tumor models in mice, which showed increasing branch order (i.e., shorter segment lengths) at higher generations, variability in lengths that did not seem to correspond hierarchically, and other unusual properties such as loop structures or long nonbranched segments; however, in our studies vessel diameters did vary widely, particularly at 10 days, as in previous studies [26,31,37]. The particular vascular architecture in the xenografts in this study may reflect heterogeneity in neovascular tree structure depending on the tumor type; for example, in our previous studies with this method we observed that neovascular trees in xenografted B16 melanomas consisted primarily of a single axial artery interspersed with small-diameter, relatively straight lateral branches, as opposed to the evidently more tortuous architecture of the

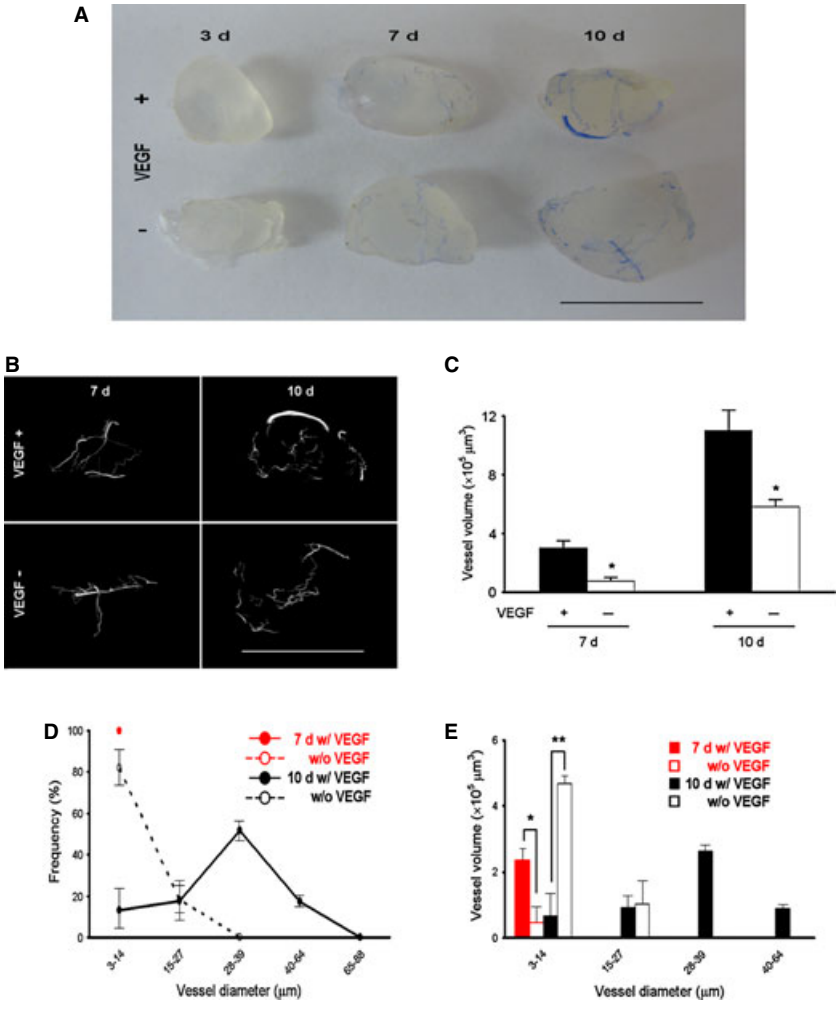

Figure 5. Matrigel plug neovasculature 3D modeling and analysis by X-ray micro-CT scanning in WT mice. (**A**) Macroscopic appearance of Matrigel plugs with or without VEGF at three days (left), seven days (middle), and 10 days (right). Bar, 10 mm. (**B**) Images of 3D models of neovasculature in Matrigel plugs (top, +VEGF; bottom, -VEGF; left, seven days; right, 10 days) acquired by X-ray micro-CT scanning at 3-μm voxel resolution and 3D reconstruction. Bar, 10 mm. (**C**) Total vessel volumes in 3D reconstructed images from Matrigel plugs derived in WT mice. $n = 3$, * $p < 0.001$. (**D**) Frequency distribution of the vascular diameters in Matrigel plugs at seven days (red lines) and 10 days (black lines). Dotted lines, −VEGF; solid lines, +VEGF. (**E**) Individual vessel volumes plotted against vascular diameters in Matrigel plugs from (**D**) (*$p < 0.001$, **$p < 0.0001$).

LLC tumor vasculature [24]. The basic structure of sprouting from a large axial vessel appears to be a common feature of tumor neovasculature [13]. However, a relatively small range of examples of micro-CT 3D reconstructions of tumor neovasculature have been reported to date, making broad, direct comparisons with other modeling or reconstruction efforts difficult. As 3D reconstructions or models of tumor vasculature continue to be examined, more thorough characterization of the distinctive nature of tumor angiogenesis may emerge.

Vascular parameters such as vascular network flow pathways, hemodynamics, and the distribution and morphologies or other properties of cells of the vessel wall cannot be determined directly with this method, as the vascular tree reconstructions are generated from casts of the patent vessel lumens. For example, tumor vessels cannot be assumed to be cylindrical—which has direct implications for hemodynamic properties [13]—but this level of architectural detail was not evident in branch point diameter measurements. However, SSA and MVD determinations provide surrogate indications of overall transport capacity of the vasculature, and here we find SSA in LLC tumors comparable with previously reported levels for colonic carcinoma xenografts, suggesting a similar degree of vessel caliber in the LLC xenografts [13]. MVD levels were also within a similar range to other carcinoma xenografts [13]. MVD, based on intervessel distance, is determined by the balance of local angiogenic and antiangiogenic factors, as well as by other factors such as

local nutrient concentrations; thus, our results suggest an increase in both angiogenesis as well as metabolic burden of the tumor cells [18]. Furthermore, coupling hemodynamic assessments such as by dynamic contrast-enhanced MRI or CT [11,21,27] with micro-CT-based tree reconstruction, can be explored in animal models as a way to determine flow variability within the tumor neovasculature (e.g., tissue blood flow, blood volume, mean transit time, and capillary permeability) as functions of the tree architecture [4,20]. Hence, each of these imaging and modeling approaches, including cast reconstructions such as in this study, is alone insufficient to yield the complete spectrum of vascular parameters, but combinatorial approaches as well as continual refinement of these methods can improve imaging and subsequent analysis further. Another obvious drawback to the method is that it is invasive, and the animal subjects have to be sacrificed to perform the experiments. Thus, one animal must be used for each time point or other variable. The structure of interest must be able to be accommodated by the scanner; in our case the specimen size limit was 50 mm in height, width, and length [24,40]. This method also could conceivably be used to evaluate vasculogenesis and to map vascular structures in developed organs and soft tissues. Finally, this method cannot be used for human subjects as it is an *ex vivo* micro-CT technique.

PERSPECTIVE

This study establishes a standardized approach to *ex vivo* micro-CT scanning, reconstruction and measurement of vascular volumes, branch point diameters and angles, segment length distribution, and other architectural parameters, including the microcirculation. By applying a nonbiased, thresholded depletion of background X-ray absorbance in scan processing, small diameter vessels can be reconstructed accurately, while eliminating excess voxels from the reconstructions. This allows for precision in quantitation of vascular geometries, which will be particularly valuable in investigations of the unique properties of neovasculature in pathological settings such as in solid tumors. This approach was further used to confirm perfusion in Matrigel plugs, and to measure the vascular parameters in the plugs. Thus, this approach can be utilized for a broad range of studies in macro- and microvascular biology.

ACKNOWLEDGMENTS

This work was supported by NIH grants HL093416 to L.E.G., DK064344 to R.S., 1S10RR026727 and NIH-NCRR, BRS S10 shared equipment grant to M.F.B., and American Heart Association Postdoctoral Fellowship 12POST12040257 to S.L. We thank Robin Pixley for assistance with micro-CT and Phil Salmon for assistance with tortuosity calculations.

DISCLOSURES

The authors declare no competing financial interests or other disclosures.

REFERENCES

1. Azegrouz H, Trucco E, Dhillon B, MacGillivray T, MacCormick IJ. Thickness dependent tortuosity estimation for retinal blood vessels. *Conf Proc IEEE Eng Med Biol Soc* 1: 4675–4678, 2006.
2. Baatout S. Endothelial differentiation using Matrigel (review). *Anticancer Res* 17: 451–455, 1997.
3. Baluk P, Hashizume H, McDonald DM. Cellular abnormalities of blood vessels as targets in cancer. *Curr Opin Genet Dev* 15: 102–111, 2005.
4. Bauerle T, Komljenovic D, Berger MR, Semmler W. Multi-modal imaging of angiogenesis in a nude rat model of breast cancer bone metastasis using magnetic resonance imaging, volumetric computed tomography and ultrasound. *J Vis Exp* 66: e4178, 2012.
5. Bian XW, Wang QL, Xiao HL, Wang JM. Tumor microvascular architecture phenotype (t-map) as a new concept for studies of angiogenesis and oncology. *J Neurooncol* 80: 211–213, 2006.
6. Bouxsein ML, Boyd SK, Christiansen BA, Guldberg RE, Jepsen KJ, Muller R. Guidelines for assessment of bone microstructure in rodents using micro-computed tomography. *J Bone Miner Res* 25: 1468–1486, 2010.
7. Bullitt E, Gerig G, Pizer SM, Lin W, Aylward SR. Measuring tortuosity of the intracerebral vasculature from MRA images. *IEEE Trans Med Imaging* 22: 1163–1171, 2003.
8. Cai W, Chen X. Multimodality molecular imaging of tumor angiogenesis. *J Nucl Med* 49(Suppl. 2): 113S–128S, 2008.
9. Chappell JC, Wiley DM, Bautch VL. How blood vessel networks are made and measured. *Cells Tissues Organs* 195: 94–107, 2012.
10. Costouros NG, Diehn FE, Libutti SK. Molecular imaging of tumor angiogenesis. *J Cell Biochem Suppl* 39: 72–78, 2002.
11. Cuenod CA, Fournier L, Balvay D, Guinebretiere JM. Tumor angiogenesis: pathophysiology and implications for contrast-enhanced MRI and CT assessment. *Abdom Imaging* 31: 188–193, 2006.
12. Downey CM, Singla AK, Villemaire ML, Buie HR, Boyd SK, Jirik FR. Quantitative ex-vivo micro-computed tomographic imaging of blood vessels and necrotic regions within tumors. *PLoS One* 7: e41685, 2012.
13. Folarin AA, Konerding MA, Timonen J, Nagl S, Pedley RB. Three-dimensional analysis of tumour vascular corrosion casts using stereoimaging and micro-computed tomography. *Microvasc Res* 80: 89–98, 2010.
14. Fox SB. Assessing tumor angiogenesis in histological samples. *Methods Mol Biol* 467: 55–78, 2009.
15. Fukumura D, Duda DG, Munn LL, Jain RK. Tumor microvasculature and microenvironment: novel insights through intravital imaging in pre-clinical models. *Microcirculation* 17: 206–225, 2010.
16. Grabherr S, Hess A, Karolczak M, Thali MJ, Friess SD, Kalender WA, Dirnhofer R, Djonov V. Angiofil-mediated visualization of the vascular system by microcomputed tomography: a feasibility study. *Microsc Res Tech* 71: 551–556, 2008.

17. Hegen A, Blois A, Tiron CE, Hellesoy M, Micklem DR, Nor JE, Akslen LA, Lorens JB. Efficient in vivo vascularization of tissue-engineering scaffolds. *J Tissue Eng Regen Med* 5: e52–e62, 2011.
18. Hlatky L, Hahnfeldt P, Folkman J. Clinical application of antiangiogenic therapy: microvessel density, what it does and doesn't tell us. *J Natl Cancer Inst* 94: 883–893, 2002.
19. Kerbel RS. Tumor angiogenesis. *N Engl J Med* 358: 2039–2049, 2008.
20. Kim E, Stamatelos S, Cebulla J, Bhujwalla ZM, Popel AS, Pathak AP. Multiscale imaging and computational modeling of blood flow in the tumor vasculature. *Ann Biomed Eng* 40: 2425–2441, 2012.
21. Koh TS, Shi W, Thng CH, Ho JT, Khoo JB, Cheong DL, Lim TC. Assessment of tumor blood flow distribution by dynamic contrast-enhanced CT. *IEEE Trans Med Imaging* 32: 1504–1514, 2013.
22. Lang S, Muller B, Dominietto MD, Cattin PC, Zanette I, Weitkamp T, Hieber SE. Three-dimensional quantification of capillary networks in healthy and cancerous tissues of two mice. *Microvasc Res* 84: 314–322, 2012.
23. Langheinrich AC, Ritman EL. Quantitative imaging of microvascular permeability in a rat model of lipopolysaccharide-induced sepsis: evaluation using cryostatic micro-computed tomography. *Invest Radiol* 41: 645–650, 2006.
24. Lee S, Wurtzel JG, Singhal SS, Awasthi S, Goldfinger LE. RALBP1/RLIP76 depletion in mice suppresses tumor growth by inhibiting tumor neovascularization. *Cancer Res* 72: 5165–5173, 2012.
25. Less JR, Posner MC, Skalak TC, Wolmark N, Jain RK. Geometric resistance and microvascular network architecture of human colorectal carcinoma. *Microcirculation* 4: 25–33, 1997.
26. Less JR, Skalak TC, Sevick EM, Jain RK. Microvascular architecture in a mammary carcinoma: branching patterns and vessel dimensions. *Cancer Res* 51: 265–273, 1991.
27. Liu P, Li J, Zhang C, Xu LX. Micro-CT molecular imaging of tumor angiogenesis using a magnetite nano-cluster probe. *J Biomed Nanotechnol* 9: 1041–1049, 2013.
28. Malinda KM. In vivo matrigel migration and angiogenesis assays. *Methods Mol Med* 46: 47–52, 2001.
29. Marxen M, Thornton MM, Chiarot CB, Klement G, Koprivnikar J, Sled JG, Henkelman RM. MicroCT scanner performance and considerations for vascular specimen imaging. *Med Phys* 31: 305–313, 2004.
30. Minnich B, Lametschwandtner A. Lengths measurements in microvascular corrosion castings: two-dimensional versus three-dimensional morphometry. *Scanning* 22: 173–177, 2000.
31. Miodonski AJ, Bugajski A, Litwin JA, Piasecki Z. Vascular architecture of human urinary bladder carcinoma: a SEM study of corrosion casts. *Virchows Arch* 433: 145–151, 1998.
32. Norrby K. In vivo models of angiogenesis. *J Cell Mol Med* 10: 588–612, 2006.
33. Ocak I, Baluk P, Barrett T, McDonald DM, Choyke P. The biologic basis of in vivo angiogenesis imaging. *Front Biosci* 12: 3601–3616, 2007.
34. Phongkitkarun S, Kobayashi S, Kan Z, Lee TY, Charnsangavej C. Quantification of angiogenesis by functional computed tomography in a Matrigel model in rats. *Acad Radiol* 11: 573–582, 2004.
35. Savai R, Langheinrich AC, Schermuly RT, Pullamsetti SS, Dumitrascu R, Traupe H, Rau WS, Seeger W, Grimminger F, Banat GA. Evaluation of angiogenesis using micro-computed tomography in a xenograft mouse model of lung cancer. *Neoplasia* 11: 48–56, 2009.
36. Schambach SJ, Bag S, Groden C, Schilling L, Brockmann MA. Vascular imaging in small rodents using micro-CT. *Methods* 50: 26–35, 2009.
37. Schoenfeld A, Levavi H, Breslavski D, Amir R, Ovadia J. Three-dimensional modelling of tumor-induced ovarian angiogenesis. *Cancer Lett* 87: 79–84, 1994.
38. Takahashi Y, Akishima-Fukasawa Y, Kobayashi N, Sano T, Kosuge T, Nimura Y, Kanai Y, Hiraoka N. Prognostic value of tumor architecture, tumor-associated vascular characteristics, and expression of angiogenic molecules in pancreatic endocrine tumors. *Clin Cancer Res* 13: 187–196, 2007.
39. Taub M, Wang Y, Szczesny TM, Kleinman HK. Epidermal growth factor or transforming growth factor alpha is required for kidney tubulogenesis in matrigel cultures in serum-free medium. *Proc Natl Acad Sci U S A* 87: 4002–4006, 1990.
40. Vegesna AK, Sloan JA, Singh B, Phillips SJ, Braverman AS, Barbe MF, Ruggieri MR, Sr, Miller LS. Characterization of the distal esophagus high-pressure zone with manometry, ultrasound and micro-computed tomography. *Neurogastroenterol Motil* 25: 53-e6, 2013.
41. Vukicevic S, Kleinman HK, Luyten FP, Roberts AB, Roche NS, Reddi AH. Identification of multiple active growth factors in basement membrane Matrigel suggests caution in interpretation of cellular activity related to extracellular matrix components. *Exp Cell Res* 202: 1–8, 1992.

SUPPORTING INFORMATION

Additional Supporting Information may be found in the online version of this article:

Movie clip S1. Representative 3D micro-CT reconstruction of the vasculature in a seven-day LLC tumor derived in a WT mouse.

Movie clip S2. Representative 3D micro-CT reconstruction of the vasculature in a 10-day LLC tumor derived in a WT mouse.

Experimental Gerontology 72 (2015) 204–217

Contents lists available at ScienceDirect

Experimental Gerontology

journal homepage: www.elsevier.com/locate/expgero

Prolonged performance of a high repetition low force task induces bone adaptation in young adult rats, but loss in mature rats

Vicky S. Massicotte [a], Nagat Frara [a], Michele Y. Harris [a], Mamta Amin [a], Christine K. Wade [b], Steven N. Popoff [a], Mary F. Barbe [a,c,*]

[a] Department of Anatomy and Cell Biology, Temple University School of Medicine, 3500 North Broad St., Philadelphia, PA 19140, USA
[b] Department of Physical Therapy, Thomas Jefferson University, Philadelphia, PA 19107, USA
[c] Department of Physical Therapy, Temple University, Philadelphia, PA 19140, USA

ARTICLE INFO

Article history:
Received 8 July 2014
Received in revised form 6 October 2015
Accepted 26 October 2015
Available online 27 October 2015

Section Editor: Christiaan Leeuwenburgh

Keywords:
Repetitive strain injury
Musculoskeletal
Bone
Inflammation
MicroCT
Aging
Radius

ABSTRACT

We have shown that prolonged repetitive reaching and grasping tasks lead to exposure-dependent changes in bone microarchitecture and inflammatory cytokines in young adult rats. Since aging mammals show increased tissue inflammatory cytokines, we sought here to determine if aging, combined with prolonged performance of a repetitive upper extremity task, enhances bone loss. We examined the radius, forearm flexor muscles, and serum from 16 mature (14–18 months of age) and 14 young adult (2.5–6.5 months of age) female rats after performance of a high repetition low force (HRLF) reaching and grasping task for 12 weeks. Young adult HRLF rats showed enhanced radial bone growth (e.g., increased trabecular bone volume, osteoblast numbers, bone formation rate, and mid-diaphyseal periosteal perimeter), compared to age-matched controls. Mature HRLF rats showed several indices of radial bone loss (e.g., decreased trabecular bone volume, and increased cortical bone thinning, porosity, resorptive spaces and woven bone formation), increased osteoclast numbers and inflammatory cytokines, compared to age-matched controls and young adult HRLF rats. Mature rats weighed more yet had lower maximum reflexive grip strength, than young adult rats, although each age group was able to pull at the required reach rate (4 reaches/min) and required submaximal pulling force (30 force-grams) for a food reward. Serum estrogen levels and flexor digitorum muscle size were similar in each age group. Thus, mature rats had increased bone degradative changes than in young adult rats performing the same repetitive task for 12 weeks, with increased inflammatory cytokine responses and osteoclast activity as possible causes.

1. Introduction

Work-related musculoskeletal disorders (WMSDs), also known as repetitive strain injuries and work-related overuse injuries, are the most reported types of occupational illnesses. According to the U.S. Bureau of Labor Statistics, WMSDs account for 34% of lost workday injuries and illnesses in the US, and cost on the order of $100 billion annually (OSHA, 2014; Bureau of Labor Statistics, 2012). Hand and wrist injuries are prevalent in occupations requiring upper extremity repetitive tasks, particularly with advancing age (Foss et al., 2011; Gerr et al., 2002). People above 35 years of age have increased numbers of days away from work (an indicator of illness severity), and people aged 45–54 have a higher incidence of work-related injuries (Bureau of Labor Statistics, 2011). Since age is a risk factor for these disorders, and since the average age of the American and international work force is rapidly increasing due to economic realities, more WMSD cases are predicted (Silverstein, 2008; Association of Occupational and Environmental Clinics, 2009; World Health Organization, 2007; WHO Scientific Group, 2003). Yet, the underlying mechanisms of these disorders are incompletely understood. The 2010 National Manufacturing Agenda of the National Institute of Occupational Safety and Health cites the need for etiologic research in determining the contribution of biomechanical mechanisms towards the development of tissue injury and musculoskeletal disorders (NIOSH, 2011).

It is well known that chronic cyclical tissue overload, in general, affects bone morphometry (Green et al., 2011; Pearson and Lieberman, 2004; Warden et al., 2005; Sample et al., 2010; Robling et al., 2001; Burr et al., 2002). A small number of studies have examined changes occurring in upper extremity bones as a consequence of prolonged performance of occupational tasks. Increased incidence of hand/wrist osteoarthritis and reduced bone mass has been identified in female dentists and teachers with heavy or one-sided hand workloads (Ding et al., 2010; Solovieva et al., 2005; Vehmas et al., 2005).

* Corresponding author at: Department of Anatomy and Cell Biology, Temple University School of Medicine, 3500 North Broad St., Philadelphia, PA 19140, USA.
E-mail address: mary.barbe@temple.edu (M.F. Barbe).

http://dx.doi.org/10.1016/j.exger.2015.10.014
0531-5565/

Bone scans of patients with upper extremity MSDs show increased blood flow and pooling (suggestive of inflammation) in affected forearm bones (Amorim et al., 2006; al-Nahhas et al., 1997). Such changes can increase osteopenia and fracture risk. Premenopausal women with carpal tunnel syndrome, a type of upper extremity MSD, have decreased bone mineral density in the distal radius, ulna, and metacarpal bones, compared to control subjects (Erselcan et al., 2001; Savas et al., 2007). Although still under investigation, such bone changes may be due to increases in inflammatory cytokines occurring with prolonged performance of occupational tasks (Barbe et al., 2013a; Carp et al., 2007; Rechardt et al., 2013; Rechardt et al., 2011; Riondino et al., 2011; Jain et al., 2014), since similar cytokine increases in other chronic inflammatory conditions and in vitro stimulate osteoclastogenesis and activity and impair osteoblast differentiation (Guo et al., 2008; Kulkarni et al., 2012; Lacey et al., 2009; Lange et al., 2010; Thomas, 2010; Rani et al., 2010).

Aging is also linked to bone degradative changes and decreased bone mass (Khosla et al., 2011; Srinivasan et al., 2003; Turner, 2007; Turner et al., 1995). One possible cause may be the increased inflammatory cytokine levels and responses in tissues of aging mammals, compared to young adults (Ershler and Keller, 2000; Orjalo et al., 2009; Stowe et al., 2010; Xin et al., 2011a; Cevenini et al., 2010). Although not yet examined to date, the combination of both aging and prolonged performance of an upper extremity repetitive task, may also enhance forelimb bone osteopenia and increase fracture risk.

We have developed an operant rat model of upper extremity WMSDs in which rats learn a reaching and grasping task for a food reward. We have shown that prolonged repetitive tasks lead to either trabecular bone adaptation or pathological bone changes, dependent on repetition rate, force load, and duration of task (Jain et al., 2014; Rani et al., 2010; Barr et al., 2003; Barbe et al., 2013b). Performance of a negligible or low force repetitive reaching and grasping task for 6–12 weeks by young adult rats induces radial bone adaptation, concomitant with transient increases in bone inflammatory cytokines (Barr et al., 2003; Barbe et al., 2013b). In contrast, performance of a high repetition high force (HRHF) task for 12 weeks by young adult rats leads to significant losses in trabecular bone volume and cortical thinning are in the radius, concomitant with higher and more sustained increases in inflammatory cytokines (Barbe et al., 2013b; Driban et al., 2011; Rani et al., 2009). Although we have yet to examine the response of bones to prolonged performance of repetitive tasks in mature rats (14–18 months of age), similar aged rats have increased inflammatory cytokines in serum and tendons after a 12-week high repetition low force (HRLF) task, compared to young adult rats performing the same task (Xin et al., 2011a; Kietrys et al., 2012). The inflammatory cytokines were the same that affect bone cell homeostasis and induce net bone loss (interleukin-1beta and tumor necrosis factor alpha) (Lacey et al., 2009; Lange et al., 2010; Mihara et al., 1995).

Thus, the effects of performing repetitive tasks on bone architecture need further evaluation to assess if aging combined with prolonged performance of a moderate demand repetitive task enhances bone inflammation and loss, compared to young adult rats performing the same task. We sought to determine if mature adult rats (14–18 months of age) performing an upper extremity high repetition low force (HRLF) task for 12 weeks have increased bone degradative changes, compared to young adult rats performing the same task (2.5–6.5 months of age) in parallel with task- and age-related increases in bone inflammatory cytokines. We also examined for the first time, the effects of prolonged task performance on cortical microarchitecture at the mid-diaphyseal region of the radius. We hypothesized that aging combined with prolonged HRLF task performance would negatively affect both trabecular and cortical microarchitecture in the radius due to increased osteoclastic activity and reduced osteogenic adaptation, compared to young adult task rats (which will show increased trabecular bone volume and other forms of bone adaptation).

2. Materials and methods

2.1. Animals and experimental design overview

The Temple University Institutional Animal Care and Use Committee approved all experiments in compliance with NIH guidelines for the care and use of laboratory animals. Female rats were used in this study because: 1) Human females have a higher incidence of work-related musculoskeletal disorders than males (Gerr et al., 2002; Srilatha et al., 2011; Ratzlaff et al., 2007; Cote, 2012); and 2) for comparison to bone data from our past studies on female rats using this model (Jain et al., 2014; Barr et al., 2003; Barbe et al., 2013b; Driban et al., 2011; Barbe et al., 2008). All rats were housed in a central animal facility in separate cages with a 12 h light:dark cycle, and free access to water and environment enrichment toys. All rats were provided with equal rations of food reward pellets and Purina rat chow daily. All rats were inspected weekly and again post-mortem for presence of illness or tumors in order to reduce confounders for serum cytokine increases (if present, rats were excluded). To further reduce illness-related confounders, additional sentinel rats were examined for presence of viral or other infections as part of the regular veterinary care (none were detected).

As shown in Fig. 1A, 55 young adult rats (2.5 months of age at the onset of experiments, and 6.5 months of age at completion) were randomly assigned to 3 groups: normal control rats (NC, $n = 20$), food restricted control rats (FRC, $n = 21$), and 12 weeks high repetition low force task rats (HRLF, $n = 14$). Fifty-four retired-breeders (14 months of age at the onset of experiments, and 18 months of age at completion) were randomly assigned to similar groups. However, 7 mature rats were excluded from the study due to renal failure, presence of tumors, or mortality. Thus, only 47 mature rats were included by the end of the study: NC, $n = 18$; FRC, $n = 13$; HRLF, $n = 16$ rats (Fig. 1A). The total number of rats by study end was 102.

The experimental design was as follows (diagramed in Fig. 1A). First, all rats were handled for 10 min/day for 1 week. Then, all but normal control rats were food-restricted for 5–7 days to no more than 10–15% less than their naive weight to initiate interest in food reward pellets. After that week, all food-restricted rats (FRC and HRLF rats) were provided extra rat chow to gain weight quickly back to only 5% less than the age-matched NC rats, where they were maintained for the duration of the experiment. All rats were weighed weekly and food allotments were adjusted accordingly so that young adult rats gained weight across the weeks of the experiment as a consequence of normal growth, and so that mature rats maintained weight. HRLF task rats first trained to learn the task in an approximately 4-week training period of 15 min/day for 5 days/week (described further below), before moving on to performing the HRLF task for 2 h/day, 3 days/week for 12 weeks (described further below). The NC and FRC rats rested until euthanasia at age-matched time points as HRLF rats.

Data from FRC rats was compared to NC rat data. No significant differences were observed between these two groups for any outcome analyzed. Therefore, results of FRC and NC groups were combined into a single control (C) group for each age group: Young adult $C = 41$; Mature $C = 31$.

2.2. Task apparatuses

Custom-designed operant behavior chambers were used (Fig. 2A–G), as previously described (Barbe et al., 2013b; Rani et al., 2009; Clark et al., 2004). Briefly, rats were trained to reach through a portal located at shoulder height (Fig. 2A–C) to isometrically pull on a vertical 1.5 mm metal bar attached to a load cell (Futek Advanced Sensor Technology, Irvine, CA) positioned 2.5 cm outside of the chamber wall (Fig. 2D), for a food reward (Fig. 2E). Light and auditory indicators (Med Associates) lasting 5 s each, cued the animal to attempt a reach (Fig. 2F,G). The load cell output was interfaced with a signal conditioner (Analog Devices, Norwood, MA), which amplified and filtered the signal before it was sampled

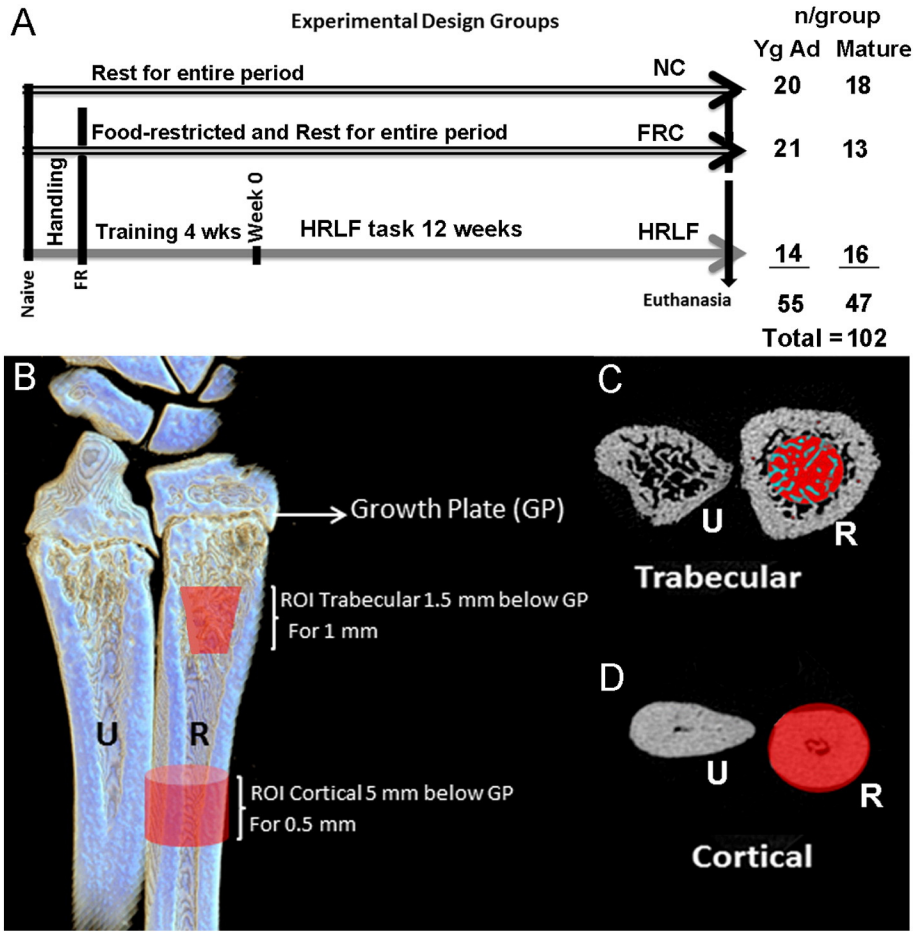

Fig. 1. Experimental design and regions of radial bone analyzed. (A) Young adult (2.5 months at onset) and mature (15 months at onset) Sprague-Dawley rats were randomly assigned to normal control (NC), food restriction control (FRC), and 12 week high repetition low force (HRLF) task groups. Number of rats per group is shown. All rats were handled for one week before onset of food restriction (FR) to ±5% less than weights of age-matched NC rats. Both FRC rats and HRLF rats were food restricted until euthanasia to encourage interest in food reward pellets. After a training period of 4 weeks in which HRLF rats learned to perform the reaching and lever grasping task, this group performed the task for 12 weeks. (B) Distal metaphyseal trabeculae and diaphyseal cortical bone regions in the radius (R) that were analyzed using micro-computerized tomography (MicroCT) in subcohorts of rats from each group. Locations of regions of interest (ROI) are as indicated. The ulna (U) was not analyzed, as we have shown it to be less affected than the radius. (C,D) Transaxial slice regions of metaphyseal trabecular bone and mid-diaphyseal cortical bone used in volumes of interest for microCT are highlighted in red. Radius (R) and ulna (U) are indicated.

digitally at 100 Hz with Force Lever software (Med Associates, St. Albans, VT). The metal lever bar and its load cell were interfaced with custom written Force-Lever software that allowed a choice of a set force level that the rat had to pull and then hold for at least 50 milliseconds (ms) (Kietrys et al., 2011a), before a food reward was provided (version 1.03.02, Med Associates, St. Albans, VT). The force transducer was encased in a custom made metal holder bolted to the floor of the chamber (Fig. 2G). The rats were trained to grasp the force lever bar and pull toward the chamber wall at a force effort of 15% of their mean maximum pulling force (30 force-grams = 0.23 Newtons) for at least 50 ms (Kietrys et al., 2011a). If reach and force criteria for the task (defined below) were met within a 5 s cueing period, a 45 mg food pellet was dispensed via a tube into a trough located at floor height for the animal to lick up (Fig. 2E–G). A 1:1 mix of purified grain and banana-flavored food reward pellets (Bioserve, NJ, USA) was used throughout the study.

2.3. Training regimen

HRLF rats were first trained to learn the reaching and handle-pulling task during a 4-week period for 10 min/day, 5 days/week, in which they ramped upwards towards the HRLF task level force. During this period, the rats moved through several stages of training, as previously described (Jain et al., 2014; Barbe et al., 2013c). Briefly, in week 1 of training, they were placed in a plastic box outfitted with Plexiglas portal and plastic trough located at shoulder height, and introduced to 45 mg food reward pellets. When rats learned to reach (without a specified reach rate) into the trough for the food pellets (typically 3 days), they were moved to operant chambers, where they learned to pull the force lever attached to a force transducer. In week 1, rats learned to grasp and pull on the force lever bar with a negligible force without any specified repetition rate, for a food reward. In week 2, rats were required to pull at 11 g of force (5% of their maximum pulling force). By the beginning of week 4, they were required to pull at 15% of their maximum pulling force (30 g of grip force), without any specified repetition rate. By the end of the 4-week training period, rats were able to perform the HRLF task of four reaches/min at 15% of their maximum pulling force. Trained rats reached this HRLF level only during the last 3–4 days of their 4th week of training at 10 min/day, 5 days/week.

2.4. Task regimen

Trained rats went on to perform the high repetition low force (HRLF) task at a low force at a reach rate of 4 reaches/min, for 2 h/day, four 30 min sessions/day, 3 days/week, for a total of 12 weeks. The daily task was divided into four 30-min sessions separated by 1.5 h each in order to avoid satiation. The rats had to grasp the force handle and exert an isometric pull for at least 50 ms with a graded force effort of 15% ± 5% of their naïve maximum voluntary pulling force. Rats were allowed to use their preferred limb to reach (the "reach" limb) (Fig. 2C,D).

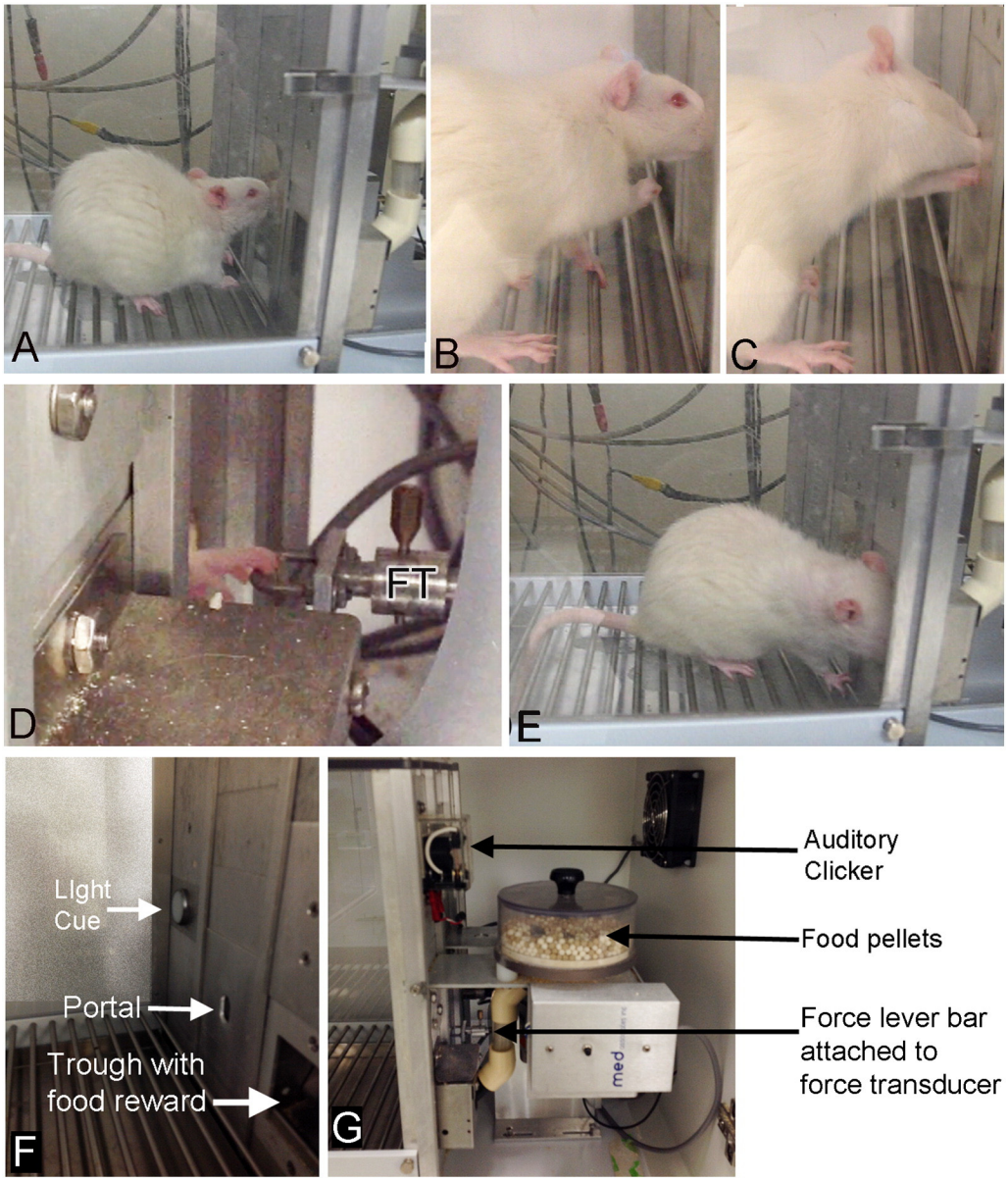

Fig. 2. Operant behavioral task apparatus. (A) Rat waiting for auditory and light cues with snout in portal. (B,C) Rat reaches into portal, and extends arm to the force lever bar with right forepaw. (D) Rat grasps and isometrically pulls a force lever bar attached to a force transducer (FT), until the force threshold (30 g grip-force; 15% of their mean maximum pulling force) is reached and held for 50 ms. (E) Rat retrieves a foot pellet reward by mouth from the food trough. (F) Photo of inside of chamber showing light cue, portal and trough for food reward. (G) Photo of outside of chamber showing auditory clicker, food pellet dispenser and force lever bar attached to force transducer, which is in a metal stabilizing holder that is bolted down to the chamber floor.

2.5. Determination of voluntary reach performance behaviors and grip strength

Force lever data were recorded continuously during task sessions for later calculation of dependent variables (reach rate, reach phase time, grasp phase time, duration of task performance, and voluntary grasp force on the lever bar) via an automated script (MatLab; Mathworks, Natick, MA), as previously described (Clark et al., 2004; Elliott et al., 2008; Kietrys et al., 2011b). Briefly, reach rate was the mean number of reaches performed per minute. Reach phase time was defined as the mean time spent in seconds performing the reaching task on a given day. Grasp phase time was the mean time spent in seconds pulling on the force lever bar for all reaches on a given day. Duration of task performance was the mean number of minutes per day that a rat participated in the task (expressed as a percentage of the target of 120 min). Voluntary grasp force was mean grasp force on the lever bar, and was required to be a graded effort of 15% of their mean maximum grip strength. Data for each variable was calculated on the last day of week 12 for eight young adult HRLF rats and thirteen mature HRLF rats, and averaged across the four sessions. Force lever data could not be determined for control rats, as they did not perform the task.

Maximum reflexive grip strength was measured in all C and HRLF animals using a rat grip strength recording unit (Ugo-Basile-Grip-Strength-Meter, Stoelting, Wood Dale, IL), by an examiner that was naïve to group assignment. This was assayed at baseline (the naive time point), after food restriction (1 week later), after training (week 0, which was 4 weeks later), and every 3 weeks thereafter, The test was repeated 5 times/trial, and the maximum grip strength per trial for the preferred reach limb is reported.

2.6. Analysis of serum bone turnover markers and estrogen using ELISA

All rats were euthanized with an overdose of sodium pentobarbital (Nembutal; 120 mg/kg body weight) at 18 h after completion of the

final task session to avoid any "exercise" induced changes in blood or bone cytokine profiles, as previously described (Xin et al., 2011a). Blood was collected by cardiac puncture using a 23-gauge needle, stored on ice for 30 min, then centrifuged at 1800 *g* for 20 min at 4 °C, flash-frozen, and stored at −80 °C until analyzed for serum osteocalcin (ELISA kit from Immunodiagnostic Systems, Rat-MID Osteocalcin EIA # AC-12F1), a marker of bone formation from: young adult NC rats, n = 6; young adult FRC rats, n = 6, young adult HRLF rats, n = 8; mature NC rats, n = 7; mature FRC rats, n = 7, mature HRLF rats, n = 13. Estradiol levels (Elisa kit from Calbiotech SKU: ES180S-100) were also analyzed in young adult rats (n = 31) and mature rats (n = 10). Osteocalcin is a non-collagenous protein of the bone matrix that is synthesized by osteoblasts, making the measure of serum an indicator of bone formation. Serum estradiol levels were analyzed to determine if age-related hormonal changes were contributing to bone changes. The individuals carrying out these ELISA assays were naive to group assignment and age.

2.7. Morphological analyses

Approximately one-half of the animals were utilized for microCT and histological analyses: young adult NC rats, n = 10; young adult FRC rats, n = 7; young adult HRLF rats, n = 8; mature NC rats, n = 9; mature FRC rats, n = 6, and mature HRLF rats, n = 8. These animals were euthanized by lethal overdose (Nembutal, 120 mg/kg body weight), perfused transcardially with 4% paraformaldehyde in 0.1 M PO_4 buffer (pH 7.4), forelimb bones were collected, cleaned of soft tissues, and stored in phosphate buffered saline with sodium azide until microCT and histological analysis of the radius and ulna from the reach limbs. Young adult MicroCT analyses was performed on n = 5–9/group and then for histomorphometry (described below). The remaining bones of this subcohort were processed for histomorphometry.

2.7.1. MicroCT imaging and analysis

MicroCT analysis of bones from n = 5–9/group was performed according to recent guidelines (Bouxsein et al., 2010) and as previously described (Jain et al., 2014; Barbe et al., 2013c). Skyscan volume rendering software (CTVox) and volume rendering software (CTVol) was used to render the 3D models and transaxial sections, shown in Fig. 1B and C,D, respectively. The forelimb bones (radius and ulna) of each rat's reach limb were scanned from their distal ends proximally towards the elbow, to a diaphyseal site that was 10 mm proximal from the growth plate, as shown in Fig. 1B, using a SkyScan 1172, 12 megapixel, high-resolution cone-beam microCT scanner (Bruker, Kontich, Belgium), using the following settings: a pixel resolution size of 5.89 μm, x-ray source spot size of 300 nm, Al 0.5 mm filter, voltage of 59 kV, current of 167 μA, rotation step of 0.40°, frame averaging of 5. Each scan was approximately 45 min per set of forelimb bones. During reconstruction of the images using cone-beam reconstruction software based on the Feldkamp algorithm (Skyscan NRecon), a ring artifact correction of 10, and a beam hardening correction of 60% were applied to all samples. This process yielded more than 2700 tomographic sections, 5.89 μm in thickness, in the axial plane, for each set of forelimb bones.

Since we have previously shown that performance of this reaching and grasping upper extremity task induces greater changes in the radius than in the ulna, we focused our morphological assays on the radius (Jain et al., 2014). Using the Skyscan CT Analyzer (CTAn) software, two regions of interest (ROI) of the radius were delineated using a region of interest tool, and then binarized separately. The metaphyseal trabecular bone ROI was delineated from 1.5 to 2.5 mm below the center of the distal growth plate (Fig. 1B). The volume of interest (VOI) for the trabecular microarchitecture variables was a consistent circle shape within a few pixels of the endocortical margin (Fig. 1C). The cortical diaphyseal ROI was delineated from 5 to 5.5 mm below the distal growth plate (Fig. 1B). The VOI was defined by circling the outside of the cortical bone surface (Fig. 1D). The saved data sets were segmented into binary images. Because of a low noise and the relative high resolution of the data sets, we used simple global thresholding methods. For trabecular bone, an upper threshold of 255 and a lower threshold of 95 were used to delineate each pixel as "bone" or non-bone. For the cortical analysis, the upper threshold remained 255 while the lower threshold was increased to 125. Despeckling was performed at a 2D setting of 50 pixels prior 2D and 3D analyses, and the shrink-wrap feature was set to cover holes of more than 50 pixels for the cortical analysis. The person carrying out the microCT analyses was naive to group assignment and age.

Trabecular bone morphometric traits were computed from binarized images using direct 3D techniques that do not rely on prior assumptions from the underlying structures. Trabecular bone volume per total volume (BV/TV), mean trabecular thickness (Tb.Th), mean trabecular number (Tb.N), mean trabecular separation (Tb.Sp), and degree of anisotropy (DA) indices were measured (in DA, 0 represents isotropic organization). Also, the structure model index (SMI) was measured to determine the prevalence of plate- or rod-like trabecular structures, where 0 represents "plates", 2 represents "rods" and 3 "cylinders" (Hildebrand and Ruegsegger, 1997).

Cortical bone morphometric traits were computed from binarized images using 2D techniques. Total cross-sectional area inside the periosteal envelope (Tt.Ar), cortical bone area (Ct.Ar), cortical area fraction (Ct.Ar/Tt.Ar), marrow area (Ma.Ar), periosteal perimeter (Ps.Pm), and average cortical thickness (Ct.Th) were analyzed. Additionally, data about closed pore volume (Po.V (cl)) was gathered.

For assay of bone mineral density (BMD), a set of 3 calcium hydroxyapatite phantoms of rat bones was scanned (partially in air; partially in water) using the same settings as for the bones. Houndsfield units for the phantoms, air and water were calculated and then used to compute columetric BMD of the segmented metaphyseal trabeculae with surrounding marrow space for the radius of animal analyzed using microCT. BMD of the mid-diaphyseal cortical bone (segmented from marrow space) was also calculated.

2.7.2. Histomorphometry

Bones that had been assayed for microCT, as well as from additional rats as indicated above in section 2.7, were used for histomorphometry according to the recommendations of the American Society for Bone and Mineral Research (Dempster et al., 2013; Parfitt et al., 1987). Half of the bones from each group underwent plastic embedding, and half underwent paraffin embedding. The individuals carrying out all histomorphometric analyses and cell counts were blinded to treatment.

To measure dynamic bone formation parameters, calcein (i.p., 10 mg/kg body weight) had been previously injected at 9 and 2 days before euthanasia. Then, fixed forearm bones underwent plastic embedding, in which they were first preserved in 70% ethanol, before being embedded, undecalcified, into methyl methacrylate resin. These bones were sectioned into 5 μm longitudinal sections, placed onto charged slides (Fisher Scientific, Tissue Path Superfrost Slides), and dried at 60 °C overnight. Unstained plastic-embedded sections of the radius were used for dynamic histomorphometric analysis (i.e., measurement of calcein labeling) and static histomorphometric analysis to assess changes in bone structure and remodeling. Trabeculae were assayed in the distal metaphysis beginning 150 μm below the

Table 1
Task performance outcomes in week 12.

Attribute	Young adult 12-week HRLF	Mature 12-week HRLF	Statistical findings
Reaches/min	4.83 ± 2.037	4.71 ± 1.1	n.s.
Reach phase time (s)	1.69 ± 0.16	1.76 ± 0.13	n.s.
Grasp phase time (s)	1.20 ± 0.20	0.92 ± 0.13	n.s.
Duration (% of 120 min)	72.78 ± 8.10	77.47 ± 8.53	n.s.
Mean voluntary pulling force (%)	15.74 ± 4.40	16.49 ± 2.44	n.s.

Mean voluntary pulling force of 15% = a mean of 30 g of grip force; values shown are mean ± sem.

chondro-osseous junction of the secondary spongiosa and 50 μm in from the surrounding cortical bone using a 20× objective and image analysis software (BIOQUANT Osteo II, Bioquant Image Analysis Corp., Nashville, TN), and using methods described by Parfitt et al. (Parfitt et al., 1987). Bone formation rate (BFR) was assessed in unstained calcein-labeled sections by measuring single-labeled surface for single perimeter (sL.Pm), double-labeled surface (dL.Pm), and the interlabel distance in the dL.Pms. From this, mineral apposition rate (MAR, mM/day) and bone formation rate normalized to bone surface (BFR/BS) were calculated (Brennan et al., 2011).

Unstained plastic embedded sections were also analyzed using both bright field and polarized light microscopy to visualize if woven bone formation had occurred. The area of a field at 300× magnification containing woven bone volume was chosen using Bioquant manual thresholded selection methods, as was the area of bone volume. Woven bone volume/total bone volume (Wo.V./BV. %) was reported.

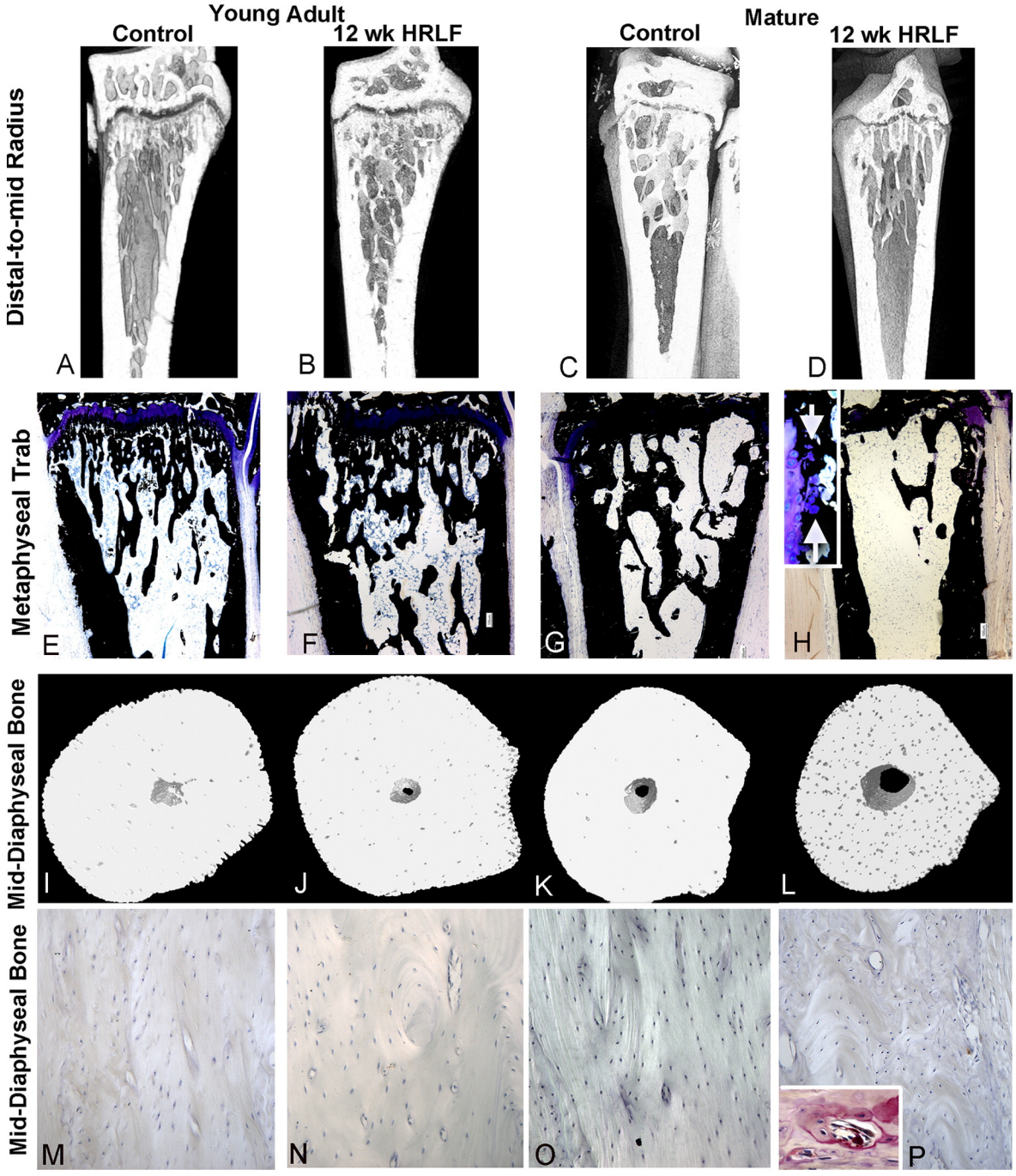

Fig. 3. Representative microCT and microscope images of distal radius. (A–D) Representative 3D images generated using CTVox, a volume rendering software, of trabecular bone area analyzed in the radius for each group. These 3D reconstructions are located from the distal growth plate towards the mid-diaphysis. (E–H) Representative von Kossa stained sections of a distal radius from each group. Scale bar = 100 μm. The inset in panel H shows a number of osteoclast resorptive spaces in the distal radius of a mature HRLF rat. (I–L) Representative transaxial 3D microCT images, generated using a surface rendering software program, of the mid-diaphyseal cortical bone of the radius from each group. These transaxial reconstructions are located from 5 to 5.5 mm proximal to the distal growth plates. (M–P) Representative polarized light images from the mid-diaphyseal cortical bone of the radius from each group, taken with a 20× objective and differential interference contrast optics. The inset in panel P shows an osteoclast resorptive space in the distal radius of a mature HRLF rat; this section is stained with TRAP and a TRAP-stained osteoclast is visible in this space.

Adjacent sections were deplasticized and stained with Masson's trichrome to detect osteoblasts, von Kossa with toluidine blue counterstain for the staining of mineralized bone, or were processed for tartrate-resistant acid phosphatase (TRAP) staining to detect osteoclasts, as per manufacturer's instructions (Sigma-Aldrich Acid Phosphatase kit 387A). Osteoid volume per bone volume (OV/BV), osteoid width (O.Wi), osteoid surface per bone surface (OS/BS), and osteoblast numbers per bone surface (Ob.N/BS) on trabecular surfaces were determined in Masson's trichrome stained sections. Numbers of osteoclasts (multinucleated TRAP + cells) per bone surface (N.Oc/BS) were counted in TRAP stained sections on trabecular surfaces in the secondary spongiosa, using a Nikon E800 microscope interfaced with an image analysis program (Bioquant Osteo 2012 v12.1). Since TRAP is also known to stain macrophages and other mononuclear cells of the monocyte-macrophage lineage (Chen et al., 2007; Dempster, 2000; Mueller et al., 2006; Iolascon et al., 2014), only large cells with 3 or more nuclei were counted, as previously described. Osteoclast resorption spaces (number per bone surface area; defined as spaces in cortical bone in which osteoclasts were present) and arterial spaces were counted in mid-diaphyseal cortical bone.

Flexor digitorum muscles were collected from the same rats and limbs, postfixed by immersion overnight in 4% paraformaldehyde in phosphate buffer (pH 7.4). A cross-sectional piece of the entire flexor digitorum muscle, of 1.5 mm in thickness, was removed with a scalpel from the mid-region of the muscle at its widest point. This cross-sectional piece was equilibrated in sucrose for 3 days, and then cryosectioned into cross-sectional slices of 14 μm thick each. These sections were mounted on slides, dried and stained with H&E. An image analysis program (Bioquant) was used to measure the cross-sectional area (CSA) of the entire muscle belly in mm^2 using a 2X objective. Three sections were counted per histomorphometric analysis parameter.

2.8. Analysis of bone inflammatory cytokines using ELISA

After collection of blood, the radial and ulnar bones were collected and flash-frozen from: young adult NC rats, n = 8; young adult FRC rats, n = 8, young adult HRLF rats, n = 6; mature NC rats, n = 9; mature FRC rats, n = 7; mature HRLF rats, n = 8. Bones were powdered, homogenized and assessed for interleukin (IL)-1β, tumor necrosis factor-alpha (TNF-α), IL-6 and IL-10 using commercially available ELISA kits (BioSourceTM, Invitrogen Life Sciences, CA), as described previously (Barbe et al., 2008). Each sample was run in duplicate in a blinded manner. ELISA assay data (pg cytokine protein) were normalized to μg total protein, which was determined using a bicinchoninic acid (Pierce BCA Protein assay #23,225. Thermo Scientific, MA). The individual carrying out these ELISA assays was blinded to treatment.

2.9. Statistical analyses

An unpaired, two-tailed, t-test was used to compare the reach performance variables in young adult versus mature HRLF rats. For the microCT, histomorphometric and ELISA data, mixed-model two-way and one-way ANOVAs were performed to determine differences between and among groups. Repeated measures ANOVAs were used to compare body weight and grip strength data across weeks. For each ANOVA, the Bonferroni post-hoc method for multiple comparisons was used. Adjusted p-values are reported, and after adjustment, a p-value of <0.05 was considered statistically significant. Two-tailed Pearson's correlation tests were used to compare to trabecular BV/TV with serum estrogen levels, and with the animal weights at euthanasia. Data are expressed as mean ± standard error of the mean (SEM). Two-way ANOVA results and significant post-hoc findings are listed with the individual graphs.

3. Results

3.1. Voluntary task parameters were similar in each age group of HRLF rats

Each age group of HRLF rats was able to perform the task at the expected reach and force parameters (Table 1). For example, each age group was able to pull at the required submaximal 15% of mean voluntary pulling force (30 g of voluntary grip force).

3.2. MicroCT analysis shows trabecular bone adaptation in the radius to the HRLF task in young adult rats, yet degradative changes in mature HRLF rats

There were no significant differences in any microCT or bone cell count variables observed between NC and FRC of young adult rats, or

Table 2
MicroCT results for radial bone (6 μm voxel resolution).

	Young adult		Mature adult		Statistical findings
Attribute	C	12-week HRLF	C	12-week HRLF	Factors: Age and task group
Distal radial metaphyseal trabeculae					
BV/TV (%)	33.86 ± 2.46	61.08 ± 13.92 [a]	34.88 ± 9.22	22.28 ± 1.76[a,b]	Interaction p = 0.04
Tb.Th (mm)	0.06 ± 0.004	0.14 ± 0.04 [a]	0.10 ± 0.03	0.06 ± 0.003[a,b]	Interaction p = 0.01
Tb.N (1/mm)	4.14 ± 0.35	5.84 ± 0.94 [a]	4.57 ± 0.62	4.06 ± 0.18 [b]	Interaction p < 0.05
Tb.Sp (mm)	0.12 ± 0.008	0.12 ± 0.03	0.18 ± 0.01 [b]	0.20 ± 0.006 [b]	Age: p = 0.0001
DA	0.50 ± 0.04	0.38 ± 0.03 [a]	0.46 ± 0.05	0.57 ± 0.02 [ab]	Interaction p = 0.008
SMI	2.10 ± 0.14	0.16 ± 0.58 [a]	2.11 ± 0.34	1.00 ± 0.21	Task Gp p = 0.001
BMD Tb (g/cm^3)	7.20 ± 2.16	23.00 ± 3.74 [a]	14.49 ± 1.97	22.07 ± 2.33	Task Gp p = 0.0008
Mid-diaphyseal radial cortical bone					
Tt. Ar (mm^2)	1.51 ± 0.022	1.45 ± 0.10	1.62 ± 0.08	1.73 ± 0.06[b]	Age p = 0.01
Ct.Ar (mm^2)	1.38 ± 0.05	1.36 ± 0.20	1.53 ± 0.06	1.60 ± 0.046	Age p = 0.03
Ct.Ar/Tt.Ar (%)	91.13 ± 3.84	80.27 ± 10.44	95.06 ± 2.26	92.06 ± 0.94	n.s.
M.Ar (mm^2)	0.09 ± 0.02	0.05 ± 0.004[a]	0.04 ± 0.015	0.14 ± 0.02[a,b]	Interaction p = 0.004
Ps.Pm (mm)	4.79 ± 0.03	5.57 ± 0.38	4.99 ± 0.15	5.16 ± 0.09	Task p = 0.03
Ct.Th (mm)	0.48 ± 0.04	0.50 ± 0.07[a]	0.57 ± 0.03[b]	0.53 ± 0.01[a]	Interaction p = 0.004
Po.V (cl) (mm^3)	0.0004 ± 0.00008	0.006 ± 0.003	0.04 ± 0.002	0.01 ± 0.005[a,b]	Task p = 0.004; Age p = 0.03
BMD Ct (g/cm^3)	97.37 ± 2.93	110.69 ± 3.70[a]	95.54 ± 2.44	92.36 ± 6.01[b]	Interaction p = 0.04
Wo.BV/BV (%)	12.25 ± 3.57	4.20 ± 2.13	14.80 ± 4.81	37.43 ± 5.64[a,b]	Interaction p = 0.006
Resorptive spaces ($1/mm^2$)	0.86 ± 0.86	0.21 ± 0.02	0.11 ± 0.03	0.39 ± 0.07[a,b]	Task p = 0.002
Vascular profiles ($1/mm^2$)	4.09 ± 0.43	4.97 ± 0.36	6.51 ± 1.06	10.13 ± 1.14[a,b]	Task p = 0.02

[a] $p < 0.05$, compared to age-matched control group.
[b] $p < 0.05$, compared to matched young adult counterpart group (control or task); values shown are mean ± sem.

between NC and FRC of mature rats (data not shown), likely due to the food restriction of only 5% less than the age-matched NC rats (data shown later in results). Therefore, NC and FRC data were combined by age, into one control (C) group per age group, hereafter.

Fig. 3A–D shows representative 3D images of the distal trabecular metaphyseal region of the radius, and shows an increase in trabecular bone volume in young adult HRLF rats, compared to the other groups. We quantified these differences using microCT (Table 2), and observed loading-induced bone adaptation in young adult HRLF rats as increased BV/TV, Tb.Th, Tb.N and trabecular BMD, compared to young adult C rats. The degree of anisotropy (DA) also improved (decreased) in trabeculae of young adult HRLF rats, compared to young adult C rats. The trabecular shape changed from rod-like to plate-like with HRLF task performance, indicated as decreased SMI, a change known to increase bone strength (Liu et al., 2010). An increase in bone volume in young adult HRLF rats was also seen in von Kossa stained sections, compared to the other groups (Fig. 3E–H). Note, 3D and histological images also show an increase in trabecular bone proximally towards the mid-diaphyseal region of the radius in young adult HRLF rats, than in young adult C rats (Fig. 3B versus A).

In contrast, mature rats performing the HRLF task showed several indices of bone loss in the distal radial trabeculae, including decreased BV/TV and Tb.Th, compared to mature C rats and to young adult HRLF rats (Fig. 3A–H; Table 2). Mature HRLF rats also had decreased trabecular numbers (Tb.N) and increased trabecular separation (Tb.Sp), compared to young adult HRLF rats (Table 2). The microCT 3D and histological images show loss of trabecular bone proximally towards the mid-diaphyseal radius in mature HRLF rats (Fig. 3D,H), findings not seen in young adult HRLF or C rats. Mature HRLF rats had increased DA, compared to mature C and young adult HRLF rats, indicative of more unevenly distributed trabeculae (Table 2). On a positive note, mature HRLF rats showed one index of bone adaptation to the task, that being a lower SMI than mature C rats, although the magnitude of this change was less than seen in young adult HRLF rats and did not reach significance. Trabecular BMD was also increased in mature HRLF rats, compared to mature C rats, although this increase did not reach significance (Table 2).

3.3. MicroCT analysis shows cortical bone growth in the radius of young adult HRLF rats, but thinning and increased porosity in mature HRLF rats

Mid-diaphyseal bone growth was observed in the radius of young adult HRLF rats (Table 2 lower half). This was observed as decreased Ma.Ar (indicative of endosteal bone formation), increased Ps.Pm (indicative of periosteal growth), and increased cortical bone thickness (Ct.Th), compared to young adult C rats. There was also an increase in cortical bone BMD in young adult HRLF rats, compared to young adult C rats.

In contrast, mature HRLF rats had increased Ma.Ar and cortical thinning, compared to mature C rats (despite starting with thicker cortical bones than young adult C rats; Table 2). Mature task rats also showed an increased volume of closed pores (Po.V (cl)), indicative of increased cortical bone porosity, compared to mature C rats and young adult HRLF rats (Table 2). Cortical bone BMD was lower in mature HRLF rats, than in young adult HRLF rats, although not significantly lower than mature C rats. Representative 3D images show an increase in cortical bone porosity in the mature HRLF rats and cortical thinning, compared to the other groups (Fig. 3I–L). The increased cortical bone porosity observed using microCT appeared to be due to increases in osteoclast resorptive spaces and vascular profiles in cortical radial bones of mature HRLF rats (Fig. 3P), compared to mature C rats and young adult HRLF rats (Fig. 3N,O); Table 2). A qualitative increase in osteoclast resorptive spaces was also observed in distal radial cortical of mature HRLF rats than in the other groups (Fig. 3H inset, arrows). Lastly, the mature HRLF rats showed increased woven bone in the mid-diaphyseal cortical bone (Fig. 3P), compared to the other groups (Fig. 3M–O; Table 2).

3.4. Static and dynamic bone histomorphometry shows increased radial trabecular osteoblast activity in young adult HRLF rats, compared to mature HRLF rats

Several indices of osteoblast activity and proliferation were observed in distal radial metaphyseal trabeculae of young adult HRLF rats, including increased percent osteoid volume per bone volume (OV/BV), osteoid width (O.Wi), osteoblast surface per bone surface (Ob.S/BS), and numbers of osteoblasts per bone surface (N.Ob/BS), compared to young adult C and mature HRLF rats (Fig. 4A–D). Similar adaptive bone changes were not observed in the mature HRLF rats (Fig. 4A–D). Both mineral apposition rate (MAR) and bone formation rate per bone surface (BFR/BS) were increased in distal radial metaphyseal trabeculae of young adult HRLF rats, compared to young adult C rats and mature HRLF rats (Fig. 4E and F). Representative images show increased distance between calcein double labeling in trabeculae of young adult HRLF rats, particularly compared to young adult C rats (Fig. 4H versus G). The mature C and HRLF rats showed only random areas of calcein labeling and few clear double-labeled bands (Fig. 4I and J); the latter findings indicative of very little bone growth in the radius of mature animals, with or without repetitive loading. Serum osteocalcin levels showed similar increases in young adult HRLF rats, compared to young adult C rats, and lower levels in both mature C and mature HRLF rats, compared to their young adult counterparts (Fig. 4K).

3.5. Osteoclast activity and numbers increased in mature HRLF rats

Quantification of TRAP-stained osteoclasts in the distal radial metaphyseal trabeculae showed increases in both osteoclast surface and number per bone surface (Oc.S/BS and N.Oc/BS) in mature HRLF rats, compared to mature C rats and young adult HRLF rats (Fig. 5A and B).

3.6. Greater task-induced inflammatory cytokine responses in mature rats

We next analyzed inflammatory cytokine levels in forelimb bones (radius and ulna), since we have reported increased pro-inflammatory cytokines in serum and tendons of mature HRLF rats, compared to young adult counterparts (Kietrys et al., 2012; Xin et al., 2011b), and since inflammatory cytokine levels are known to stimulate osteoclastogenesis (Guo et al., 2008; Kulkarni et al., 2012; Lacey et al., 2009; Lange et al., 2010; Thomas, 2010). Levels of each pro-inflammatory cytokine examined (IL-1beta, TNF-alpha and IL-6) were higher in mature HRLF rat bones (Fig. 6A–C), and IL-1beta and TNF-alpha were increased in mature C rats, compared to young adult C rats (Fig. 6A,B). Interestingly, IL-10 levels (a key anti-inflammatory cytokine) was lower in mature HRLF rats (Fig. 6D), compared to mature C and young adult HRLF rats. Both TNF-alpha and IL-10 were increased in young adult HRLF rats, compared to young adult C rats (Fig. 6B,D).

3.7. Animals' weights were not significantly affected by food restriction

To determine if differences in body weight could be a contributing factor to the observed bone changes, body weights were compared across the weeks and between groups at matched time points. Body weights of young adult rats showed that young adult rats in each group weighed more at week 12, than at naïve, indicating that they each gained weight similarly across the course of the experiment (Fig. 7A). Mature HRLF rats did not show any significant changes in weight, compared to mature FRC and NC rats (Fig. 7B). However, mature rats of each group were heavier than the young adult rats at each time point (Fig. 7C), although this increase in weight did not translate to increased bone in the mature rats, compared to young adult rats, as shown in the microCT results.

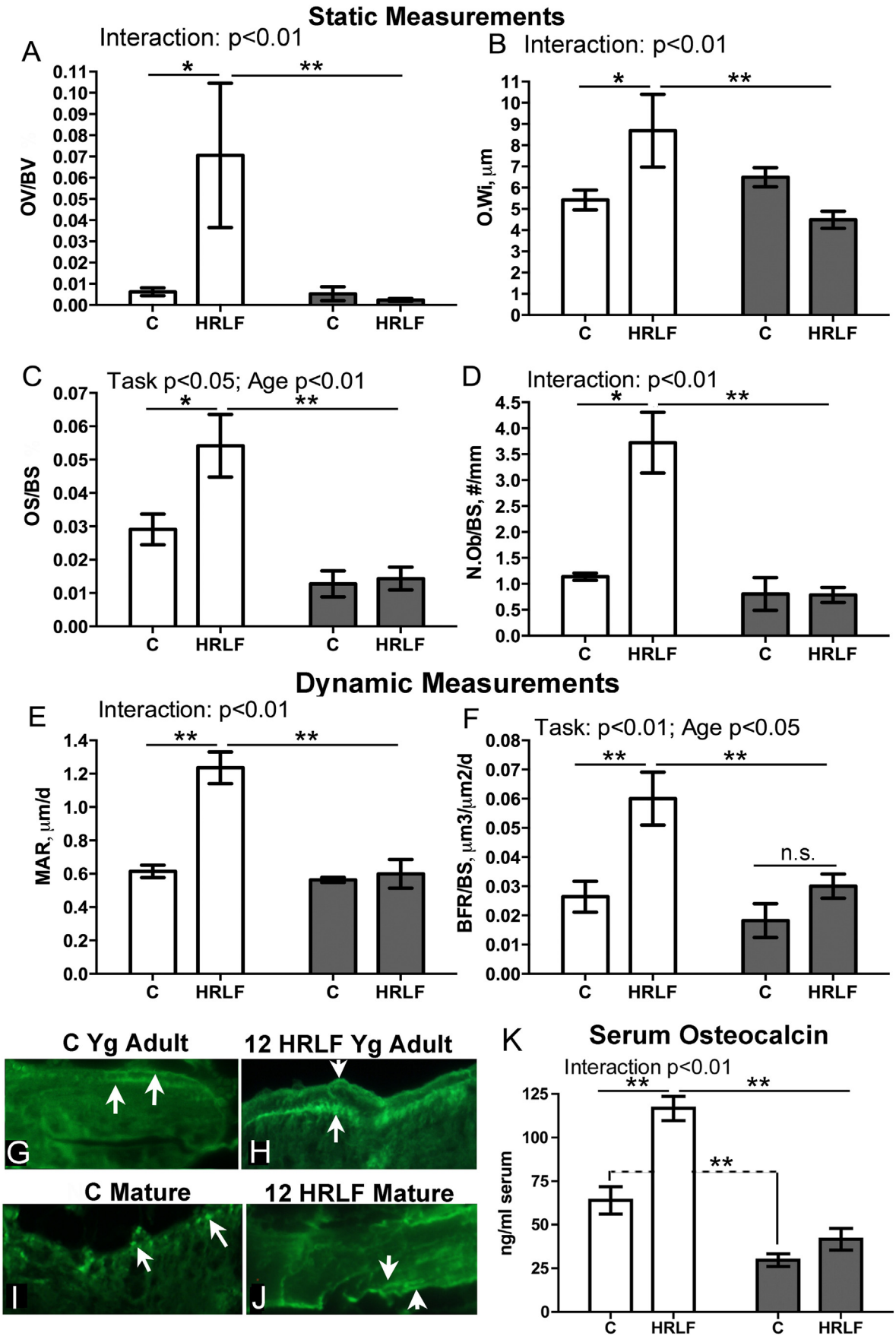
Static Measurements
A
Interaction: p<0.01
OV/BV
B Interaction: p<0.01
O.Wi, μm
C
Task p<0.05; Age p<0.01
OS/BS
D
Interaction: p<0.01
N.Ob/BS, #/mm
Dynamic Measurements
E
Interaction: p<0.01
MAR, μm/d
F
Task: p<0.01; Age p<0.05
BFR/BS, μm3/μm2/d
n.s.
C
HRLF
C Yg Adult
12 HRLF Yg Adult
G
H
C Mature
12 HRLF Mature
I
J
K
Serum Osteocalcin
Interaction p<0.01
ng/ml serum

3.8. Maximum reflexive grip strength declines are evident in mature task rats

Young adult HRLF rats showed increased maximum reflexive grip strength in weeks 3 and 6 of task performance, compared to their naïve grip strength (Fig. 7D). By week 12, maximum reflexive grip strength of young adult HRLF rats had returned to NC and FRC levels (Fig. 7D). In contrast, mature HRLF rats showed a progressive decrease in maximum reflexive grip strength (Fig. 7E), compared to naïve. When comparing the two HRLF cohorts, young adult HRLF rats showed lower maximum reflexive grip strength than mature rats at naïve, but greater maximum reflexive grip strength than mature rats by week 6 (Fig. 7F).

3.9. No significant changes in the forelimb flexor muscles were observed with task or age

Differences in muscle size between the age groups were also examined as a possible contributing factor to the observed bone changes. Young adult HRLF rats had a similar mean cross sectional area as young adult C rats (56.08 ± 2.04 versus 50.84 ± 3.17, $p = 0.11$), as did mature HRLF rats, compared to mature C rats (47.90 ± 8.06 versus 40.09 ± 4.38, $p = 0.21$). There were also no significant differences between age groups (Two way ANOVA: Age $p = 0.08$, Task $p = 0.10$, Interaction $p = 0.97$).

3.10. Estrogen levels were similar in young adult and mature rats, and do not correlate with trabecular bone volume

To determine if bone changes observed were caused by sex hormone changes, we tested serum estradiol levels and found that mature rats had similar estrogen levels as the young adult rats (Supplemental Fig. 1), indicating that the mature rats were pre-menopausal. No significant correlation was observed between serum estrogen levels and BV/TV in either group separately, or when both age groups were combined (Supplemental Fig. 1), or between serum estrogen levels and Ct.Th and Ma.Ar changes (data not shown, $p > 0.05$). There was also no correlation between trabecular BV/TV and the rats' weights in either group separately, or when both age groups were combined (Supplemental Fig. 1).

4. Discussion

4.1. Bone adaptation occurs in young adult HRLF rats by week 12

We found that 12 weeks of performance of a HRLF task by young adult rats induced bone remodeling and net bone formation in the distal radial metaphyseal trabeculae, as well as positive adaptive changes in the mid-diaphyseal cortical bone. This adaptation was evident in the distal radius as increased trabecular bone volume ratio, thickness and numbers, and bone mineral density. Trabecular bone adaptation in the young adult HRLF rats was also supported by a decrease in DA, a change associated with improved trabecular bone organization, and a decrease in the SMI, indicative of a transition from rod-like to plate-like trabecular shape, a change associated with higher mechanical strength (Hildebrand and Ruegsegger, 1997; Ding et al., 2003; Akhter et al., 2007; McLaughlin et al., 2002). In the mid-diaphyseal cortical bone of young adult HRLF rats, marrow area was decreased (indicative of growth at the endosteal surface), periosteal perimeter was the increased osteoclastic resorption (indicative of periosteal growth), cortical thickness was increased, and the cortical BMD was increased. Each are positive adaptive changes that should reduce the risk of bone fracture (Turner et al., 1995; Srinivasan et al., 2012). The increased osteoblast numbers and activity and increased MAR and BFR in the young adult HRLF rats, compared to unloaded control rats, indicate an increase in bone formation in response to performance of this moderate level task for 12 weeks. These data extend prior findings in this model, showing increased trabecular bone volume ratio in the distal radius of young adult rats that had performed the HRLF task for 12 weeks, compared to rats performing easier or more challenging tasks (Barbe et al., 2013b). Combined, they show that the level of loading in this particular reaching and grasping task (4 reaches/day at 30 force-grams), consistently applied 3 days/week, 2 h/day, for 12 weeks, was sufficient to induce osteogenesis and net bone growth in the radius of young adult rats.

4.2. Trabecular bone loss, cortical thinning and increased porosity in mature HRLF rats

In contrast, performance of the same HRLF task for 12 weeks by mature rats induced decreases in trabecular bone volume/tissue volume, thickness and numbers, compared to mature C rats and compared to young adult HRLF rats. This was in spite of taking care to complete the studies using the same experimental methodology (see Table 1) and equipment. Animals were purchased from the same vendor, housed in the same room, and fed the same diet; the only obvious difference in this regard was their age and weights. The mature rats were heavier than the young adult rats, although this increase in weight did not translate to increased bone in the mature rats. We observed a decrease in SMI in both mature and young adult HRLF rats, a change typically associated with improved trabecular bone structure (Hildebrand and Ruegsegger, 1997; Ding et al., 2003; Akhter et al., 2007; McLaughlin et al., 2002). The mature HRLF rats showed a mix of both rods and plates (less of a decrease in SMI), while the young adult HRLF rats transitioned primarily to the stronger plate-like structure (a greater decrease in SMI). These SMI findings on their own suggest that longer performance of the HRLF task should have positive effects on trabecular bone structure in mature rats. However, the mature HRLF also had significant increases in the degree of anisotropy (DA) in the distal radial trabeculae. Increased DA is indicative of disorganization in trabecular distribution and a weaker bone that is less resistant to mechanical loading due to increased stiffness (Ding et al., 2003). The mature HRLF rats failed to demonstrate osteogenesis (no change in osteocalcin or osteoblast numbers or activity) after task performance. This low osteogenic response in the mature HRLF rats is consistent with prior studies showing that more vigorous loading or longer loading periods may be necessary to induce an osteogenic response in aging mammals (Turner, 2007; Turner et al., 1995; Srinivasan et al., 2012; Leppanen et al., 2008). Reports about how aging affects the osteogenic potential of mesenchymal cells are conflicting, with some studies stating that aging does not affect osteoblast recruitment, differentiation and activity (Leskela et al., 2003), while others state that there is an age-related decline in the osteogenic potential of bone marrow cells (Mueller and Glowacki, 2001) that can be improved by physical activity in rats (Hell et al., 2012). We did not observe such improvement in the mature rats with performance of this 12-week high repetition low force task. The increased osteoclast and inflammatory cytokine response with this 30 force-grams of loading regimen suggests that more vigorous loading may be counterintuitive; thus, longer loading periods at even a lower loading force may be needed to induce bone formation in the mature rats.

The mature HRLF rats also showed several negative morphometric changes in their mid-diaphyseal cortical bone, including increased marrow area, thinning, porosity, osteoclastic resorptive spaces, arterial spaces,

Fig. 4. Static osteoblast and dynamic histomorphometric measurements in distal metaphyseal trabecular region of radii of young adult and mature control (C) and 12-week high repetition low force (HRLF) rats. (A) Osteoid volume normalized to bone volume (OV/BV). (B) Osteoid width (O.Wi). (C) Osteoblast surface normalized to bone surface (Ob.S/BS). (D) Cellular density of osteoblasts (N.Ob) normalized to bone surface (BS). (E) Trabecular mineral apposition rate in the radius (MAR). (F) Trabecular bone formation rate (BRF), normalized to bone surface (BS). (G–H) Representative microscope images showing calcein double labeling in radial trabeculae of young adult rats. (I–J) Representative microscope images showing calcein labeling in radial trabeculae of mature rats, and shows only spotty calcein labeling in each. (K) Serum levels of osteocalcin, assayed using ELISA. Two-way ANOVA results are shown in individual panels, and Mean ± SEM is shown. *: $p < 0.05$ and **: $p < 0.01$; n.s. = not significant.

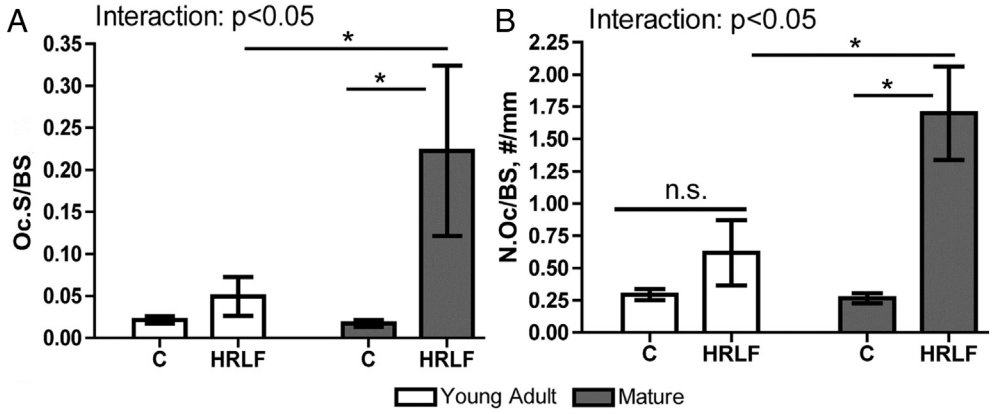

Fig. 5. Histomorphometric measurements of osteoclasts in distal metaphyseal trabecular region of the radius of young adult and mature control (C) and 12-week high repetition low force (HRLF) rats. (A) Osteoclast surface, normalized to bone surface (Oc.S/BS). (B) Number of osteoclasts, normalized to bone surface (N.Oc/BS). Two-way ANOVA results are shown in individual panels, and Mean ± SEM is shown. *:$p < 0.05$; n.s. = not significant.

and woven bone. An increase in marrow area can offer increased torsion strength and flexibility if cortical thickness and bone diameter are maintained, since bending strength of bone is exponentially related to its diameter (Saine et al., 2011). However, in the mature HRLF rats, the cortical thinning was due to a lack of a compensatory increase in the periosteal perimeter as the endosteal perimeter increased. Such cortical thinning is typically linked to reduced cortical bone quality (Khosla et al., 2011; Keaveny et al., 2010). Increased porosity is considered to not affect bone strength if pores are concentrated to the endocortical region (Burr et al., 2001). However, the increased pores were evenly distributed throughout the cortical bone of the mature rats (Fig. 3L) and were the result of evenly distributed increases in osteoclastic resorptive spaces and vascular profiles. This matches a prior report of increased osteoclastic resorption spaces contributing to increased microCT-detected porosity (Wu et al., 2013). Increased intra-cortical porosity has been linked to increased fragility, microdamage and fracture risk, and is considered a key indicator of osteopenia (Borah et al., 2010; Burr et al., 1997; Dhainaut et al., 2013; Nishiyama et al., 2010). These findings combined show increased metaphyseal trabecular and diaphyseal cortical bone degradative changes, with only a few indices of adaptation, in mature rats performing this moderate demand upper extremity task.

4.3. Links between aging, task-induced tissue inflammation and bone remodeling

Inflammatory changes were present in forelimb bones involved in performing the HRLF task in both mature and young adult rats. The small, yet significant, increases in TNFalpha and the increased osteoblastic response in young adult HRLF rats are similar to findings from other studies showing that low doses of TNF-alpha can stimulate osteoblast proliferation and osteogenic differentiation (Mumme et al., 2012; Cho et al., 2002; Cho et al., 2010). However, much greater increases in inflammatory cytokines were seen in forelimb bones of mature HRLF rats. This results are similar to our prior reports of increased inflammatory cytokine in tendons and serum of mature HRLF rats, compared to young adult HRLF rats (Xin et al., 2011a; Kietrys et al., 2012). Increased inflammatory cytokine level variations in bones are known to affect both bone formation and resorption (Lacey et al., 2009; Thomas, 2010; Rani et al., 2010; Mumme

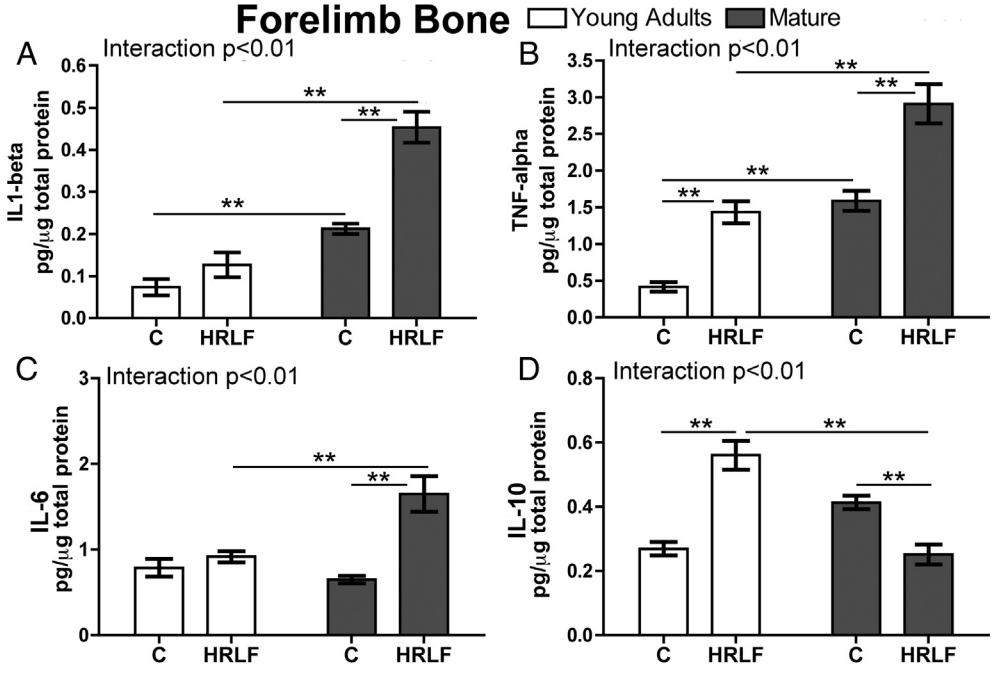

Fig. 6. Inflammatory cytokines in forelimb bones of young adult and mature control (C) and 12-week high repetition low force (HRLF) rats. (A) IL-1beta, (B) TNF-alpha, (C) IL-6, and (D) IL-10. Two-way ANOVA results are shown in individual panels, and Mean ± SEM is shown. **: $p < 0.01$.

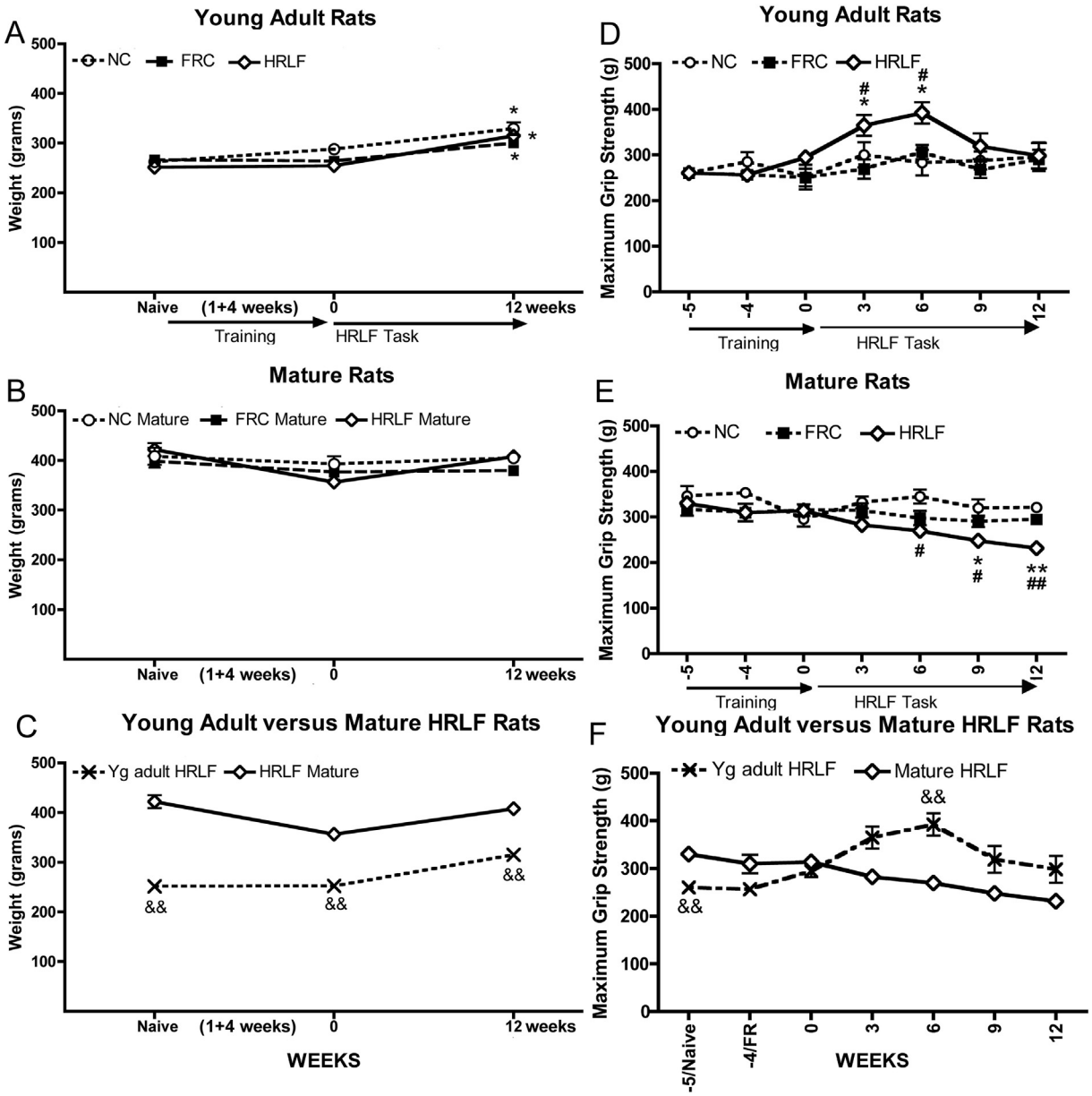

Fig. 7. Body weights and maximum grip strength of young adult and mature rats across weeks of experiment. Data shown for normal control (NC), food restriction control (FRC), and 12-week high repetition low force (HRLF) task rats from each age group. (A–C) Body weights of young adult control and HRLF rats, mature control and HRLF rats, and young adult versus mature HRLF rats. (D) Grip strength of young adult rats from naïve to task week 12. (E–F) Grip strength of young adult control and HRLF rats, mature control and HRLF rats, and young adult versus mature HRLF rats. Two-way ANOVA results are shown in individual panels, and Mean ± SEM is shown. *: $p < 0.05$, and **: $p < 0.01$, compared to naïve time point; #: $p < 0.05$ and ##: $p < 0.01$, compared to age-matched NC and FRC rats; &&: $p < 0.01$, compared to matching group of mature HRLF rats.

et al., 2012; Gravallese, 2002). TNF-alpha and IL1-beta are produced by osteoclasts and interfere with osteoblast differentiation and proliferation (Lacey et al., 2009; Lange et al., 2010) in a dose-dependent manner by promoting loss of bone morphogenetic proteins (Guo et al., 2008; Barr et al., 2003; Kaneki et al., 2006). We have previously shown in this model that anti-inflammatory doses of ibuprofen, provided as a secondary intervention, reduced TNF-alpha and IL-1beta levels, and prevented loss of bone volume in young adult rats performing a high repetition high force task for 12 weeks (Jain et al., 2014). An ergonomic task reduction intervention in which young adult rats were moved from a high repetitive high force task in week 4, to a low repetition low force task for another 8 weeks, also reduced inflammatory cytokine levels and lead to enhanced bone formation (Barbe et al., 2015). These two studies support an underlying bone inflammatory cytokine mechanism in this model that was further enhanced by aging in rats involved in performing this repetitive loading task for 12 weeks.

The lower IL-10 response in the mature HRLF rats is consistent with other studies showing a dysregulation of the IL-10 response as a consequence of aging (Cevenini et al., 2010; Salvioli et al., 2006). The decline in IL-10 response in the mature rats may also be contributing to the increased pro-inflammatory cytokine response.

4.4. Other possible contributing factors to observed bone changes in mature rats

Several potential contributing factors can be ruled out. There were no significant differences in reach performance parameters assayed or estrogen levels in the young adult HRLF versus mature HRLF rats, ruling out these factors as contributors to the observed group differences. Body weight did not appear to be a contributing factor to the degradative bone changes observed in the mature rats in this study since they weighed more than the young adult rats. There was also no significant

correlation between the rats' weights and bone volume ratios of either age group (Supplemental Fig. 1). Measurements of the cross-sectional area of the flexor muscle at its widest point showed no statistically significant increases between or among the 4 groups, although there was a marginal increase in muscle girth in mature HRLF rats, compared to mature C rats. This marginal increase was apparently not enough to trigger an osteogenic bone response and also failed to rescue maximum reflexive grip strength declines. Regarding the maximum reflexive grip strength declines, we have previously shown that increased inflammatory cytokines in serum, nerves and tendons of mature HRLF rats correlated with declines in maximum reflexive grip strength (Kietrys et al., 2012; Xin et al., 2011b; Elliott et al., 2010). The decrease in maximum reflexive grip strength in the mature rats appears to be a myalgia-generated or even central sensitization pain response, as reported previously (Barbe et al., 2008; Elliott et al., 2008; Elliott et al., 2010; Elliott et al., 2009a; Elliott et al., 2009b), that did not affect the mature HRLF rats' abilities to perform this submaximal grasping task in which the HRLF rats had to reach at 15% of their maximum grip strength (see Table 1).

4.5. Limitations

There are some limitations in this study. For consistency in loading, the 30 g grip force used as the pulling force target (15% of maximum pulling force was used in both age groups, even though the mature rats weighed more and had a slightly higher grip strength at naïve than the young adult rats. While this may seem like a limitation, increasing the pulling force target would likely have increased the bone degradative changes further in the mature HRLF rats. Second, for the cytokine analyses, we collected and homogenized together both ulna and radial bones. Therefore, the inflammatory cytokine data is representative of changes in both of these bones, rather than in just the radius. Next, the serum levels of osteocalcin are representative of bone formation occurring in all bones involved in performing the task, not just the radius. Therefore, another limitation of this study is that we did not examine other bony sites of the upper extremity for morphological changes. Lastly, this study was performed in rats and until a similar longitudinal study is performed in young adult and mature human subjects with WMSDs, caution is warranted.

5. Conclusions

The radial bones of young adult female rats show positive adaptation and bone growth to this low force repetitive task. In contrast, in the mature rats performing the same reaching and grasping task, fewer osteogenic changes, and metaphyseal trabecular and cortical bone degradative changes were observed. The observed group differences in bone formation versus bone loss responses were not due to differences in strain rate (repetition rate or grasping force levels), estrogen levels, or flexor muscle cross-section area. The reduced radial bone quality in the mature rats indicates that prolonged performance of even moderate demand upper extremity, hand intensive task may increase the risk of fracture or osteopenia, matching results from human subjects showing reduced bone mass in females with heavy or one-sided hand workloads (Ding et al., 2010; Solovieva et al., 2005; Vehmas et al., 2005), and decreased bone mineral density in distal forearm bones of subjects with carpal tunnel syndrome (Erselcan et al., 2001; Savas et al., 2007). Our findings of increased bone inflammatory cytokines and osteoclast activity in the mature HRLF rat bones, combined with recent findings of reduced cytokines and preservation of bone volume after anti-inflammatory treatments (Jain et al., 2014; Barbe et al., 2015), supports an underlying inflammatory mechanism that should be considered in future intervention studies on animal and human subjects with WMSDs.

Supplementary data to this article can be found online at http://dx.doi.org/10.1016/j.exger.2015.10.014.

Conflict of Interests

None of the authors have any conflicts of interest issues to declare.

Acknowledgments

Research reported in this publication was supported by the National Institute of Arthritis and Musculoskeletal and Skin Diseases of the National Institutes of Health under award number AR056019 to MFB. The content is solely the responsibility of the authors and does not necessarily represent the official views of the National Institutes of Health. We would like to thank Shreya Amin and Roshanak Razmpour for sectioning the tissues.

References

Akhter, M.P., et al., 2007. Transmenopausal changes in the trabecular bone structure. Bone 41 (1), 111–116.
Amorim, B.J., et al., 2006. Low sensitivity of three-phase bone scintigraphy for the diagnosis of repetitive strain injury. Sao Paulo Med. J. 124 (3), 145–149.
Association of Occupational and Environmental Clinics, 2009. Healthy Aging for a Sustainable Workforce. Electronic Library of Contruction Occupational Safety and Health. CPWR - The Center for Construction Research and Training (http://www.elcosh.org/document/1684/957/d000987/2b-.html).
Barbe, M.F., et al., 2008. Serum and tissue cytokines and chemokines increase with repetitive upper extremity tasks. J. Orthop. Res. 26 (10), 1320–1326.
Barbe, M.F., et al., 2013a. The interaction of force and repetition on musculoskeletal and neural tissue responses and sensorimotor behavior in a rat model of work-related musculoskeletal disorders. BMC Musculoskelet. Disord. 14, 303.
Barbe, M.F., et al., 2013b. The interaction of force and repetition on musculoskeletal and neural tissue responses and sensorimotor behavior in a rat model of work-related musculoskeletal disorders. BMC Musculoskelet. Disord. 14 (1), 303.
Barbe, M.F., et al., 2013c. The interaction of force and repetition on musculoskeletal and neural tissue responses and sensorimotor behavior in a rat model of work-related musculoskeletal disorders. BMC Musculoskelet. Disord. 14 (1), 303.
Barbe, M.F., et al., 2015. Ergonomic task reduction prevents bone osteopenia in a rat model of upper extremity overuse. Ind. Health 53 (3), 206–221.
Barr, A.E., et al., 2003. Repetitive, negligible force reaching in rats induces pathological overloading of upper extremity bones. J. Bone Miner. Res. 18 (11), 2023–2032.
Borah, B., et al., 2010. Risedronate reduces intracortical porosity in women with osteoporosis. J. Bone Miner. Res. 25 (1), 41–47.
Bouxsein, M.L., et al., 2010. Guidelines for assessment of bone microstructure in rodents using micro-computed tomography. J. Bone Miner. Res. Off. J. Am. Soc. Bone Miner. Res. 25 (7), 1468–1486.
Brennan, T., et al., 2011. Abrogation of Cbl–PI3K interaction increases bone formation and osteoblast proliferation. Calcif. Tissue Int. 89 (5), 396–410.
Bureau of Labor Statistics, 2011. Nonfatal occupational injuries and illnesses requiring days away from work. (http://www.bls.gov/news.release/osh2.nr0.htm News Release USDL-12-2204, November 8, 2012, 2012).
Bureau of Labor Statistics, 2012. Nonfatal Occupational Injuries and Illnesses Requiring Days Away from Work. U.S. Department of Labor (http://www.bls.gov/news.release/osh2.nr0.htm. 2012 01/05/2011; Available from: http://www.bls.gov/news.release/osh2.nr0.htm).
Burr, D.B., Robling, A.G., Turner, C.H., 2002. Effects of biomechanical stress on bones in animals. Bone 30 (5), 781–786.
Burr, D.B., et al., 1997. Bone microdamage and skeletal fragility in osteoporotic and stress fractures. J. Bone Miner. Res. 12 (1), 6–15.
Burr, D.B., et al., 2001. Intermittently administered human parathyroid hormone(1–34) treatment increases intracortical bone turnover and porosity without reducing bone strength in the humerus of ovariectomized cynomolgus monkeys. J. Bone Miner. Res. 16 (1), 157–165.
Carp, S.J., et al., 2007. Inflammatory biomarkers increase with severity of upper-extremity overuse disorders. Clin. Sci. 112 (5), 305–314.
Cevenini, E., et al., 2010. Age-related inflammation: the contribution of different organs, tissues and systems. How to face it for therapeutic approaches. Curr. Pharm. Des. 16 (6), 609–618.
Chen, P., et al., 2007. Increases in BMD correlate with improvements in bone microarchitecture with teriparatide treatment in postmenopausal women with osteoporosis. J. Bone Miner. Res. 22 (8), 1173–1180.
Cho, T.J., Gerstenfeld, L.C., Einhorn, T.A., 2002. Differential temporal expression of members of the transforming growth factor beta superfamily during murine fracture healing. J. Bone Miner. Res. 17 (3), 513–520.
Cho, H.H., et al., 2010. NF-kappaB activation stimulates osteogenic differentiation of mesenchymal stem cells derived from human adipose tissue by increasing TAZ expression. J. Cell. Physiol. 223 (1), 168–177.
Clark, B.D., et al., 2004. Performance of a high-repetition, high-force task induces carpal tunnel syndrome in rats. J. Orthop. Sports Phys. Ther. 34 (5), 244–253.
Cote, J.N., 2012. A critical review on physical factors and functional characteristics that may explain a sex/gender difference in work-related neck/shoulder disorders. Ergonomics 55 (2), 173–182.

Dempster, D.W., 2000. The contribution of trabecular architecture to cancellous bone quality. J. Bone Miner. Res. 15 (1), 20–23.
Dempster, D.W., et al., 2013. Standardized nomenclature, symbols, and units for bone histomorphometry: a 2012 update of the report of the ASBMR Histomorphometry Nomenclature Committee. J. Bone Miner. Res. 28 (1), 2–17.
Dhainaut, A., et al., 2013. Cortical hand bone porosity and its association with distal radius fracture in middle aged and elderly women. PLoS One 8 (7), e68405.
Ding, M., Odgaard, A., Hvid, I., 2003. Changes in the three-dimensional microstructure of human tibial cancellous bone in early osteoarthritis. J. Bone Joint Surg. Br. 85 (6), 906–912.
Ding, H., et al., 2010. Hand osteoarthritis and pinch grip strength among middle-aged female dentists and teachers. Scand. J. Rheumatol. 39 (1), 84–87.
Driban, J.B., et al., 2011. Joint inflammation and early degeneration induced by high-force reaching are attenuated by ibuprofen in an animal model of work-related musculoskeletal disorder. J. Biomed. Biotechnol. 2011, 691412.
Elliott, M.B., Barr, A.E., Barbe, M.F., 2009a. Spinal substance P and neurokinin-1 increase with high repetition reaching. Neurosci. Lett. 454 (1), 33–37.
Elliott, M.B., et al., 2008. Peripheral neuritis and increased spinal cord neurochemicals are induced in a model of repetitive motion injury with low force and repetition exposure. Brain Res. 1218, 103–113.
Elliott, M.B., et al., 2009b. High force reaching task induces widespread inflammation, increased spinal cord neurochemicals and neuropathic pain. Neuroscience 158 (2), 922–931.
Elliott, M.B., et al., 2010. Performance of a repetitive task by aged rats leads to median neuropathy and spinal cord inflammation with associated sensorimotor declines. Neuroscience 170 (3), 929–941.
Erselcan, T., et al., 2001. Carpal tunnel syndrome leads to significant bone loss in metacarpal bones. J. Bone Miner. Metab. 19 (5), 317–320.
Ershler, W.B., Keller, E.T., 2000. Age-associated increased interleukin-6 gene expression, late-life diseases, and frailty. Annu. Rev. Med. 51, 245–270.
Foss, L., et al., 2011. The impact of workplace risk factors on long-term musculoskeletal sickness absence: a registry-based 5-year follow-up from the Oslo health study. J. Occup. Environ. Med. 53 (12), 1478–1482.
Gerr, F., et al., 2002. A prospective study of computer users: I. Study design and incidence of musculoskeletal symptoms and disorders. Am. J. Ind. Med. 41 (4), 221–235.
Gravallese, E.M., 2002. Bone destruction in arthritis. Ann. Rheum. Dis. 61 (Suppl. 2) (ii84-6).
Green, J.O., et al., 2011. Age-related changes in human trabecular bone: relationship between microstructural stress and strain and damage morphology. J. Biomech. 44 (12), 2279–2285.
Guo, R., et al., 2008. Ubiquitin ligase Smurf1 mediates tumor necrosis factor-induced systemic bone loss by promoting proteasomal degradation of bone morphogenetic signaling proteins. J. Biol. Chem. 283 (34), 23084–23092.
Hell, R.C., et al., 2012. Physical activity improves age-related decline in the osteogenic potential of rats' bone marrow-derived mesenchymal stem cells. Acta Physiol. (Oxf) 205 (2), 292–301.
Hildebrand, T., Ruegsegger, P., 1997. Quantification of bone microarchitecture with the structure model index. Comput. Methods Biomech. Biomed. Engin. 1 (1), 15–23.
Iolascon, G., et al., 2014. Bone quality and bone strength: benefits of the bone-forming approach. Clin. Cases Min. Bone Metab. 11 (1), 20–24.
Jain, N.X., et al., 2014. Bone loss from high repetitive high force loading is prevented by ibuprofen treatment. J. Musculoskelet. Neuronal Interact. 14 (1), 78–94.
Kaneki, H., et al., 2006. Tumor necrosis factor promotes Runx2 degradation through up-regulation of Smurf1 and Smurf2 in osteoblasts. J. Biol. Chem. 281 (7), 4326–4333.
Keaveny, T.M., et al., 2010. Age-dependence of femoral strength in white women and men. J. Bone Miner. Res. 25 (5), 994–1001.
Khosla, S., et al., 2011. Forum on aging and skeletal health: summary of the proceedings of an ASBMR workshop. J. Bone Miner. Res. 26 (11), 2565–2578.
Kietrys, D.M., Barr, A.E., Barbe, M.F., 2011a. Exposure to repetitive tasks induces motor changes related to skill acquisition and inflammation in rats. J. Mot. Behav. 43 (6), 465–476.
Kietrys, D.M., Barr, A.E., Barbe, M.F., 2011b. Exposure to repetitive tasks induces motor changes related to skill acquisition and inflammation in rats. J. Mot. Behav. 43 (6), 465–476.
Kietrys, D.M., et al., 2012. Aging contributes to inflammation in upper extremity tendons and declines in forelimb agility in a rat model of upper extremity overuse. PLoS One 7 (10), e46954.
Kulkarni, R.N., et al., 2012. Mechanical loading prevents the stimulating effect of IL-1beta on osteocyte-modulated osteoclastogenesis. Biochem. Biophys. Res. Commun. 420 (1), 11–16.
Lacey, D.C., et al., 2009. Proinflammatory cytokines inhibit osteogenic differentiation from stem cells: implications for bone repair during inflammation. Osteoarthr. Cartil. 17 (6), 735–742.
Lange, J., et al., 2010. Action of IL-1beta during fracture healing. J. Orthop. Res. 28 (6), 778–784.
Leppanen, O.V., et al., 2008. Pathogenesis of age-related osteoporosis: impaired mechano-responsiveness of bone is not the culprit. PLoS One 3 (7), e2540.
Leskela, H.V., et al., 2003. Osteoblast recruitment from stem cells does not decrease by age at late adulthood. Biochem. Biophys. Res. Commun. 311 (4), 1008–1013.
Liu, X.S., et al., 2010. Individual trabeculae segmentation (ITS)-based morphological analysis of high-resolution peripheral quantitative computed tomography images detects abnormal trabecular plate and rod microarchitecture in premenopausal women with idiopathic osteoporosis. J. Bone Miner. Res. 25 (7), 1496–1505.
McLaughlin, F., et al., 2002. Glucocorticoid-induced osteopenia in the mouse as assessed by histomorphometry, microcomputed tomography, and biochemical markers. Bone 30 (6), 924–930.
Mihara, M., et al., 1995. Interleukin-6 (IL-6) induces the proliferation of synovial fibroblastic cells in the presence of soluble IL-6 receptor. Br. J. Rheumatol. 34 (4), 321–325.
Mueller, S.M., Glowacki, J., 2001. Age-related decline in the osteogenic potential of human bone marrow cells cultured in three-dimensional collagen sponges. J. Cell. Biochem. 82 (4), 583–590.
Mueller, D., et al., 2006. The 3D-based scaling index algorithm: a new structure measure to analyze trabecular bone architecture in high-resolution MR images in vivo. Osteoporos. Int. 17 (10), 1483–1493.
Mumme, M., et al., 2012. Interleukin-1beta modulates endochondral ossification by human adult bone marrow stromal cells. Eur. Cell Mater. 24, 224–236.
al-Nahhas, A.M., et al., 1997. 99Tcm-MDP blood-pool phase in the assessment of repetitive strain injury. Nucl. Med. Commun. 18 (10), 927–931.
NIOSH, 2011. National Manufacturing Agenda - June 2010. ([cited 2011 October 23]; Available from: http://www.cdc.gov/niosh/nora/comment/agendas/manuf/).
Nishiyama, K.K., et al., 2010. Postmenopausal women with osteopenia have higher cortical porosity and thinner cortices at the distal radius and tibia than women with normal aBMD: an in vivo HR-pQCT study. J. Bone Miner. Res. 25 (4), 882–890.
Orjalo, A.V., et al., 2009. Cell surface-bound IL-1alpha is an upstream regulator of the senescence-associated IL-6/IL-8 cytokine network. Proc. Natl. Acad. Sci. U. S. A. 106 (40), 17031–17036.
OSHA, 2014. Prevention of work-related musculoskeletal disorders. ([cited 2014 06/22/2014]; Available from: https://www.osha.gov/pls/oshaweb/owadisp.show_document?p_table=UNIFIED_AGENDA&p_id=4481).
Parfitt, A.M., et al., 1987. Bone histomorphometry: standardization of nomenclature, symbols, and units. Report of the ASBMR Histomorphometry Nomenclature Committee. J. Bone Miner. Res. 2 (6), 595–610.
Pearson, O.M., Lieberman, D.E., 2004. The aging of Wolff's "law": ontogeny and responses to mechanical loading in cortical bone. Am. J. Phys. Anthropol. 125 (S39), 63–99.
Rani, S., et al., 2009. Periostin-like-factor and periostin in an animal model of work-related musculoskeletal disorder. Bone 44 (3), 502–512.
Rani, S., et al., 2010. Role of TNF alpha and PLF in bone remodeling in a rat model of repetitive reaching and grasping. J. Cell. Physiol. 225 (1), 152–167.
Ratzlaff, C.R., Gillies, J.H., Koehoorn, M.W., 2007. Work-related repetitive strain injury and leisure-time physical activity. Arthritis Rheum. 57 (3), 495–500.
Rechardt, M., et al., 2011. Soluble IL-1RII and IL-18 are associated with incipient upper extremity soft tissue disorders. Cytokine 54 (2), 149–153.
Rechardt, M., et al., 2013. Associations of metabolic factors and adipokines with pain in incipient upper extremity soft tissue disorders: a cross-sectional study. BMJ Open 3 (8), e003036.
Riondino, S., et al., 2011. Functional impairment in video terminal operators is related to low-grade inflammation. Int. Arch. Occup. Environ. Health 84 (7), 745–751.
Robling, A.G., Burr, D.B., Turner, C.H., 2001. Skeletal loading in animals. J. Musculoskelet. Neuronal Interact. 1 (3), 249–262.
Saine, M.E., et al., 2011. Hypothalamic suppression during adolescence varies by bone envelope. Med. Sci. Sports Exerc. 43 (4), 608–616.
Salvioli, S., et al., 2006. Inflamm-aging, cytokines and aging: state of the art, new hypotheses on the role of mitochondria and new perspectives from systems biology. Curr. Pharm. Des. 12 (24), 3161–3171.
Sample, S.J., et al., 2010. Systemic effects of ulna loading in male rats during functional adaptation. J. Bone Miner. Res. 25 (9), 2016–2028.
Savas, S., et al., 2007. Metacarpal bone density in carpal tunnel syndrome patients without thenar atrophy. Rheumatism 22, 15–19.
Silverstein, M., 2008. Meeting the challenges of an aging workforce. Am. J. Ind. Med. 51 (4), 269–280.
Solovieva, S., et al., 2005. Hand use and patterns of joint involvement in osteoarthritis. A comparison of female dentists and teachers. Rheumatology (Oxford) 44 (4), 521–528.
Srilatha, et al., 2011. Prevalence of work-related wrist and hand musculoskeletal disorders (WMSD) among computer users. J. Clin. Diagn. Res. 5 (3), 605–607.
Srinivasan, S., Gross, T.S., Bain, S.D., 2012. Bone mechanotransduction may require augmentation in order to strengthen the senescent skeleton. Ageing Res. Rev. 11 (3), 353–360.
Srinivasan, S., et al., 2003. Enabling bone formation in the aged skeleton via rest-inserted mechanical loading. Bone 33 (6), 946–955.
Stowe, R.P., et al., 2010. Plasma cytokine levels in a population-based study: relation to age and ethnicity. J. Gerontol. A Biol. Sci. Med. Sci. 65 (4), 429–433.
Thomas, T., 2010. [New actors in bone remodelling: a role for the immune system]. Bull. Acad. Natl Med. 194 (8), 1493–1503 (discussion 1503-4).
Turner, C.H., 2007. Aging and fragility of bone. J. Musculoskelet. Neuronal Interact. 7 (4), 342–343.
Turner, C.H., Takano, Y., Owan, I., 1995. Aging changes mechanical loading thresholds for bone formation in rats. J. Bone Miner. Res. 10 (10), 1544–1549.
Vehmas, T., et al., 2005. Hand workload and the metacarpal cortical index. A study of middle-aged teachers and dentists. Osteoporos. Int. 16 (6), 672–680.
Warden, S.J., et al., 2005. Bone adaptation to a mechanical loading program significantly increases skeletal fatigue resistance. J. Bone Miner. Res. 20 (5), 809–816.
WHO Scientific Group, 2003. The Burden of Musculoskeletal Conditions at the Start of the New Millennium.
World Health Organization, 2007. Workers' Health: Global Plan of Action.
Wu, B., et al., 2013. Self-repair of rat cortical bone microdamage after fatigue loading in vivo. Int. J. Endocrinol. 2013, 321074.
Xin, D.L., et al., 2011a. Aging enhances serum cytokine response but not task-induced grip strength declines in a rat model of work-related musculoskeletal disorders. BMC Musculoskelet. Disord. 12, 63.
Xin, D.L., et al., 2011b. Aging enhances serum cytokine response but not task-induced grip strength declines in a rat model of work-related musculoskeletal disorders. BMC Musculoskelet. Disord. 12, 63.